



Università degli Studi di Cagliari

PHD DEGREE

Chemical Sciences and Technologies

Cycle XXXIII

TITLE OF THE PHD THESIS

Synthesis and characterization of nanostructured adsorbents for
the removal of inorganic and organic pollutants from water

Scientific Disciplinary Sector

CHIM/02

PhD Student : Giulia Rossella Delpiano

Supervisor : Andrea Salis

Co-supervisor : Edmond Magner

Co-supervisor : Katia Testa

Final exam. Academic Year 2019/2020

Thesis defence: January 2022 Session

Abstract

In recent years water contamination is reaching alarming levels, since the concentration of pollutants present in seas, lakes and streams has far exceeded water self-purifying capacity. The most widespread sources responsible for water pollution are urban and industrial dumps containing a vast range of dangerous substances. Despite wastewaters are always subjected to purification treatments, a complete remediation is not always possible. The most common pollutants are heavy metal ions and organic compounds such as phenolic compounds, polybrominated diphenyl ethers (PBDEs), polycyclic aromatic hydrocarbons (PAHs), pesticides and synthetic dyes. All these substances are highly stable and can easily bioaccumulate in living organisms as xenobiotic molecules, causing chronic and acute toxicity or carcinogenic and mutagenic effects.

Furthermore, substances as dyes can cause changes to the aquatic ecosystem as they absorb the sunlight limiting its penetration into deep waters, thus inhibiting the photosynthesis of aquatic plants and thus limiting the water re-oxygenation capacity.

In such a scenario, in the last few decades the scientific community has put a great deal of effort into the improvement of wastewater remediation processes. Among the various treatments, adsorption is one of the most useful thanks to its simplicity and low cost. The great advancement in nanotechnology has paved the way for new highly effective nanostructured adsorbent materials. These generally porous nanoadsorbents are characterized by a high surface area and high surface/volume ratio, which greatly influence their adsorption capacity.

The purpose of this thesis work was the development of new mesoporous adsorbents, namely functionalized ordered mesoporous silica (OMS) and metal organic frameworks (MOFs) for the removal of heavy metal ions and organic dyes two types of pollutants commonly present in wastewaters..

Both OMS and MOFs are characterized by high surface area, high surface/volume ratio, geometrical order, and easy synthesis or functionalization.

SBA-15 OMS and Fe-BTC type MOF have been successfully synthesized and characterized by means of different techniques, such as small angle X rays scattering (SAXS), powder X-rays diffraction (XRD), N₂ physisorption, transmission and scanning electron microscopy (TEM and SEM), thermogravimetric analysis (TGA) and Fourier transform infrared spectroscopy (FT-IR).

SBA-15 was functionalized with two different organic ligands, namely triethylenetetramine (TETA) and 2,8-dithia-5-aza-2,6-pyridinophane macrocycle (PyNS₂), to obtain two different adsorbents, named SBA-TETA and SBA-PyNS₂ which have been tested against some heavy metal ions (Cu²⁺, Zn²⁺ and Cd²⁺).

The Fe-BTC, without further modifications, was instead tested as an adsorbent of two highly toxic organic dyes, such as Alizarin red S (ARS) and Malachite Green (MG).

All adsorption experiments were monitored using Inductive Coupled Plasma Optical Emission Spectroscopy (ICP-OES) or UV-Vis Spectroscopy. This allowed the experimental determination of the adsorption capacity q of the three adsorbents, their thermodynamic and kinetic parameters.

In the case of SBA-15-based adsorbents, further investigations on their properties were carried out by means of potentiometric titrations.

INDEX

ABSTRACT.....	1
1 - WATER POLLUTION	5
1.1 - HEAVY METALS	7
1.1.1 - Zinc	9
1.1.2 - Copper	10
1.1.3 - Cadmium.....	11
1.2 - ORGANIC DYES	11
1.2.1 - Malachite Green	14
1.2.2 - Alizarin Red S	14
1.3 - WATER REMEDIATION TREATMENTS	15
1.3.1 - Precipitation.....	16
1.3.2 - Oxidation	17
1.3.3 - Ion-exchange.....	19
1.3.4 - Membrane filtration.....	19
1.3.5 - Flocculation.....	20
1.3.6 - Adsorption	21
1.3.7 - Bio-sorption	22
2 - ADSORBENT MATERIALS	23
2.1 - ORDERED MESOPOROUS SILICA (OMS).....	23
2.2 - METAL-ORGANIC FRAMEWORKS (MOFs)	27
3 - KINETICS AND THERMODYNAMICS OF ADSORPTION.....	29
3.1 - ADSORPTION ISOTHERMS.....	31
3.1.1 - Langmuir model	33
3.1.2 - Freundlich model.....	34
3.1.3 - Temkin model.....	36
3.2 - ADSORPTION KINETICS	37
3.2.1 - Pseudo-First Order model.....	38
3.2.2 - Pseudo-Second Order model.....	39
3.2.3 - Intraparticle Diffusion model.....	39
4 - CHARACTERIZATION TECHNIQUES	42
4.1 - X-RAYS TECHNIQUES.....	43
4.1.1 - Small Angle X-Rays Scattering (SAXS)	45
4.1.2 - Powder X-Rays Diffraction (XRD)	47
4.3 - NITROGEN PHYSISORPTION.....	48
4.4 - ELECTRON MICROSCOPY	50
4.4.1 - Transmission Electron Microscopy (TEM)	51
4.4.2 - Scanning Electron Microscopy (SEM).....	53
4.6 - THERMOGRAVIMETRIC ANALYSIS (TGA).....	54
4.7 - FOURIER TRANSFORM INFRARED SPECTROSCOPY (FTIR)	55
4.7.1 - Total Attenuated Reflectance (ATR) sampling system.....	57

4.8 - UV-VIS ABSORPTION SPECTROSCOPY	58
4.9 - INDUCTIVELY COUPLED PLASMA OPTICAL EMISSION SPECTROSCOPY (ICP-OES)	60
4.10 - POTENTIOMETRIC TITRATIONS	61
4.10.1 - <i>The Glass Electrode (GE)</i>	64
5 - AIM OF THE THESIS.....	66
5.1 - FUNCTIONALIZED OMS FOR THE ADSORPTION OF HEAVY METAL IONS	66
5.2 - FE-BTC TYPE MOF FOR THE ADSORPTION OF ORGANIC DYES.....	69
REFERENCES	71
PAPER I	
PAPER II	
PAPER III	
PAPER IV	
AKNOWLEDGEMENTS.....	

1 - Water pollution

In recent decades, the pollution of the planet has reached alarming levels that have led to a real environmental emergency. Particularly, water contamination is reaching alarming levels for many ecosystem. Water has a great self-purifying power due to its ability to absorb oxygen from the atmosphere and its high solvent capacity that allows it to dissolve most of the pollutants introduced into it. Unfortunately, nowadays the concentration of contaminants present in seas, lakes and streams has far exceeded its self-purifying capacity. Soil and atmosphere pollution also indirectly contribute to water contamination. As a matter of fact, substances as fertilizers or pesticides distributed in the soil by agricultural activities and very fine gases and dust diffused into the air by industrial activities, heating systems and use of fossil fuels, are then carried by rain into rivers, seas and oceans.

Textile, tanning, food, cosmetic and pharmaceutical industries in continuous growth contribute strongly to the spillage of bio-recalcitrant and hazardous chemicals in the environment.¹

The most widespread sources responsible for water pollution are urban and industrial dumps containing a vast range of dangerous substances. This phenomenon is directly related to the disproportionate growth in global population. In various parts of the world, and particularly in developing countries, wastewaters are directly discharged into water bodies such as rivers, lakes and seas. On the other hand, in industrialized countries, despite wastewaters are subjected to purification treatments, it is not always possible to completely remove the pollutants present in it.

Pollutants can be divided into three categories: biological, organic and inorganic.

Biological contaminants include bacteria and viruses responsible for waterborne diseases, such as hepatitis, cholera, typhoid fever, dysentery, polio, etc.

Inorganic pollutants are metals, salts and minerals which are naturally present in the environment, but whose concentration and distribution in the environment is altered by various anthropogenic activities such as mining, metallurgical and chemical processes. The toxicity of these substances derives from their accumulation in the food chains.² In this category, heavy metal ions are of

considerable concern to the scientific community due to their devastating effects on the health of living organisms.

The category of organic pollutants is certainly the richest, because it embraces a wide variety of substances ranging from food waste, to phenolic compounds, polybrominated diphenyl ethers (PBDEs), polycyclic aromatic hydrocarbons (PAHs), per- and polyfluoroalkyl substances (PFAS), pesticides, petroleum, dyes and organochlorine pesticides (OCPs).^{3,4} The feature that makes them highly dangerous is their persistence, because of their high lipid solubility, lipophilicity and hydrophobicity, which causes a strong bioaccumulation.⁵ Organic chemicals are linked to the poisoning of kidney, liver and cerebral nervous system, while inorganic ions (such as heavy metals and their derivatives) cause hypertension, infantile cyanosis, poisoning and cancer.⁶

The consequences of water pollution are devastating for the environment since, in addition to the direct effects on health of living species, pollutants trigger mechanisms capable of altering the entire ecosystem. For instance, substances rich in nitrogen and phosphorus as fertilizers or detergents, cause an enrichment of the waters in nutritional salts, which increases the production of algae, aquatic plants and fitoplancton. The consistent biomass thus formed requires - at the end of its life cycle - a significant amount of oxygen for its degradation by microorganisms. This creates an anoxic environment and an exponential growth of anaerobic organisms which, by decomposing the organic substance in the absence of oxygen, release toxic compounds, such as ammonia and hydrogen sulfide (H₂S). This phenomenon, known as water eutrophication, reduces biodiversity and causes structural changes to the ecosystem.

Another alarming phenomenon is due to water soluble dyes. Due to their high ability to absorb sunlight, they prevent its penetration into deep waters, thus inhibiting the photosynthesis processes of the aquatic flora. This results into a decrease in the availability of oxygen for marine fauna.

As part of this thesis, we wanted to focus on the water remediation from heavy metals and dyes by means of porous adsorbents.

1.1 - Heavy Metals

Conventionally, heavy metals are defined as those elements characterized by high atomic weight and density higher than 4.5 g/cm^3 . However, the term "heavy metal" is considered imprecise and misleading, as asserted by the International Union of Pure and Applied Chemistry.⁷ The elements listed as heavy metals range from transition metals (from vanadium to zinc), to alkali metals (as barium), to non-metals (as selenium), to metalloids (as arsenic), and are generally associated with pollution and toxic effects. For this reason, Pourret et al. have proposed the replacement of the term "heavy metals" with the term "Potentially Toxic Element(s)" (PTEs), abandoning the definition based solely on atomic weight.⁸ These elements share common characteristics such as cationic character with different oxidation states and the strong aptitude to form molecular complexes in the cytoplasm.

PTEs are natural components of the earth's crust which cannot be degraded or destroyed. They can be found in the form of hydroxides, oxides, sulfides, sulfates, phosphates, silicates and organic compounds, and are usually present in trace amounts in natural waters because of volcanic eruptions, rock weathering, biogenic sources and wind-borne soil particles. Unfortunately, the amount of PTEs present in the waters is increased disproportionately due to anthropogenic activities such as automobile exhaust (release of Pb), smelting (release of As, Cu and Zn), insecticides (release of As) and fossil fuels burning (release of Ni, V, Hg and Se).² The most common metal pollution in freshwater comes from mining activity. The acid solutions used in the drainage processes designed to free the heavy metals from the natural matrix, are generally disperse into the groundwater.

PTEs penetrate into aquatic organisms, where can be stored in species tissues, (particularly fatty tissues) thus becoming part of the food chain of other species, including humans. Some heavy metals, such as Fe, Cu and Zn, are defined "essential metals" because they play a key role in the functionality of the cells of living organisms and, in right concentration, are necessary for their survival. However, if in excess they are not metabolized by the body and thus accumulate in the soft

tissues, giving rise to toxic effects on health. On the contrary, elements such as As, Pb, Cd, Ni, Hg, Cr, Co are highly toxic even at very low concentrations, as they have no biological function.

The solubility of heavy metals ions increases with decreasing pH. Once dissolved in water, PTEs in their ionic form become quite dangerous as they can displace essential metals from their biological sites causing malfunctioning of the cellular processes. Alternatively, they can react with other ions generating new toxic compounds inside the body, such as reactive oxygen (ROS) and nitrogen (RNS) species.⁹ ROS include hydroxyl radical ($\cdot\text{OH}$), superoxide ($\text{O}_2^{\cdot-}$) and hydrogen peroxide (H_2O_2), while RNS include nitric oxide ($\text{NO}\cdot$) and its derivative peroxynitrite (ONOO^-).

ROS and RNS are cellular metabolites that are produced in a para-physiological way in the living organism during normal metabolic processes involving lipids, proteins, carbohydrates and nucleic acids.¹⁰ Antioxidant enzymes such as glutathione (GSH) compensate the natural production of ROS and RNS, protecting proteins and other oxidizable compounds. When exogenous stimuli increase the concentration of RNS and ROS beyond that which is physiologically tolerated, oxidative stress phenomena occur, causing a direct alteration of biomolecules. This causes inflammatory conditions, lipids peroxidation,¹¹ DNA damages, neoplastic and atherosclerotic degenerations.¹²

In **Table 1** the maximum permitted concentrations (MPC) for PTEs in natural waters recommended by the EPA (Environmental Protection Agency) for the protection of human health, are reported.

Table 1. Maximum permitted concentrations (MPC) for PTEs in natural waters recommended by the EPA.

	<i>Hg</i>	<i>Pb</i>	<i>Cd</i>	<i>Fe</i>	<i>Ni</i>	<i>Cr</i>	<i>Se</i>	<i>Mn</i>	<i>Ba</i>
MPC (mg/m ³)	0.144	5	10	300	13.4	50	10	50	1000

These numbers are useful for comparing the degree of toxicity of the various elements in question. Mercury appears to be the most dangerous element among these mentioned, followed by lead, cadmium and selenium.

1.1.1 - Zinc

Zinc is a ubiquitous trace element essential in a several biological processes as catalytic, structural, and regulatory ion. It is crucial for the growth and development of animals, microorganism and plants, since it is essential constituent of hundreds proteins¹³ and cofactor of approximately 200 enzymes such as metalloproteinases, transferases, phosphatases and oxidoreductases.¹² For instance, as a cofactor for superoxide dismutase (SOD) and component of metallothioneins (MTs), zinc is indispensable to maintain a proper antioxidant status of the living organisms.^{14,15} MTs are proteins which favor the excretion of heavy metals like Pb, As and Hg from the body, while SOD is a metal enzyme responsible for the limitation of free-radicals proliferation, by dissociating the superoxide anion ($O_2^{\cdot-}$) into molecular oxygen. Moreover, zinc contributes to the synthesis of nucleic acids (DNA and RNA),¹⁴ stabilizes insulin hexamers,¹⁵ and regulates the activity of thymic hormones involved in the T lymphocytes maturation process.¹²

Zinc is introduced into the body through the diet, but its excess in food and water due to environmental pollution, leads to a higher than natural intake (which should be 2.5 and 10 *mg/day*).¹² The excessive supplementation brings to adverse effects such as the suppression of copper absorption.¹⁵ More precisely, in response to the excess of Zn, an increase of MTs occurs and, since MTs express greater affinity for Cu, the latter get bound by these proteins and no longer pumped into the circulation.¹⁶ This Zn-induced Cu deficiency triggers gastrointestinal reactions, hepatic deterioration and is one of the causes of hypochromic anemia.¹⁷

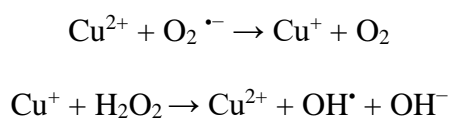
Beyond dietary intake, zinc exposures can occur even through dermal route by overuse of topical products (ointments, cosmetics, sunscreen, etc)¹⁸ containing zinc oxide (ZnO), renowned for its good transparency and refractive index properties. In nature ZnO does not exist in bulk quantities, but it is largely synthetically manufactured and commercialized. An annual production of 500 tons is estimated and about 70% is used by the cosmetic industry.¹⁹ ZnO nanoparticles can penetrate the cell membrane and other biological barriers, causing cellular dysfunctions. They also contribute to the

generation of reactive oxygen species,²⁰ resulting in oxidative stress, DNA damage, cytotoxicity and apoptosis.²¹

1.1.2 - Copper

Copper is present in different chemical forms throughout the earth crust, water and atmosphere. As an essential trace element, Cu plays an important role in several biological functions, as it is a constituent of numerous proteins and is involved in the activity of a wide range of enzymes like feroxidase, cytochrome C oxidase (CcO), superoxide dismutase (SOD), amine oxidase, laccase, catechol oxidase, tyrosinase etc.¹² These species are implicated in the development of bones and connective tissues, brain, heart and nervous system, but also in the formation of red blood cells, absorption/transport of iron, and in the metabolism of cholesterol and glucose. Furthermore, Cu even stimulates the immune system and collaborates in the elimination of free radicals.

As all the essential metals, copper is introduced into the living beings through the diet (with optimal uptake of 2 *mg/day*) and then eliminated by of biliary excretion. Copper chaperones are transporters proteins responsible of the transfer of Cu to its final destination or efflux out of cells when its concentration exceeds the optimum level.¹² Indeed, its cycle within the body (uptake, distribution, utilization and excretion) must be tightly regulated because excessive concentration of Cu can lead to the production of highly reactive oxidative species, able to cause devastating effects in cells, DNA, proteins and lipids. In the +2 oxidation state, copper can take place to the Fenton reaction, according to which Cu^{2+} , in the presence of superoxide $\text{O}_2^{\bullet -}$ or biological reductants (as ascorbic acid), can be reduced to Cu^+ and catalyze the formation of hydroxyl radical (OH^\bullet) through the decomposition of hydrogen peroxide H_2O_2 ¹²:



Moreover, both Cu(I) and Cu(II) have high affinity for cysteine, methionine, and histidine aminoacids, and can induce the displacement of other essential metal ions from their proteins active sites.

1.1.3 - Cadmium

Cadmium is a polluting agent classified as carcinogen. As a matter of fact, it is not involved in the in physiological processes of living organisms. Hence, since it has no biological function, Cd uptake, albeit in traces, can cause highly toxic effect both in plants and animals.

In plants, oxidation stress induced by Cd provokes a decrease of mineral nutrients uptake, inhibits seed germination, alters chlorophyll biosynthesis and photosynthesis.²²⁻²⁴ In both animals and plants, adsorbed Cd could also trigger the burst of ROS and RNS, highly destructive for cells metabolism and integrity, and causing DNA mutations.²⁵

Cadmium is released into the atmosphere from waste sites, incinerators, plants that smelt and refine metals or product batteries and plastics. In everyday life, it is also possible to inhale Cd directly by smoking tobacco or electronic cigarette,²⁶ by heating fishes coming from polluted water, or by dermal route though the use of particular cadmium pigments, which can also be inadvertently ingested in dry form.

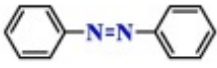
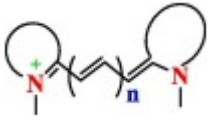
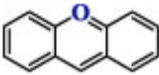
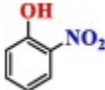
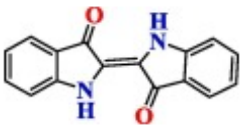
1.2 - Organic dyes

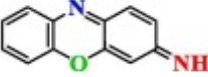
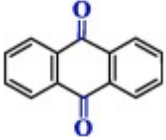
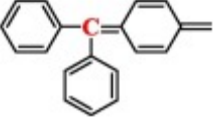
Before 19th century, dyes were extracted from natural sources (plants, insects, minerals) and, compared to synthetic dyes, were less toxic and more easily biodegradable.^{27,28} The first synthetic dye to have been mass-produced is the Mauvenine (also known as Aniline Purple), discovered serendipiously by W.H. Perkin in 1896 during his attempt to synthesize a compound for the treatments of malaria.^{29,30} Nowadays, commercially available synthetic dyes are more than 10000. They find application in cosmetics, printing, color photography, finishing processing of leather, pharmaceutical, etc, but the principal consumer of dyes is the textile industries.⁶

Their annual production for textile industry worldwide amounts to 700000 tons, and nearly 10% is discharged to environment after dyeing processes.³¹ Indeed, up to 50% of the dyes used are not fixed to the textile fibers, and persist in the liquid phase.^{32,33}

Organic dyes are characterized by an aromatic structure (normally based on rings of benzene, naphthaline or anthracene, etc.) composed by three fundamental groups : the chromophore, the auxochrome and the matrix.³⁰ The chromophore, capable of absorbing light radiation in the visible spectrum range (380-750 nm) thanks to the delocalized electrons of double bonds, represents the active site of the dye. The most common chromophores are nitro ($-\text{NO}_2$), azo ($-\text{N}=\text{N}-$), nitroso ($-\text{N}=\text{O}$), thiocarbonyl ($-\text{C}=\text{S}$), carbon-sulphur ($=\text{C}=\text{S}$; $\equiv\text{C}-\text{S}-\text{S}-\text{C}\equiv$), carbonyl ($-\text{C}=\text{O}$) and ethylene ($-\text{C}=\text{C}-$) groups. The auxochrome are ionizable groups which allows the fixation of the dye, and may be acidic ($-\text{COOH}$, $-\text{SO}_3$ and $-\text{OH}$) or basic ($-\text{NH}_2$, $-\text{NHR}$ and $-\text{NR}_2$). The rest of the atoms of the molecule correspond to the matrix.³⁰ A short classification based on chromophores is shown in Table 2.

Table 2. Classification of organic dyes based on chromophore groups.

Azo	
Cyanine	
Xanthene	
Nitro	
Indigoid	

Ozanine	
Antraquinone	
Thiophenil	

The degree of conjugation modulates the color of the dye and its intensity. For instance, when the number of aromatic nuclei increases, the high activity of the electrons π generates a displacement towards the long wavelength. Similarly, when an electron-donor auxochromic group (amino, hydroxy, alkoxy, etc.) is placed on a conjugated aromatic system joining the conjugation of the *p*-system, the resulting hyperconjugation leads to an enlargement of the absorbed wavelength range that gives rise to darker colors.

The complex design of these mainly aromatic structures is designed to satisfy the needs of the industries, providing lasting colors with high chemical and photolytic stability. The downside is that this high stability allows a large amount of synthetic dyes withstands conventional remediation treatments, and is therefore discharged into the environment, where persists thanks to its strong resistance against biodegradation.⁶

Once into the water bodies, these dyes absorb and reflect the sunlight stopping its penetration into deep waters, inhibiting the photosynthetic activities of aquatic plants and thus limiting the water re-oxygenation capacity.

Furthermore, the potentially toxic nature of these compounds represents an increasing hazard both in fishes and mammals. In fact, they tend to bioaccumulate as xenobiotic molecules, causing chronic and acute toxicity, disturbance of blood formation, carcinogenic and mutagenic effects.⁶

1.2.1 - Malachite Green

Malachite Green (MG) is a triphenyl cationic dye (IUPAC name [4-[[4-(dimethylamino)phenyl]-phenylmethylidene]cyclohexa-2,5-dien-1-ylidene]-dimethylazanium) commercialized as chloride or oxalate.

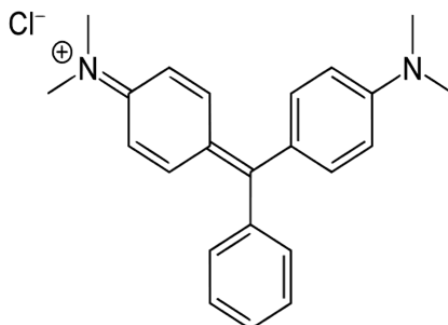


Figure 1. Molecular structure of Malachite Green (MG).

This organic salt finds application as fluorochrome counterstain in histology,³⁴ as antifungal drug in aquacultures,³⁵ and as dyeing agent of wool, leather, silk and fiber products in textile industries from which it is then spilled into the environment with the wastewaters.

However, MG is highly toxic and cannot undergo efficient biodegradation.^{36,37} Indeed, enters the food chain being readily absorbed by fishes where it is reduced by intestinal flora to leucomalachite green (LMG) metabolites.^{38,39} These metabolites persist in the tissues for as long as ten days and causes mutagenic and carcinogenic effects both in fishes and mammals.^{36,40-43} MG is therefore banned worldwide since 2002 for aquacultural use, and restricted in US and European manufacturing industries,⁴⁴ but it may still be used illegally, because of its low cost and high efficacy.³⁷

1.2.2 - Alizarin Red S

Alizarin Red S (ARS) is a water-soluble anionic dye of the anthraquinon class,⁴⁵ more precisely the sodium salt of 3,4-dihydroxy-9,10-dioxo-9,10-dihydroanthracene-2-sulfonic acid, also known as Mordant Red 3 or Alizarin Carmine.

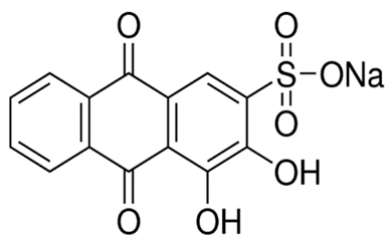


Figure 2. Molecular structure of Alizarin Red S (ARS).

It is used in the field of histology, thanks to its ability to chelate calcium to form an orange/red Lake pigment useful to stain calcium deposits in tissues⁴⁶⁻⁴⁸ or evaluate distribution of bone in developing embryos. ARS is also widely used in geology to stain and differentiate carbonate minerals and fossils,⁴⁹ and in marine science to mark daily growth layers in living corals.⁵⁰

Apart from applications in scientific research, ARS is even largely used for industrial dyeing of woven fabrics, wool, and cotton textiles to produce a deep and durable red color.^{51,52}

Like almost all organic dyes, ARS is characterized by high thermal, biological and optical stability because of its aromatic structures. Therefore it cannot be degraded completely via general biological and physicochemical processes.^{53,54}

ARS shares similar structure with flavonoids, a class of polyphenols from plants and fungi able to inhibit many enzymes.⁵⁵⁻⁵⁸ ARS can induce functional and conformational changes in enzymes such as catalase and cytochrome P450 isoenzymes, which have an important antioxidant function against oxidative damages induced by xenobiotics.⁵⁹ Hence, ARS can exploit mutagenic and carcinogenic effects. Many studies demonstrated that ARS can even bind serum albumins, and this enables it to reach any part of the organism by means of the blood.^{60,61}

1.3 - Water remediation treatments

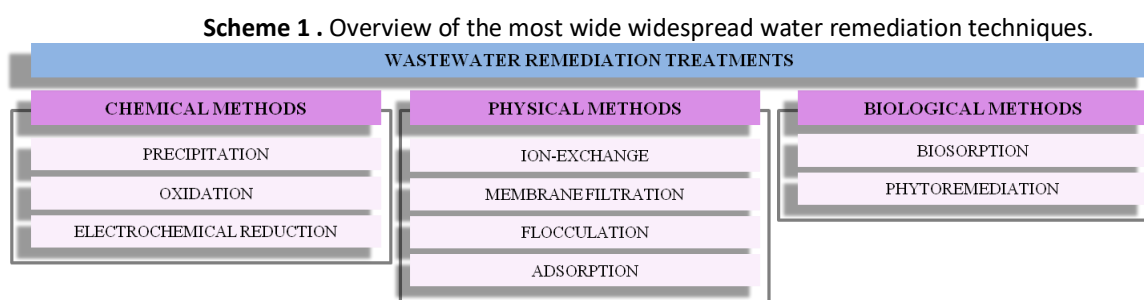
The methods currently used for the treatment of water contaminated by heavy metals and organic dyes are listed in the following paragraphs.

The conventional methods for the removal of polluting agents from water can be divided in physical, chemical and biological treatments.¹⁶² Physical techniques include adsorption, filtration, ion exchange, sedimentation, flocculation and extraction.

Chemical remediation techniques include oxidation methods, photocatalysis, enzymatic degradation, electrochemical transformation and precipitation. However these methods imply the use of expensive chemicals even though they are quite effective.⁶³ Biological approach mainly exploits the action of microbes for the degradation of pollutants. Other bioremediation techniques include phytoremediation, biofiltration and flocculation etc. Despite these approaches have been employed for the degradation of harmful pollutants from different sources, are time consuming, complicated, expansive and furthermore less efficient and specific.

In such a scenario, in the last few decades scientific community has made efforts devolved to the improvements of these remediation processes through the development of more efficient nano-based techniques.⁶⁴

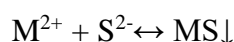
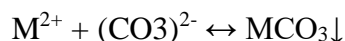
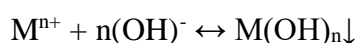
The most common remediation techniques are summarized in **Scheme 1** and described in the following paragraphs.



1.3.1 - Precipitation

Heavy metals can be removed by forming insoluble species (**Table 3**) by adding alkaline reagents as hydroxides (caustic soda NaOH, slaked lime Ca(OH)₂, magnesium hydroxide Mg(OH)₂), carbonates (slaked lime CaCO₃, soda ash Na₂CO₃), oxides (quicklime CaO), sulfides (iron sulfides FeS, alkali

and alkaline earths sulfides CaS and Na₂S, ammonium sulfide NH₄S, hydrogen sulfide H₂S) and/or artificially increasing the pH to exceed the solubility point.^{65,66}



The resulting metal oxides/carbonates/oxides precipitates are lastly removed from the stream by physical means, such as sedimentation or filtration.²

Precipitation, given the simplicity of its implementation and its low cost, represents the most commonly practiced in the industrial field.⁶⁴

Table 3. Summary of the *pks* values of some heavy metal ions precipitates.⁶⁷

	<i>Cu</i>	<i>Zn</i>	<i>Ni</i>	<i>Fe</i>	<i>Co</i>	<i>Pb</i>	<i>Cd</i>	<i>Hg</i>
OH⁻	14.7	15.7	14.7	15.1	14.8	16.1	13.6	25.4
CO₃²⁻	11.5	10.0	6.9	10.2	10.0	13.1	12.0	-
S²⁻	35.2	23.0	18.5	17.2	20.4	27	26.1	47.0

Hydroxide precipitation is the most widespread in metal removal due to its low cost and to the ease of recovering the metal hydroxides by flocculation and sedimentation at pH 8-11. However, sulfide precipitation has some advantages over hydroxide precipitation, such as lower solubility of metal sulfides, lower pH range and higher kinetic.⁶⁸

1.3.2 - Oxidation

The purpose of the oxidation processes is to destroy the organic pollutants into the water bulk transforming them in non-harmful compounds, without the need of separation and post-treatment processes.⁶⁹ There are several methods for oxidizing pollutants, including enzymatic catalysis, photocatalysis, the fenton reaction, etc.⁷⁰

Enzymatic approaches are based on the use of enzymes (e.g. peroxidases) generally immobilized on solid supports (mesoporous silica, MOFs), which guarantee their protection from hostile environment, stabilization and reuse.^{71,72}

The Fenton reaction is a radical-induced degradation based on the use of hydrogen peroxide H₂O₂ and iron cations Fe²⁺ which react generating hydroxyl radicals according to the reaction :⁷³



The Fenton reaction was discovered in 1876 by Henry John Horstman Fenton, who noted the color change of tartaric acid in presence of H₂O₂ and Fe²⁺ salts.⁷⁴ Fenton and modifier electro-Fenton processes have been extensively used for the degradation of benzene ring compounds, pesticides and azo-dyes.^{6,75} The disadvantages concerning the use of the Fenton process are the strict pH range, high cost due to the high H₂O₂ consumption, and loss of efficiency due to the accumulation of ferric sludge.⁷⁶

Photocatalysis is based on the use of metal-oxide semiconductor (generally nano-sized) photocatalysts which, being invested by radiations of suitable wavelength, get excited with the creation of a hole-electron pair able to cause the oxidation of chemical species adsorbed on the support surface. The transformation products are harmless substances.⁷⁷ The most common photocatalysts are TiO₂-based. Since the photocatalysts do not directly take part in the chemical transformation, they are reusable without loss of efficacy. The main disadvantage of these semiconductors is that their absorption spectrum falls more in the UV region than in the visible region. Moreover, although they do not undergo degradation, they are subject to fouling and coking phenomena, which make part of the active sites inaccessible, which makes periodic regeneration necessary to restore an acceptable level of activity.

1.3.3 - Ion-exchange

Ion-exchange is based on a reversible chemical reaction, in which ionic pollutants present in contaminated water replace other ions with same electrical charge present in the structure of a solid matrix, from which they can be retrieved later (**Figure 3**).⁷⁸

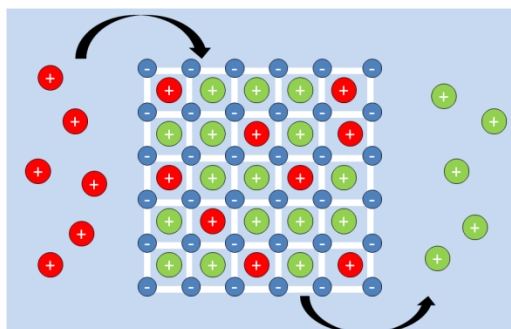


Figure 3 . Schematic representation of ion-exchange.

The exchange matrices are generally porous solids, such as zeolites, clays, synthetic resins, activated carbon and resins (highly ionic, covalently cross-linked, insoluble polyelectrolytes).^{66,79} The type of matrix and the pH regulation are the factors that control the selectivity of the process. The disadvantage of this method is that it can be applicable only to low concentration of contaminants.⁸⁰ Ion exchangers are able to exchange either positively-charged ion (cation exchanger) or negatively-charged ion (anion exchanger) depending on the insoluble acid or base.⁸¹ The synthetic organic ion exchange resins are the most commonly employed, and are characterized by the presence of a hydrophobic part (uncharged carbohydrate group) and a hydrophilic part.⁸²

1.3.4 - Membrane filtration

Filtration by means of membranes can eliminate a wide range of organic and inorganic contaminants, and suspended solids. This technology is very effective for the remediation of waters containing high concentration of pollutants, furthermore is rapid, require small space and generates low solid waste.⁶⁴ Membrane filtration technologies include principally ultrafiltration (UF), nano-filtration (NF) and reverse osmosis (RO).²

UF and NF consist in the use of porous mechanical filters the contaminants. UF membranes are characterized by pore size range from 5 to 20 nm, while NF membranes have pores one order of magnitude smaller, enable them to eliminate a greater number of substances. In RO, the process is driven by pressure, since the small size of the pores (in the order of 0.1 nm) does not confer spontaneity to the filtration, thus the completion of a mechanical work to cancel the effect of osmotic pressure is required. For this reason, even though RO is more efficient than UF, it requires more energy and is therefore more expensive. Furthermore, due to their tiny pores, RO membranes are more vulnerable to fouling (generally irreversible), which compromises their effectiveness and recyclability.

Usually, the membranes do not simply represent a physical obstacle determined by the size of the pores, but exploit the different chemical affinity of the species. In order to increase selectivity and efficiency, the surface of the membranes can be modified with the introduction of suitable functionalizing agents.⁸³

1.3.5 - Flocculation

Flocculation is a water and wastewater treatment technology whereby destabilization and consequent aggregation of pollutants in flocs thanks to the use of flocculating agents. The flocs can be later separated through sedimentation.⁴ Flocculants are generally chemicals with opposite charge to that of the pollutant to be removed. Once the pollutant is neutralized, the small suspended particles are capable of sticking together forming the flocs. The extent of flocculation depends on the opportunities for contact between the particles and therefore on the concentration of the particles and their size, but also on the velocity gradients in the system. Indeed, high-energy rapid-mix promote particle collisions that is needed to achieve good flocculation.⁶⁶

Inorganic flocculants are generally salts of multivalent metals, and are the most commonly used because of their low-cost and ease of use, although they have low flocculation efficiency and can generate secondary pollution due to a residue metal concentration in the treated water.⁸⁴

Even organic polymeric flocculants, although being much more effective, have the disadvantage of being poorly biodegradable. On the contrary, biopolymers based flocculants are highly environmental friendly but are needed in large dosage due to its moderate flocculating efficiency. Thus, recently different alternatives based on synthetic polymers grafted onto natural polymers are being studied, in order to combine the best properties of both.^{85,86}

1.3.6 - Adsorption

Adsorption is the process by which ions, atoms or molecules (adsorbate) adhere to the surface of a solid material (adsorbent). This phenomenon is limited to the surface, hence differs from absorption which implies the penetration of the fluid to the entire volume of a material (**Figure 4**).

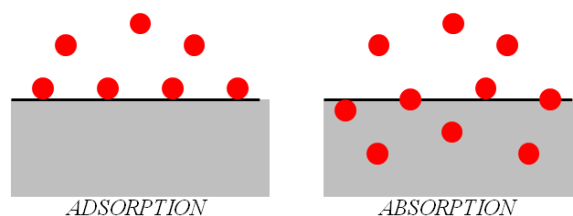


Figure 4. Representation of adsorption and absorption processes.

The characteristics of the adsorbent are crucial for the effectiveness of the treatment. Adsorbents must be inert and chemically stable materials, possibly recyclable and characterized, above all, by a high surface area. Nano-based approaches are economic and more efficient for the remediation of polluted water. Indeed, porous nanomaterials, which offer several advantages such as high surface area, better adsorption capacity and low costs, are the most popular for the implementation of this type of treatment. The most used adsorbents are activated carbon, silica, alumina, clay, metal oxides (such as CuO), molecular sieves and, in recent years, Metal Organic Frameworks (MOFs) are also attracting considerable interest. The choice of the material is made based on the type of substances to be adsorbed, and on the type of interaction to be exploited.

Depending on the type of interactions that are established between adsorbate and adsorbent, a distinction can be made between physical adsorption (based on weak interactions such as London's

forces, Van der Waals interactions and dipole-dipole forces) and chemical adsorption (based on stronger interactions such as chemical bonds). Physical adsorption is generally exploited, but the functionalization of the adsorbent material surface with suitable functional groups or molecules, allows for chemiadsorbing the pollutants, thus making the process more specific. In the aqueous environment, the improving factors of the adsorption process are high surface area, low surface binding energy, adsorption activity, chemical activity and lack of internal diffusion resistance.

The limit of the adsorption is that the adsorbent material loses efficiency with very concentrated solution due to a quick saturation with the adsorbate.²

1.3.7 - Bio-sorption

Biosorption refers to the removal of pollutants from water systems using biological materials as adsorbents. Biosorbents contain a wide variety of functional sites (i.e. carboxyl, imidazole, sulphhydryl, amino, phosphate, sulfate, thioether, phenol, carbonyl, amide and hydroxyl groups) and are easily available. Examples of bioadsorbents are bacteria, fungi, yeast, algae, industrial wastes (e.g. biomass wastes from fermentation and food industry), agricultural wastes (e.g. peels, shells, kernels)⁸⁷ and other polysaccharide materials, etc.⁸⁸ The pretreatment and modification of biosorbents aiming to improve their sorption capacity was introduced and evaluated. However, the biosorption easily reaches a breakthrough when applied to highly polluted solutions,² furthermore it is a slow process and the regeneration of the biosorbents is difficult.⁸⁹

2 - Adsorbent materials

Adsorbent materials can be classified as purely inorganic (silica, metal oxides, combined metal-silica based materials), purely organic (hollow carbon particles, organic polymers) or hybrid organic-inorganic materials (organosilica, Metal-Organic-Frameworks).⁹⁰

Generally the adsorbents have porous structure (**Figure 5**) which provides them a high surface area.

According to IUPAC (International Union Pure and Applied Chemistry), porous materials are classified on the basis of the pore diameter \emptyset :

- macroporous material: $\emptyset > 50$ nm;
- mesoporous material: $2 < \emptyset < 50$ nm;
- microporous materials: $\emptyset < 2$ nm.

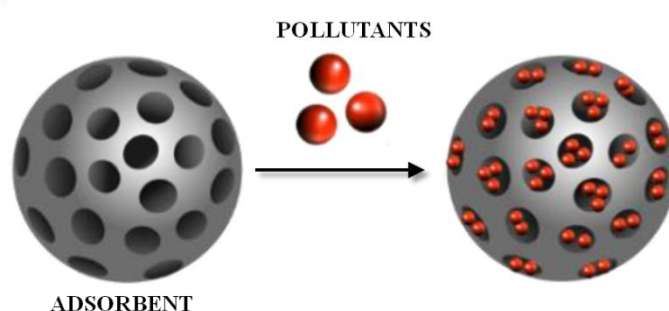


Figure 5. Representation of the pollutants adsorption performed by a porous material.

2.1 - Ordered Mesoporous Silica (OMS)

In the last decades, the interest for ordered mesoporous silica (OMS) has increased thanks to their characteristics such as the high surface area (up to $1000 \text{ m}^2/\text{g}$), high surface/volume ratio, uniformity of pore size ($2\text{-}20 \text{ nm}$), high structural order, excellent stability towards high temperatures, acidic pH, microbial attack, biocompatibility.^{91,92} These peculiar characteristics make OMS particularly suitable towards a wide range of applications such as nanomedicine,^{93,94} adsorption, catalysis and biocatalysis,⁷¹ and biosensing etc.

Furthermore, the OMS synthesis is very easy and reproducible,⁹⁵ and allows an easy modulation of the physical parameters of the material (size, pore dimensions, surface area, morphology and wall thickness).^{96,97}

The first method of direct synthesis of mesostructured silicas was published in 1992 by scientists of the Mobil Oil Corporation, who synthesized and characterized a new family of silica based mesoporous materials called M41S, with cubic phases (MCM-48), lamellar phases (MCM-50), and hexagonal phases (MCM-41).⁹⁸ Few years later, in 1998, the synthesis of another hexagonal OMS, similar to MCM-41, but constituted by larger particle and pore sizes, named SBA-15 (Santa Barbara Amorphous) was published.⁹⁹ MCM-41 and SBA-15 are surely the most famous silica-based mesostructures.^{100,101}

The mechanism at the base of OMS synthesis was initially defined as Liquid Crystal Templating Mechanism (LCT). Later studies contradicted the LCT mechanism and supported the hypothesis proposed by Monnier of a mechanism called Cooperative Templating Mechanism (CTM)¹⁰² (**Figure 6**) consisting of a cooperative formation of inorganic-organic interfaces in the synthesis of silicates mesostructures.¹⁰³

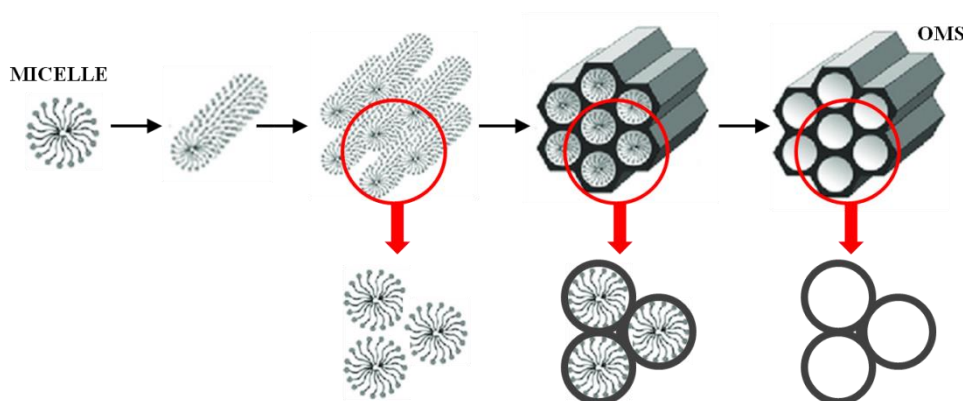


Figure 6. Schematic representation of the cooperative templating mechanism (CTM).

Surfactants dissolved in aqueous medium above their *critical micelle concentration* (CMC) generate supramolecular aggregates known as micelles thanks to the non covalent intermolecular interactions (such as hydrophobic interaction, van der Waals forces, including London forces, Keesom and Debye interaction, hydrogen bonds). By interacting with each other, the micelles form liquid

crystals, which will form a "mold" on which the silica structure will be modeled by polymerization of its polyanionic precursor (tetraalkoxysilane).

Indeed, the tetraalkoxysilane molecules (Tetraethylorthosilicate TEOS, Tetramethylorthosilicate TMOS, Glycidoxypropyltrimethoxysilane GPTMS), that constitute the precursors of silica, interact with the micellar systems arranging themselves on their external surface, reducing the micelles mobility and stabilizing the dispersion.¹⁰⁴

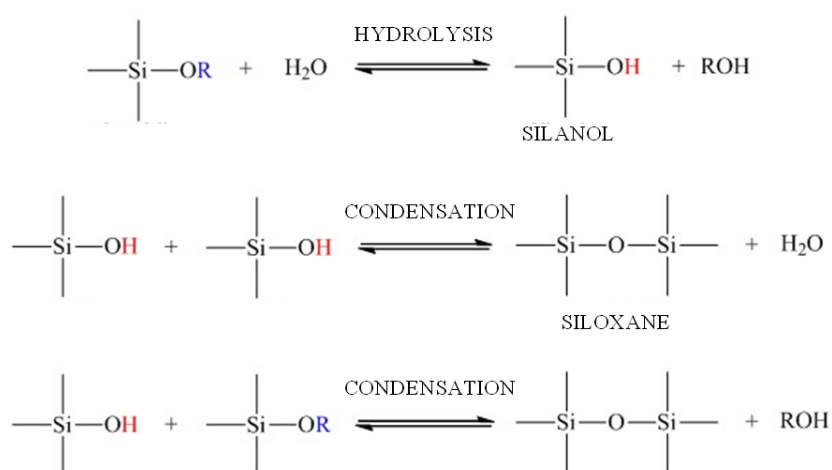


Figure 7. Polymerization mechanism of tetraalkoxysilane during the silica synthesis.

Tetraalkoxysilane molecules then polymerize (**Figure 7**) generating mesoporous silica particles in which the surfactant is trapped inside the pores.¹⁰⁵ In some case, an hydrothermal treatment at higher temperature is carried out to complete the assembly of micelles and the polymerization of the silica source. Finally, the mesostructured material is recovered after surfactant removal by solvent extraction and/or by calcination.¹⁰⁶

The final structure (lamellar, hexagonal, discrete cubic and bicontinuous cubic) and the morphology (spherical, rod-shaped, wire-shaped, etc) of the different types of OMS materials are determined by the different synthesis conditions, in particular by the type of surfactant and its concentration as well as by the reaction environment, namely pH and temperature which influence the surfactant CMC.¹⁰¹ For instance, SBA-15 mesoporous silica, that has a hexagonal array of unconnected tubular pores with a size distribution ranging from 7.5 to 32.0 nm,⁹⁹ requires the use of amphiphilic triblock copolymers as template, such as Pluronic 123 (comprising poly-ethylene oxide and poly-propylene

oxide in an alternating linear fashion, PEO-PPO-PEO),¹⁰⁷ with long hydrophobic tails. P123 establishes hydrogen bonds with the OH groups of the silica precursor through the oxygen atoms of its oxyethylene groups.¹⁰⁶

Moreover, the final array and the porosity of mesoporous silica can be further influenced by the use of certain additives, such as linear alkanes or aromatic compounds¹⁰⁸ known as swelling agents (1,3,5-trimethylbenzene or mesitylene is the most commonly used) which, once tend to distribute in the core of hydrophobic chains of surfactants, causing a change in the packing structure and enlarging the pores.¹⁰⁹

OMS, given their high surface area, are already excellent adsorbents, but there is the possibility of making the adsorption more selective by chemically modifying the OMS surface with appropriate (functionalizing) molecules able to selectively bind the polluting species.

The functionalization of OMS can be carried out according to two different procedures:^{110,111}

- ***co-condensation***: simultaneous condensation of the silica precursor with the functionalizing agent, which has the advantage of allowing a homogeneous functionalization. The limit of this method lies in the fact that the functional group on the functionalizing agent must be sufficiently lipophilic to penetrate the wall of the micelles, but at the same time not too bulky to cause the instability of the micelles.¹¹²
- ***post-synthesis functionalization*** : the synthesized mesoporous material is treated with a functionalizing agent consisting of an organotrialkoxysilane containing the functional group of interest (**Figure 8**). The advantage of post-synthesis functionalization is to keep the initial mesoporous structure of the silica unaltered, but the disadvantage could be due to an inhomogeneous distribution of the functionalization, caused by the diffusion of the reagents through the pore channels and by steric factors.¹¹³

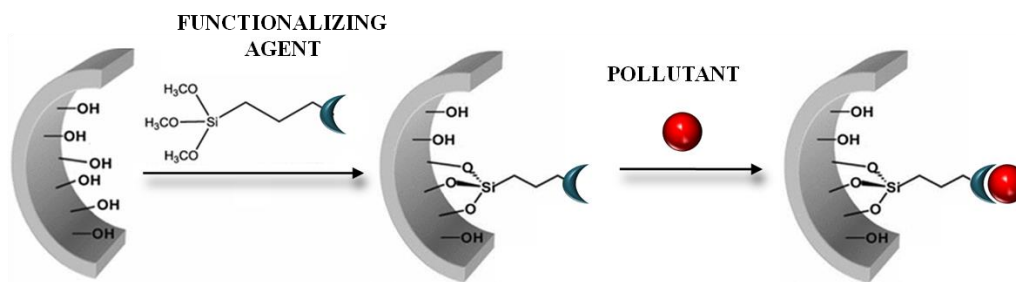


Figure 8. Schematic representation of post-synthesis functionalization of silica.

2.2 - Metal-Organic Frameworks (MOFs)

Yaghi et al. coined the term Metal-Organic Frameworks (MOFs) in 1995, referring to the material they synthesized constituted by a copper 4,4'-bipyridyl complex.¹¹⁴ MOFs are a new class of hybrid organic–inorganic crystalline porous solid (**Figure 9**) having a one-, two- or three-dimensional structure^{14,114–116} consisting of metal ions (or clusters) coordinated by organic mono-, di-, tri-, or tetravalent ligands (linkers) / bearing several complexing groups (carboxylates, phosphonates, imidazolates, etc.).¹¹⁷

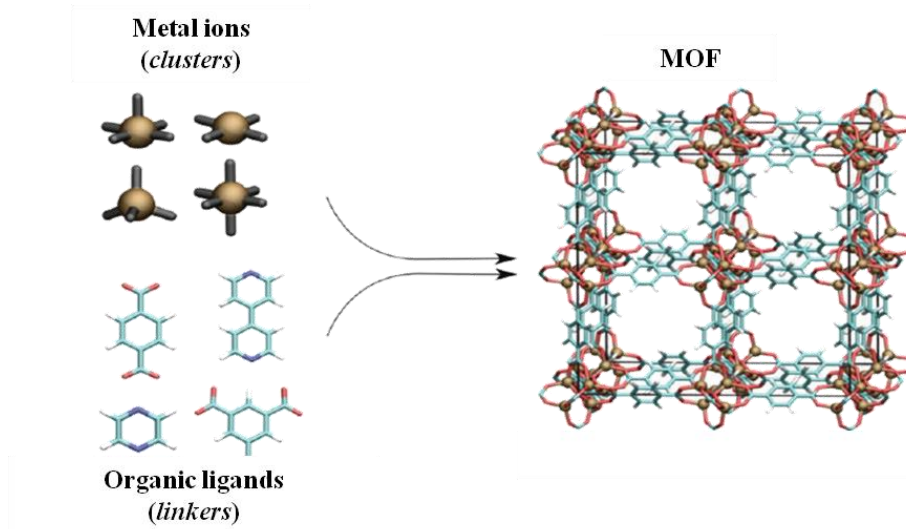


Figure 9. Structure of MOFs.

Their structure and properties are dictated by the choice of the metal and the linker; for example, the size and shape of the pores depend on the metal's coordination preference, as it determines how many ligands can bind to the metal and in which orientation. The recent development of new

synthesis and protocols allowed to create MOFs with a wide range of metal-linker matches with tailored network structure, geometrical order, and properties.

It should be considered that the potential porosity can be compromised due to the dynamicity and changes in structure.¹¹⁸ For this reason, linkers containing aromatic rings are generally used, which bestow greater rigidity to the system.

Their captivating features, such as large surface area, synthetic versatility, tunable functionality, structural order make them the ideal candidate for a multitude of applications, for instance gas separation, catalysis, biotechnology, sensing, enzyme immobilization¹¹⁹ and environmental purposes. In this thesis work, a Fe-BTC MOF has been synthesized and tested as an adsorbent for the removal of organic dyes from water. The Fe-BTC, commercially known as Basolite F300, consists of iron building units with oxidation state +3 connected by trimesate linkers (1,3,5-benzenetricarboxylate also called BTC).¹²⁰

Fe^{3+} has a coordination number of 6 and surrounds itself with six linker units according to an octahedral geometry. In contrast to renowned copper-based commercial MOF Cu-BTC (known as HKUST-1) (Copper 1,3,5 benzenetricarboxylate) the structure of FeBTC is characterized by poor crystallinity, indeed since it is not even an amorphous material, literature defines it as disordered.¹²⁰

Among all the various synthetic procedures present in the literature, the one proposed by Sanchez-Sanchez in 2015 was exploited during this thesis work,¹²¹ because it is a facile and rapid method practicable under environmentally and economically sustainable conditions (few minutes at room temperature using water as solvent).

3 - Kinetics and thermodynamics of Adsorption

Adsorption is defined as the accumulation of the particles of a fluid (adsorbate) at the interface between the fluid medium and the surface of a solid (adsorbent). The reduction of the translational freedom of the adsorbed particles implies a decrease of entropy ($\Delta S_{Ads} < 0$).¹²² Thus, accordingly to equation :

$$\Delta G_{Ads}^0 = \Delta H_{Ads} - T\Delta S_{Ads} \quad (1)$$

a spontaneous adsorption process ($\Delta G_{Ads}^0 < 0$) must be exothermic ($\Delta H_{Ads} < 0$).¹²³ Depending on the strength of the adsorbent-adsorbate interaction, two types of adsorption can be distinguished.¹²⁴ Weak interactions, that is London, Debye and Keesom (van der Waals) forces are responsible of physical adsorption, or **physisorption**. This is a reversible process characterized by low enthalpy (ΔH_{ads}) values of the order of the latent heat of condensation that is about 20 kJ/mol (**Figure 10**). Physical adsorption could take place with the formation of a multilayer adsorbate on the adsorbent surface (**Figure 10B**).

Chemical adsorption or **chemisorption** occurs instead when much stronger interactions, like true covalent bonds, are formed between the adsorbent and the adsorbate. Chemisorption is characterized by the formation of a monolayer of adsorbate on adsorbent surface (**Figure 10A**) and, since involves electron transferring/sharing, has a high adsorption enthalpy (ΔH_{ads}) which is comparable with the covalent bond energies, in the range $40\text{-}400 \text{ kJ/mol}$ and is irreversible.^{124,125}

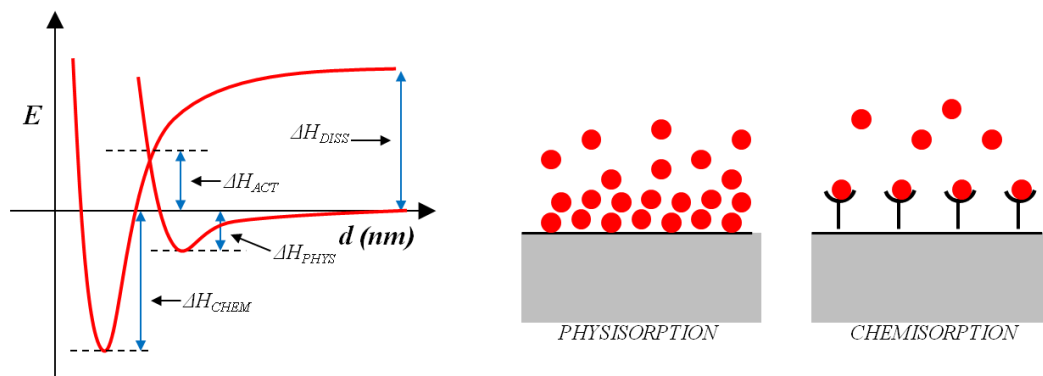
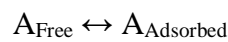


Figure 10. A) Potential energy curves for chemisorption and physisorption; B) Visual representation of chemisorption and physisorption phenomena.

The coverage degree or coverage fraction (θ) is defined as the ratio between the number of adsorbing sites occupied by the adsorbate particles and the number of total sites of the adsorbent ($0 \leq \theta \leq 1$):

$$\theta = \frac{n^{\circ} \text{ occupied sites}}{n^{\circ} \text{ sites}} \quad (2)$$

The adsorption is a dynamic process, as it consists of the simultaneous adsorption and desorption of the adsorbate A in solution, respectively characterized by the adsorption rate constant (k_a) and the desorption rate constant (k_d):¹²⁶



It follows that, the overall rate of the adsorption process, which corresponds to the variation of the coverage fraction as a function of time ($r = d\theta/dt$), is the difference between adsorption rate (r_a) and desorption rate (r_d):

$$r = \frac{d\theta}{dt} = r_a - r_d \quad (3)$$

In an experimental context at a liquid/solid interface, the coverage fraction (θ) is generally replaced with the adsorption capacity (q), defined as the adsorbed amount of adsorbate per unit mass of the adsorbent, according to the following equation :

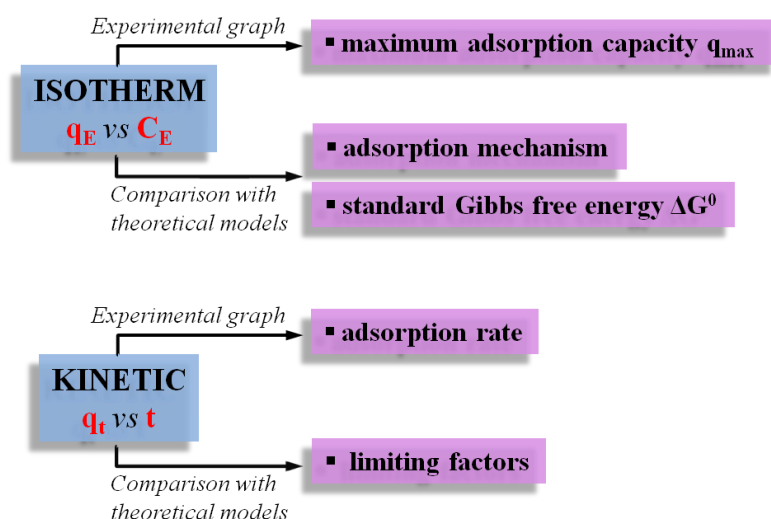
$$q = \frac{(C_0 - C)V}{m_{\text{Adsorbent}}} \quad (4)$$

where C_0 and C are respectively the initial and the final concentration of the adsorbent, V is the volume of the adsorbing solution, and $m_{\text{Adsorbent}}$ is the mass of the adsorbent. It can be expressed either in $mg_{\text{Adsorbate}}/g_{\text{Adsorbent}}$ or $mmol_{\text{Adsorbate}}/g_{\text{Adsorbent}}$.

The experimental determination of the adsorption capacity q is fundamental to describe the adsorption systems. Specifically, its trend as a function of concentration of the adsorbate at the equilibrium or as a function of time, allows to characterize the adsorption systems both from the thermodynamic and kinetic point of view.

Since adsorption can occur through different mechanism, it is necessary to compare the obtained experimental data with the trends foreseen by some thermodynamic or kinetic models through fitting procedures. By fitting the experimental data with the equations proposed by the various models, it is possible to establish - relying on the correlation coefficients and residuals - which model best describes the investigated system. Once the best fitting is established - and the type of mechanism involved have been identified - it is possible to obtain some characteristic quantities as fitting parameters characterizing the process (**Scheme 2**).

Scheme 2. Summary of the information obtainable from adsorption isotherms and kinetics.



3.1 - Adsorption Isotherms

The adsorption isotherm describes the equilibrium thermodynamics of the adsorption process at constant temperatures. The equilibrium occurs when the difference between adsorption and desorption rate ($r_a - r_d$) is zero :

$$r = \frac{d\theta}{dt} = r_a - r_d = 0 \quad (5)$$

The isotherm depends on the characteristics of the adsorbent, the nature of the adsorbate and for solid/liquid interface also by operational conditions such as pH and ionic strength (in the case of adsorption from aqueous solutions). Experimentally, the adsorption is carried out by putting in

contact the solid adsorbent with the solution containing the adsorbate at a constant temperature. The contact time must be sufficient to establish the equilibrium between the concentration of the adsorbate at the solid surface and that in the bulk solution. The determination of the experimental adsorption isotherm requires that several adsorption experiments are carried out using increasing concentrations of adsorbate. The adsorption capacity q_E is calculated as a function of the adsorbate concentration in solution at equilibrium, C_E , according with the following equation :

$$q_E = \frac{(C_0 - C_E)V}{m_{Adsorbent}} \quad (6)$$

The comparison with theoretical isotherm models is carried out putting the experimental values of q_E and C_E in the equations of each isotherm model chosen. Since there are numerous types of interactions that can be established between adsorbate and adsorbent, there are just as many various models of isotherms, each characterized by its own parameters. The evaluation of the correlation coefficients allows to identify the model that best represents the experimental data.

Correlating the experimental isotherm with a theoretical isotherm model allows to understand which interaction mechanisms are involved in the adsorption process.

Among the several isotherms which have been reported in the literature,¹²⁷ the three most common models (Langmuir, Freundlich and Temkin) are described below. It is even possible to calculate the constant of the fitting model (K), which is then used to obtain the thermodynamic equilibrium constant (K_e^0) :^(Lima 2019)

$$K_e^0 = \frac{K \cdot MM_{Adsorbate} \cdot [Adsorbate]^0}{\gamma} \quad (7)$$

where $MM_{Adsorbate}$ is the molecular mass of the adsorbate, $[Adsorbate]^0$ is the standard concentration of the adsorbate (1 mol/L), and γ is the activity coefficient (dimensionless) that can be considered to have a value of 1 in dilute solution. The K_e^0 is useful to calculate the standard Gibbs free energy for the adsorption process (ΔG_{Ads}^0), according to the relationship :^(Lima 2019)

$$\Delta G_{Ads}^0 = -RT \ln K_e^0$$

3.1.1 - Langmuir model

Langmuir adsorption isotherm model was originally developed for the description of gas adsorption on solid.

According to this model, the adsorption on the surface of the adsorbent does not proceed beyond the formation of a monolayer, and occurs in correspondence with defined sites, all equivalent and characterized by the same degree of affinity towards the adsorbate. It is therefore a homogeneous process, devoid of steric hindrances, lateral interactions, and transmutations on the superficial plane. Langmuir adsorption is therefore a specific type of adsorption which consists in the formation of a single layer of adsorbate on the surface of the adsorbent (monolayer adsorption).

The Langmuir model assumes that the adsorption rate r_a is proportional to the concentration (C) of the adsorbate A and to the number of vacant sites ($1-\theta$) :

$$r_a = k_a \cdot C(1 - \theta) \quad (8)$$

while the desorption rate r_d is proportional to the coverage degree of the solid :

$$r_d = k_d \cdot \theta \quad (9)$$

At the equilibrium, when the adsorption and desorption rates are equivalent ($r_a = r_d$), we obtain :

$$k_a \cdot C(1 - \theta) - k_d \cdot \theta = 0 \quad (10)$$

hence :

$$k_a \cdot C(1 - \theta) = k_d \cdot \theta \quad (11)$$

In this case, θ is given by :

$$\theta = \frac{KC}{1+KC} \quad (12)$$

where $K=k_a/k_d$ is the equilibrium adsorption constant.

Defining the coverage fraction θ as the ratio between the adsorption capacity at the equilibrium (q_E) and the maximum adsorption capacity (q_{max}), the Langmuir Isotherm equation is obtained :

$$q_E = \frac{q_{max} \cdot K_L \cdot C_E}{1+(K_L \cdot C_E)} \quad (13)$$

where K_L is the Langmuir constant (L/mg) and q_{max} is the maximum monolayer coverage capacity (mg/g). The Langmuir constant is an index of the affinity between adsorbate and adsorbent, therefore the greater the K_L , the more the adsorption will be favored. Obviously the K_L value depends on the nature of the adsorbent and the adsorbate, as well as on the temperature since adsorption is an exothermic process and therefore disadvantaged by the temperature increase.¹²⁸ This model is very useful for comparing adsorbent materials.

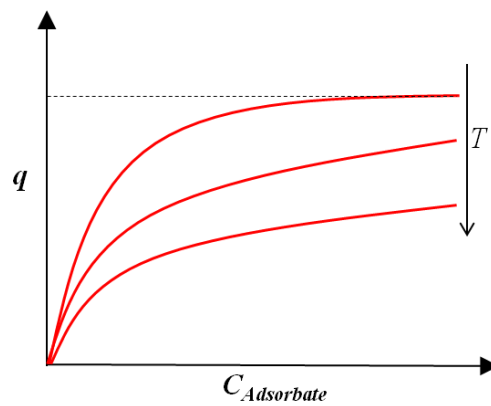


Figure 11. Langmuir isotherm profile.

As shown in **Figure 11**, according to the Langmuir equation (**Eq.13**) the adsorption increases with the increase in the equilibrium concentration of the adsorbate, until a plateau is reached, corresponding to the maximum adsorption capacity of the adsorbent (q_{max}) and the completion of the monolayer ($\theta \rightarrow 1$). This is the first piece of information that can be gleaned from the experimental data, but to go further it is necessary to compare the experimental data with theoretical models.

The linearized form is most frequently used for fitting experimental data:^{88,129}

$$\frac{C_E}{q_E} = \frac{1}{K_L \cdot q_{max}} + \frac{C_E}{q_{max}} \quad (14)$$

3.1.2 - Freundlich model

The Freundlich model is suitable for adsorbents characterized by a heterogeneous surface and patchwise topography, without non-uniform distribution of the active sites and active sites energies.¹²⁴

The Freundlich model assumes that the adsorption rate r_a is proportional to the concentration (C) of the adsorbate A :

$$r_a = k_a \cdot C \quad (15)$$

while the desorption rate r_d exponentially depends on the coverage fraction θ :

$$r_d = k_d \cdot \theta^n \quad (16)$$

At the equilibrium, when the adsorption rate is zero, we obtain :

$$k_a \cdot C_E = k_d \cdot \theta^n \quad (17)$$

$$\theta = \left(\frac{k_a}{k_d}\right)^{1/n} \cdot C_E^{1/n} \quad (18)$$

Defining the constant K_F as :

$$K_F = \left(\frac{k_a}{k_d}\right)^{1/n} \quad (19)$$

and passing from the coverage fraction θ to the adsorption capacity q_E , the Freundlich isotherm equation is obtained :¹³⁰¹³¹

$$q_E = K_F \cdot C_E^{1/n} \quad (20)$$

where $1/n$ (dimensionless) and K_F (L/mg) are the heterogeneity factor and the support capacity, respectively. These parameters are characteristic of each adsorbate-adsorbent pair and are also called Freundlich constants, both dependent on temperature.

The heterogeneity factor $1/n$ indicates the intensity of the adsorption and its value determines the shape of the q_E vs C_E plots, which can be linear for $n=1$ or nonlinear for $n \neq 1$.¹³² In particular, when $1/n > 0$ the adsorption process is favorable, becoming irreversible when $n = 1$ and unfavorable when $n > 1$.¹²⁷

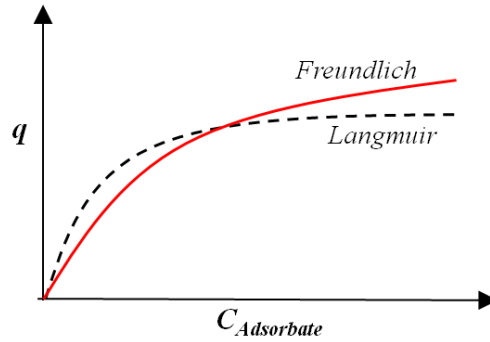


Figure 12. Comparison between Freundlich and Langmuir isotherms trend.

On the basis of Freundlich equation, the adsorption increases greatly with the increase of adsorbate concentration, then approaching a constant value at high concentration but without establishing a limit of the adsorption capacity. Thus, the slope of the curve is high at low-solute concentrations, and decreases with increasing solute concentration. This is an important limitation of the Freundlich equation, wherewith theoretically adsorption process carries on indefinitely (**Figure 12**).

The linearized form of the Freundlich equation is given by :

$$\ln q_E = \ln K_F + \frac{1}{n} \cdot \ln C_E \quad (21)$$

3.1.3 - Temkin model

Temkin isotherm model takes into consideration the interaction between the adsorbent and the adsorbate only for an intermediate concentration range and where the binding energies are uniformly distributed.^{124,127}

Temkin isotherm is based on the assumption that the adsorption enthalpy ΔH is not constant, but decreases linearly during the adsorption phenomenon due to the increase of surface coverage. Temkin isotherm is well suited to gas phase systems, but is not as appropriate for describing complex aqueous phase adsorption systems.

The coverage fraction θ based on the assumptions of this model is given by :

$$\theta = k_1 \cdot \ln k_2 \cdot C_E \quad (22)$$

Expressing through the adsorption capacity q_E , and defining the constants k_1 and k_2 as follows :

$$k_1 = \frac{RT}{b_T} \quad (23)$$

$$k_2 = A_T \quad (24)$$

the Temkin isotherm equation is thus obtained :

$$q_E = \frac{RT}{b_T} \ln A_T \cdot C_E \quad (25)$$

where b_T is the Temkin constant, and A_T is the Temkin equilibrium binding constant. The linear form is given by :

$$q_E = \frac{RT}{b_T} \ln A_T + \frac{RT}{b_T} \ln C_E \quad (26)$$

3.2 - Adsorption Kinetics

Adsorption kinetics describes the trend of the adsorption capacity q_t as a function of the contact time t between adsorbate and adsorbent.

$$q_t = \frac{(C_0 - C_t)V}{m_{Adsorbent}} \quad (27)$$

Identifying the kinetic model that best describes the system under examination allows to understand which are the factors that affect the adsorption rate and the adsorption mechanism. The experimental data of q_t vs. t are fitted within the equations of different kinetic models. The evaluation of the correlation coefficients allows to identify the model that best fits the experimental data. It is then possible to obtain the kinetic constant of the model (k) and - for some models - also the maximum adsorption capacity (q_{max}) to be then compared with the value obtained by the experimental isotherm. Since, as already mentioned, adsorption has received a lot of interest in the purification of waters and industrial effluents, the modeling of the kinetics is important for the prediction of uptake rates and for gaining more insight into the adsorption mechanisms.¹³³

Assuming that the adsorption rate r_a is proportional to the concentration (C) of the adsorbate A and to the number of vacant sites ($1-\theta$) :

$$r_a = k_a \cdot C(1 - \theta) \quad (28)$$

while the desorption rate r_d is proportional to the coverage degree of the solid :

$$r_d = k_d \cdot \theta \quad (29)$$

the overall rate equation ($r = d\theta/dt$) is given by :

$$r = \frac{d\theta}{dt} = r_a - r_d \quad (30)$$

$$r = \frac{d\theta}{dt} = k_a \cdot C(1 - \theta) - k_d \cdot \theta \quad (31)$$

Expressing the decrease of the adsorbate concentration in the solution due to the adsorption as :

$$C = C_0 - \beta\theta \quad (32)$$

where C_0 is the initial concentration of the adsorbate, C is the its concentration at any time, and β is a constant value defined as :

$$\beta = \frac{C_0 - C_e}{\theta_e} \quad (33)$$

where C_e is the equilibrium concentration of A and θ_e is the equilibrium coverage fraction, finally a general equation is obtained, which allows the derivation of various kinetic models using different conditions :¹²⁶

$$\frac{d\theta}{dt} = k_a \cdot (C_0 - \beta\theta)(1 - \theta) - k_d \cdot \theta \quad (34)$$

3.2.1 - Pseudo-First Order model

Pseudo-First Order (PFO) kinetic was developed by Lagergren in 1898, indeed it is also known as the Lagergren kinetic model. PFO, that can successfully be applied for the high concentration of adsorbate, represents an adsorption process that depends only on the nature of the adsorbates and is more inclined towards physisorption.

The condition is that the initial concentration of adsorbate is very high compared to $\beta\theta$, ($C_0 \gg \beta\theta$); then the $\beta\theta$ term in the general Eq.32 can be ignored and through a series of steps, the final form of the PFO kinetic is obtained :^{126,132}

$$\frac{dq_t}{dt} = k^I (q_E - q_t) \quad (35)$$

where k^I (s^{-1}) is the rate constant of this adsorption reaction.

Integrating the equation with boundary conditions $q_t = 0$ at $t = 0$ and $q_t = q_t$ at $t = t$, the linear relation can be obtained as:

$$\ln(q_E - q_t) = \ln q_E - k^I \cdot t \quad (36)$$

from which k^I can be calculated as the slope of $\ln(q_E - q_t)$ versus time t .

The pseudo-first order kinetic occurs when a reaction is 2nd order overall but is first order with respect to two reactants, generally because one of the reagent is in large excess, so it can be assumed that its concentration does not change significantly during the course of the reaction.¹³⁴

3.2.2 - Pseudo-Second Order model

The Pseudo-Second Order (PSO) kinetics assumes that the rate-limiting step is the chemisorption. It follows that the adsorption rate is independent of the adsorbate concentration but depends solely on the adsorption capacity.

If C_0 is not too high for the $\beta\theta$ term to be ignored in Eq.32, through a series of steps, the differential form of the PSO kinetic is obtained :¹²⁶

$$\frac{dq_t}{dt} = k^{II} (q_E - q_t)^2 \quad (37)$$

where k^{II} is the equilibrium rate constant of the PSO model ($g/mg \cdot min$).

Then integrating the **Eq.37**, the following linear relation can be obtained :

$$\frac{t}{q_t} = \frac{1}{k^{II} \cdot q_E^2} + \frac{t}{q_E} \quad (38)$$

the reactions in which one parameter is thought to be constant among the three parameter dependent reactions

3.2.3 - Intraparticle Diffusion model

The Intraparticle Diffusion (IPD) model was first employed by Boyd et al. in 1947 to model ion exchange kinetics in zeolites. It is the most popular model used in the literature about liquid/solid adsorption kinetics to describe diffusion-controlled adsorption processes. Nevertheless, the IPD

model was initially introduced for pure diffusion, without taking the adsorption process into account (except in the limit of very low adsorbate concentration).¹³⁵ This model can be used to find whether external transport or intraparticle transport governs the rate of adsorption processes.¹³⁶ This model assumes that internal diffusion of the adsorbate is the slowest step, resulting in the rate-controlling step during the adsorption process, whereas the adsorption is almost instantaneous.¹³⁷

The IPD equation is :

$$q_t = k^i \cdot t^{1/2} + x_i \quad (39)$$

where k^i is the IPD rate constant ($mg/g \cdot min^{1/2}$) and x_i is a constant correlated with diffusion resistance (calculated as the intercept of first order equation) and proportional to the thickness of boundary layer (mg/g).^{136,138,139}

The plot of q_t vs $t^{1/2}$ generally presents different straight lines with different slope.^{139,140} This means that the adsorption process involves different steps.

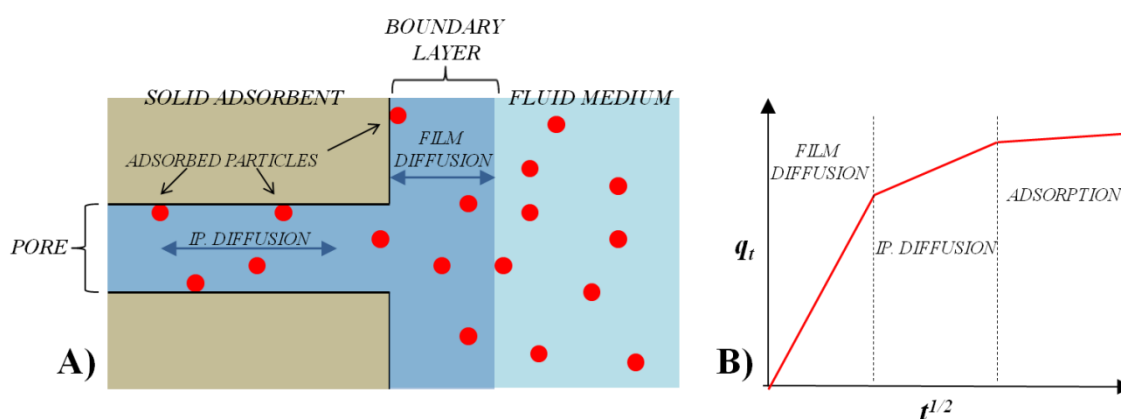


Figure 13. A) Representation of diffusion-controlled adsorption of adsorbate particles onto a porous adsorbent; B) Intraparticle Diffusion (IPD) kinetics graph.

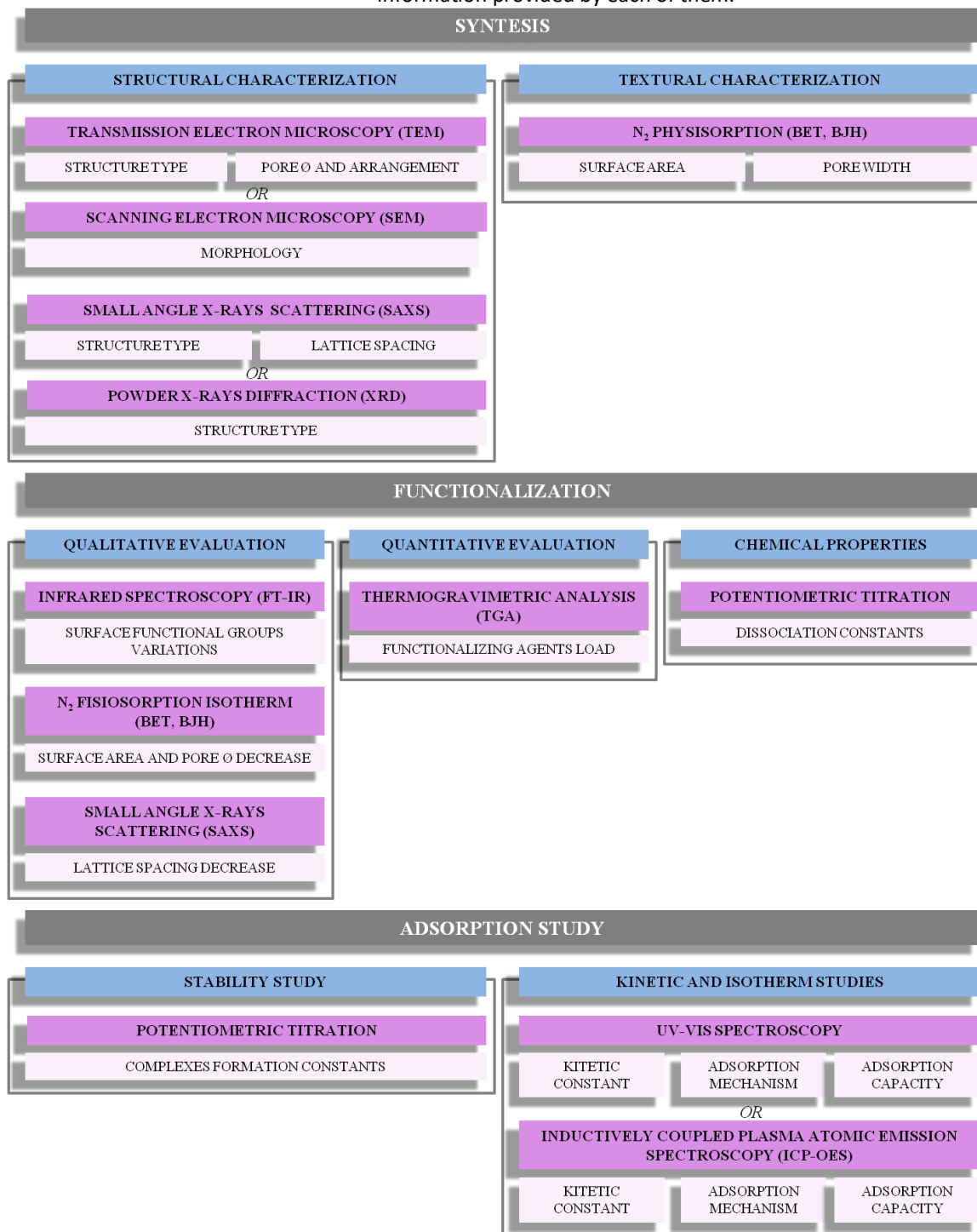
According to the **Figure 13B**, the first straight line represents the external mass transport of adsorbate from bulk solution through the boundary layer (**Figure 13A**) toward the adsorbent outer surface (film diffusion).¹⁴¹ The larger the intercept x_i the greater the boundary layer effect against the mass transfer. The second line represents the diffusion into the pores (IPD), that generally depends on concentration, temperature, pore width, surface morphology, etc.¹⁴⁰ Finally the third line represents the adsorption at the active sites i.e. the final equilibrium step characterized by stable

value of q .^{141,142} The slope of the three straight lines (k^i) represent the kinetic constant of the relative step (film diffusion, intraparticle diffusion, adsorption).¹⁴³

4 - Characterization techniques

During this work, various instrumental techniques were used to characterize the synthesized materials and test their properties as adsorbents.

Scheme 3. Summary of the characterization techniques employed during the various experimental phases, and the information provided by each of them.



Scheme 3 shows a summary of all the techniques used during each phases of this work, and the informations obtained through each of them.

4.1 - X-Rays techniques

X-rays are the portion of the electromagnetic spectrum with a wavelength between 10 *nm* and 1 *pm*. Due to their high energy X-rays are characterized by a huge penetrating power, which is widely used for analytical purposes. When the X-rays penetrate inside a material, they induce the electrons to oscillate with the same frequency and amplitude of the incident radiation, and consequently emit a secondary radiation of the same energy (frequency and amplitude) but different trajectory (diffusion or elastic scattering).

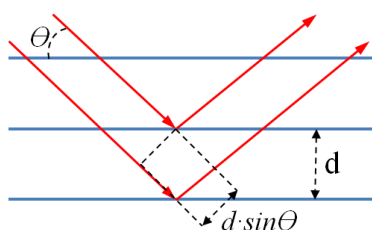


Figure 14. Representation of the X-rays scattering by the atomic planes of a material.

The X-rays diffracted by the various atomic planes recombine in output constructively or destructively according to Bragg's law:

$$n\lambda = 2d \cdot \sin \theta \quad (40)$$

where λ is the wavelength, d is the distance between the scattering planes, θ is the angle between the planes of the sample and the incident beam (**Figure 14**).

If the difference in path $2d \cdot \sin \theta$ between the two rays is an integer multiple of the wavelength ($n\lambda$), then the two rays will constructively interact at the output, while if the path difference $2d \cdot \sin \theta$ between the two rays is a fractional multiple of the wavelength ($n\lambda/2$), then the two rays will interfere destructively output. These interference phenomena can be revealed by a detector giving rise to a diffraction pattern. Knowing the wavelength of the incident radiation λ and the angle of the diffracted ray 2θ , it is possible to obtain the distance between the planes d .

The X-ray diffraction from the various families of identifiable planes (described by a triple of numbers - $h k l$ - called Miller indices) (**Figure 15**) within a crystalline structure will give rise to a diffraction pattern characteristic of the structure, where each peak corresponds to a family of planes.

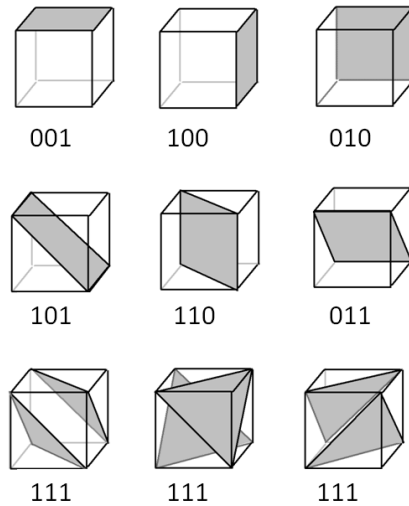


Figure 15. Atomic planes and their relative Miller indices.

The X-rays source, called X-ray tube (**Figure 16**), consists of a glass tube under vacuum containing a filament (cathode) which, heated by current, expels electrons by thermionic effect. These negatively charged particles are accelerated by a high voltage towards an anode (high atomic weight metal) ripping off its electrons from the innermost levels, thus forcing electrons of the external levels to fill the gaps formed with the emission of energy (X-rays).

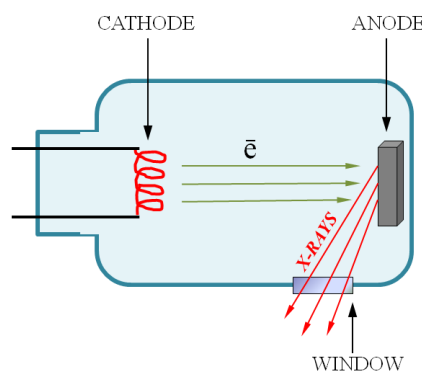


Figure 16. Representation of a X-rays tube.

The fundamental parameters that differentiate the various X-ray analysis techniques are the nature of the anode of the X-ray tube (and therefore the incident wavelength) and the angle at which the X-rays reach the sample.

4.1.1 - Small Angle X-Rays Scattering (SAXS)

As is evident from Bragg's Law, the greater the characteristic length (d), the smaller the scattering angle will be. Small Angle X-Rays Scattering (SAXS) is an important technique for analyzing structure and fluctuations on the nano-scale, where characteristic lengths are between 1 and 100 nm . The scattered rays at the output are collected by a detector within a range of low angles (0.1° - 10°) which provides information about the characteristic distances of the crystalline planes, structure, etc., while the transmitted rays are eliminated by means of a beamstop (**Figure 16**) that totally absorbs them.

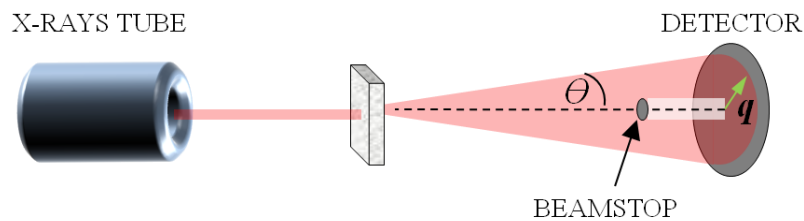


Figure 16. Simple scheme of SAXS experiment.

The scattering curve is obtained by recording the intensity I of the scattered beam as a function of the scattering vector q (nm^{-1}) defined as:

$$q = \frac{2\pi}{d} \quad (41)$$

A linear detector, with 1024 vertical channels, initially provides a curve of the intensity of the diffracted beam as a function of the affected channel. This is then converted in q (nm^{-1}) units by suitable software.

The different regions of the scattering curve (**Figure 17**) are associated with domains of specific dimensions. The scattering region at very small angles (Guinier region) provides information regarding the size of the system under consideration, while the larger q region provides information on the shape and structure. In particular, the last part of the curve (Porod region) is associated with the structure of the interphase (between particle and solvent).

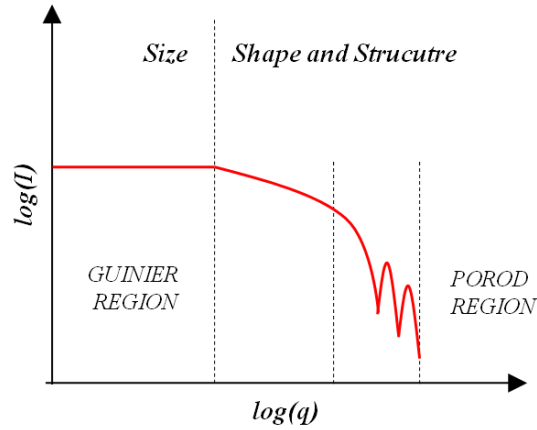


Figure 17. Regions of the scattering curve.

The information obtained depends on the degree of supramolecular order of the sample; for example, in the case of diluted macromolecule solutions, the shape and radius of gyration can be determined, while in the case of highly ordered systems (such as liquid crystals) a structural model for the molecular organization can be determined.

In the case of ordered mesoporous materials, SAXS analysis permits to characterize the long-range order and the lattice parameter of the structure. In the case of SBA-15 mesoporous silica, for example, the cell is hexagonal, and the lattice parameter corresponds to:

$$a = d\sqrt{(h^2 \cdot k^2 \cdot l^2)} \quad (42)$$

During this thesis work the SAXS technique was exploited for the structural characterization of the synthesized silica-based samples. In particular, the SAXS equipment used is an S3-MICRO SWAXS camera system equipment (HECUS X-ray Systems, Graz, Austria) (**Figure 18**).



Figure 18. Picture of the HECUS X-ray System.

4.1.2 - Powder X-Rays Diffraction (XRD)

X-ray diffraction (XRD) occurs when X-ray wavelength λ and the d-spacing have a comparable size. Differently by SAXS, the explored angular region ranges from 5° to 50° .

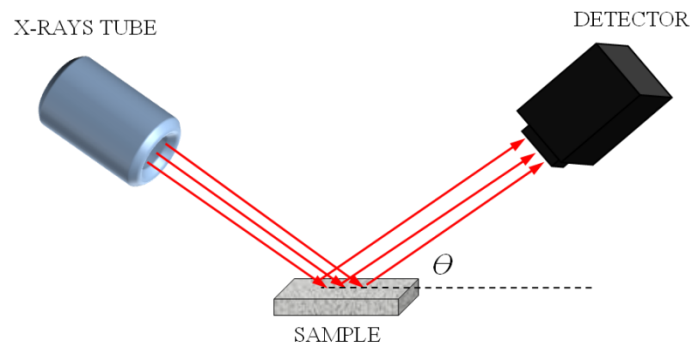


Figure 19. Simple scheme of XRD experiment

The diffractogram shows the intensity of the radiation diffracted by the sample as a function of the angle 2θ between the X-rays source and the detector (**Figure 19**), which is made to vary during the measurement. The geometrical 3D topology of atoms produces peaks of characteristic position and intensity. Indeed, the position of the peaks depends on the d-spacing, which can be obtained from indexing, while the line broadening at half the maximum intensity of the peaks (w_{FWHM}) depends in an inversely proportional way on the size of the particles (D), in accordance with the Debye-Scherrer law:

$$w_{FWHM} = \frac{K \cdot \lambda}{D \cdot \cos\theta} \quad (43)$$

where K is a dimensionless shape factor (~ 1) which varies with the actual shape of the crystallite, λ is the X-ray wavelength (nm) and θ is the Bragg angle.

The intensity of the peaks depends on the atomic weight of the atoms of the unit cell and on their position inside the cell.

During this thesis work the XRD technique was exploited for the characterization of the synthesized Fe-BTC MOF. In particular, the XRD equipment used is an X'Pert Pro PANalytical (**Figure 20**).



Figure 20. Picture of the X'Pert Pro PANalytical.

4.3 - Nitrogen physisorption

N₂ physisorption is one of the most widely used procedures for determining the textural parameters of porous materials. During the measurement, the sample is placed in a burette, inside which N₂ is pumped with increasing pressure (P) from vacuum to saturation pressure (P_0). Once the saturation pressure is reached, the pressure is decreased and the N₂ gets desorbed. By plotting the amount of adsorbed and desorbed N₂ at constant temperature (usually -196°C) as a function of the equilibrium gas pressure (or relative pressure, P/P_0) the adsorption/desorption isotherms are obtained.

According with IUPAC six types of experimental isotherms have been classified (**Figure 21**).^{144,145}

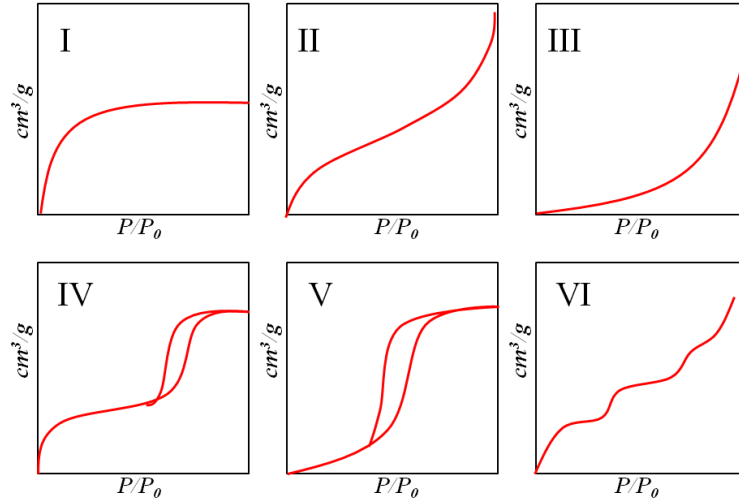


Figure 21. IUPAC classification of the adsorption isotherms.

The main method to determine the specific surface of a porous material is the one developed by Brunauer Emmett and Teller, therefore called the B.E.T. method.

This method is based on the evaluation of the volume V of gas (N_2) adsorbed by the solid at various pressures (P), from which the theoretical volume of an adsorbed monomolecular layer (V_m) is calculated using the following equation:

$$\frac{P_0}{V(P_0 - P)} = \frac{1}{C V_m} + \frac{P(C-1)}{V_m C P_0} \quad (44)$$

where C is the B.E.T constant. Once V_m has been obtained, the surface area S_{BET} (m^2/g) can be calculated by:

$$S_{BET} = \frac{V_m \cdot N \cdot s}{a} \quad (45)$$

where N is the Avogadro's number, s is the molecular cross sectional area of the adsorbing species (N_2) and a is the mass of the sample.

Another textural parameter that can be obtained by N_2 physisorption isotherms is the pore size distribution of a porous material. One of most used method is the Barrett-Joyner-Halenda (BJH) method, based on the Kelvin equation:

$$\ln \frac{P}{P_0} = \frac{-2\sigma V}{RT} \cdot \frac{1}{r} \quad (46)$$

where r is the Kelvin radius, σ is the surface tension, V is the molar volume of the adsorbate (N_2), R is the ideal gas constant and T is the absolute temperature.

From the appropriate processing of the data obtained from N₂-physisorption isotherms it is also possible, with the application of B.J.H. or other methods, to determine the pore size distribution of the material.

During this thesis work, N₂-physisorption isotherms were used to verify the mesoporous nature of the synthesized adsorbents, SBA-15 and Fe-BTC (associated with type IV isotherms) and to determine their respective surface area and pore size distribution. Furthermore, in the case of functionalized silica adsorbents, this technique allowed an evaluation of the decrease in pore size and surface area following the functionalization processes. An ASAP 2020 apparatus was used during this thesis work (**Figure 22**).



Figure 22. Picture of the ASAP 2020.

4.4 - Electron Microscopy

Microscopes are tools that allow the direct or indirect observation of small objects. The resolving power of a microscope is inversely proportional to the lateral resolution (d), defined as the minimum distance between two distinguishable points:

$$d = 0,6098 \frac{\lambda}{AN} \quad (47)$$

Since the lateral resolution (d) is proportional to the wavelength of the radiation that reaches the sample, it is clear that very small objects can be observable only with radiations of very small λ .

Electron microscopes using a beam of electrons rather than photons as a radiation source, possess a resolving power that greatly exceeds that of optical microscopes, since the wavelength of electrons is significantly smaller than that of light.

The electron source (electron gun) consists of a filament of tungsten (W) or lanthanum hexaboride (LaB_6) with a crystallite at the tip. The filament is connected to a system of resistances which, due to the thermionic effect, makes it to emit electrons (cathode ray) which are accelerated towards an anode (+) through a potential difference. The cathode ray has a wavelength which depends on the acceleration potential of the electrons (V):

$$\lambda = \frac{1.23}{\sqrt{V}} \quad (48)$$

The use of electrons makes it necessary both to work under vacuum to avoid interaction with air, and to replace normal lenses with electromagnetic lenses to avoid interaction with materials outside the sample. Hence, the main components of the electron microscope are contained within a hollow column about one meter high, inside which the vacuum is maintained (10^{-4} mbar).

4.4.1 - Transmission Electron Microscopy (TEM)

In the transmission electron microscope a beam of electrons arrives on the sample with an angle θ , which partly pass through the sample (transmission) and partly diffracted by it at an angle θ . The transmitted electrons are focused to form an enlarged image of the cross section of the sample, which can be projected on a photographic layer/fluorescent screen or revealed by a CCD-camera (**Figure 23**). A bright-field image is obtained choosing the direct beam, while the scattered electrons from the sample produce a dark-field image.

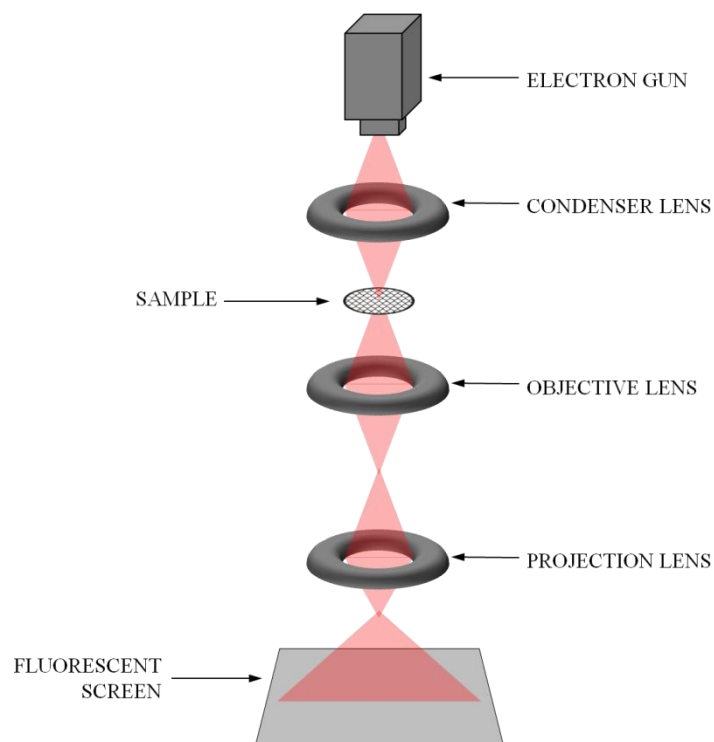


Figure 23. Schematic representation of a Transmission Electron Microscope.

During this thesis work, a Hitachi-H7000 TEM equipment (**Figure 24**) was used to obtain images relating to the structure of the synthesized silica-based samples (SBA-15).



Figure 24. Picture of Hitachi-H7000 TEM.

4.4.2 - Scanning Electron Microscopy (SEM)

Differently from TEM, in scanning electron microscopes the electron beam passes through scanning coils, that deflect the beam on the sample like a brush in the x and y axes so that it scans in a raster fashion over the surface of the sample. A detector detects the backscattered electrons from the sample (characterized with the same λ as the primary beam) and a lateral detector detects the secondary electrons emitted by the sample (with a lower λ than that of the primary beam)(**Figure 25**), thus generating a tridimensional image of the surface structure. SEM is very useful for characterizing the morphology and shape of particles.

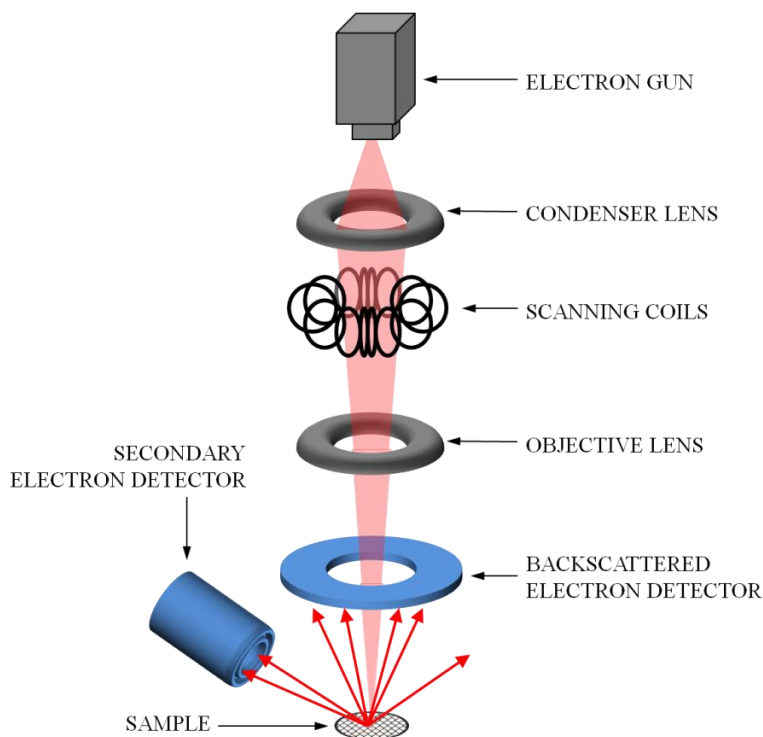


Figure 25. Schematic representation of a Scanning Electron Microscope.

During this thesis work, Hitachi SU-70 SEM equipment (**Figure 26**) was used for the morphological characterization of the synthesized Fe-BTC MOF.



Figure 26. Picture of Hitachi SU-70.

4.6 - Thermogravimetric Analysis (TGA)

Thermogravimetry is an analytical technique that measures the variation in the mass of a sample as a function of temperature. A melting pot (generally made of alumina) containing the sample is placed inside the furnace, made up of a material that is heated by Joule effect, is saturated with inert gas (N_2) and eventually also with an oxidizing gas (O_2 , which guarantees the decomposition of the sample). The plate on which the melting pot is placed is connected by means of a rod to a piezoelectric which constitutes the balance of the system (Figure 27).

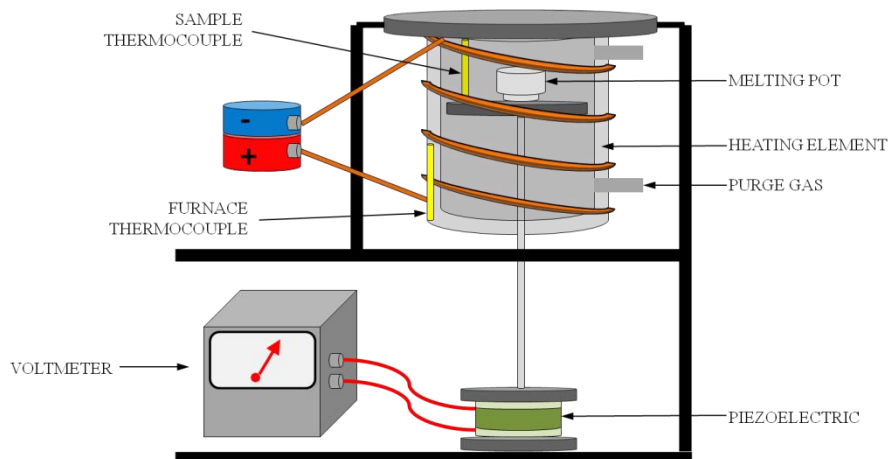


Figure 27. Schematic representation of a TGA apparatus.

As the temperature increases, the substances contained in the sample melt at their characteristic melting temperatures. In the thermogravigram the decrease in the mass of the sample ($M\%$) due to the melting is recorded as a function of the temperature. From these graphs it is possible to evaluate the thermal stability of a sample and to obtain a quantitative analysis of mass losses as a function of temperature. This is very useful, for example, for quantitatively assessing the degree of functionalization of a material.

A STA6000 Perkin Elmer TGA (**Figure 28**) was used for the thermogravimetric analysis of both bare/functionalized SBA-15 and Fe-BTC.

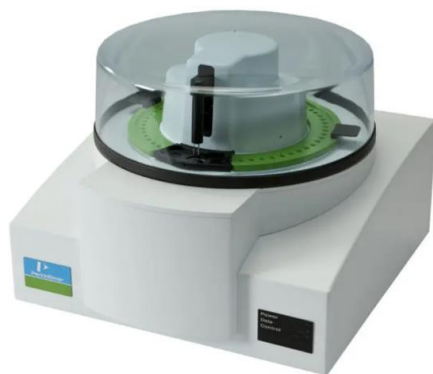


Figure 28. Picture of STA6000 Perkin Elmer.

4.7 - Fourier Transform Infrared Spectroscopy (FTIR)

Infrared (IR) spectroscopy is an analytical technique for the identification of organic and inorganic samples, by studying their interaction with infrared radiation. When a molecule interacts with an IR radiation, it can absorb its light energy and use it to pass from its fundamental vibrational state to an excited vibrational state. Vibrations include interatomic distance variations (*stretching*) and deformations of the bond angle (*bending*).

The necessary condition for an IR radiation to originate a vibrational transition consists in the occurrence of a change in the molecular electric dipole following the change in position of the atoms. Therefore homoatomic molecules (such as N_2 or O_2) are not active in the infrared, while non-polar

molecules such as CO₂ can resonate with the radiation only thanks to the asymmetrical vibrations that produce an instant dipole.

In an IR absorption experiment, infrared radiation is sent to the sample and then it is measured at the output which wavelengths of this radiation have been absorbed. In this way, an IR spectrum is obtained, which reports the Transmittance % values (ratio between the intensity of the radiation exiting the sample and the incident one) as a function of the frequency (expressed in cm⁻¹ wave numbers).

$$T = \frac{I}{I_0} \quad (49)$$

Each peak present in the spectrum indicates a specific vibrational transition of the type of bond involved, which makes it possible to identify the presence of certain functional groups, whose peaks always fall in the spectral region between 4000 and 1250 cm⁻¹, called in fact "functional group region".

The conventional method for acquiring IR spectra involves the use of a monochromatic source whose wavelength is gradually varied to cover the entire spectral range, but this approach requires quite a long time. In fact, modern spectrometers exploit broadband sources, and the sample absorptions relating to the different wavelengths are distinguished using a Michelson interferometer.

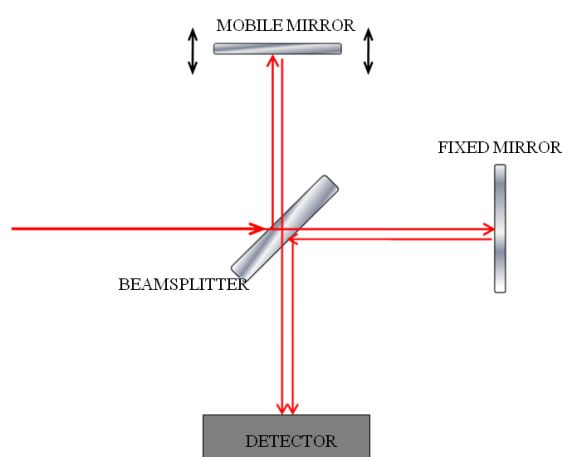


Figure 29. Schematic representation of a Michelson interferometer.

The beam exiting the sample is divided by a semi-reflective mirror, called divider or beamsplitter, into two beams, addressed respectively to two mirrors, one of which is fixed and one mobile, which reflect them again on the beamsplitter, which sends them to the detector (**Figure 29**).

The movement of one of the two mirrors introduces a variable path difference between the two reflected beams, so that when they recombine to reach the detector, they will have a phase difference that will sometimes cause a destructive interference (when the path difference is a multiple fractional wavelength) and sometimes constructive interference (when the path difference is an integer multiple of the wavelength). The interferometer therefore creates an intensity spectrum in the space (or time) domain called interferogram, which is converted into a spectrum in the frequency domain by means of a mathematical algorithm that takes the name of Fourier Transform (or F-Transform).

4.7.1 - Total Attenuated Reflectance (ATR) sampling system



Figure 30. Picture of a ATR sampling system.

For the IR analysis of certain samples, the ATR (Attenuated Total Reflectance) sampling system (**Figure 30**) can be used, which allows some advantages such as the possibility of analyzing such a sample, without any previous preparation, and therefore also not to modify or destroy the sample, which can be recovered at the end of the analysis.

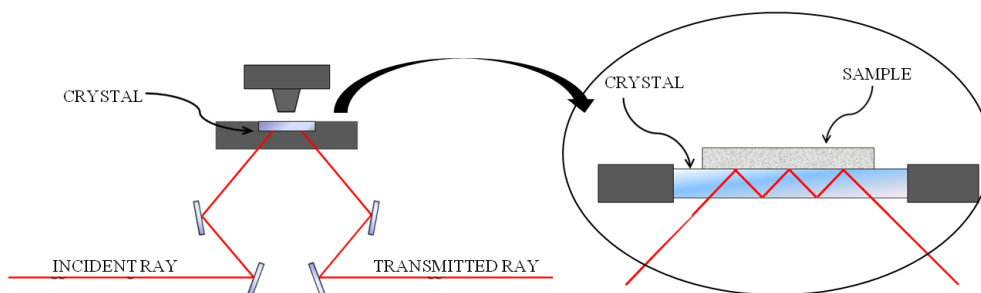


Figure 31. Schematic representation of ATR sampling system.

In this technique, the sample is placed in close contact with an optical element called an internal reflection element (or ATR crystal) consisting of a crystal with a high refractive index. The IR radiation emitted by the source passes through this element with an angle of incidence greater than the critical angle, generating a phenomenon of total reflection which is repeated numerous times (**Figure 31**). A portion of the reflected radiation, called an evanescent wave penetrates the sample, from which it can be absorbed, leading to an attenuation of the outgoing radiation, precisely called Total Attenuated Reflectance (ATR).

During this thesis work a FTIR analyses were carried out to verify the occurrence of the functional groups onto the surface of the synthesized silica after the grafting procedure. A Bruker Tensor 27 spectrophotometer equipped with a diamond-ATR accessory and a DTGS detector was used.

4.8 - UV-Vis Absorption Spectroscopy

UV-Vis Spectroscopy is a technique based on the study of the absorption of monochromatic radiations of the visible and ultraviolet spectral region by molecules. In a common UV-Vis absorption experiment, the radiation emitted by a source (incandescent or deuterium lamp) is splitted up by a monochromator which selects the wavelength to be sent to the sample; the monochromatic radiation invests the cuvette containing the sample solution and then reaches the detector with a lower intensity (I) than that emitted by the source (I_0) (**Figure 32**), proportionally to the extent of absorption.

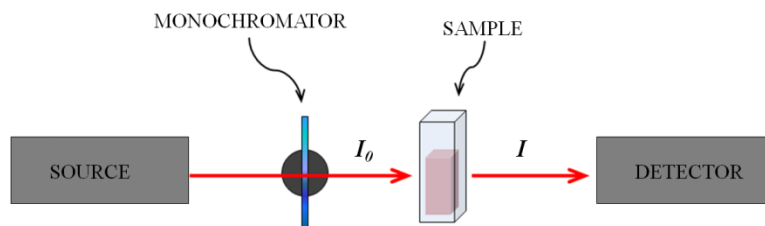


Figure 32. Simple scheme of a UV-Vis spectroscopy experiment.

The extent of light absorption is quantified by the "absorbance" (A), defined as the logarithm of the ratio between the intensity of the incident radiation (I_0) and that transmitted radiation (I) :

$$A = \log \frac{I_0}{I} \quad (50)$$

Moreover, the absorbance can also be calculated using the Lamber-Beer law:

$$A = \varepsilon \cdot l \cdot C \quad (51)$$

which corresponds to the equation of a straight line of the type $y = mx$, where C is the concentration of the sample solution, l the optical path (thickness in cm of the sample) and ε the molar absorption coefficient.

However, the linearity of the absorption trend with respect to the concentration is guaranteed only within a certain range of concentrations above which it is affected by collateral chemical-physical phenomena (for example precipitation). It follows that in the context of the quantitative analysis, the samples must always be suitably diluted.

By recording the absorbance values for each wavelength, it is possible to obtain the specific absorption spectrum of the substance, which can be useful in the qualitative investigation.



Figure 33. Picture of Cary 60 spectrophotometer.

During this thesis work, a Cary 60 UV-Vis spectrophotometer (Agilent) (**Figure 33**) was used to evaluate the decrease in the concentration of dyes and heavy metal ions (colorimetric assay with oxalyldihydrazide) present in the waters subjected to adsorption treatment.

4.9 - Inductively Coupled Plasma Optical Emission Spectroscopy (ICP-OES)

ICP-OES is an analytical emission spectroscopy technique for the detection of chemical elements based on the use of the inductively coupled plasma.

The plasma torch is composed of three concentric quartz tubes inside which a stream of argon (Ar) is fluxed and then ionized by the strong electromagnetic field generated by a radiofrequency coil (working at 27 or 40 MHz) surrounding the tip of the torch tube (inductive coupling). The plasma thus generated has a stable temperature in the range from 6000 to 10000 K resulting from the inelastic collisions occurring between the neutral and ionized Ar atoms. A peristaltic pump delivers the sample solution into a nebulizer, where it is converted into a fine mist then directly introduced inside the plasma flame through the narrow tube in the center of the torch (**Figure 34**). Thanks to the high temperature and high electron density of the plasma, the sample gets immediately ionized, emitting electromagnetic radiations whose wavelengths are characteristic of the elements present in the sample. The emission radiations are sent to the spectrophotometer by which they are translated in the form of an emission spectrum where the intensity of each peak is proportional to the concentration of the elements within the sample.¹⁴⁶¹⁴⁷

ICP-OES allows simultaneous analysis of all elements present in the sample with high sensitivity (in the order of *ppb* and lower). The plasma torch operates at temperatures that are almost double those used in the Atomic Absorption Spectrophotometry AAS (which operates between 2000 and 3000 K) and is therefore able to excite and detect various elements otherwise difficult to analyze with AAS.

During this thesis, the ICP-OES was used to evaluate the decrease in the concentration of heavy metal ions present in the waters subjected to adsorption treatment.

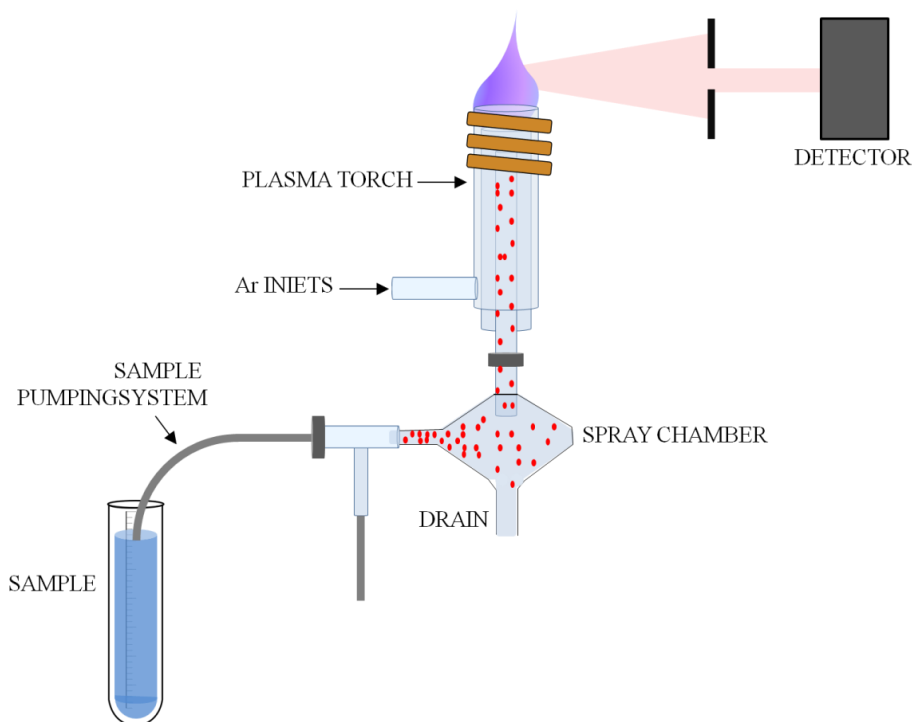


Figure 34. Schematic representation of ICP-OES apparatus.

4.10 - Potentiometric titrations

During this thesis work, potentiometric titrations were used to determine the ligand content on the OMS surface, its protonation constants, and successively stability constants of the formed metal/ligand complexes. Moreover, the charge of the ligand and its complexes, together with stoichiometry of the complexes were established.

Generally, ligands are weak acids or bases, so it is possible to obtain information on the nature of the system by measuring the pH variation with a glass electrode (GE). The potential measured by this electrode depends on the activity of the H^+ ion through Nernst's law:

$$E = E_0 + \frac{RT}{F} \ln a_{H^+} + E_j \quad (52)$$

where E_0 is the standard potential of the electrode (V), E_j is the liquid junction potential of the cell (V), T (K) is the absolute temperature, R is the universal gas constant ($8.314 \text{ J}\cdot\text{mol}^{-1}\cdot\text{K}^{-1}$), F is the Faraday constant ($9.65 \cdot 10^4 \text{ mol}\cdot\text{C}^{-1}$) and a_{H^+} is the H^+ ion's activity.

Activity and concentration are related through the following relationship:

$$a_{H^+} = \gamma_{H^+} [H^+] \quad (53)$$

where γ_{H^+} is the activity coefficient, that is constant if the ionic strength is constant, and approaches to 1 when the concentrations of the other species are lower (10%) than that of the ionic strength:

$$a_{H^+} = [H^+] \quad (54)$$

At 25°C (298 K), the **Eq.52** can be transformed into:

$$E = E_0 + 59.16 \cdot \log[H^+] \quad (55)$$

In a system where the H^+ concentration is varied, the complexes formation constants, can be determined only if ligand, proton and metal analytical concentrations are known. For this reason, the concentration of the free ligand and its protonation constants are determined separately in the titration curve without metal ions. From this relation:

$$n_i = \frac{[H^+]_0 - [H^+]_i}{[L]} \quad (56)$$

where $[L]$ is the ligand concentration, $[H^+]_0$ is the protons initial concentration and $[H^+]_i$ is the protons concentration at the point i , it is possible to calculate, for any titration point, the average number of bound protons n , which therefore depends on the pH, on the number of species present and deprotonation constants. Once the protonation constants (pKa) of the ligand are known, the complexes formation constants can be obtained calculating the average concentration of ligands per metal ion using the following equation:

$$Z_i = \frac{[L]_0 - [L]_i}{[M]_0} \quad (57)$$

where Z is a function of the global formation constant of the $M_pL_rH_q$ complex ($Z = f(\beta_{pqr})$) defined as :

$$\beta_{pqr} = \frac{[M_pL_rH_q]}{[M]^p[L]^r[H]^q} \quad (58)$$

The complex formation curve can be obtained by plotting Z against $\log [L]_i$.

The speciation distribution curves can be provided by plotting the percentages (or partial mole fraction) or equilibrium concentrations of the different chemical species present in the solution as a function of pH.¹⁴⁸



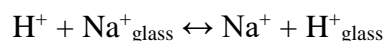
Figure 35. Picture of automatic Metrohm titrator.

Hyperquad program¹⁴⁹ was used to calculate the ligand concentration and its protonation constants; moreover, stability constants of the formed metal/ligand complexes were calculated. The calculation method starts from the stoichiometry of the complex and from an initial $\log\beta$ proposed by the operator. Then, the $\log\beta$ value is refined with the least squares method. The Ordinary Least Squares method (OLS) is an optimization (or regression) technique that permits to find the best fitting function (represented by an optimal curve -or regression curve), which comes as close as possible to a dataset (typically points of the plane). In particular, the proper function must be the one that minimizes the sum of the squares of the distances between the observed data and those of the curve that represents the function itself.

Computational modeling provides a very important alternative approach to the controlled instrumental methods for determining speciation, and can be helpful understanding experimentally obtained findings and reduce the experimental effort required.¹⁵⁰

4.10.1 - The Glass Electrode (GE)

The glass electrode (GE) (Figure 36) is used to measure the potential (mV) as it allows a quick and precise measurement of the activity of hydrogen ions in solution. The active part of the GE consists of a bulb-shaped glass membrane made of alkaline and alkaline-earth metal ions silicates; these cations occupy tetrahedral cavities in the crystal lattice of the glass, where they are maintained by electrostatic forces. The external surface of the membrane is made by thin layer of gel, in which H⁺ cations (or monovalent cations) penetrate and move from one cationic gap to another. The same phenomenon occurs on the internal surface of the membrane, which contacts with the inner buffer solution at known pH. The central anhydrous layer of the membrane, ensures electrical contact between the two solutions. Ion exchange reaction occurs between the smaller cations on the membrane and the H⁺ ions in the analyte solution, which do not cross the glass membrane:



Therefore, when internal and external solutions have different pH, a potential difference called "membrane potential" (E_M) is established between the two faces of the membrane, as described by the equation:

$$E_M = \frac{RT}{F} \ln \frac{[H^+]_{OUT}}{[H^+]_{IN}} = 0.059 (pH_{OUT} - pH_{IN}) \quad (59)$$

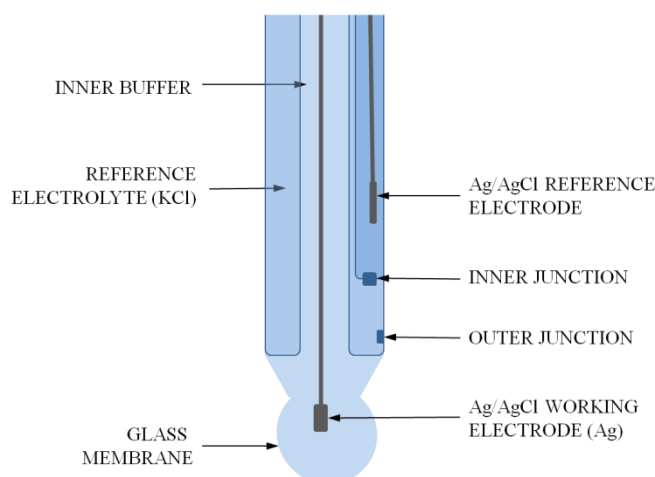


Figure 36. Representation of a Glass Electrode (GE).

This potential difference can be measured by connecting two solutions with two electrodes, one internal and the other external (considered a reference electrode).

The calibration of the pH-meter allows you to adapt the electrode to certain conditions to ensure that exactly Nernst's law, i.e., that at 25 °C the e.m.f. varies by 59.16 mV for each pH unit. Before collecting potentiometric data of the ligand and its metal complexes, it is necessary to calibrate the electrode and verify the electrode's standard reduction potential (E_0) and the concentration of the titrant (NaOH was used in this thesis work). At each addition of titrant before the equivalence point the concentration of the proton H^+ is given by the equation:

$$[H^+] = \frac{C_0V_0 - C_TV_T}{V_0 + V_T} \quad (60)$$

where C_0 and V_0 are the initial concentration and volume of the acid, and C_T and V_T are the concentration and the volume of the titrant.

When plotting the resulting potential as a function of the titrant's volume a sigmoidal curve can be obtained (Figure 37).

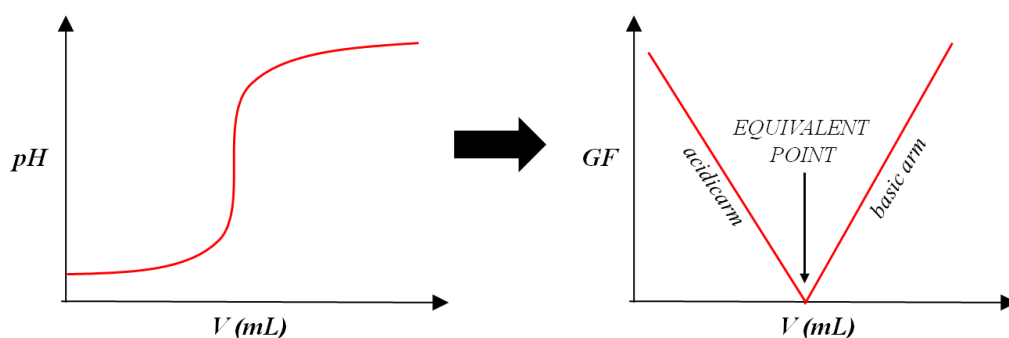


Figure 37. Sigmoidal titration curve transformation using the Gran's method.

The sigmoidal curve can be converted into 'V' shape curve, by using the Gran's method where the points $V_T \cdot 10^{-E/0.05916}$ are plotted as a function of V_T according to the following equation:

$$C_0V_0 - C_TV_T = V_0 + V_T \cdot 10^{\frac{-E}{0.05916}} \quad (61)$$

The Gran plot consists of two straight lines (branches), characterized by slopes of opposite sign, which intersect on the abscissa at the equivalence point. From this graph it is possible to calculate the electrode potential (E_0), titrant's concentration, and pK_w value.

5 - Aim of the thesis

The purpose of this thesis work was the removal of heavy metal ions and organic dyes from water by adsorption through the use of synthetic nanostructured materials, such as functionalized ordered mesoporous silica (OMS) and metal-organic frameworks (MOFs).

5.1 - Functionalized OMS for the adsorption of heavy metal ions

Chelating molecules are the best tools for capturing heavy metal ions. However, since the formation of complexes in the homogeneous phase would not be useful to remove the aforementioned metals from the water, a heterogenization of the chelating agents is necessary. OMS do not in themselves represent an innovative material, but thanks to their huge surface area and the presence of superficial silanols, they can be easily used for the immobilization of a very wide range of molecules with considerable loads. For this reason, the OMS have been considered excellent candidates as supports for the ligands selected for this work.

Firstly, the synthesis of the SBA-15 type silica were carried out according to Zhao et al. procedure.⁹⁹ Then, in order to obtain more efficient and specific adsorbent for the removal of heavy metal ions, the post synthesis surface functionalizations with two different organic ligands, namely Triethylenetetramine (TETA) and 2,8-dithia-5-aza-2,6-pyridinophane macrocycle (PyNS₂), were performed.

Triethylenetetramine (TETA) is a commercial linear organic molecule containing four chelating amino groups (two primary and two secondary) whose degree of protonation depends on the pH. In aqueous medium, these or amino groups are able to coordinate Cu²⁺ and Zn²⁺ ions generating stable complexes. Heterogenized TETA has been already used for different purposes, such as Cu²⁺ ion selective membranes, realization of hybrid membranes for nanofiltration. In the context of adsorption, the functionalization of different materials with TETA has given rise to excellent absorbent materials. For instance, TETA has been successfully immobilized on mesoporous silica for

CO₂ capture on biomass and hybrid magnetic graphene¹⁵¹ for the adsorption of organic dyes, and on magnetic coreshell particles of silica-coated iron oxide, for the removal of Pb²⁺ and Cu²⁺ from water.¹⁵²

The 2,8-dithia-5-aza-2,6-pyridinophane (PyNS₂) is a N₂S₂-donating 12-membered macrocycle, where a pyridine ring ensures rigidity to the structure and a certain distance between the electron donating atoms. Macrocycles are exceptionally interesting due to their ability to coordinate various metal ions (both alkaline earth and transition metals) on adapting their structure and changing the nature of donor atoms. The selectivity can be regulated according to the soft-hard properties of the electron donor atoms, and to the conformation and size of the macrocycle. The studies carried out by Blake et al.¹⁵³ have shown that PyNS₂ is able to stably coordinate Cu²⁺, Hg²⁺, Cd²⁺ and Pb²⁺ forming 1: 1 complexes thanks to the soft S-donors. By virtue of this, PyNS₂ functionalized with different fluorescent subunits, such as coumarins,¹⁵⁴ naphthol-benzoxazoles,¹⁵⁴ quinoline derivatives,¹⁵⁵¹⁵⁶ and anthracene derivatives, turned out to be an excellent fluorescent chemosensor for the detection of heavy metal ions, both in liquid and solid state.

To the best of our knowledge, the PyNS₂ has never been used for environmental remediation purposes.

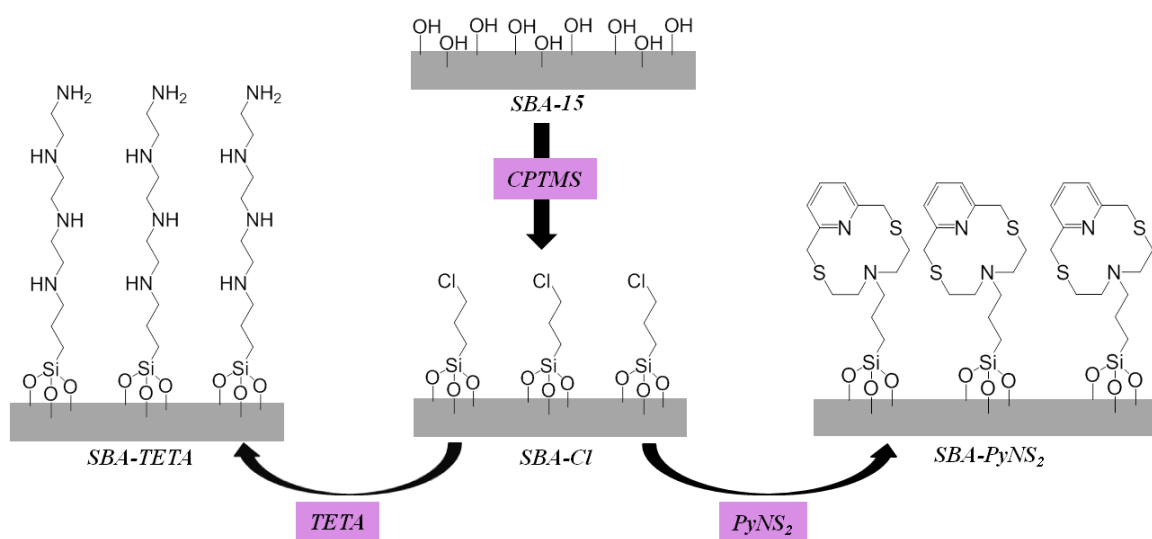


Figure 38. Functionalization of SBA-15 with TETA and with PyNS₂.

Since the direct covalent grafting of TETA and PyNS₂ onto SBA-15 is not possible, in both cases an intermediate functionalization with chloropropyltrimethoxysilane (CPTMS) was carried out (**Figure 38**), in order to introduce the ligands in a second step by nucleophilic substitution with the exiting of Cl⁻.

The silica-based adsorbents thus obtained (SBA-TETA and SBA-PyNS₂) were characterized from a structural, textural and chemical point of view by means of Small Angle X-Rays Scattering (SAXS), Transmission Electron Microscopy (TEM), N₂ physisorption, Thermogravimetric Analysis (TGA), Fourier-Transform Infrared spectroscopy (FT-IR) and potentiometric titration.

At last, batch adsorption experiments were conducted to evaluate the adsorbing performance of SBA-TETA and SBA-PyNS₂ against some heavy metal ions. By monitoring these experiments with UV-Vis spectrophotometric analysis (through colorimetric method) and Inductively Coupled Plasma Optical Emission Spectroscopy (ICP-OES), and then fitting the experimental data with some isotherms and kinetic models, the thermodynamic and kinetic parameters of the adsorption processes were determined. In addition, potentiometric studies allowed to obtain information about the stoichiometry and stability of the various adsorbent-metal ions pairs.

The study of SBA-TETA material and its adsorbing performances towards Cu²⁺ and Zn²⁺ are the content of **PAPER I** and **PAPER II**. In particular, **PAPER I** fully elucidates the synthesis and characterization of SBA-TETA, and describes the experiments (isotherms and kinetics) that have been carried out in order to determine the kinetic and thermodynamic adsorption parameters. **PAPER II**, realized in collaboration with the KAUST (King Abdullah University of Science and Technology of Saudi Arabia), re-confirms **PAPER I** data through the use of potentiometry, Electron Paramagnetic Resonance (EPR) and Solid State Nuclear Magnetic Resonance (ssNMR), and represents the first example in the literature of ligand content quantification of a functionalized material by means of potentiometric technique. Furthermore **PAPER II** provides an in-depth study of the solution equilibria of Cu-SBA-TETA and Zn-SBA-TETA complexes.

PAPER III presents the synthesis and characterization of SBA-PyNS₂ and its adsorbing performances towards Cu²⁺ and Cd⁺. Both systems Cu- SBA-PyNS₂ and Cd-SBA-PyNS₂ have been studied from the kinetic and thermodynamic point of view, and their stability and speciation in solution were determined by means of the potentiometric method.

5.2 - Fe-BTC type MOF for the adsorption of organic dyes

Numerous examples of highly performing MOFs for the adsorption of organic dyes are reported in the literature. However, the procedures adopted for the synthesis of the vast majority of these MOFs, implies poorly eco-sustainable operational conditions, such as high temperature, organic solvents, toxic reagents, long reaction time, etc. For this reason, one of the aims of this thesis work was the study of the adsorption capacities of a MOF synthesized by means of a mild synthesis procedure, and compare its performance with those of similar materials obtained by anti-ecological synthesis.

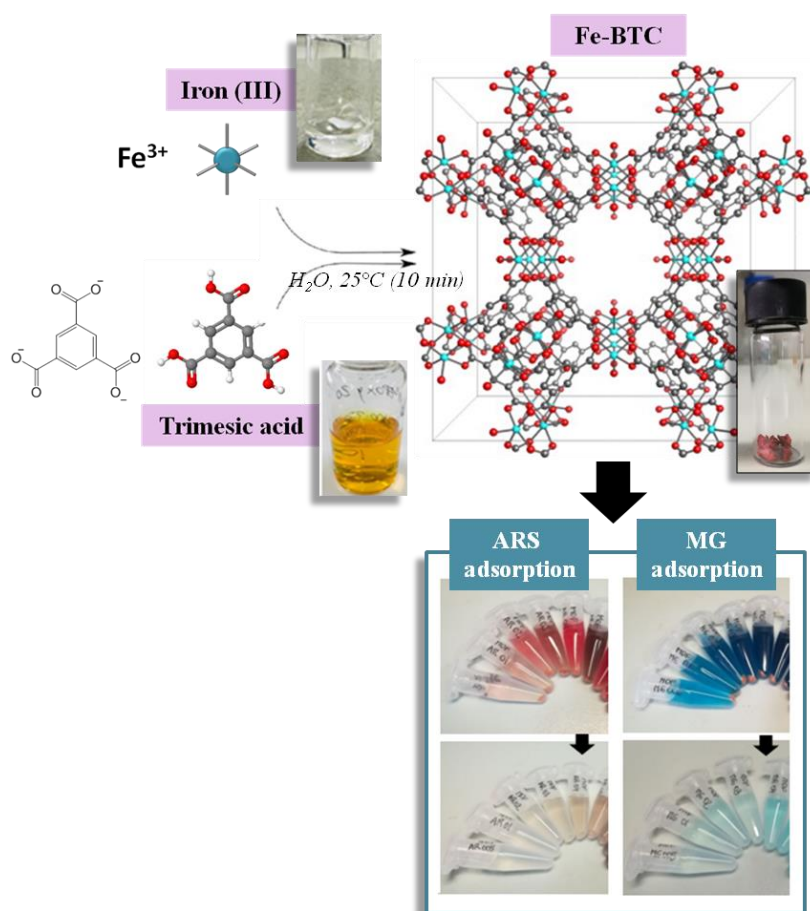


Figure 39. FeBTC synthesized according to the Sanchez-Sanchez procedure and its application as a dye adsorbent.

For this purpose, a MOF made of iron and trimesic acid, Fe-BTC, was synthesized exploiting the synthetic procedure proposed by Sanchez-Sanchez in 2015,¹²¹ which is facile, rapid and practicable under environmentally and economically sustainable conditions (few minutes at room temperature using water as solvent) (**Figure 39**). As fully described in **PAPER IV**, thus synthesized Fe-BTC has been characterized by means of Powder X-rays Scattering (XRD), Scanning Electron Microscopy (SEM), N₂ physisorption, Thermogravimetric Analysis (TGA) and Fourier-Transform Infrared spectroscopy (FT-IR). Then batch adsorption experiments were conducted to evaluate the adsorbing performance of Fe-BTC against Malachite Green (MG) and Alizarin Red S (ARS) organic dyes. The thermodynamic and kinetic parameters related to both the adsorption processes, were determined by monitoring these experiments by means of UV-Vis spectrophotometric analysis, and then comparing the obtained experimental data with the trend proposed by some theoretical models.

References

- (1) Yadav, N.; Garg, V. K.; Chhillar, A. K.; Rana, J. S. Detection and Remediation of Pollutants to Maintain Ecosustainability Employing Nanotechnology: A Review. *Chemosphere* **2021**, *280*, 130792.
- (2) Masindi, V.; Muedi, K. L. Environmental Contamination by Heavy Metals. In *Heavy Metals*; InTech, 2018.
- (3) El-Shahawi, M. S.; Hamza, A.; Bashammakh, A. S.; Al-Saggaf, W. T. An Overview on the Accumulation, Distribution, Transformations, Toxicity and Analytical Methods for the Monitoring of Persistent Organic Pollutants. *Talanta* **2010**, *80* (5), 1587–1597.
- (4) Negrete-Bolagay, D.; Zamora-Ledezma, C.; Chuya-Sumba, C.; De Sousa, F. B.; Whitehead, D.; Alexis, F.; Guerrero, V. H. Persistent Organic Pollutants: The Trade-off between Potential Risks and Sustainable Remediation Methods. *J. Environ. Manage.* **2021**, *300*, 113737.
- (5) Van Ael, E.; Covaci, A.; Blust, R.; Bervoets, L. Persistent Organic Pollutants in the Scheldt Estuary: Environmental Distribution and Bioaccumulation. *Environ. Int.* **2012**, *48*, 17–27.
- (6) Ismail, M.; Akhtar, K.; Khan, M. I.; Kamal, T.; Khan, M. A.; M. Asiri, A.; Seo, J.; Khan, S. B. Pollution, Toxicity and Carcinogenicity of Organic Dyes and Their Catalytic Bio-Remediation. *Curr. Pharm. Des.* **2019**, *25* (34), 3645–3663.
- (7) Duffus, J. H. “HEAVY METALS”-A MEANINGLESS TERM? (IUPAC Technical Report). *Pure Appl. Chem* **2002**, *74*, 1999–2001.
- (8) Pourret, O.; Hursthouse, A. It’s Time to Replace the Term “heavy Metals” with “potentially Toxic Elements” When Reporting Environmental Research. *Int. J. Environ. Res. Public Health* **2019**, *16*, 4446.
- (9) Berni, R.; Luyckx, M.; Xu, X.; Legay, S.; Sergeant, K.; Hausman, J. F.; Lutts, S.; Cai, G.; Guerriero, G. Reactive Oxygen Species and Heavy Metal Stress in Plants: Impact on the Cell Wall and Secondary Metabolism. *Environ. Exp. Bot.* **2019**, *161*, 98–106.

- (10) Di Meo, S.; Reed, T. T.; Venditti, P.; Victor, V. M. Role of ROS and RNS Sources in Physiological and Pathological Conditions. *Oxid. Med. Cell. Longev.* **2016**, *2016*, 44.
- (11) Wu, S.; Hu, C.; Yang, X.; Tan, Q.; Yao, S.; Zhou, Y.; Wang, X.; Sun, X. Molybdenum Induces Alterations in the Glycerolipidome That Confer Drought Tolerance in Wheat. *J. Exp. Bot.* **2020**, *71* (16), 5074–5086.
- (12) Jan, A. T.; Azam, M.; Siddiqui, K.; Ali, A.; Choi, I.; Haq, Q. M. R. Heavy Metals and Human Health: Mechanistic Insight into Toxicity and Counter Defense System of Antioxidants. *Int. J. Mol. Sci.* **2015**, *16* (12), 29592–29630.
- (13) Dempsey, C.; McCormick, N. H.; Croxford, T. P.; Seo, Y. A.; Grider, A.; Kelleher, S. L. Marginal Maternal Zinc Deficiency in Lactating Mice Reduces Secretory Capacity and Alters Milk Composition. *J. Nutr.* **2012**, *142* (4), 655–660.
- (14) Shi, X.; Xu, H.; Wu, Y.; Zhao, Y.; Meng, H. M.; Li, Z.; Qu, L. Two-Dimension (2D) Cu-MOFs/aptamer Nanoprobe for In Situ ATP Imaging in Living Cells. *J. Anal. Test.* **2021**, *5* (2), 165–173.
- (15) Lewicka, I.; Kocylowski, R.; Grzesiak, M.; Gaj, Z.; Oszukowski, P.; Suliburska, J. Selected Trace Elements Concentrations in Pregnancy and Their Possible Role - Literature Review. *Ginekol. Pol.* **2017**, *88*, 509–514.
- (16) Roberts, E. A.; Schilsky, M. L. Diagnosis and Treatment of Wilson Disease: An Update. *Hepatology* **2008**, *47*, 2089–2111.
- (17) Chen, J.; Jiang, Y.; Shi, H.; Peng, Y.; Fan, X.; Li, C. The Molecular Mechanisms of Copper Metabolism and Its Roles in Human Diseases. *Eur. J. Physiol.* **2020**, *472*, 1415–1429.
- (18) Subramaniam, V. D.; Prasad, S. V.; Banerjee, A.; Gopinath, M.; Murugesan, R.; Marotta, F.; Sun, X. F.; Pathak, S. Health Hazards of Nanoparticles: Understanding the Toxicity Mechanism of Nanosized ZnO in Cosmetic Products. *Drug Chem. Toxicol.* **2019**, *42*, 84–93.
- (19) Piccinno, F.; Gottschalk, F.; Seeger, S.; Nowack, B. Industrial Production Quantities and Uses

- of Ten Engineered Nanomaterials in Europe and the World. *J. Nanoparticle Res.* **2012**, *14*, 1109.
- (20) Hackenberg, M.; Gustafson, P.; Langridge, P.; Shi, B. J. Differential Expression of microRNAs and Other Small RNAs in Barley between Water and Drought Conditions. *Plant Biotechnol. J.* **2015**, *13* (1), 2–13.
- (21) Schieber, M.; Chandel, N. S. ROS Function in Redox Signaling and Oxidative Stress. *Curr. Biol.* **2014**, *24*.
- (22) Abbas, T.; Rizwan, M.; Ali, S.; Zia-ur-Rehman, M.; Farooq Qayyum, M.; Abbas, F.; Hannan, F.; Rinklebe, J.; Sik Ok, Y. Effect of Biochar on Cadmium Bioavailability and Uptake in Wheat (*Triticum Aestivum* L.) Grown in a Soil with Aged Contamination. *Ecotoxicol. Environ. Saf.* **2017**, *140*, 37–47.
- (23) Irshad, M. A.; Rehman, M. Z. ur; Anwar-ul-Haq, M.; Rizwan, M.; Nawaz, R.; Shakoor, M. B.; Wijaya, L.; Alyemeni, M. N.; Ahmad, P.; Ali, S. Effect of Green and Chemically Synthesized Titanium Dioxide Nanoparticles on Cadmium Accumulation in Wheat Grains and Potential Dietary Health Risk: A Field Investigation. *J. Hazard. Mater.* **2021**, *415*, 125585.
- (24) Feng, J.; Jia, W.; Lv, S.; Bao, H.; Miao, F.; Zhang, X.; Wang, J.; Li, J.; Li, D.; Zhu, C.; et al. Comparative Transcriptome Combined with Morpho-Physiological Analyses Revealed Key Factors for Differential Cadmium Accumulation in Two Contrasting Sweet Sorghum Genotypes. *Plant Biotechnol. J.* **2018**, *16* (2), 558–571.
- (25) Wu, S.; Hu, C.; Wang, X.; Wang, Y.; Yu, M.; Xiao, H.; Shabala, S.; Wu, K.; Tan, Q.; Xu, S.; et al. Cadmium-Induced Changes in Composition and Co-Metabolism of Glycerolipids Species in Wheat Root: Glycerolipidomic and Transcriptomic Approach. *J. Hazard. Mater.* **2022**, *423*, 127115.
- (26) Farsalinos, K. E.; Voudris, V.; Poulas, K. Are Metals Emitted from Electronic Cigarettes a Reason for Health Concern? A Risk-Assessment Analysis of Currently Available Literature.

Int. J. Environ. Res. Public Health **2015**, *12* (5), 5215–5232.

- (27) Sivakumar, V.; Anna, J. L.; Vijayeeswarri, J.; Swaminathan, G. Ultrasound Assisted Enhancement in Natural Dye Extraction from Beetroot for Industrial Applications and Natural Dyeing of Leather. *Ultrason. Sonochem.* **2009**, *16* (6), 782–789.
- (28) Silva, P. M. dos S.; Fiaschitello, T. R.; Queiroz, R. S. de; Freeman, H. S.; Costa, S. A. da; Leo, P.; Montemor, A. F.; Costa, S. M. da. Natural Dye from Croton Urucurana Baill. Bark: Extraction, Physicochemical Characterization, Textile Dyeing and Color Fastness Properties. *Dye. Pigment.* **2020**, *173*, 107953.
- (29) Travis, A. S. Perkin's Mauve: Ancestor of the Organic Chemical Industry. *Source Technol. Cult.* **1990**, *31*, 51–82.
- (30) Benkhaya, S.; M'rabet, S.; El Harfi, A. A Review on Classifications, Recent Synthesis and Applications of Textile Dyes. *Inorg. Chem. Commun.* **2020**, *115*, 107891.
- (31) Chandanshive, V. V.; Kadam, S. K.; Khandare, R. V.; Kurade, M. B.; Jeon, B. H.; Jadhav, J. P.; Govindwar, S. P. In Situ Phytoremediation of Dyes from Textile Wastewater Using Garden Ornamental Plants, Effect on Soil Quality and Plant Growth. *Chemosphere* **2018**, *210*, 968–976.
- (32) Yuan, H.; Chen, L.; Cao, Z.; Hong, F. F. Enhanced Decolourization Efficiency of Textile Dye Reactive Blue 19 in a Horizontal Rotating Reactor Using Strips of BNC-Immobilized Laccase: Optimization of Conditions and Comparison of Decolourization Efficiency. *Biochem. Eng. J.* **2020**, *156*, 107501.
- (33) Rajeswari, A.; Vismaiya, S.; Pius, A. Preparation, Characterization of Nano ZnO-Blended Cellulose Acetate-Polyurethane Membrane for Photocatalytic Degradation of Dyes from Water. *Chem. Eng. J.* **2017**, *313*, 928–937.
- (34) Guidry, G. A Method for Counterstaining Tissues in Conjunction with the Glyoxylic Acid Condensation Reaction for Detection of Biogenic Amines. *J. Histochem. Cytochem.* **1999**, *47*,

261–264.

- (35) Kaylor, L.; Skelly, P.; Alsarrani, M.; Subir, M. Enhanced Malachite Green Photolysis at the Colloidal-Aqueous Interface. *Chemosphere* **2022**, *287*, 131953.
- (36) Mao, Y.; Yang, S.; Xue, C.; Zhang, M.; Wang, W.; Song, Z.; Zhao, X.; Sun, J. Rapid Degradation of Malachite Green by CoFe₂O₄-SiC Foam under Microwave Radiation. *R. Soc. Open Sci.* **2018**, *5* (6).
- (37) Chen, G.; Miao, S. HPLC Determination and MS Confirmation of Malachite Green, Gentian Violet, and Their Leuco Metabolite Residues in Channel Catfish Muscle. *J. Agric. Food Chem.* **2010**, *58* (12), 7109–7114.
- (38) Henderson, A. L.; Schmitt, T. C.; Heinze, T. M.; Cerniglia, C. E. Reduction of Malachite Green to Leucomalachite Green by Intestinal Bacteria. *Appl. Environ. Microbiol.* **1997**, *63*, 4099–4101.
- (39) Srivastav, A. K.; Roy, D. Malachite Green (Triarylmethane Dye) and Pyceze (Bronopol) Induced Histopathological and Biochemical Changes in the Liver of Stinging Catfish *Heteropneustes Fossilis* (Bloch, 1794). *Indian J. Fish.* **2016**, *63* (1), 135–139.
- (40) Kwan, P. P.; Banerjee, S.; Shariff, M.; Yusoff, F. M. Persistence of Malachite Green and Leucomalachite Green in Red Tilapia (*Oreochromis Hybrid*) Exposed to Different Treatment Regimens. *Food Control* **2020**, *108*, 106866.
- (41) Mittelstaedt, R. A.; Mei, N.; Webb, P. J.; Shaddock, J. G.; Dobrovolsky, V. N.; McGarrity, L. J.; Morris, S. M.; Chen, T.; Beland, F. A.; Greenlees, K. J.; et al. Genotoxicity of Malachite Green and Leucomalachite Green in Female Big Blue B6C3F1 Mice. *Mutat. Res. - Genet. Toxicol. Environ. Mutagen.* **2004**, *561* (1–2), 127–138.
- (42) Culp, S. J.; Mellick, P. W.; Trotter, R. W.; Greenlees, K. J.; Kodell, R. L.; Beland, F. A. Carcinogenicity of Malachite Green Chloride and Leucomalachite Green in B6C3F1 Mice and F344 Rats. *Food Chem. Toxicol.* **2006**, *44* (8), 1204–1212.

- (43) Ali, F.; Bibi, S.; Ali, N.; Ali, Z.; Said, A.; Wahab, Z. U.; Bilal, M.; Iqbal, H. M. N. Sorptive Removal of Malachite Green Dye by Activated Charcoal: Process Optimization, Kinetic, and Thermodynamic Evaluation. *Case Stud. Chem. Environ. Eng.* **2020**, *2*, 1000025.
- (44) Gopinathan, R.; Kanhere, J.; Banerjee, J. Effect of Malachite Green Toxicity on Non Target Soil Organisms. *Chemosphere* **2015**, *120*, 637–644.
- (45) Slimani, R.; El Ouahabi, I.; Benkaddour, S.; Hiyane, H.; Essoufy, M.; Achour, Y.; El Antri, S.; Lazar, S.; El Haddad, M. Removal Efficiency of Textile Dyes from Aqueous Solutions Using Calcined Waste of Eggshells as Eco-Friendly Adsorbent: Kinetic and Thermodynamic Studies. *Chem. Biochem. Eng. Q.* **2021**, *35*, 43–56.
- (46) Wang, L.; Liu, S.; Ren, C.; Xiang, S.; Li, D.; Hao, X.; Ni, S.; Chen, Y.; Zhang, K.; Sun, H. Construction of Hollow Polydopamine Nanoparticle Based Drug Sustainable Release System and Its Application in Bone Regeneration. *Int. J. Oral Sci.* **2021**, *13*.
- (47) Grotheer, V.; Skrynecki, N.; Oezel, L.; Grassmann, J.; Windolf, J.; Suschek, C. V. Osteogenic Differentiation of Human Mesenchymal Stromal Cells and Fibroblasts Differs Depending on Tissue Origin and Replicative Senescence. *Sci. Rep.* **2021**, *11*, 11968.
- (48) Luo, H.; Li, D.; Chen, Z.; Wang, B.; Chen, S. Manufacturing and Banking Canine Adipose-Derived Mesenchymal Stem Cells for Veterinary Clinical Application. *BMC Vet. Res.* **2021**, *17*, 96.
- (49) Malik, A.; Einbinder, S.; Martinez, S.; Tchernov, D.; Haviv, S.; Almuly, R.; Zaslansky, P.; Polishchuk, I.; Pokroy, B.; Stolarski, J.; et al. Molecular and Skeletal Fingerprints of Scleractinian Coral Biomineralization: From the Sea Surface to Mesophotic Depths. *Acta Biomater.* **2021**, *120*, 263–276.
- (50) Darrenougue, N.; De Deckker, P.; Eggins, S.; Payri, C. Sea-Surface Temperature Reconstruction from Trace Elements Variations of Tropical Coralline Red Algae. *Quat. Sci. Rev.* **2014**, *93*, 34–46.

- (51) Zhang, Z.; Chen, H.; Wu, W.; Pang, W.; Yan, G. Efficient Removal of Alizarin Red S from Aqueous Solution by Polyethyleneimine Functionalized Magnetic Carbon Nanotubes. *Bioresour. Technol.* **2019**, *293*, 122100.
- (52) Burakov, A.; Neskromnaya, E.; Babkin, A. Removal of the Alizarin Red S Anionic Dye Using Graphene Nanocomposites: A Study on Kinetics under Dynamic Conditions. *Mater. Today Proc.* **2019**, *11*, 392–397.
- (53) Sujitha, R.; Ravindhranath, K. Extraction of Anionic Dye, Alizarin Red S, from Industrial Waste Waters Using Active Carbon Derived from the Stems of *Achyranthes Aspera* Plant as Bio-Adsorbent. *Der Pharma Chem.* **2016**, *8*, 63–73.
- (54) Mamat, M.; Roslan, N.; Bulat, K. H. K.; Abdullah, M. A. A.; Jaafar, A. M. Evaluation on Adsorption Isotherms of Alizarin Red S Dye Removal by Nickel/aluminium Layered Double Hydroxide. *IOP Conf. Ser. Mater. Sci. Eng.* **2018**, *440*.
- (55) Zhu, J.; Zhang, X.; Li, D.; Jin, J. Probing the Binding of Flavonoids to Catalase by Molecular Spectroscopy. *J. Mol. Struct.* **2007**, *843* (1–3), 38–44.
- (56) Krych, J.; Gebicka, L. Catalase Is Inhibited by Flavonoids. *Int. J. Biol. Macromol.* **2013**, *58*, 148–153.
- (57) Gebicka, L.; Krych-Madej, J. The Role of Catalases in the Prevention/promotion of Oxidative Stress. *J. Inorg. Biochem.* **2019**, *197*, 110699.
- (58) Majumder, D.; Das, A.; Saha, C. Catalase Inhibition an Anti Cancer Property of Flavonoids: A Kinetic and Structural Evaluation. *Int. J. Biol. Macromol.* **2017**, *104*, 929–935.
- (59) Hu, S.; Yuan, D.; Liu, Y.; Zhao, L.; Guo, H.; Niu, Q.; Zong, W.; Liu, R. The Toxic Effects of Alizarin Red S on Catalase at the Molecular Level. *RSC Adv.* **2019**, *9*, 33368–33377.
- (60) Lemlikchi, W.; Sharrock, P.; Fiallo, M.; Nzihou, A.; Mecherri, M. O. Hydroxyapatite and Alizarin Sulfonate ARS Modeling Interactions for Textile Dyes Removal from Wastewaters. *Procedia Eng.* **2014**, *83*, 378–385.

- (61) Wu, H.; Zhao, X.; Wang, P.; Dai, Z.; Zou, X. Electrochemical Site Marker Competitive Method for Probing the Binding Site and Binding Mode between Bovine Serum Albumin and Alizarin Red S. *Electrochim. Acta* **2011**, *56* (11), 4181–4187.
- (62) Sharma, M.; Jain, P.; Mishra, A.; Mehta, A.; Choudhury, D.; Hazra, S.; Basu, S. Variation of Surface Area of Silica Monoliths by Controlling Ionic Character/chain Length of Surfactants and Polymers. *Mater. Lett.* **2017**, *194*, 213–216.
- (63) Sharma, M.; Choudhury, D.; Hazra, S.; Basu, S. Effective Removal of Metal Ions from Aqueous Solution by Mesoporous MnO₂ and TiO₂ Monoliths: Kinetic and Equilibrium Modelling. *J. Alloys Compd.* **2017**, *720*, 221–229.
- (64) Krishnan, S.; Zulkapli, N. S.; Kamyab, H.; Taib, S. M.; Din, M. F. B. M.; Majid, Z. A.; Chaiprapat, S.; Kenzo, I.; Ichikawa, Y.; Nasrullah, M.; et al. Current Technologies for Recovery of Metals from Industrial Wastes: An Overview. *Environ. Technol. Innov.* **2021**, *22*, 101525.
- (65) Benalia, M. C.; Youcef, L.; Bouaziz, M. G.; Achour, S.; Menasra, H. Removal of Heavy Metals from Industrial Wastewater by Chemical Precipitation: Mechanisms and Sludge Characterization. *Arab. J. Sci. Eng.* **2021**.
- (66) Shrestha, R.; Ban, S.; Devkota, S.; Sharma, S.; Joshi, R.; Tiwari, A. P.; Kim, H. Y.; Joshi, M. K. Technological Trends in Heavy Metals Removal from Industrial Wastewater: A Review. *J. Environ. Chem. Eng.* **2021**, *9*, 105688.
- (67) Blais, J. F.; Djedidi, ; Z; Cheikh, ; R Ben; Tyagi, ; R D; Mercier, G. Metals Precipitation from Effluents: Review. *Pactical Period. Hazardous, Toxic Radioact. waste Manag.* **2008**, *135*.
- (68) Lewis, A. E. Review of Metal Sulphide Precipitation. *Hydrometallurgy* **2010**, *104* (2), 222–234.
- (69) Saracino, M.; Emmi, S.; Zanelli, A. Water Remediation 2.0: Advanced Oxidation Processes. *Chim. Ambient.* **2015**.

- (70) Ghime, D.; Ghosh, P. Advanced Oxidation Processes: A Powerful Treatment Option for the Removal of Recalcitrant Organic Compounds. *IntechOpen* **2019**.
- (71) Pitzalis, F.; Monduzzi, M.; Salis, A. A Bionzymatic Biocatalyst Constituted by Glucose Oxidase and Horseradish Peroxidase Immobilized on Ordered Mesoporous Silica. *Microporous Mesoporous Mater.* **2017**, *241*, 145–154.
- (72) Pitzalis, F.; Carucci, C.; Naseri, M.; Fotouhi, L.; Magner, E.; Salis, A. Lipase Encapsulation onto ZIF-8: A Comparison between Biocatalysts Obtained at Low and High Zinc/2-Methylimidazole Molar Ratio in Aqueous Medium. *ChemCatChem* **2018**, *10* (7), 1578–1585.
- (73) Tsuneda, T. Fenton Reaction Mechanism Generating No OH Radicals in Nafion Membrane Decomposition. *Sci. Rep.* **2020**, *10* (1).
- (74) Wardman, P.; Candeias, L. P. *Fenton Chemistry: An Introduction*; 1996; Vol. 145.
- (75) O'Shea, K. E.; Dionysiou, D. D. Advanced Oxidation Processes for Water Treatment. *J. Phys. Chem. Lett.* **2012**, *3*, 2112–2113.
- (76) Xu, M.; Wu, C.; Zhou, Y. Advancements in the Fenton Process for Wastewater Treatment. *IntechOpen* **2019**.
- (77) Fraiese, A.; Naddeo, V.; Uyguner-Demirel, C. S.; Prado, M.; Cesaro, A.; Zarra, T.; Liu, H.; Belgiorno, V.; Ballesteros, F. Removal of Emerging Contaminants in Wastewater by Sonolysis, Photocatalysis and Ozonation. *Glob. Nest J.* **2019**, *21* (2), 98–105.
- (78) Coman, V.; Robotin, B.; Ilea, P. Nickel Recovery/removal from Industrial Wastes: A Review. *Resour. Conserv. Recycl.* **2013**, *73*, 229–238.
- (79) Wawrzekiewicz, M.; Hubicki, Z. Anion Exchange Resins as Effective Sorbents for Removal of Acid, Reactive, and Direct Dyes from Textile Wastewaters. *IntechOpen* **2015**.
- (80) Lan, Y.; Du, Q.; Tang, C.; Cheng, K.; Yang, F. Application of Typical Artificial Carbon Materials from Biomass in Environmental Remediation and Improvement: A Review. *J. Environ. Manage.* **2021**, *296*, 113340.

- (81) Al-Asheh, S.; Aidan, A. A Comprehensive Method of Ion Exchange Resins Regeneration and Its Optimization for Water Treatment. In *Promising Techniques for Wastewater Treatment and Water Quality Assessment*; IntechOpen, 2020.
- (82) Amphlett, J. T. M.; Choi, S.; Parry, S. A.; Moon, E. M.; Sharrad, C. A.; Ogden, M. D. Insights on Uranium Uptake Mechanisms by Ion Exchange Resins with Chelating Functionalities: Chelation vs. Anion Exchange. *Chem. Eng. J.* **2020**, *392*, 123712.
- (83) Baharuddin, N. H.; Sulaiman, N. M. N.; Aroua, M. K.; Nawawi, M. G. M.; Kassim, M. A.; Othman, M. R.; Dahlan, I. Starch as Novel Water Soluble Biopolymer in Removal Mixtures Heavy Metal Ions via Polymer Enhanced Ultrafiltration. In *AIP Conference Proceedings*; American Institute of Physics Inc., 2019; Vol. 2124.
- (84) Lee, C. S.; Robinson, J.; Chong, M. F. A Review on Application of Flocculants in Wastewater Treatment. *Process Saf. Environ. Prot.* **2014**, *92*, 489–508.
- (85) Sun, Y.; Li, D.; Lu, X.; Sheng, J.; Zheng, X.; Xiao, X. Flocculation of Combined Contaminants of Dye and Heavy Metal by Nano-Chitosan Flocculants. *J. Environ. Manage.* **2021**, *299*, 113589.
- (86) Teh, C. Y.; Budiman, P. M.; Shak, K. P. Y.; Wu, T. Y. Recent Advancement of Coagulation-Flocculation and Its Application in Wastewater Treatment. *Ind. Eng. Chem. Res.* **2016**, *55*, 4363–4389.
- (87) Grabi, H.; Derridj, F.; Lemlikchi, W.; Guénin, E. Studies of the Potential of a Native Natural Biosorbent for the Elimination of an Anionic Textile Dye Cibacron Blue in Aqueous Solution. *Sci. Rep.* **2021**, *11* (1).
- (88) Wang, J.; Chen, C. Biosorbents for Heavy Metals Removal and Their Future. *Biotechnol. Adv.* **2009**, *27*, 195–226.
- (89) Sameera, V.; Naga Deepthi, C.; Srinu Babu, G.; Ravi Teja, Y. Role of Biosorption in Environmental Cleanup. *J. Microb. Biochem. Technol.* **2011**, *3* (3).

- (90) Khin, M. M.; Nair, A. S.; Babu, V. J.; Murugan, R.; Ramakrishna, S. A Review on Nanomaterials for Environmental Remediation. *Energy Environ. Sci.* **2012**, *5*, 8075–8109.
- (91) Hartmann, M.; Kostrov, X. Immobilization of Enzymes on Porous Silicas – Benefits and Challenges. *Chem. Soc. Rev.* **2013**, *42*, 6277.
- (92) Medda, L.; Casula, M. F.; Monduzzi, M.; Salis, A. Adsorption of Lysozyme on Hyaluronic Acid Functionalized SBA-15 Mesoporous Silica: A Possible Bioadhesive Depot System. *Langmuir* **2014**, *30*, 12996–13004.
- (93) Nairi, V.; Medda, L.; Monduzzi, M.; Salis, A. Adsorption and Release of Ampicillin Antibiotic from Ordered Mesoporous Silica. *J. Colloid Interface Sci.* **2017**, *497*, 217–225.
- (94) Delpiano, G. R.; Casula, M. F.; Piludu, M.; Corpino, R.; Ricci, P. C.; Vallet-Regí, M.; Sanjust, E.; Monduzzi, M.; Salis, A. Assembly of Multicomponent Nano-Bioconjugates Composed of Mesoporous Silica Nanoparticles, Proteins, and Gold Nanoparticles. *ACS Omega* **2019**, *4* (6).
- (95) Salis, A.; Fanti, M.; Medda, L.; Nairi, V.; Cugia, F.; Piludu, M.; Sogos, V.; Monduzzi, M. Mesoporous Silica Nanoparticles Functionalized with Hyaluronic Acid and Chitosan Biopolymers. Effect of Functionalization on Cell Internalization. *ACS Biomater. Sci. Eng.* **2016**, *2*, 741–751.
- (96) Baeza, A.; Manzano, M.; Colilla, M.; Vallet-Regi, M. Recent Advances in Mesoporous Silica Nanoparticles for Antitumor Therapy: Our Contribution. *Biomater. Sci.* **2016**, *4*, 803–813.
- (97) Feinle, A.; Elsaesser, M. S.; Hüsing, N. Sol–gel Synthesis of Monolithic Materials with Hierarchical Porosity. *Chem. Soc. Rev.* **2016**, *45* (12), 3377–3399.
- (98) Galarneau, A.; Iapichella, J.; Brunel, D.; Fajula, F.; Bayram-Hahn, Z.; Unger, K.; Puy, G.; Demesmay, C.; Rocca, J. L. Spherical Ordered Mesoporous Silicas and Silica Monoliths as Stationary Phases for Liquid Chromatography. *J. Sep. Sci.* **2006**, *29* (6), 844–855.
- (99) Zhao, D.; Feng, J.; Huo, Q.; Melosh, N.; Fredrickson, G. H.; Chmelka, B. F.; Stucky, G. D. Triblock Copolymer Syntheses of Mesoporous Silica with Periodic 50 to 300 Angstrom

- Pores. *Science* **1998**, 279 (5350), 548–552.
- (100) Salis, A.; Medda, L.; Cugia, F.; Monduzzi, M. Effect of Electrolytes on Proteins Physisorption on Ordered Mesoporous Silica Materials. *Colloids Surfaces B Biointerfaces* **2016**, 137, 77–90.
- (101) Magner, E. Immobilisation of Enzymes on Mesoporous Silicate Materials. *Chem. Soc. Rev.* **2013**, 42, 6213.
- (102) Palmqvist, A. E. C. Synthesis of Ordered Mesoporous Materials Using Surfactant Liquid Crystals or Micellar Solutions. *Curr. Opin. Colloid Interface Sci.* **2003**, 8, 145–155.
- (103) Kresge, C. T.; Leonowicz, M. E.; Roth, W. J.; Vartuli, J. C.; Beck, J. S. Ordered Mesoporous Molecular Sieves Synthesized by a Liquid-Crystal Template Mechanism. *Nature* **1992**, 359 (6397), 710–712.
- (104) Pallach, R.; Keupp, J.; Terlinden, K.; Frenzel-Beyme, L.; Kloß, M.; Machalica, A.; Kotschy, J.; Vasa, S. K.; Chater, P. A.; Sternemann, C.; et al. Frustrated Flexibility in Metal-Organic Frameworks. *Nat. Commun.* **2021**, 12 (1).
- (105) Alothman, Z. A. A Review: Fundamental Aspects of Silicate Mesoporous Materials. *Materials (Basel)*. **2012**, 5 (12), 2874–2902.
- (106) Cervantes-Martinez, C. V.; Stébé, M. J.; Emo, M.; Lebeau, B.; Blin, J. L. Hierarchical Mesoporous Silica Templated by the Combination of Fine Emulsion and Micelles. *Microporous Mesoporous Mater.* **2020**, 305.
- (107) Nguyen, Q. N. K.; Yen, N. T.; Hau, N. D.; Tran, H. L. Synthesis and Characterization of Mesoporous Silica SBA-15 and ZnO/SBA-15 Photocatalytic Materials from the Ash of Brickyards. *J. Chem.* **2020**, 2020.
- (108) Katiyar, A.; Ji, L.; Smirniotis, P. G.; Pinto, N. G. Adsorption of Bovine Serum Albumin and Lysozyme on Siliceous MCM-41. *Microporous Mesoporous Mater.* **2005**, 80 (1–3), 311–320.
- (109) Schmidt-winkel, P.; Lukens, W. W.; Zhao, D.; Yang, P.; Chmelka, B. F.; Stucky, G. D.; Uni, V.; Barbara, S. Mesocellular Siliceous Foams with Uniformly Sized Cells and Windows. *Am.*

Chem. Soc. **1999**, No. 9, 254–255.

- (110) Trewyn, B. G.; Slowing, I. I.; Giri, S.; Chen, H. T.; Lin, V. S. Y. Synthesis and Functionalization of a Mesoporous Silica Nanoparticle Based on the Sol-Gel Process and Applications in Controlled Release. *Acc. Chem. Res.* **2007**, *40*, 846–853.
- (111) Kamarudin, N. H. N.; Jalil, A. A.; Triwahyono, S.; Salleh, N. F. M.; Karim, A. H.; Mukti, R. R.; Hameed, B. H.; Ahmad, A. Role of 3-Aminopropyltriethoxysilane in the Preparation of Mesoporous Silica Nanoparticles for Ibuprofen Delivery: Effect on Physicochemical Properties. *Microporous Mesoporous Mater.* **2013**, *180*, 235–241.
- (112) Han, Y. R.; Park, J. W.; Kim, H.; Ji, H.; Lim, S. H.; Jun, C. H. A One-Step Co-Condensation Method for the Synthesis of Well-Defined Functionalized Mesoporous SBA-15 Using Trimethylsilylanes as Organosilane Sources. *Chem. Commun.* **2015**, *51* (96), 17084–17087.
- (113) Hoang Thi, T. T.; Cao, V. Du; Nguyen, T. N. Q.; Hoang, D. T.; Ngo, V. C.; Nguyen, D. H. Functionalized Mesoporous Silica Nanoparticles and Biomedical Applications. *Mater. Sci. Eng. C* **2019**, *99*, 631–656.
- (114) Yaghi, O. M.; Li, H. Hydrothermal Synthesis of a Metal-Organic Framework Containing Large Rectangular Channels. *Angew. Chem., Int. Ed. Engl* **1995**, *117*, 1400–1402.
- (115) López-Periago, A.; Vallcorba, O.; Frontera, C.; Domingo, C.; Ayllón, J. A. Exploring a Novel Preparation Method of 1D Metal Organic Frameworks Based on Supercritical CO₂. *Dalt. Trans.* **2015**, *44* (16), 7548–7553.
- (116) Wang, C.; Wang, H.; Luo, R.; Liu, C.; Li, J.; Sun, X.; Shen, J.; Han, W.; Wang, L. Metal-Organic Framework One-Dimensional Fibers as Efficient Catalysts for Activating Peroxymonosulfate. *Chem. Eng. J.* **2017**, *330*, 262–271.
- (117) Czaja, A. U.; Trukhan, N.; Müller, U. Industrial Applications of Metal–organic Frameworks. *Chem. Soc. Rev.* **2009**, *38* (5), 1284–1293.
- (118) Batten, S. R.; Champness, N. R.; Chen, X. M.; Garcia-Martinez, J.; Kitagawa, S.; Öhrström,

- L.; O’Keeffe, M.; Suh, M. P.; Reedijk, J. Terminology of Metal-Organic Frameworks and Coordination Polymers (IUPAC Recommendations 2013). *Pure Appl. Chem.* **2013**, *85* (8), 1715–1724.
- (119) Mehta, J.; Bhardwaj, N.; Bhardwaj, S. K.; Kim, K. H.; Deep, A. Recent Advances in Enzyme Immobilization Techniques: Metal-Organic Frameworks as Novel Substrates. *Coord. Chem. Rev.* **2016**, *322*, 30–40.
- (120) Sciortino, L.; Alessi, A.; Messina, F.; Buscarino, G.; Gelardi, F. M. Structure of the FeBTC Metal-Organic Framework: A Model Based on the Local Environment Study. *J. Phys. Chem. C* **2015**, *119* (14), 7826–7830.
- (121) Sanchez-Sanchez, M.; De Asua, I.; Ruano, D.; Diaz, K. Direct Synthesis, Structural Features, and Enhanced Catalytic Activity of the Basolite F300-like Semiamorphous Fe-BTC Framework. *Cryst. Growth Des.* **2015**, *15* (9), 4498–4506.
- (122) Dauenhauer, P. J.; Abdelrahman, O. A. A Universal Descriptor for the Entropy of Adsorbed Molecules in Confined Spaces. *ACS Cent. Sci.* **2018**, *4* (9), 1235–1243.
- (123) Lin, K.; Zhao, Y. P. Entropy and Enthalpy Changes during Adsorption and Displacement of Shale Gas. *Energy* **2021**, 221.
- (124) Al-Ghouti, M. A.; Da’ana, D. A. Guidelines for the Use and Interpretation of Adsorption Isotherm Models: A Review. *Journal of Hazardous Materials*. Elsevier B.V. July 5, 2020.
- (125) Hasan, I.; Bhatia, D.; Walia, S.; Singh, P. Removal of Malachite Green by Polyacrylamide-G-Chitosan γ -Fe₂O₃ Nanocomposite-an Application of Central Composite Design. *Groundw. Sustain. Dev.* **2020**, *11*.
- (126) Azizian, S. Kinetic Models of Sorption: A Theoretical Analysis. *J. Colloid Interface Sci.* **2004**, 47–52.
- (127) Ayawei, N.; Ebelegi, A. N.; Wankasi, D. Modelling and Interpretation of Adsorption Isotherms. *J. Chem.* **2017**, No. 2017.

- (128) Shimizu, S.; Matubayasi, N. Temperature Dependence of Sorption. *Langmuir* **2021**, *37*.
- (129) Shi, Z.; Li, L.; Xiao, Y.; Wang, Y.; Sun, K.; Wang, H.; Liu, L. Synthesis of Mixed-Ligand Cu-MOFs and Their Adsorption of Malachite Green. *RSC Adv.* **2017**, *7* (49), 30904–30910.
- (130) Patiha; Firdaus, M.; Wahyuningsih, S.; Nugrahaningtyas, K. D.; Hidayat, Y. Derivation and Constants Determination of the Freundlich and (Fractal) Langmuir Adsorption Isotherms from Kinetics. *Mater. Sci. Eng.* **2018**, *333*.
- (131) Skopp, J. Derivation of the Freundlich Adsorption Isotherm from Kinetics. *J. Chem. Educ.* **2009**, *86*.
- (132) El Bardiji, N.; Ziat, K.; Naji, A.; Saidi, M. Fractal-Like Kinetics of Adsorption Applied to the Solid/Solution Interface. *ACS Omega* **2020**, *5* (10), 5105–5115.
- (133) Simonin, J.-P. On the Comparison of Pseudo-First Order and Pseudo-Second Order Rate Laws in the Modeling of Adsorption Kinetics. *J. Chem. Eng.* **2016**, *10*.
- (134) Schnell, S.; Mendoza, C. The Condition for Pseudo-First-Order Kinetics in Enzymatic Reactions Is Independent of the Initial Enzyme Concentration. *Biophys. Chem.* **2004**, *107* (2), 165–174.
- (135) Simonin, J. P.; Bouté, J. Intraparticle Diffusion Adsorption Model to Describe Liquid/solid Adsorption Kinetics. *Rev. Mex. Ing. Quim.* **2016**, *15*, 161–173.
- (136) Bețianu, C. S.; Cozma, P.; Roșca, M.; Ungureanu, E. D. C.; Mămăligă, I.; Gavrilescu, M. Sorption of Organic Pollutants onto Soils: Surface Diffusion Mechanism of Congo Red Azo Dye. *Processes* **2020**, *8* (12), 1–19.
- (137) An, B. Cu(II) and As(V) Adsorption Kinetic Characteristic of the Multifunctional Amino Groups in Chitosan. *Processes* **2020**, *8* (9).
- (138) Bizi, M. Sulfamethoxazole Removal from Drinking Water by Activated Carbon: Kinetics and Diffusion Process. *Molecules* **2020**, *25* (20).
- (139) Singh, S. K.; Townsend, T. G.; Mazyck, D.; Boyer, T. H. Equilibrium and Intra-Particle

- Diffusion of Stabilized Landfill Leachate onto Micro- and Meso-Porous Activated Carbon. *Water Res.* **2012**, *46* (2), 491–499.
- (140) Wu, F. C.; Tseng, R. L.; Juang, R. S. Initial Behavior of Intraparticle Diffusion Model Used in the Description of Adsorption Kinetics. *Chem. Eng. J.* **2009**, *153* (1–3), 1–8.
- (141) Torrik, E.; Soleimani, M.; Ravanchi, M. T. Application of Kinetic Models for Heavy Metal Adsorption in the Single and Multicomponent Adsorption System. *Int. J. Environ. Res.* **2019**, *13* (5), 813–828.
- (142) Podder, M. S.; Majumder, C. B. Biosorption of As(III) and As(V) on the Surface of TW/MnFe₂O₄ Composite from Wastewater: Kinetics, Mechanistic and Thermodynamics. *Appl. Water Sci.* **2017**, *7* (6), 2689–2715.
- (143) Finkel, M.; Grathwohl, P.; Cirpka, O. A. A Travel Time-Based Approach to Model Kinetic Sorption in Highly Heterogeneous Porous Media via Reactive Hydrofacies. *Water Resour. Res.* **2016**, *52* (12), 9390–9411.
- (144) Thommes, M.; Kaneko, K.; Neimark, A. V.; Olivier, J. P.; Rodriguez-Reinoso, F.; Rouquerol, J.; Sing, K. S. W. Physisorption of Gases, with Special Reference to the Evaluation of Surface Area and Pore Size Distribution (IUPAC Technical Report). *Pure Appl. Chem.* **2015**, *87* (9–10), 1051–1069.
- (145) Sing, K. S. W.; Everett, D. H.; Haul, R. A. W.; Moscou, L.; Pierotti, R. A.; Rouquerol, J.; Siemieniewska, T. Reporting Physisorption Data for Gas/solid Systems with Special Reference to the Determination of Surface Area and Porosity Reporting Physisorption Data for Gas/solid Systems-with Special Reference to the Determination of Surface Area and Porosity. *Pure Appl. Chem.* **1985**, *57*, 603–619.
- (146) Caruso, F.; Mantellato, S.; Palacios, M.; Flatt, R. J. ICP-OES Method for the Characterization of Cement Pore Solutions and Their Modification by Polycarboxylate-Based Superplasticizers. *Cem. Concr. Res.* **2017**, *91*, 52–60.

- (147) Lee, H. C. Review of Inductively Coupled Plasmas: Nano-Applications and Bistable Hysteresis Physics. *Appl. Phys. Rev.* **2018**, *5* (1).
- (148) Berto, S.; Crea, F.; Daniele, P. G.; De Stefano, C.; Prenesti, E.; Sammartano, S. Potentiometric and Spectrophotometric Characterization of the UO₂₂₊-Citrate Complexes in Aqueous Solution, at Different Concentrations, Ionic Strengths and Supporting Electrolytes. *Radiochim. Acta* **2012**, *100* (1), 13–28.
- (149) Gans, P.; Sabatini, A.; Vacca, A. Investigation of Equilibria in Solution. Determination of Equilibrium Constants with the HYPERQUAD Suite Programs. *Talanta* **1996**, *43*, 1739–1753.
- (150) Kiss, T.; Enyedy, É. A.; Jakusch, T. Development of the Application of Speciation in Chemistry. *Coord. Chem. Rev.* **2017**, *352*, 401–423.
- (151) Yan, J.; Li, K. A Magnetically Recyclable Polyampholyte Hydrogel Adsorbent Functionalized with β -Cyclodextrin and Graphene Oxide for Cationic/anionic Dyes and Heavy Metal Ion Wastewater Remediation. *Sep. Purif. Technol.* **2021**, 277.
- (152) Wang, Z.; Yao, M.; Wang, X.; Li, S.; Liu, Y.; Yang, G. Influence of Reaction Media on Synthesis of Dialdehyde cellulose/GO Composites and Their Adsorption Performances on Heavy Metals. *Carbohydr. Polym.* **2020**, 232.
- (153) Blake, A. J.; Bencini, A.; Caltagirone, C.; Filippo, G. De; Dolci, L. S.; Garau, A.; Isaia, F.; Lippolis, V.; Mariani, P.; Prodi, L.; et al. A New Pyridine-Based 12-Membered Macrocyclic Functionalised with Different Fluorescent Subunits; Coordination Chemistry towards CuII, ZnII, CdII, HgII, and PbII †. *Dalt. Trans.* **2004**, 2771–2779.
- (154) Lvova, L.; Di Natale, C.; Paolesse, R.; Giorgi, L.; Fusi, V.; Garau, A.; Lippolis, V. Photographic Detection of Cadmium(II) and Zinc(II) Ions. *Procedia Eng.* **2016**, *168*, 346–350.
- (155) Aragoni, M. C.; Arca, M.; Bencini, A.; Blake, A. J.; Caltagirone, C.; De Filippo, G.; Devillanova, F. A.; Garau, A.; Gelbrich, T.; Hursthouse, M. B.; et al. Tuning the

Selectivity/specificity of Fluorescent Metal Ion Sensors Based on N2S2 Pyridine-Containing Macrocyclic Ligands by Changing the Fluorogenic Subunit: Spectrofluorimetric and Metal Ion Binding Studies. *Inorg. Chem.* **2007**, *46* (11), 4548–4559.

- (156) Shamsipur, M.; Zahedi, M. M.; De Filippo, G.; Lippolis, V. Development of a Novel Flow Injection Liquid-Liquid Microextraction Method for the on-Line Separation and Preconcentration for Determination of zinc(II) Using 5-(8-Hydroxy-2-Quinolinylmethyl)-2,8-Dithia-5-Aza-2,6-Pyridinophane as a Sensitive and Selective Fluorescent Chemosensor. *Talanta* **2011**, *85* (1), 687–693.

Paper I



Adsorption of Cu^{2+} and Zn^{2+} on SBA-15 mesoporous silica functionalized with triethylenetetramine chelating agent

Joanna Izabela Lachowicz^a, Giulia Rossella Delpiano^a, Davide Zanda^a, Marco Piludu^{b,c}, Enrico Sanjust^{b,c}, Maura Monduzzi^{a,c,d,*}, Andrea Salis^{a,c,d,*}

^a Dipartimento di Scienze Chimiche e Geologiche, Università di Cagliari, Cittadella Universitaria, S.S. 554 bivio Sestu, 09042, Monserrato, Cagliari, Italy

^b Dipartimento di Scienze Biomediche, Università di Cagliari, Cittadella Universitaria, S.S. 554 bivio Sestu, 09042, Monserrato, Cagliari, Italy

^c Consorzio Interuniversitario per lo Sviluppo dei Sistemi a Grande Interfase (CSGI), Unità Operativa Univ. Cagliari, Italy

^d Centro NanoBiotecnologie Sardegna (CNBS), Unità Operativa Univ. Cagliari, Italy

ARTICLE INFO

Keywords:

Functionalized mesoporous silica

Triethylenetetramine

Adsorption kinetics

Adsorption isotherm

Cu^{2+} Zn^{2+}

ABSTRACT

Mesoporous silica particles, based on SBA-15 matrix, were functionalized with triethylenetetramine (TETA), and characterized by transmission electron microscopy (TEM), small angle X-ray scattering (SAXS), and N_2 -adsorption/desorption isotherms (surface area and pore size distribution). The functionalization of SBA-15 with TETA to obtain SBA-TETA was confirmed by Fourier transform infrared spectroscopy (FTIR) and thermogravimetric analysis (TGA). SBA-TETA functional material was used for the adsorption of Cu^{2+} and Zn^{2+} metal ions from aqueous solutions at pH 4 and $T = 298 \text{ K}$. The adsorption kinetics was faster for Zn^{2+} with respect to Cu^{2+} ions, and could be described by the pseudo-second order model indicating the chemisorption of the metal ions as the rate-determining step of the adsorption process. Adsorption isotherms at 298 K were carried out, and the experimental data analyzed with Freundlich, Temkin, and Langmuir models. Among the isotherm models, Langmuir gave the best fitting of the experimental data, allowing to quantify the maximal adsorbable amount of Cu^{2+} (23.9 mg g^{-1}) and Zn^{2+} (13.6 mg g^{-1}) by SBA-TETA. Moreover, the Langmuir constant, K_L , was used to calculate the thermodynamic adsorption constant K^0 and the associated ΔG^0 , namely $-21.7 \text{ kJ mol}^{-1}$ and $-28.4 \text{ kJ mol}^{-1}$ for Cu^{2+} and Zn^{2+} adsorption processes, respectively. These values are better than those reported in similar works, likely due to the superior performance of TETA chelating agent respect to conventional alkyl-amino ligands once grafted on SBA-15 surface.

1. Introduction

Nowadays, environmental pollution has become a very important issue. Among different pollutants, heavy metals represent a highly toxic category [1–3]. They enter in biological organisms through the food chain and can thus be assumed also by humans [3]. The accumulation of heavy metals in the body can lead to various diseases, such as hormonal or nervous system disorders, as well as various types of inflammations and tumors [3]. Mine waters are acidic aqueous solutions mainly containing relatively high concentrations of metals (e.g. Fe^{3+} , Al^{3+} , Cu^{2+} , Zn^{2+} , etc.) [4]. They can pollute nearby surface and ground waters causing a pH decrease as well as the accumulation of heavy metals. All around the world there are many abandoned mines as, for example, in Australia where more than 50,000 inactive mines have been counted [5]. Abandoned mines constitute a long-term source

of pollution for natural waters with high potential negative impact on aquatic organisms, plants, and humans. The established treatments for mine waters are based on the use of limestone or other basic reagents which neutralize the solution and precipitate metal ions in the form of hydroxides [6,7]. This method is limited by the high associated costs, such as reagent consumption, and further treatment of the obtained solid phase [4,5]. On the other hand, due to the increasing demand of specific metals (i.e. Cu^{2+} , Zn^{2+}) in various technological fields, it might be economically interesting to carry out their selective recovery from mine waters [8]. Adsorption is an economic and effective method which may be used for both heavy metals removal from wastewaters and their recovery for technological reuse [4,9]. Several pollutant adsorbents have been described in the literature [10–13]. Each of them has both advantages and disadvantages. For example, biosorbents coming from vegetable waste are cheap but with low performance

* Corresponding author at: Dipartimento di Scienze Chimiche e Geologiche, Università di Cagliari, Cittadella Universitaria, S.S. 554 bivio Sestu, 09042, Monserrato, Cagliari, Italy.

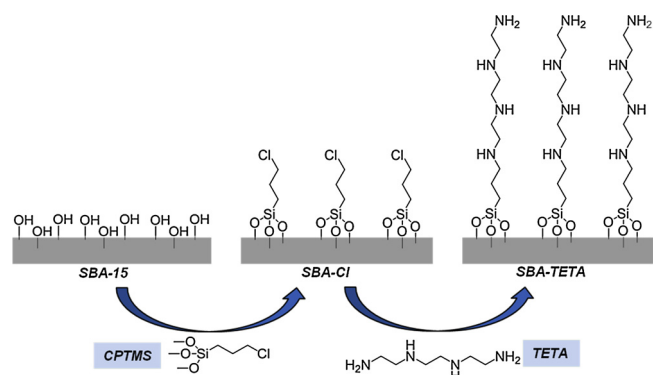
E-mail address: asalis@unica.it (A. Salis).

<https://doi.org/10.1016/j.jece.2019.103205>

Received 4 April 2019; Received in revised form 7 June 2019; Accepted 7 June 2019

Available online 10 June 2019

2213-3437/ © 2019 Elsevier Ltd. All rights reserved.



Scheme 1. Functionalization of SBA-15 with CPTMS and TETA to obtain SBA-Cl and SBA-TETA respectively.

associated to their low surface area [10]. On the contrary, more efficient adsorbents, such as graphene oxide and activated carbon, are either expensive or offer a limited possibility of surface functionalization needed to customize pollutant adsorption [11,14]. Among a variety of adsorbents, ordered mesoporous silicas (i.e. SBA-15, MCM-41, etc.) are very interesting and versatile materials because of their high surface area, uniform pore size distribution, and easy surface functionalization. All these features, together with a low production cost, constitute primary advantages of ordered mesoporous silica respect to other materials with high pollutants adsorption capacities [14]. Beside adsorption [15–21], the applications of mesoporous silica span from catalysis [22–24], biocatalysis [25–28], sensing [29–32], and nanomedicine [33–38]. Surface functionalization with suitable molecules carrying binding groups provide a usual strategy to make mesoporous silica effective adsorbents for specific chemical species. Triethylenetetramine (TETA, Scheme 1) molecule is characterized by four chelating amino (two primary and two secondary) groups which can occur in differently protonated forms as a function of pH [39]. When dissolved in aqueous solutions TETA is able to form stable complexes with Cu^{2+} and Zn^{2+} ions [40]. Taking advantage of its chelating power, TETA has been heterogenized for different applications, such as the realization of hybrid membranes for nanofiltration [41], or Cu^{2+} ion selective membranes through an ion-imprinting method [42]. Moreover, TETA was also used to functionalize the biomass from *Funalia trogii* to obtain a bioadsorbent for Congo red dye [43], KIT-6 mesoporous silica for CO_2 capture [44], and silica-coated iron oxide-based magnetic particles for the adsorption of Pb^{2+} and Cu^{2+} from water [45].

Copper and zinc are two metals which play an essential role in biological systems as they are among the main metal cofactors in many enzymes and proteins. The lack of these two metals can lead to serious dysfunctions [3], but their excess can be harmful as well [46]. Nowadays the main causes of copper and zinc pollution are represented by industrial wastewaters from the metallurgical industry, and by effluents of mining extractions [4,5].

In this work an adsorbent, based on ordered mesoporous silica (SBA-15) functionalized with TETA, was prepared for the adsorption of Cu^{2+} and Zn^{2+} metal ions from aqueous solutions. The functionalized silica material (named SBA-TETA) was carefully characterized through different techniques (TEM, SAXS, FTIR, N_2 -adsorption isotherms, TGA, and elemental analysis). The adsorption kinetics and isotherms of copper and zinc on SBA-TETA were determined at fixed values of pH (= 4) and temperature (298 K) by means of ICP-OES spectroscopy. This study allowed to quantify the adsorption capacity of SBA-TETA material with respect to Cu^{2+} and Zn^{2+} ions, and the thermodynamic constant along with the Gibbs free energy of the adsorption process, as well as the adsorption kinetic mechanism. The obtained kinetic and thermodynamic parameters are of extreme importance for the possible application of SBA-TETA as an adsorbent for Cu^{2+} and Zn^{2+} for both environmental and technological purposes.

2. Materials and methods

2.1. Chemicals

Pluronic copolymer P123 (EO20PO70EO20) tetraethylorthosilicate, TEOS ($\geq 99\%$); (3-chloropropyl)trimethoxysilane, CPTMS ($\geq 97\%$); triethylenetetramine, TETA ($\geq 97\%$); copper chloride dihydrate, $\text{CuCl}_2 \cdot 2 \text{H}_2\text{O}$ ($\geq 99,0\%$), anhydrous toluene ($\geq 99,7\%$), dimethylformamide (DMF, $\geq 99,9\%$), acetone ($\geq 99\%$) HCl (37%), NaCl, NaOH pellets were purchased from Sigma Aldrich (Milano, Italy). Copper stock solutions (1000 ± 2 ppm in HNO_3 2% m/m) and (1007 ppm in HNO_3 1% m/m) were purchased from Fluka Analytical and Aldrich Chemical Company, respectively. Zinc stock solution (10000 ppm in HNO_3 5% m/m) was from Ricca Chemical Company. Zinc chloride salt, ZnCl_2 (97%) was purchased from Carlo Erba. Diethyl ether (99.8%), and ethanol (99.8%) were purchased from Honeywell.

2.2. Synthesis of SBA-TETA

SBA-15 mesoporous silica was synthesized according to Zhao et al. [47]. The functionalization with (3-chloropropyl)trimethoxysilane (CPTMS) was carried out by dispersing 1 g of obtained SBA-15 in 25 mL of anhydrous toluene, adding 700 μL of CPTMS [48] and keeping the mixture under stirring at 110°C overnight. The resulting SBA-Cl (Scheme 1) was collected by filtration, washed with diethyl ether and water and dried under vacuum. A mass of 0.5 g of SBA-Cl was dispersed in 14 mL of anhydrous toluene, then the solution containing 0.56 g of TETA dissolved in 1 mL of DMF was added. The resulting suspension was kept under stirring at 110°C for 24 h. SBA-TETA (Scheme 1) was recovered by filtration, washed with diethyl ether and dried under vacuum overnight [48].

2.3. Physico-chemical characterizations

Transmission Electron Spectroscopy (TEM) analysis of SBA-15 was performed with a Jeol JEM 1400 Plus, operating at 120 kV. The hexagonal structure was also determined by small-angle X-rays scattering (SAXS) analysis. Patterns were recorded with a S3-MICRO SWAX camera system (Hecus X-ray System, Graz, Austria). $\text{CuK}\alpha$ radiation of wavelength 1.542 \AA was provided by a Genix X-ray generator, operating at 30 kV and 0.4 mA. N_2 adsorption/desorption isotherms at 77 K were carried out on a ASAP 2020 instrument to obtain the textural parameters of the materials such as the surface area (Brunauer-Emmett-Teller, B.E.T.) [49], pore size distribution (Barrett-Joyner-Halenda, B.J.H.) [50]. Before analysis SBA-15 sample was heated at 110°C at a rate of $1^\circ\text{C}/\text{min}$ under vacuum for 12 h, whereas functionalized samples were heated at 80°C and outgassed under the same conditions. FTIR analyses, to verify the occurrence of chloro-propyl group and TETA ligand on functionalized SBA-15, were carried out through a Bruker Tensor 27 spectrophotometer equipped with a diamond-ATR accessory and a DTGS detector. A number of 128 scans with a resolution of 2 cm^{-1} were averaged in the spectral range $4000 \text{ cm}^{-1} - 400 \text{ cm}^{-1}$. To quantify the functionalization percentage elemental analysis (Perkin Elmer Series II 2400) were achieved. Thermal analysis data were collected with a STA6000 - Perkin Elmer in the $25-850^\circ\text{C}$ range, under oxygen flow (heating rate = $10^\circ\text{C}/\text{min}$; flow rate = 40 mL min^{-1}).

2.4. Determination of Cu^{2+} and Zn^{2+} concentrations through ICP-OES measurements

The copper and zinc concentrations in aqueous solutions were analyzed by inductively coupled plasma optical emission spectrometry (ICP-OES). The operational parameters were: RF Power: 1.2 kW. Plasma gas: 12 L min^{-1} , Aux gas: 1.0 L min^{-1} , Nebulizer flow 0.7 L min^{-1} . Emission lines (nm): Cu (327.395, 324.754 and 213.598) and Zn

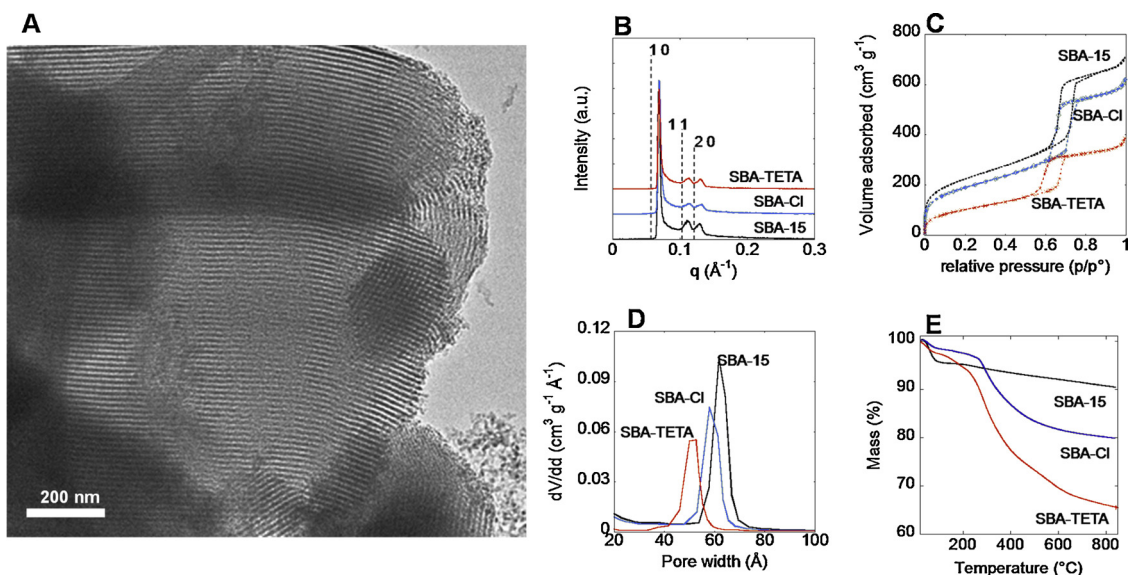


Fig. 1. Characterization of mesoporous silica samples. A) TEM images of the SBA-15 sample. Bar = 200 nm. B) SAXS patterns of SBA-15, SBA-Cl, and SBA-TETA samples. C) N_2 -adsorption/desorption isotherms. D) Pore size distribution calculated (BJH method) from the desorption branch. E) Thermogravimetric analysis (TGA).

(213.857, 202.548 and 206.200). No spectral interference was observed. The standard solutions ranging from 0.5 to 50 mg/L in 1% nitric acid were prepared by the analytical dilution of standard zinc and copper solutions.

2.5. Metal ions adsorption studies

The metal ion (Cu^{2+} or Zn^{2+}) adsorption kinetics on SBA-TETA and SBA-15 were carried out by suspending 3 mg of mesoporous adsorbent in 2 mL of 10 mg L^{-1} metal solution for time intervals ranging from 10 min to 24 h at pH 4. All samples were kept under rotation (22 rpm) at 298 K. The process was then stopped, and the solution was filtered through $\varnothing 0.2\ \mu\text{m}$ syringe cellulose filter (Minisart Syringe Filter). For the isotherm studies, mesoporous materials were treated with metal ion solutions of variable concentration, ranging from 5 to 400 mg L^{-1} ; the reactions were stopped after 24 h. The residual copper and zinc concentrations in the water solution after adsorption on SBA-TETA were quantified by ICP-OES. Each experiment was carried out at least in triplicate.

2.5.1. Adsorption kinetic models

The adsorption kinetics was quantified by measuring the decrease of metal ion (either copper or zinc) concentration in the adsorbing solution, at given times (q_t) through the following equation [13,38]:

$$q_t = \frac{(C_i - C_t) \cdot V}{m} \quad (1)$$

where C_i and C_t are the metal ion concentrations expressed as mg L^{-1} at time = 0 and time = t, respectively; V is the volume of the solution (mL) and m is the mass of the adsorbent (g).

Different kinetic models were used to analyze the experimental data. According with the pseudo-first order model [51]:

$$\ln(q_e - q_t) = \ln q_e - k't \quad (2)$$

q_e is the amount of ion adsorbed at equilibrium, that is the equilibrium loading (mg g^{-1}); k' is the pseudo-first order constant (min^{-1}).

Alternatively, kinetic data were analyzed by means of the pseudo-second order model [51]:

$$\frac{t}{q_t} = \frac{1}{k'' \cdot q_e^2} + \frac{t}{q_e} \quad (3)$$

where k'' is the pseudo-second order constant ($\text{g mg}^{-1} \text{min}^{-1}$).

Finally, the intraparticle diffusion model [51]:

$$q_t = k_i t^{1/2} + x_i \quad (4)$$

where k_i is the intraparticle diffusion constant ($\text{mg g}^{-1} \text{min}^{-1/2}$), was used.

2.5.2. Adsorption isotherms

The adsorption isotherms were determined by plotting the adsorbed amount of Cu^{2+} and Zn^{2+} (mg g^{-1}) versus the equilibrium concentration of Cu^{2+} and Zn^{2+} (mg L^{-1}) in the adsorbing solution. The experimental data were fitted through three different isotherm models' - namely Freundlich, Langmuir, and Temkin [52].

The linearized Freundlich adsorption isotherm equation is:

$$\ln q_e = \ln K_F + \frac{1}{n} \ln C_e \quad (5)$$

where $1/n$ (dimensionless) and K_F (L mg^{-1}) are the heterogeneity factor and the support capacity, respectively. These parameters are characteristic of each adsorbate-adsorbent pair and are also called Freundlich constants [52]. Freundlich model deals with heterogeneous adsorbents surfaces on which the adsorbate molecules form a multilayer.

Langmuir isotherm considers homogeneous adsorbents with equivalent and localized adsorption sites that allow the formation only of a monolayer of adsorbate. The linearized Langmuir equation is:

$$\frac{C_e}{q_e} = \frac{1}{K_L \cdot q_M} + \frac{1}{q_M} \cdot C_e \quad (6)$$

where K_L is the Langmuir constant (L mg^{-1}) and q_M (mg g^{-1}) is the maximum monolayer coverage capacity.

Finally, Temkin isotherm [52] was used. This model considers the adsorbate-adsorbent interactions. The adsorption enthalpy of the adsorbed molecules/ions in the layer decreases linearly with coverage due to adsorbate-adsorbent interactions. The linearized Temkin equation is

$$q_e = \frac{RT}{b_T} \ln A_T + \frac{RT}{b_T} \ln C_e \quad (7)$$

where b_T is the Temkin constant and A_T (L mg^{-1}) is the Temkin equilibrium binding constant.

Table 1
Characterization of original and functionalized SBA-15 samples.

Sample	^a S_{BET} (m ² g ⁻¹)	^b V_p (cm ³ g ⁻¹)	^c d_p (Å)	^d a (Å)	^e mass loss (%)	^f mass loss (%)	^g L(mg g ⁻¹)
SBA-15	813	1.01	61.4	108 ± 4	4.5	5.0	–
SBA-Cl	667	0.94	57.8	110 ± 5	2.8	18.5	135
SBA-TETA	373	0.60	51.4	107 ± 3	2.9	31.9	134

^a Surface area calculated by the BET method.

^b Pore volume from the desorption branch calculated at $p/p^0 = 0.99$ by BJH method.

^c Pore diameter calculated by applying the BJH method to the isotherm desorption branch.

^d Lattice parameter obtained by SAXS $a = d \cdot 2/(3)^{0.5} \cdot (h^2 + k^2 + hk)^{0.5}$.

^e Mass loss at $T < 200$ °C.

^f Mass loss at $T > 200$ °C.

^g Amount of functional group grafted to SBA-15 surface calculated from TGA data.

3. Results and discussion

3.1. Physico-chemical characterizations

The TEM image in Fig. 1A shows the porous structure of SBA-15 constituted by parallel channels. The structural characteristics of the synthesized materials were determined by small angle X-ray scattering (SAXS) as shown in Fig. 1B. The SAXS pattern of SBA-15, reporting the scattering intensity (arbitrary units) as a function of the scattering vector q (Å⁻¹), has the typical SAXS pattern of hexagonal phases. Indeed, the pattern displays an intense peak relative to the reflections of the planes 10, and two less intense peaks due to 11 and 20 planes. The structural order is retained after the functionalization, showing a value of the lattice parameter a , around 107–110 Å (Table 1). The textural characterization of mesoporous silica samples was carried out through N₂ adsorption/desorption isotherms at 77 K, as shown in Fig. 1C. All samples show a hysteresis cycle due to capillary condensation typical of mesoporous materials. The isotherms of SBA-Cl and SBA-TETA samples occur at lower volumes (lower amount of adsorbed N₂) than SBA-15. This behavior is clearly due to the decrease of the surface area and of the porous volume of the material because of post-synthesis functionalization (Fig. 1C, and Table 1). For the same reason, a decrease in the mean pore diameter, that is of the maximum of the pore size distribution (Fig. 1D and Table 1), is also observed. The specific surface area (S_{BET}), pore volume (V_p) and the mean pore diameter (d_p) values agree with the other parameters trend. Fig. 1E shows the thermogravimetric analysis (TGA) of SBA-15, SBA-Cl and SBA-TETA samples. The mass loss (%) values ($T > 200$ °C), (see Table 1), confirm the successful functionalization of SBA-15 with CPTMS and then with TETA ligand. In particular, TGA allowed to estimate the amount of TETA ligand grafted on SBA-15 which was 134 mg g⁻¹ (Table 1). This value is comparable with 128 mg g⁻¹ obtained by elemental analysis (Table S2, Supplementary material file).

Fourier transform infrared spectroscopy (FTIR) was used to verify the successful functionalization of SBA-15 with CPTMS and TETA ligand (Fig. 2). SBA-15 spectrum presents an intense band at 1070 cm⁻¹ due to the stretching of the -Si-O-Si- bonds, and a less intense band at 960 cm⁻¹ assigned to Si-OH stretching. The intensity decrease of the 960 cm⁻¹ band in the spectrum of SBA-Cl sample indicates the reaction of the silanol groups with CPTMS for the introduction of the chloropropyl groups on SBA-15 surface. In the spectrum of the SBA-Cl, a weak band at 690 cm⁻¹ is likely due to the stretching of aliphatic C-Cl bonds [18]. SBA-TETA spectrum shows a medium intensity band at 1650 cm⁻¹ [42], similar to those at 1660 cm⁻¹ and 1630 cm⁻¹, due to -NH₂ bending, found in the FTIR spectrum of free TETA (Fig. 2A) [45]. The bands in Fig. 2A at 3320 cm⁻¹ and 3250 cm⁻¹, characteristic of -NH₂ stretching, are not observed in the SBA-TETA sample. Conversely, SBA-TETA spectrum shows some weak bands around the 2990 cm⁻¹, 2930 cm⁻¹, and 1430 cm⁻¹ due to the stretching and bending of the C-H bonds of the aliphatic chains, respectively, like those at 2930 cm⁻¹, 2830 cm⁻¹, 1470 cm⁻¹ and 1380 cm⁻¹, observed in the

spectrum of free TETA. These spectral results confirm the successful functionalization of SBA-15 to obtain both SBA-Cl and SBA-TETA materials.

3.2. Adsorption kinetics of Cu²⁺ and Zn²⁺ on SBA-TETA

The adsorption kinetics of copper and zinc on SBA-TETA from an aqueous solution was then studied. The adsorption pH = 4 was chosen after the analysis of speciation diagrams of copper and zinc hydrolysis (Fig. S1, Supplementary material file). At this pH there is no precipitation of copper and zinc hydroxides. Fig. 3A shows the adsorption kinetics, that is, the adsorbed amount of copper and zinc ions, q_t (mg g⁻¹), as a function of the contact time, t (min). As the contact time increases, q_t increases until a constant value - corresponding to the adsorption equilibrium - is reached. Fig. 3A also shows that adsorption on SBA-TETA is faster for Zn²⁺ than for Cu²⁺ ions. Indeed, the former reaches the equilibrium in about 180 min, whereas 480 min are needed for the latter. Fig. S2 (Supplementary material file) shows the very low adsorption amount of Cu²⁺ on SBA-15. This confirms the importance of SBA-15 surface functionalization to obtain an effective adsorbent.

The experimental data were analyzed according to different kinetic models, namely, the pseudo-first order, the pseudo-second order and the intraparticle diffusion models [53,54]. The linearized plots for the various kinetic models are shown in Fig. 3B–D, whereas the different kinetic parameters (i.e. kinetic constants, adsorbed amount at the equilibrium, etc.) obtained by the application of the different models, are listed in Table 2.

Among the different models, the pseudo-first order gives the worst fitting as demonstrated by the low correlation coefficient values (Table 2) obtained for both Cu²⁺ and Zn²⁺ ions adsorption. The pseudo-second order model, instead, show a very good fit with the experimental kinetic data for both ions. Remarkably, the adsorbed amount at the equilibrium, the q_e values, obtained through the pseudo-second order fitting, are very similar to those obtained in Fig. 2A at equilibrium. The kinetic constants confirm that adsorption on SBA-TETA surface is faster for Zn²⁺ ($k'' = 1.20 \times 10^{-2}$ g mg⁻¹ min⁻¹) with respect to Cu²⁺ ($k'' = 8.31 \times 10^{-3}$ g mg⁻¹ min⁻¹) ions. According to the pseudo-second order model, the rate-limiting step is the chemisorption which involves the formation of a coordination bonds as it would occur in our case between SBA-TETA and Cu²⁺ or Zn²⁺ [10]. The intraparticle diffusion model was also used to fit our kinetic results. Fig. 3D shows the variation of q_t versus $t^{0.5}$, shows three straight lines with different slopes, representing the different kinetic constants of the different steps involved in the adsorption process of both Cu²⁺ and Zn²⁺ ions. The first constant, k_{i1} , can be associated to the diffusion of the metal ions from the bulk to the external adsorbent's surface. This rate constant has the highest value indicating that the process is fast (external diffusion step). The second constant, k_{i2} , is lower than the former, and indicates a slower process, usually associated to the diffusion within silica mesopores (internal diffusion step). According with Da'na et al. the third constant, k_{i3} , has no kinetic meaning since, at

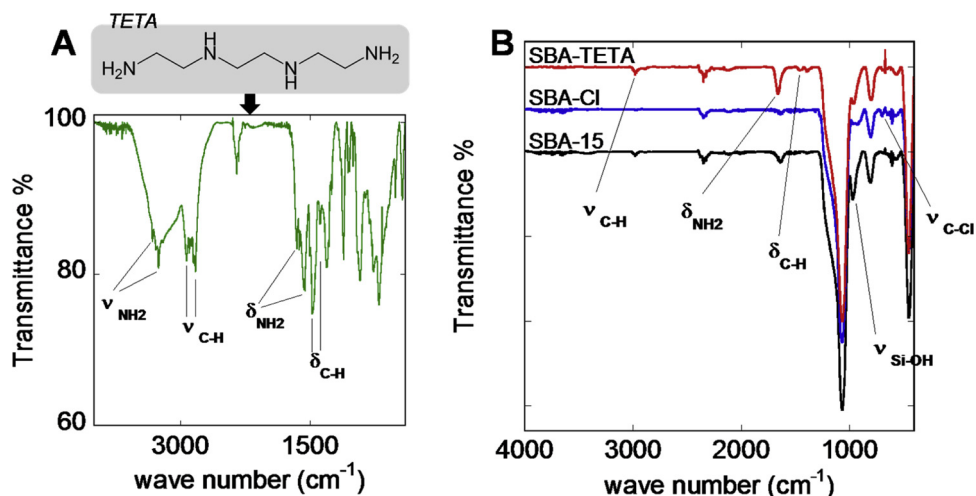


Fig. 2. FTIR spectra of A) free TETA, B) mesoporous silica synthesized samples SBA-15, SBA-Cl, and SBA-TETA.

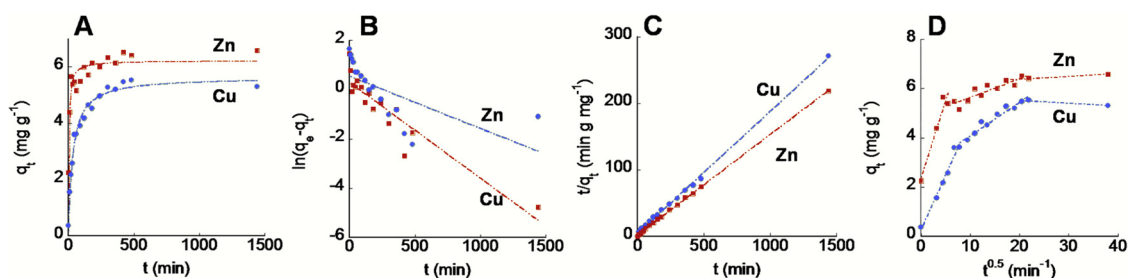


Fig. 3. Adsorption kinetics of Cu²⁺ and Zn²⁺ on SBA-TETA. A) Adsorbed amount q_t versus time. B) Pseudo-first order model; C) Pseudo-second order model; D) Intraparticle diffusion model. Initial metal ion concentration = 10 ppm; pH = 4; stirring speed = 22 rpm; T = 298 K.

Table 2
Comparison among kinetic models for copper and zinc adsorption on SBA-TETA.

	$q_{e \text{ exp}} \text{ (mg g}^{-1}\text{)}$	Pseudo-first order			Pseudo-second order			Intraparticle Diffusion		
		$k' \text{ (min}^{-1}\text{)}$	$q_{e \text{ cal}} \text{ (mg g}^{-1}\text{)}$	R	$k'' \text{ (g mg}^{-1} \text{ min}^{-1}\text{)}$	$q_{e \text{ cal}} \text{ (mg g}^{-1}\text{)}$	R	$k_i \text{ (g mg}^{-1} \text{ min}^{-0.5}\text{)}$	$x_i \text{ (mg g}^{-1}\text{)}$	R
Cu ²⁺	5.64	2.12×10^{-3}	1.75	0.645	8.31×10^{-3}	5.44	0.999	0.446; 0.136; -0.012	0.268; 2.722; 5.745	0.988; 0.975; 0.948
Zn ²⁺	6.22	3.89×10^{-3}	1.36	0.927	1.20×10^{-2}	6.61	0.999	0.631; 0.076; 0.012	2.354; 4.878; 6.148	0.970; 0.910; 0.993

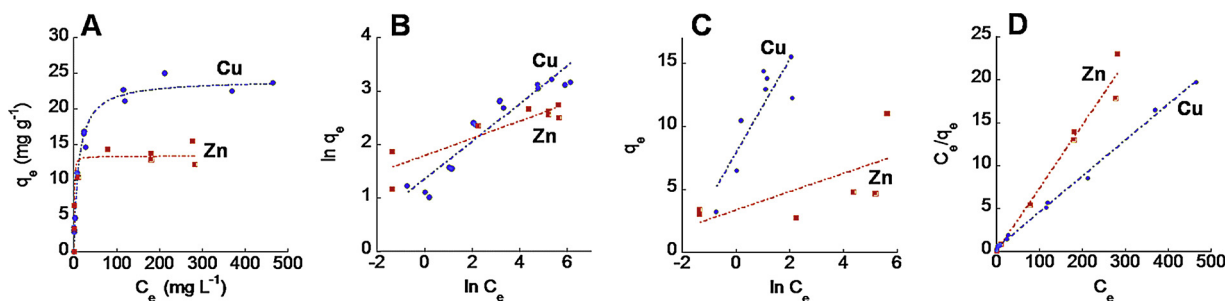
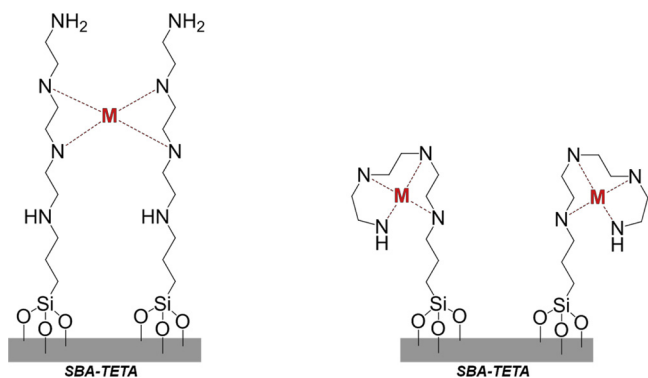


Fig. 4. Comparison between copper and zinc adsorption isotherms on SBA-TETA. A) q_e as a function of the equilibrium concentration C_e . Adsorption data were fitted using linearized isotherms B) Freundlich; C) Temkin; and D) Langmuir. Adsorption experiments were carried out for 24 h at pH = 4 and T = 298 K.

Table 3
Comparison among different adsorption isotherm models.

Ion	Freundlich			Temkin			Langmuir				
	$K_F \text{ (L mg}^{-1}\text{)}$	$1/n$	R	b_T	$A_T \text{ (L mg}^{-1}\text{)}$	R	$K_L \text{ (L mg}^{-1}\text{)}$	$q_M \text{ (mg g}^{-1}\text{)}$	R	K_e°	$\Delta G^\circ \text{ (kJ mol}^{-1}\text{)}$
Cu ²⁺	3.88	0.35	0.943	6.67×10^2	8.37	0.864	0.10	23.9	0.999	6.42×10^3	-21.7
Zn ²⁺	6.02	0.16	0.905	3.41×10^3	102	0.646	1.44	13.6	0.989	9.40×10^4	-28.4



Scheme 2. Possible mechanism of metal ion (M) coordination by TETA donor atoms on SBA-TETA. The metal ion (Cu^{2+} , Zn^{2+}) could be coordinated by the nitrogen atoms of either two adjacent TETA chains or by those of the same chain.

those $t^{0.5}$ values, the almost horizontal line corresponds to the equilibrium adsorption capacity, indicating the saturation of SBA-TETA material [51]. Hence, we can conclude that the pseudo-second order model gives the best description of our kinetic data, and the chemisorption is the limiting step of the whole adsorption process.

3.3. Adsorption isotherm of Cu^{2+} and Zn^{2+} on SBA-TETA

The determination of adsorption isotherms is extremely important since they provide the evaluation of the performance of an adsorbent material toward the removal of specific undesired pollutants. The adsorption isotherms of Cu^{2+} and Zn^{2+} ions on SBA-TETA, obtained at pH 4 and 298 K, are shown in Fig. 4A. SBA-TETA adsorbs copper at a higher extent than zinc. Indeed, the maximal adsorbed amounts, corresponding to the plateaus in Fig. 4A, are 23.9 mg g^{-1} and 13.6 mg g^{-1} for copper and zinc, respectively. Although zinc adsorption is characterized by a higher kinetic constant than copper (Fig. 3), a higher amount of the latter is adsorbed. This finding agrees with previous studies in aqueous solution where free TETA showed a preferential binding capacity toward copper with respect to zinc ions [40].

Experimental data in Fig. 4A were then analyzed with Freundlich (Fig. 4B), Temkin (Fig. 4C) and Langmuir (Fig. 4D) isotherm models [55]. As shown by the plots in Fig. 4B–D, the Langmuir model fits the experimental data better than Freundlich and Temkin models as demonstrated by a higher correlation coefficient, R , listed in Table 3. Langmuir model considers the formation of a monolayer of adsorbate, whereas Freundlich's model implies adsorbate multilayers [38]. In our system adsorption would occur as a result of the formation of coordination bonds between nitrogen atoms of TETA and Cu^{2+} or Zn^{2+} ions (Scheme 2). Once all the binding sites on SBA-TETA surface are saturated, as generally observed in the case of site-specific chemical adsorption, other significant interactions responsible of a multilayer adsorption are not expected.

Since Langmuir model gave the best fitting of the experimental data, the Langmuir constant, K_L , (Table 3) was used to calculate the thermodynamic equilibrium constant K_e° by means of the equation [12,56]:

$$K_e^\circ = \frac{K_L \cdot 1000 \cdot M_{\text{ADSORBATE}} \cdot [\text{Adsorbate}]^\circ}{\gamma} \quad (13)$$

Where, $M_{\text{ADSORBATE}}$ is the atomic mass of the adsorbate (g mol^{-1}), $[\text{Adsorbate}]^\circ$ is the standard concentration of the adsorbate (1 mol L^{-1}) and γ is the activity coefficient (dimensionless). We assume that our system is diluted enough to consider $\gamma = 1$. The K_e° values obtained, were used to calculate the Gibbs energy (ΔG) of the adsorption process according to the relation:

$$\Delta G^\circ = -RT \ln K_e^\circ \quad (14)$$

where R is the universal gas constant ($8.314 \text{ J K}^{-1} \text{ mol}^{-1}$) and T is the absolute temperature (298 K). As shown in Table 3, ΔG° value turned out to be $-21.7 \text{ kJ mol}^{-1}$ for the adsorption of Cu^{2+} and $-28.4 \text{ kJ mol}^{-1}$ for the adsorption of Zn^{2+} . The adsorption processes are clearly spontaneous, in agreement with what we have experimentally observed.

A recent review, devoted to the use of functionalized mesoporous silica for heavy metal adsorption, report a comparison among different adsorbent materials toward copper adsorption [19]. Although that work reports the values of Freundlich's (K_F) and Langmuir's constant (K_L), it is difficult to compare those data with what obtained in this work, because for most of the listed values there is no indication of the temperature and pH at which the experiments were carried out. Da'na and Sayari studied the adsorption of copper on amino functionalized SBA-15 at three different temperatures (293 K, 303 K and 313 K) [57]. By means of the van't Hoff equation they found that the values of ΔG° were $-0.51 \text{ kJ mol}^{-1}$, $-4.38 \text{ kJ mol}^{-1}$, and $-7.06 \text{ kJ mol}^{-1}$ at 293 K, 303 K and 313 K, respectively. Those values are lower than that obtained for copper in this work at 298 K ($-21.7 \text{ kJ mol}^{-1}$). A possible reason for such differences can be due to the fact that TETA ligand is much more efficient toward copper coordination compared to R-NH₂ group. The more negative ΔG° value obtained for Cu^{2+} adsorption in our experiments can be the result of the chelating action of the TETA ligand grafted on SBA-15 surface. This confirms the potentiality of the SBA-TETA adsorbent synthesized in this work.

4. Conclusions

The present work was aimed to obtain a new adsorbent based on functionalized ordered mesoporous silica (SBA-15), for the removal of Cu^{2+} and Zn^{2+} ions from aqueous solutions. By means of two successive grafting steps, the surface of SBA-15 was functionalized first with a chloropropyl group and, subsequently, with triethylenetetramine (TETA) chelating agent to obtain SBA-TETA. The TEM and SAXS structural analyses of SBA-15 confirmed the typical hexagonal arrangement of pores while, from N₂ physical adsorption/desorption isotherms, both the surface area and pore size distribution of SBA-15 and of the functionalized materials, SBA-Cl and SBA-TETA, were obtained. FTIR spectroscopy demonstrated the functionalization of the materials. The functionalization was also confirmed by TGA, which also allowed to quantify the loading of TETA ligand on SBA-15. Adsorption kinetics was faster for Zn^{2+} than for Cu^{2+} ions since the equilibrium was reached after 3 h and 8 h, respectively. Both metal ions are adsorbed following pseudo-second order kinetics. The adsorption isotherms have shown that, although the material adsorbs zinc faster than copper, once the equilibrium is reached, almost a double maximal amount of copper (23.94 mg g^{-1}) with respect to zinc (13.63 mg g^{-1}) is adsorbed at pH 4. These results agree with what reported in the literature about the general greater affinity of TETA ligand toward Cu^{2+} with respect to Zn^{2+} ions. The overall results obtained here are promising for the potential use of this new type of nanostructured functional material for the adsorption/recovery of Cu^{2+} and Zn^{2+} ions from aqueous solutions.

Acknowledgments

Financial supports from, FIR 2018, RAS and Fondazione di Sardegna (CUP F72F16003070002, 2017) and MIUR (FFABR 2017) are gratefully acknowledged. GRD thanks MIUR (PON RI 2014-2020, Azione 1.1 "Dottorati Innovativi con Caratterizzazione industriale"-DOT1304455-1) for financing her PhD scholarship. We acknowledge CeSAR (Centro Servizi d'Ateneo per la Ricerca) of the University of Cagliari, Italy for access to Jeol JEM 1400 Plus Transmission Electron Microscopy facility.

Appendix A. Supplementary data

Supplementary material related to this article can be found, in the online version, at doi:<https://doi.org/10.1016/j.jece.2019.103205>.

References

- [1] S. Bolisetty, M. Peydayesh, R. Mezzenga, Sustainable technologies for water purification from heavy metals: review and analysis, *Chem. Soc. Rev.* 48 (2019) 463–487, <https://doi.org/10.1039/C8CS00493E>.
- [2] C.F. Carolin, P.S. Kumar, A. Saravanan, G.J. Joshiba, M. Naushad, Efficient techniques for the removal of toxic heavy metals from aquatic environment: a review, *J. Environ. Chem. Eng.* 5 (2017) 2782–2799, <https://doi.org/10.1016/j.jece.2017.05.029>.
- [3] F. Fu, Q. Wang, Removal of heavy metal ions from wastewaters: a review, *J. Environ. Manage.* 92 (2011) 407–418, <https://doi.org/10.1016/J.JENVMAN.2010.11.011>.
- [4] J. López, M. Reig, O. Gibert, J.L. Cortina, Recovery of sulphuric acid and added value metals (Zn, Cu and rare earths) from acidic mine waters using nanofiltration membranes, *Sep. Purif. Technol.* 212 (2019) 180–190, <https://doi.org/10.1016/j.seppur.2018.11.022>.
- [5] M.A. Hasan Johir, S. Vigneswaran, G. Naidu, S. Ryu, Y. Choi, S. Jeong, Acid mine drainage treatment by integrated submerged membrane distillation–sorption system, *Chemosphere* 218 (2018) 955–965, <https://doi.org/10.1016/j.chemosphere.2018.11.153>.
- [6] J. Skouens, C.E. Zipper, A. Rose, P.F. Ziemkiewicz, R. Nairn, L.M. McDonald, R.L. Kleinmann, Review of passive systems for acid mine drainage treatment, *Mine Water Environ.* 36 (2017) 133–153, <https://doi.org/10.1007/s10230-016-0417-1>.
- [7] G. Kaur, S.J. Couperthwaite, B.W. Hatton-Jones, G.J. Millar, Alternative neutralisation materials for acid mine drainage treatment, *J. Water Process Eng.* 22 (2018) 46–58, <https://doi.org/10.1016/j.jwpe.2018.01.004>.
- [8] R.A. Crane, D.J. Sapsford, Towards “Precision Mining” of wastewater: selective recovery of Cu from acid mine drainage onto diatomite supported nanoscale zero-valent iron particles, *Chemosphere*. 202 (2018) 339–348, <https://doi.org/10.1016/J.CHEMOSPHERE.2018.03.042>.
- [9] R. Hossain, R.K. Nekouei, I. Mansuri, V. Sahajwalla, Sustainable recovery of Cu and Sn from problematic global waste: exploring value from waste printed circuit boards, *ACS sustain. Chem. Eng.* 7 (2019) 1006–1017, <https://doi.org/10.1021/acssuschemeng.8b04657>.
- [10] L. Negriľă Nemeş, L. Bulgariu, Optimization of process parameters for heavy metals biosorption onto mustard waste biomass, *Open Chem.* 14 (2016) 175–187, <https://doi.org/10.1515/chem-2016-0019>.
- [11] C.J. Madarang, H.Y. Kim, G. Gao, N. Wang, J. Zhu, H. Feng, M. Gorrng, M.L. Kasner, S. Hou, Adsorption behavior of EDTA-Graphene oxide for Pb (II) removal, *ACS Appl. Mater. Interfaces* 4 (2012) 1186–1193, <https://doi.org/10.1021/am201645g>.
- [12] C. Jiang, X. Wang, D. Qin, W. Da, B. Hou, C. Hao, J. Wu, Construction of magnetic lignin-based adsorbent and its adsorption properties for dyes, *J. Hazard. Mater.* 369 (2019) 50–61, <https://doi.org/10.1016/j.jhazmat.2019.02.021>.
- [13] J. Tao, J. Xiong, C. Jiao, D. Zhang, H. Lin, Y. Chen, Hybrid mesoporous silica based on Hyperbranch-Substrate Nanonetwork as highly efficient adsorbent for water treatment, *ACS Sustain. Chem. Eng.* 4 (2016) 60–68, <https://doi.org/10.1021/acssuschemeng.5b00652>.
- [14] V.B. Cashin, D.S. Eldridge, A. Yu, D. Zhao, Surface functionalization and manipulation of mesoporous silica adsorbents for improved removal of pollutants: a review, *Environ. Sci. Water Res. Technol.* 4 (2018) 110–128, <https://doi.org/10.1039/c7ew00322f>.
- [15] D. Pérez-Quintanilla, I. del Hierro, A. Sánchez, I. Sierra, M. Fajardo, Preconcentration of Zn(II) in water samples using a new hybrid SBA-15-based material, *J. Hazard. Mater.* 166 (2008) 1449–1458, <https://doi.org/10.1016/j.jhazmat.2008.12.065>.
- [16] W. Wu, W. Guo, Z. Ji, Y. Liu, X. Hu, Z. Liu, Static and dynamic sorption study of heavy metal ions on amino-functionalized SBA-15, *J. Dispers. Sci. Technol.* 39 (2018) 594–604, <https://doi.org/10.1080/01932691.2017.1340845>.
- [17] M. Barczak, Synthesis and structure of pyridine-functionalized mesoporous SBA-15 organosilicas and their application for sorption of diclofenac, *J. Solid State Chem.* 258 (2018) 232–242, <https://doi.org/10.1016/j.jssc.2017.10.006>.
- [18] M. Mirzaie, A. Rashidi, H.-A. Tayebi, M.E. Yazdanshenas, Removal of anionic dye from aqueous media by adsorption onto SBA-15/Polyamidoamine dendrimer hybrid: adsorption equilibrium and kinetics, *J. Chem. Eng. Data* 62 (2017) 1365–1376, <https://doi.org/10.1021/acs.jced.6b00917>.
- [19] E. Da’na, Adsorption of heavy metals on functionalized-mesoporous silica: a review, *Microporous Mesoporous Mater.* 247 (2017) 145–157, <https://doi.org/10.1016/J.MICROMESO.2017.03.050>.
- [20] A. Salis, L. Medda, F. Cugia, M. Monduzzi, Effect of electrolytes on proteins physisorption on ordered mesoporous silica materials, *Colloids Surf. B Biointerfaces* 137 (2016) 77–90, <https://doi.org/10.1016/j.colsurfb.2015.04.068>.
- [21] Z.X. Wu, D.Y. Zhao, Ordered mesoporous materials as adsorbents, *Chem. Commun. (Camb.)* 47 (2011) 3332–3338, <https://doi.org/10.1039/C0cc04909c>.
- [22] J. Liang, Z. Liang, R. Zou, Y. Zhao, Heterogeneous catalysis in zeolites, mesoporous silica, and metal–Organic frameworks, *Adv. Mater.* 29 (2017) 1701139, <https://doi.org/10.1002/adma.201701139>.
- [23] R. Jin, D. Zheng, R. Liu, G. Liu, Silica-supported molecular catalysts for tandem reactions, *ChemCatChem*. 10 (2018) 1739–1752, <https://doi.org/10.1002/cctc.201701718>.
- [24] E.M. Usai, M.F. Sini, D. Meloni, V. Solinas, A. Salis, Sulfonic acid-functionalized mesoporous silicas: microcalorimetric characterization and catalytic performance toward biodiesel synthesis, *Microporous Mesoporous Mater.* 179 (2013) 54–62, <https://doi.org/10.1016/j.micromeso.2013.05.008>.
- [25] M. Hartmann, X. Kostrov, Immobilization of enzymes on porous silicas - benefits and challenges, *Chem. Soc. Rev.* 42 (2013) 6277–6289, <https://doi.org/10.1039/c3cs60021a>.
- [26] E. Magner, Immobilisation of enzymes on mesoporous silicate materials, *Chem. Soc. Rev.* 42 (2013) 6213–6222, <https://doi.org/10.1039/c2cs35450k>.
- [27] F. Pitzalis, M. Monduzzi, A. Salis, A bienzymatic biocatalyst constituted by glucose oxidase and Horseradish peroxidase immobilized on ordered mesoporous silica, *Microporous Mesoporous Mater.* 241 (2017) 145–154, <https://doi.org/10.1016/j.micromeso.2016.12.023>.
- [28] M. Piras, A. Salis, M. Piludu, D. Steri, M. Monduzzi, 3D vision of human lysozyme adsorbed onto a SBA-15 nanostructured matrix, *Chem. Commun. (Camb.)* 47 (2011) 7338–7340, <https://doi.org/10.1039/c1cc11840d>.
- [29] N. Lashgari, A. Badiei, G.M. Ziarani, Modification of mesoporous silica SBA-15 with different organic molecules to gain chemical sensors: a review, *Nanochemistry Res.* 1 (2016) 127–141, <https://doi.org/10.7508/nrc.2016.01.014>.
- [30] A.M. Sacara, V. Nairi, A. Salis, G.L. Turdean, L.M. Muresan, Silica-modified electrodes for electrochemical detection of malachite green, *Electroanalysis*. 29 (2017) 2602–2609, <https://doi.org/10.1002/elan.201700400>.
- [31] X. Dai, F. Qiu, X. Zhou, Y. Long, W. Li, Y. Tu, Amino-functionalized mesoporous silica modified glassy carbon electrode for ultra-trace copper(II) determination, *Anal. Chim. Acta* 848 (2014) 25–31, <https://doi.org/10.1016/j.aca.2014.08.002>.
- [32] A.-M. Sacara, F. Pitzalis, A. Salis, G.L. Turdean, L.M. Muresan, Glassy carbon electrodes modified with ordered mesoporous silica for the electrochemical detection of cadmium ions, *ACS Omega* 4 (2019) 1410–1415, <https://doi.org/10.1021/acsomega.8b03305>.
- [33] M. Vallet-Regí, L. Ruiz-Gonzalez, I. Izquierdo-Barba, J.M. Gonzalez-Calbet, Revisiting silica based ordered mesoporous materials: medical applications, *J. Mater. Chem.* 16 (2006) 26–31, <https://doi.org/10.1039/B509744D>.
- [34] L. Medda, M.F. Casula, M. Monduzzi, A. Salis, Adsorption of lysozyme on hyaluronic acid functionalized SBA-15 mesoporous silica: a possible bioadhesive depot system, *Langmuir*. 30 (2014) 12996–13004, <https://doi.org/10.1021/la503224n>.
- [35] A. Salis, M. Fanti, L. Medda, V. Nairi, F. Cugia, M. Piludu, V. Sogos, M. Monduzzi, Mesoporous Silica Nanoparticles Functionalized with Hyaluronic Acid and Chitosan Biopolymers. Effect of Functionalization on Cell Internalization, *ACS Biomater. Sci. Eng.* 2 (2016) 741–751, <https://doi.org/10.1021/acsbomaterials.5b00502>.
- [36] M. Manzano, M. Vallet-Regí, Mesoporous silica nanoparticles in nanomedicine applications, *J. Mater. Sci. Mater. Med.* 29 (2018) 65, <https://doi.org/10.1007/s10856-018-6069-x>.
- [37] B. Baumann, R. Wittig, M. Lindén, Mesoporous silica nanoparticles in injectable hydrogels: factors influencing cellular uptake and viability, *Nanoscale*. 9 (2017) 12379–12390, <https://doi.org/10.1039/c7nr02015e>.
- [38] V. Nairi, L. Medda, M. Monduzzi, A. Salis, Adsorption and release of ampicillin antibiotic from ordered mesoporous silica, *J. Colloid Interface Sci.* 497 (2017) 217–225, <https://doi.org/10.1016/j.jcis.2017.03.021>.
- [39] G. Crisponi, V.M. Nurchi, No Title, J. Aaseth, G. Crisponi, Ole Andersen (Eds.), *Chelation Ther. Treat. Met. Intox.*, Academic Press, London, 2016, pp. 35–61, <https://doi.org/10.1016/B978-0-12-803072-1/00002-X>.
- [40] V.M. Nurchi, G. Crisponi, M. Crespo-Alonso, J.I. Lachowicz, Z. Szweczek, G.J.S. Cooper, Complex formation equilibria of CuII and ZnII with triethylenetetramine and its mono- and di-acetyl metabolites, *Dalton Trans.* 42 (2013) 6161–6170, <https://doi.org/10.1039/c2dt32252h>.
- [41] M. Peydayesh, T. Mohammadi, O. Bakhtiari, Effective treatment of dye wastewater via positively charged TETA-MWCNT/PES hybrid nanofiltration membranes, *Sep. Purif. Technol.* 194 (2018) 488–502, <https://doi.org/10.1016/j.seppur.2017.11.070>.
- [42] M. Mokhtar, S.E. Dickson, Y. Kim, W. Mekky, Preparation and characterization of ion selective membrane and its application for Cu²⁺ removal, *J. Ind. Eng. Chem.* 60 (2018) 475–484, <https://doi.org/10.1016/J.JIEC.2017.11.035>.
- [43] G. Bayramoglu, M.Y. Arica, Adsorption of Congo Red dye by native amine and carboxyl modified biomass of *Funalia troglitii*: isotherms, kinetics and thermodynamics mechanisms, *Korean J. Chem. Eng.* 35 (2018) 1303–1311, <https://doi.org/10.1007/s11814-018-0033-9>.
- [44] L. Liao, Z. Lin, L. Geng, J. Wei, D. Mei, S. Chen, CO₂ adsorption properties of mixed-amine functionalized mesoporous molecular sieve KIT-6, *Mater. Res. Express* 5 (2018) 065520, <https://doi.org/10.1088/2053-1591/aacc7c>.
- [45] M.E. Mahmoud, M.S. Abdelwahab, E.M. Fathallah, Design of novel nano-sorbents based on nano-magnetic iron oxide-bound-nano-silicon oxide-immobilized-triethylenetetramine for implementation in water treatment of heavy metals, *Chem. Eng. J.* 223 (2013) 318–327, <https://doi.org/10.1016/J.CEJ.2013.02.097>.
- [46] J.I. Lachowicz, V.M. Nurchi, G. Crisponi, M. de G. Jaraquemada-Pelaez, C. Caltagirone, M. Peana, M.A. Zoroddu, Z. Szweczek, G.J.S. Cooper, Complex formation equilibria of Cu²⁺ and Zn²⁺ with Irbesartan and Losartan, *Eur. J. Pharm. Sci.* 97 (2017) 158–169, <https://doi.org/10.1016/j.ejps.2016.11.010>.
- [47] D. Zhao, J. Feng, Q. Huo, N. Melosh, G.H. Fredrickson, B.F. Chmelka, G.D. Stucky, Triblock copolymer syntheses of mesoporous silica with periodic 50 to 300 angstrom pores, *Science* 279 (80) (1998) 548–552, <https://doi.org/10.1126/science.279.5350.548>.
- [48] M.E. Mahmoud, M.S. Abdelwahab, E.M. Fathallah, Design of novel nano-sorbents based on nano-magnetic iron oxide-bound-nano-silicon oxide-immobilized-triethylenetetramine for implementation in water treatment of heavy metals, *Chem. Eng. J.* 223 (2013) 318–327, <https://doi.org/10.1016/j.ccej.2013.02.097>.

- [49] S. Brunauer, P.H. Emmett, E. Teller, Adsorption of gases in multimolecular layers, *J. Am. Chem. Soc.* 60 (1938) 309–319 doi:citeulike-article-id:4074706\rdoi: 10.1021/ja01269a023.
- [50] E.P. Barrett, L.G. Joyner, P.P. Halenda, The Determination of Pore Volume and Area Distributions in Porous Substances. I. Computations from Nitrogen Isotherms, *J. Am. Chem. Soc.* 73 (1951) 373–380, <https://doi.org/10.1021/ja01145a126>.
- [51] E. Da'na, N. De Silva, A. Sayari, Adsorption of copper on amine-functionalized SBA-15 prepared by co-condensation: kinetics properties, *Chem. Eng. J.* 166 (2011) 454–459, <https://doi.org/10.1016/J.CEJ.2010.11.017>.
- [52] I.D. Mall, V.C. Srivastava, N.K. Agarwal, I.M. Mishra, Removal of congo red from aqueous solution by bagasse fly ash and activated carbon: kinetic study and equilibrium isotherm analyses, *Chemosphere.* 61 (2005) 492–501, <https://doi.org/10.1016/J.CHEMOSPHERE.2005.03.065>.
- [53] J. Aguado, J.M. Arsuaga, A. Arencibia, M. Lindo, V. Gascón, Aqueous heavy metals removal by adsorption on amine-functionalized mesoporous silica, *J. Hazard. Mater.* 163 (2009) 213–221, <https://doi.org/10.1016/J.JHAZMAT.2008.06.080>.
- [54] M.H. Dindar, M.R. Yaftian, S. Rostamnia, Potential of functionalized SBA-15 mesoporous materials for decontamination of water solutions from Cr(VI), As(V) and Hg(II) ions, *J. Environ. Chem. Eng.* 3 (2015) 986–995, <https://doi.org/10.1016/j.jece.2015.03.006>.
- [55] Z. Saad, V. Kazpard, Y. Pouilloux, Z. Ezzeddine, I. Batonneau-Gener, H. Hamad, Divalent heavy metals adsorption onto different types of EDTA-modified mesoporous materials: effectiveness and complexation rate, *Microporous Mesoporous Mater.* 212 (2015) 125–136, <https://doi.org/10.1016/j.micromeso.2015.03.013>.
- [56] E.C. Lima, A. Hosseini-Bandegharai, J.C. Moreno-Piraján, I. Anastopoulos, A critical review of the estimation of the thermodynamic parameters on adsorption equilibria. Wrong use of equilibrium constant in the Van't Hoof equation for calculation of thermodynamic parameters of adsorption, *J. Mol. Liq.* 273 (2019) 425–434, <https://doi.org/10.1016/j.molliq.2018.10.048>.
- [57] E. Da'na, A. Sayari, Adsorption of copper on amine-functionalized SBA-15 prepared by co-condensation: equilibrium properties, *Chem. Eng. J.* 166 (2011) 445–453, <https://doi.org/10.1016/j.ccej.2010.11.016>.

Supporting information

Adsorption of Cu²⁺ and Zn²⁺ on SBA-15 mesoporous silica functionalized with triethylenetetramine chelating agent

Joanna Izabela Lachowicz,¹ Giulia Rossella Delpiano,¹ Davide Zanda,¹ Marco Piludu,^{2,3} Enrico Sanjust,^{2,3} Maura Monduzzi,^{1,3,4} Andrea Salis^{1,3,4,}*

¹ Dipartimento di Scienze Chimiche e Geologiche, Università di Cagliari, Cittadella Universitaria, S.S. 554 bivio Sestu, 09042 Monserrato, Cagliari, Italy

² Dipartimento di Scienze Biomediche, Università di Cagliari, Cittadella Universitaria, S.S. 554 bivio Sestu, 09042 Monserrato, Cagliari, Italy

³ Consorzio Interuniversitario per lo Sviluppo dei Sistemi a Grande Interfase (CSGI), Unità Operativa Univ. Cagliari, Italy.

⁴ Centro NanoBiotecnologie Sardegna (CNBS), Unità Operativa Univ. Cagliari, Italy

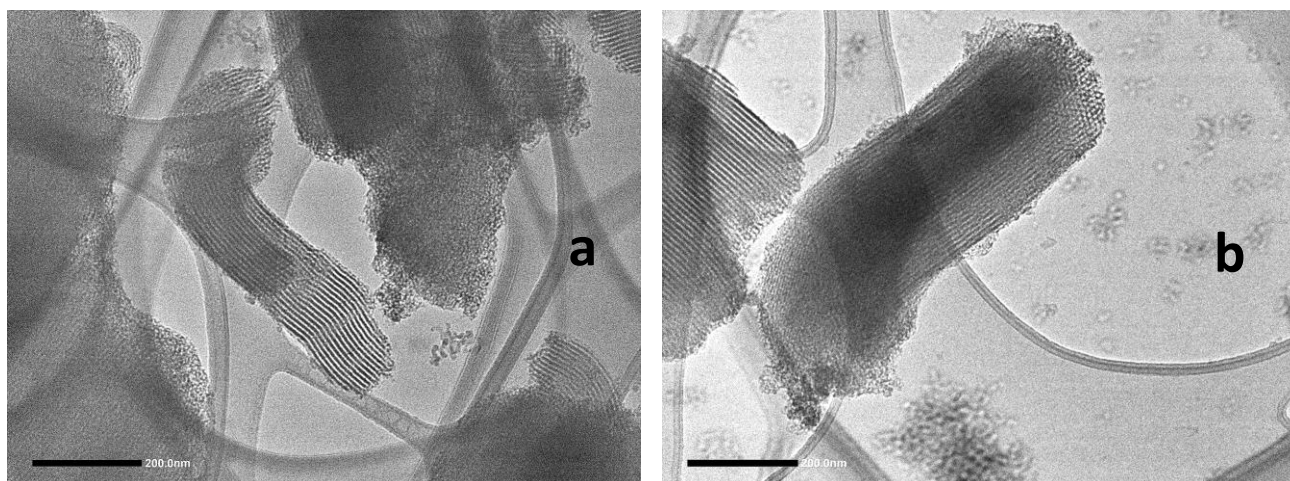


Figure S1. TEM images of a) SBA-Cl and b) SBA-TETA.

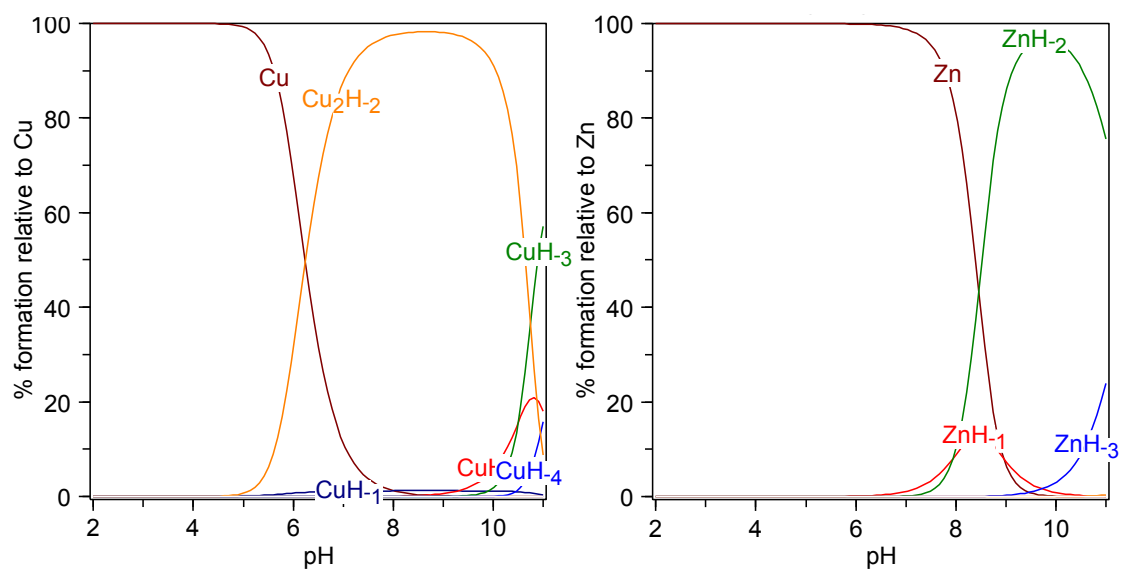


Figure S2. Speciation plots of copper and zinc ions hydrolysis in water. The constants for the Zn^{2+} and Cu^{2+} hydroxides at 25 °C and 0.1 M ionic strength, taken from Baes and Mesmer [Baes Jr, C.; Mesmer, R., *The Hydrolysis of Cations*. RE Krieger, Malabar, Wiley, New York, 1976, 1986.]. Charges are omitted for simplicity.

Table S1. Mass percentages of C, H and N in synthesized mesoporous silica samples.

Sample	% C (mass)	% C (mol)	% H (mass)	% H (mol)	% N (mass)	% N (mol)
SBA-15	0.38	0.0316	0.47	0.466	-	-
SBA-Cl	4.80	0.400	0.31	0.308	-	-
SBA-TETA	12.04	1.002	1.07	1.062	4.90 ^a	0.350

^a The amount of TETA in the sample is equal to $0.875 \text{ mmol g}^{-1}$, ($49.0 \text{ mg g}^{-1}/(14.01 \text{ g mol}^{-1} \times 4)$) corresponding to a loading of 128 mg g^{-1} , ($MM_{\text{TETA}} = 146.235 \text{ mg mmol}^{-1}$).

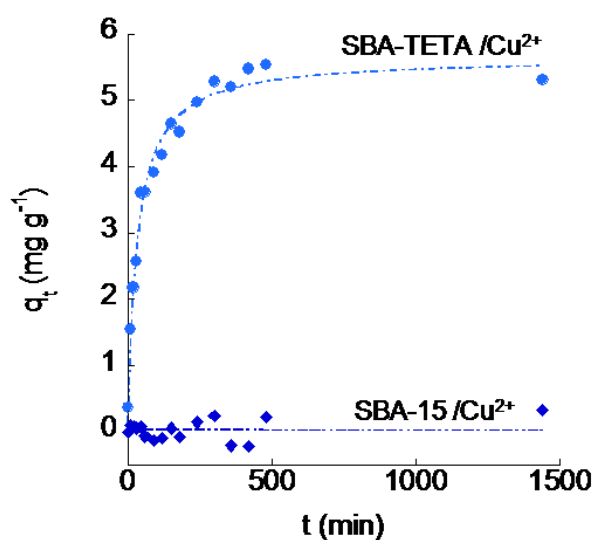


Figure S3. Comparison between Cu^{2+} adsorption kinetics on SBA-15 and SBA-TETA. Initial Cu^{2+} concentration 10 mg L^{-1} .

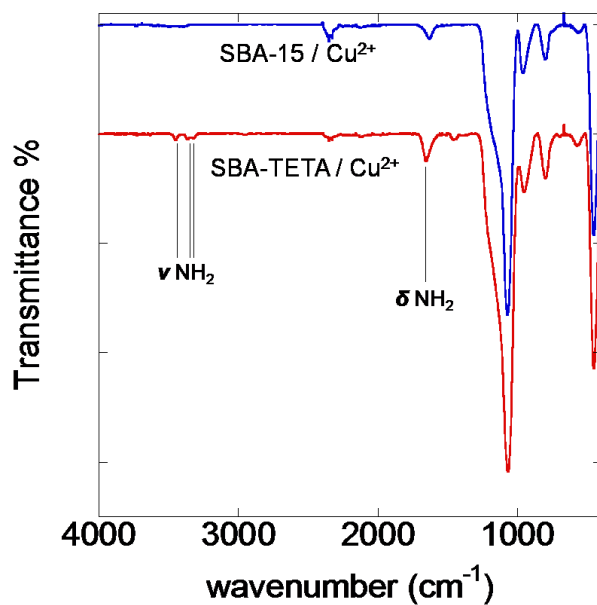


Figure S4. FT-IR spectra of SBA-15 and SBA-TETA after Cu^{2+} adsorption.

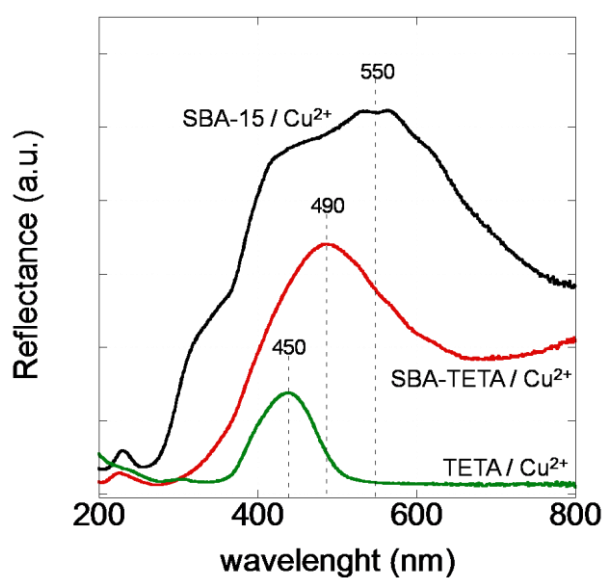


Figure S5. UV-visible reflectance spectra of SBA-15/ Cu^{2+} and SBA-TETA/ Cu^{2+} samples. The spectra are compared with that of the complex between copper and TETA in solution.

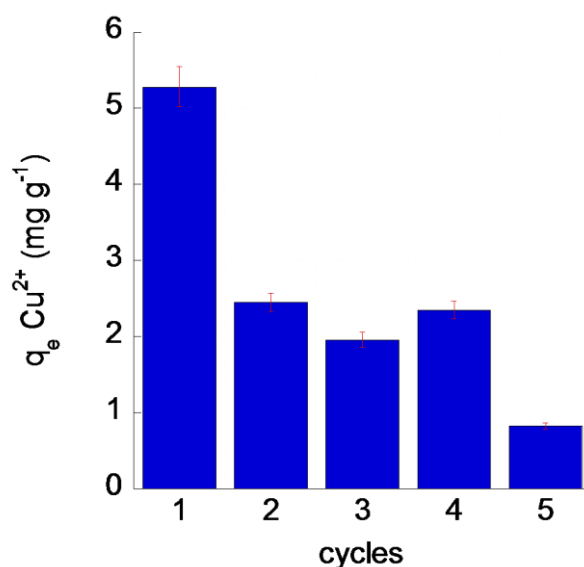


Figure S6. SBA-TETA operational stability to reuse. Five adsorption/desorption cycles of Cu^{2+} .

The operational stability to recycling of the SBA-TETA is shown in Figure S3. SBA-TETA adsorbent was dispersed in a $10 \text{ mg L}^{-1} \text{ Cu}^{2+}$ solution under stirring. The residual concentration was lower than 5 mg L^{-1} after the first adsorption cycle. To remove the adsorbed Cu^{2+} and reuse SBA-TETA adsorbent, the used sample was washed with a 0.1 M HCl solution. The desorption of Cu^{2+} is also confirmed by an instantaneous color change of the solid which turned from blue to yellowish. The regenerated adsorbent was then used for a new adsorption cycle. The adsorbed amount of Cu^{2+} decreased to about 46% respect to the first use at the second cycle. The material was reused for five adsorption cycles carrying out a washing with 0.1 M HCl before each reuse. The adsorbed amount remained stable up to the fourth reuse (44%) and decreased again (15%) at the fifth cycle. The initial decrease of adsorbent performance might be due to the acid treatment which may cause a partial release of TETA functional group from SBA-15 surface. More studies will be needed to find the optimal HCl concentration and contact time to optimize SBA-TETA performance toward Cu^{2+} removal for several adsorption/desorption cycles.

Paper II

Improving Metal Adsorption on Triethylenetetramine (TETA) Functionalized SBA-15 Mesoporous Silica Using Potentiometry, EPR and ssNMR

Joanna Izabela Lachowicz,* Abdul-Hamid Emwas, Giulia Rossella Delpiano, Andrea Salis, Marco Piludu, Lukasz Jaremko, and Mariusz Jaremko*

Nanomaterials have received growing attention in the treatment and diagnosis of neurological disorders because the low blood brain barrier permeability hinders the classical pharmacological approach. Metal ion chelators combined with nanoparticles prove effective in the treatment of neurodegeneration and are under extensive studies. Most chelating agents and metallodrugs compete with endogenous molecules for metal coordination, and do not reach the active site. Determining the competition between metallodrugs and endogenous molecules requires knowing the stability constants of formed metal complexes. In this study, for the first time, potentiometric titrations are used to determine metal complex formation constants, and to quantify ligand content in functionalized materials. This new potentiometric approach allows physico-chemical characterization of mesoporous functionalized materials and their metal adsorption capacity in water solution. The potentiometric results are compared with isotherm models obtained by spectroscopic measurements and yield rewarding data fitting. The potentiometric method described here can be extended to different types of nanostructured materials carrying surface ionizable groups.

(copper 70×10^{-6} M, zinc 350×10^{-6} M, and iron 340×10^{-6} M).^[1,2] Nanomaterials are receiving high attention in the treatment and diagnosis^[3] of neurological disorders where the classical pharmacological approach is not effective due to low blood brain barrier (BBB) permeability. An effective drug delivery method is combining of drugs with nanocarriers, for example, polymeric micelles, liposomes, lipid, and polymeric nanoparticles (NPs), that have high BBB affinities.^[4] Metal ion chelators, which are bound covalently to nanoparticles, can facilitate drug entry into the brain.^[5]

Desferrioxamine (Desferal) is an iron (Fe), aluminum (Al), copper (Cu), and zinc (Zn) chelator that showed a decrease of AD progression in clinical trials,^[2,6] even if the low BBB permeability of DFO is still debatable.^[7] DFO conjugated to polystyrene NPs of 240 nm and examined in

human cortical neurons in vitro prevented A β peptide aggregation,^[8] the main component of the amyloid plaques found in the brains of people with Alzheimer's disease.^[9] Nevertheless, low bioavailability and high toxicity restrict the use of metal chelators in humans.


Functional nanoparticles are characterized by multiple incorporation of positron emitting radionuclides and signal enhancement in positron emission tomography (PET).^[10] It has been

1. Introduction

Transition metals play pivotal roles in human metabolism in trace amounts but may be toxic when they exceed the tolerance limit. Elevated levels of copper (390×10^{-6} M), zinc (1055×10^{-6} M), and iron (940×10^{-6} M) have been reported for Alzheimer's disease (AD) in brain. This contrasts sharply with metal concentrations found in samples collected from healthy patients

Dr. J. I. Lachowicz
Department of Medical Sciences and Public Health
University of Cagliari
Cittadella Universitaria, Monserrato 09042, Italy
E-mail: lachowicz@unica.it

Dr. A.-H. Emwas
Core Labs
King Abdullah University of Science and Technology (KAUST)
Thuwal 23955-6900, Saudi Arabia

 The ORCID identification number(s) for the author(s) of this article can be found under <https://doi.org/10.1002/admi.202000544>.

© 2020 The Authors. Published by WILEY-VCH Verlag GmbH & Co. KGaA, Weinheim. This is an open access article under the terms of the Creative Commons Attribution License, which permits use, distribution and reproduction in any medium, provided the original work is properly cited.

G. R. Delpiano, Prof. A. Salis
Department of Chemical and Geological Sciences
University of Cagliari
Cittadella Universitaria, Monserrato 09042, Italy

Dr. M. Piludu
Department of Biomedical Sciences
University of Cagliari
Cittadella Universitaria, Monserrato 09042, Italy

Prof. L. Jaremko, Prof. M. Jaremko
Division of Biological and Environmental Sciences
and Engineering (BESE)
King Abdullah University of Science and Technology (KAUST)
Thuwal 23955-6900, Saudi Arabia
E-mail: Mariusz.jaremko@kaust.edu.sa

DOI: 10.1002/admi.202000544

reported that NPs with long-lived isotopes increase signal-to-noise ratio. Among different NPs, mesoporous silica nanoparticles (MSNs) are of high interest as imaging agents,^[3,11] as well as drug carriers for in vitro and in vivo^[11,12] experiments. On top of that, MSNs are environment-friendly, and are typically removed from the body through renal clearance.^[13] Moreover, the particle and pore size, shape, and surface properties of MSNs can be kept under control, making delivery even more feasible for many biomedical applications. Furthermore, the high internal surface area and pore volume of MSNs, work together with the possibility of tuning pore dimensions and mesopore surface chemistry. These properties enable loading of large cargo and tuning the interactions between the cargo and the carrier.

Copper (Cu), gallium (Ga), indium (In), yttrium (Y), and zirconium (Zr) metal ions are commonly used in PET imaging. DFO is a very efficient chelator known for ⁸⁹Zr⁴⁺ ions.^[14] Recently, pore-expanded MSNs functionalized with DFO were used to complex high quantity of ⁸⁹Zr⁴⁺ and gave a high PET signal in vivo.^[10]

Most PET contrast metal agents are delivered directly into the bloodstream where they interact with serum proteins. For this reason, the metal complexes do not reach their destination and provoke side effects in imaging. Different proteins and peptides present in the serum can compete with chelating agents for metal ions^[15] and perturb the species distributions of metal drugs/prodrugs during absorption, distribution, metabolism, and excretion processes. Indeed, it is crucial to know the rate, strength, and nature of binding between metallodrugs and serum proteins in order to better understand the pharmacokinetic properties, transport, as well as the mechanisms of action.

As accurately pointed by Debbie Crans:^[16] *“The rapidly growing popularity of solid state chemistry and its expansion into the areas of new materials and chemistry of materials has resulted in a grow in achieving the detail and species composition on the atomic level. (...) We can investigate systems at an increasing resolution, however, the processes involved in the studies are becoming less mechanistically focused in their molecular description.”*

Adsorption isotherms are routinely drawn in order to present and determine the binding capacity of a surface,^[17] but titrations and kinetic consideration are also required to determine the concentration(s).^[17] Protonation processes^[18] and simple complex formation reactions have been quantitatively described^[19] on a surface, but few studies have described surface speciation.

Triethylenetetramine (TETA) dihydrochloride, also commonly known as trientine, is a therapeutic molecule that has been used as a copper-chelating agent for second-line treatment of patients with Wilson’s disease for many decades.^[20] In recent years, it has also been tested as an experimental therapeutic molecule in diabetes, where it improves cardiac structure in patients with diabetic cardiomyopathy and left-ventricular hypertrophy.^[21] TETA is known for forming stable complexes with copper and zinc ions^[21] and functionalized SBA-TETA particles could be used as new effective chelators for zinc and copper ions in human organs.

In this study, several biophysical methods such as potentiometry, electron paramagnetic resonance (EPR), UV–vis, and solid-state nuclear magnetic resonance (ssNMR) spectroscopy were extensively and successfully used for characterization of SBA-TETA particles. Moreover, potentiometric titrations were used, to the best of our knowledge, for the first time to quantify ligand content in a functionalized nanostructured material and

to determine metal complex formation constants. We present this new potentiometric approach for the physico–chemical characterization of mesoporous functionalized materials and their metal adsorption capacity in water solution.

2. Experimental Section

2.1. Chemicals

Pluronic copolymer P123 (EO20PO70EO20) tetraethylorthosilicate, TEOS (≥99%); (3-chloropropyl)trimethoxysilane, CPTMS (≥97%); triethylenetetramine, TETA (≥97%); copper chloride dihydrate, CuCl₂·2H₂O (≥99.0%), ZnCl₂ (≥99.0%) anhydrous toluene (≥99.7%), dimethylformamide (DMF, ≥99.9%), acetone (≥99%), HCl (37%), NaCl, NaOH pellets were purchased from Sigma-Aldrich (Milano, Italy). Copper (1000 ± 2 ppm in HNO₃ 2% m/m) and zinc (1000 ± 2 ppm in HNO₃ 1% m/m) stock solutions were purchased from Fluka Analytical and Aldrich Chemical Company, respectively. Diethyl ether (99.8%), and ethanol (99.8%) were purchased from Honeywell.

2.2. Synthesis of Mesoporous Materials

SBA-15 mesoporous silica was synthesized and functionalized with CPTMS according to the method described in the previous work.^[21] Briefly, the functionalization with chloro-propyl group was carried out by dispersing 1 g of obtained SBA-15 in 25 mL of anhydrous toluene, adding 700 μL of CPTMS^[21] and keeping the mixture under stirring at 110 °C overnight. The resulting SBA-Cl was collected by filtration, washed with EtO₂ and water, and dried under vacuum.

0.5 g of SBA-Cl were dispersed in 14 mL of anhydrous toluene, then the green solution of the ligand (0.56 g of TETA dissolved in 1 mL of DMF) was added and the resulting mixture was kept under stirring at 110 °C for 24 h. The dark-yellowish suspension of SBA-TETA was recovered by filtration, washed with H₂O, EtOH, and Et₂O, and dried under vacuum overnight.

SBA-NH₂ was synthesized as a reference material for UV–vis metal coordination studies. The procedure and characterization are described in the previous paper.^[22]

2.3. Physico–Chemical Characterizations

TEM imaging was performed using a Titan CT (Thermo Fisher Scientific) operating at 300 kV equipped with a 4 k × 4 k CCD camera (Gatan, Pleasanton, CA, USA). Images were acquired in bright field using a 100 μm objective aperture under parallel illumination.

N₂ adsorption/desorption isotherms at 77 K were carried out on an ASAP 2020 instrument to obtain textural parameters of the materials such as the surface area (Brunauer-Emmett-Teller, B.E.T. theory), pore width, and distribution (Barrett-Joyner-Halenda, B.J.H. theory).^[23] Before analysis, SBA-15 samples were heated at 110 °C at a rate of 1 °C min⁻¹ under vacuum for 12 h, whereas functionalized samples were outgassed under the same conditions while heating at 80 °C.

FT-IR analysis, to verify the presence of chloro-propyl group and TETA, was carried out with a Bruker Tensor 27 spectrophotometer equipped with a diamond-ATR accessory and a DTGS detector. A number of 128 scans at a resolution of 2 cm^{-1} were averaged in the spectral range $4000\text{--}400\text{ cm}^{-1}$. To quantify the functionalization percentage, Elemental Analysis (PerkinElmer Series II 2400) and Thermogravimetric Analysis—TGA (Perkin-Elmer) were performed.

2.4. Potentiometric Measurements

Potentiometric titrations were performed in 0.1 M NaCl at $298.1 \pm 0.1\text{ K}$ using an automated Mettler Toledo titrator. The thermostated glass-cell was equipped with a magnetic stirrer system, a Mettler Toledo glass electrode, a microburet delivery tube, and an inlet–outlet tube for Argon. The combined Mettler Toledo electrode was calibrated as a hydrogen-ion concentration probe by titrating previously standardized amounts of HCl with CO_2 -free NaOH solutions and determining the equivalence point by Gran's method,^[24] which gave the standard potential, E° , and the ionic product of water ($\text{pK}_w = 13.74(1)$ in 0.1 M NaCl at 298.1 K). The computer program HYPERQUAD2013^[25] was used to calculate ligand (TETA or -OH) content (in mmol) in MMs material, MMs-ligand protonation, and complex stability constants from potentiometric data. The potentiometric titrations were prepared from acidic to alkaline conditions (the studied pH range 2.5–11.0). Solutions at 0.1 M ionic strength in NaCl were titrated at $25.0\text{ }^\circ\text{C}$ with 0.1 M NaOH . The activity of the species present in the solution was proportional to concentration, where the proportionality constant was the activity coefficient that brings the stoichiometric constant close to the thermodynamic constant. For this reason, the ionic strength was kept constant during experimental determinations of stability constants. Carbonate free sodium hydroxide solutions were prepared according to Albert and Serjeant.^[26] An mV signal drift module was used to reach equilibrium after each base addition and obtain optimal accuracy of measurements. The metal concentration in ZnCl_2 and CuCl_2 stock solutions in HCl was determined by EDTA titration. The MMs were stored at $50\text{ }^\circ\text{C}$ and cooled in a desiccator to room temperature before being weighed (analytical weight scale, precision $\pm 0.01\text{ mg}$). The working MMs content was 2.5–2.7 mg in 20 mL of water. The total mmol of the ligand in the functionalized MMs was determined by the NaOH titration and metal complex formation studies were performed at 2:1, 1:1, and 1:2 metal/ligand molar ratios. Each measurement, both for ligand protonation and metal-complex experiments, was repeated at least two times in order to verify the repeatability. The different titration curves were calculated as separated curves without significant variations in the values of the calculated stability constants. Finally, the sets of data were merged and treated simultaneously to give the final stability constants. Different equilibrium models for the complex systems were generated by eliminating and introducing different species. Only those models for which the HYPERQUAD program furnished a variance of the residuals $\sigma^2 \leq 9$ were considered acceptable. Such a condition was unambiguously met by a single model for each system.

The equilibrium concentrations of various species were computed by solving the system of mass balance equations

constructed for each component (Equations (1)–(3) for a system containing three components: M, L, and H), and these mass balance equations were then solved iteratively for the concentrations of the free components.^[27] In addition, it was necessary to know the stoichiometry and overall/cumulative stability constants ($\beta(\text{M}_p\text{L}_q\text{H}_r)$) of all associations (e.g., ligand species, LH_r ; metal complexes, $\text{M}_p\text{L}_q\text{H}_r$; and metal hydrolysis products, M_pH_r ; where p , q , and r are the stoichiometric numbers of the components in the given species) and the ionization constant of water (K_w). $\beta(\text{M}_p\text{L}_q\text{H}_r)$ was defined for the general equilibrium shown in Equation (4), where M denotes the metal ion and L is the completely deprotonated ligand

$$C_M = [\text{M}] + \sum_{i=1}^n p_i \beta_{pqr} [\text{M}]^{p_i} [\text{L}]^{q_i} [\text{H}]^{r_i} \quad (1)$$

$$C_L = [\text{L}] + \sum_{i=1}^n p_i \beta_{pqr} [\text{M}]^{p_i} [\text{L}]^{q_i} [\text{H}]^{r_i} \quad (2)$$

$$C_H = [\text{H}] + \sum_{i=1}^n p_i \beta_{pqr} [\text{M}]^{p_i} [\text{L}]^{q_i} [\text{H}]^{r_i} \quad (3)$$

$$p\text{M} + q\text{L} + r\text{H} \leftrightarrow \text{M}_p\text{L}_q\text{H}_r, \text{ as } \beta(\text{M}_p\text{L}_q\text{H}_r) = [\text{M}_p\text{L}_q\text{H}_r] / [\text{M}]^p [\text{L}]^q [\text{H}]^r \quad (4)$$

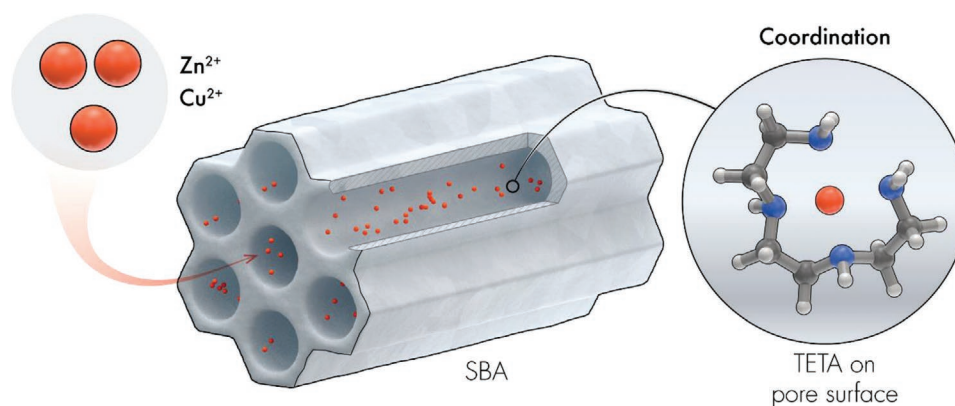
2.4.1. HySS Software Theoretical Calculations

Various computer programs were developed to produce distribution diagrams for the species formed in solution, such as HySS.^[25] Species distribution curves represented the percentages (or partial mole fractions) or equilibrium concentrations of the different chemical species present in a solution under given conditions in a representative manner.^[28] Concentration distribution curves were generally presented as a function of a single variable, such as pH, where the fixed values of the components (reagents) uniquely determined the molar ratios of the species formed.

The speciation distribution curves calculated for compounds containing dissociable protons represented the fractional contribution of each protonated (LH_r) and unprotonated (L) species in equilibrium, and thus the average number of protons bound and the actual charge of the ligand could be viewed as a function of the pH.

In these studies, HySS software^[25] was used to calculate speciation plots of free ligand (Scheme 1, Figure 1), metal complexes (Figure 2), and copper and zinc hydrolysis (Figure S3, Supporting Information) as a function of pH. The curves were calculated on the basis of proper constants: ligand protonation constants, ligand protonation constants and its metal complex formation constants, and metal hydrolysis constants, respectively. The ligand and metal concentrations used for the calculations were the same as experimental data.

The theoretical competition studies were calculated on the base of SBA-TETA protonation constants (Table 1) and complex formation constants (Table 2). The speciation diagrams (Figure 4) were calculated with the ligand and metal concentrations used in experimental competition studies with inductively coupled plasma optical emission spectrometry (ICP-OES) analysis. Moreover, the free metal concentration was calculated at pH 4.



Scheme 1. Schematic representation of SBA-TETA material and metal coordination process by TETA ligand. [Images produced by KAUST scientific illustrators. This image is original and designed specifically for the targeted publication. It should not be cropped, distorted, or in any way edited without the expressed consent of Research Publication Services. Because KAUST owns the copyright of the original image, you may cause a copyright conflict between the journal and KAUST if you modify the illustration in any way before submitting it to the journal. Any other use of the image apart from your paper (e.g., in a presentation, poster, or website) should be accompanied by credits to the journal in which it is published and to the illustrator as follows: Xabier Pita/KAUST].

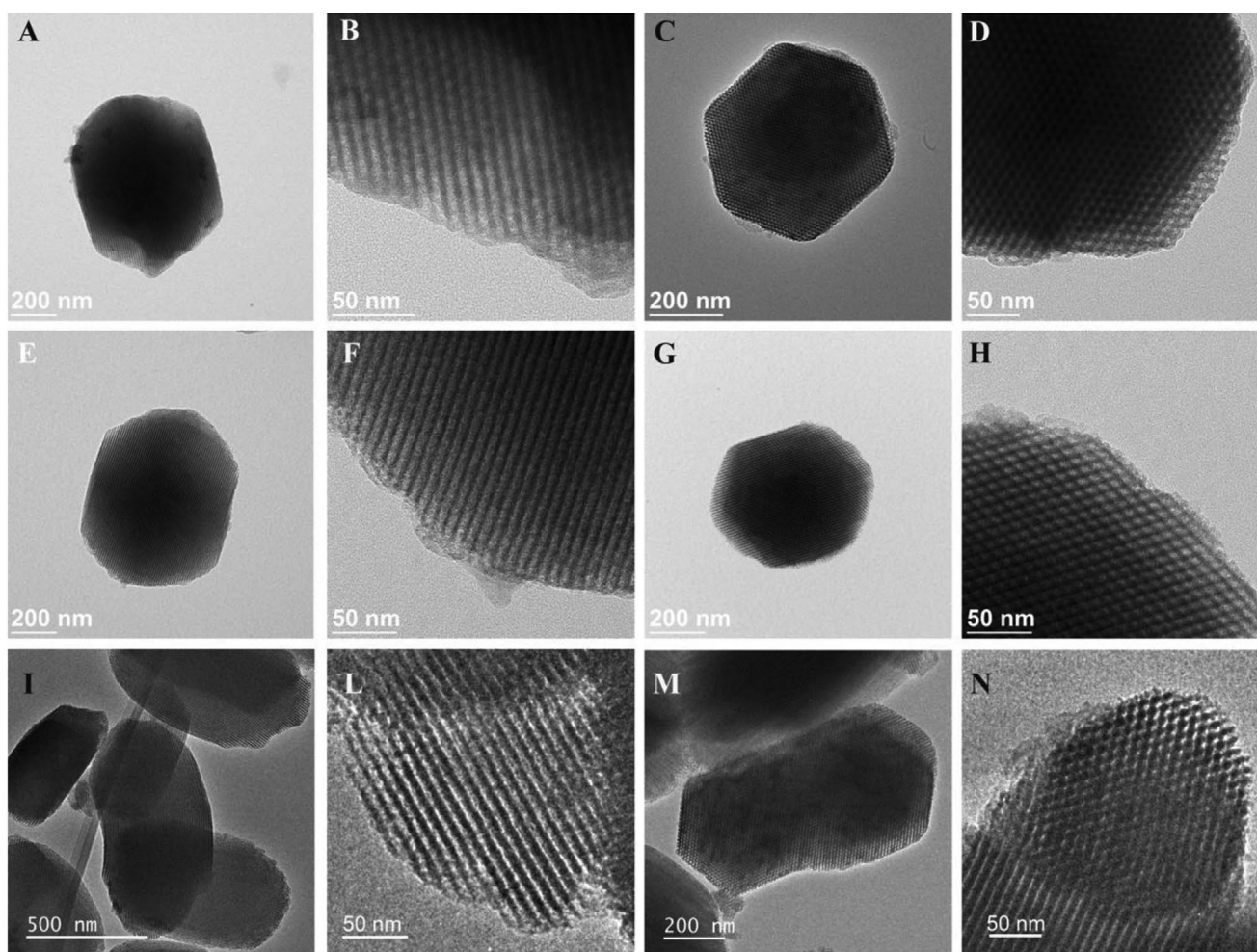


Figure 1. A–D) Transmission electron micrographs of SBA-TETA, E–H) SBA-TETA with copper ions, and I–N) SBA-TETA with zinc ions. TEM analysis highlights a well-structured mesoporous structure in all samples. Comparing their side views (A,B,E,F,I,L) and their top views (C,D,G,H,M,N) no evident structural differences are observed.

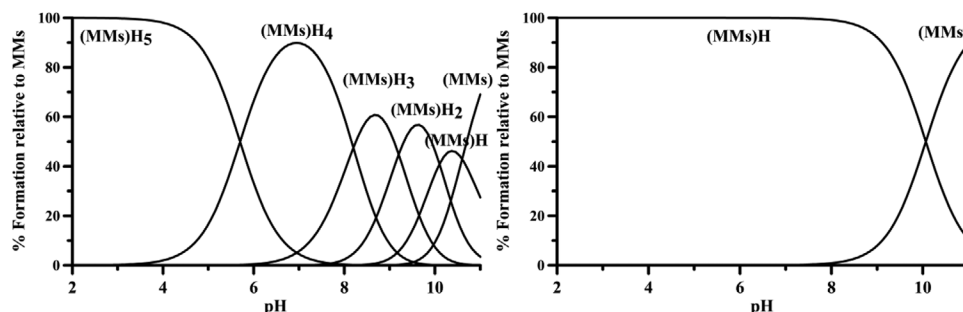


Figure 2. Speciation plots relative to the protonation of SBA-TETA (left) and SBA-15 (right). Charges are omitted for simplicity.

The HySS program was also used to calculate the $pM(\text{etal})$ value for each studied ligand. The negative logarithm of the concentration of the free metal in solution, was calculated for total [ligand] = 10^{-5} M and total [metal] = 10^{-6} M in solution at proper pH (Table 3). For the sake of comparison with literature data, the pH of 7.4 was chosen for the $p\text{Cu}$ and $p\text{Zn}$ calculations. Moreover, $p\text{Cu}$ e $p\text{Zn}$ values for SBA-TETA in different pHs were calculated (Figure 3).

2.5. ICP-OES Competition Studies

The copper and zinc concentrations in aqueous solutions were analyzed by ICP-OES (Agilent 5100). The operational parameters were: RF power: 1.2 kW. Plasma gas: 12 L min^{-1} , Aux gas: 1.0 L min^{-1} , and nebulizer flow 0.7 L min^{-1} . Emission lines (nm): Cu (327.395, 324.754, and 213.598) and Zn (213.857, 202.548, and 206.200). No spectral interference was observed. The standard solutions: 0.5–50 ppm in 1% nitric acid were prepared by the analytical dilution of standard zinc and copper solutions for linear calibration curve ($R^2 = 0.999$).

A mass of 15 mg of SBA-TETA were incubated for 24 h in 25°C with the copper and zinc 10 ppm solution and in the solution containing 10 ppm copper and 100 ppm zinc ions at pH 4. The process was stopped by filtration of the suspension, then the metal concentration in the solution was quantified through ICP-AES measurements.

2.6. Spectroscopies

SBA-15, SBA-NH₂, and SBA-TETA (20 mg each) were dissolved in 0.123 M copper solution in water (pH = 2.8). After 24 h rotation at room temperature, the solutions were centrifuged and

lyophilized (Figure S4A, Supporting Information). In the next step, the samples were re-hydrated, centrifuged, and dried in the vacuum (Figure S4B, Supporting Information). Successively, the solid-state samples were analyzed by UV-vis.

SBA-TETA, (100 mg) were dissolved in 2 mL of ZnCl₂ and CuCl₂ solutions (0.88 M, pH 4, filtered 0.2×10^{-6} M) and rotated (15 rpm) for 24 h. Afterward, the solutions were centrifuged (14 000 rpm, 30 min) and dried under vacuum. The samples were studied by ssNMR and EPR, respectively.

2.6.1. Nuclear Magnetic Resonance

All NMR experiments were performed on Bruker 400 MHz AVANACIII NMR spectrometer at magnetic field strength of 9.4 T with resonating ¹³C corresponding frequency of 100.04 MHz. The spectrometer was equipped with 4 mm Bruker double resonance MAS probe (BrukerBioSpin, Rheinstetten, Germany). All ¹³C NMR spectra were recorded under the same conditions and parameters with 14 and 12 kHz spinning rate using cross polarization CP pulse program.

The ¹³C signals were referenced to the methylene signal of adamantane at 37.78 ppm. Bruker Topspin 3.5pl7 software (Bruker BioSpin, Rheinstetten, Germany) was used for data collection and for data analysis.

2.6.2. EPR Spectroscopy

Bruker EMX PLUS spectrometer equipped with standard resonator for high sensitivity CW-EPR (Bruker BioSpin, Rheinstetten, Germany) was used to record all EPR spectra. The operating frequency was set (9.384688 GHz) and the microwave power was set to 0.625 mW with 5 G modulation

Table 1. Protonation constants (log *K*) of SBA-TETA and SBA-15 at 25.0°C and 0.1 M NaCl, in comparison with log *K* literature data^[20] of free TETA. L refers to ligand: free TETA, TETA grafted on MMs material, -OH on SBA-15 material, respectively.

Specie	TETA		Specie	SBA-TETA		SBA-15	
	log β	log <i>K</i>		log β	log <i>K</i>	log β	log <i>K</i>
(L)H	9.79(5)	9.79	(L)H	10.6(2)	10.6	10.0(1)	10.0
(L)H ₂	18.90(4)	9.11	[(L)H ₂] ⁺	20.7(1)	10.1		
(L)H ₃	25.58(2)	6.68	[(L)H ₃] ²⁺	29.9(1)	9.2		
(L)H ₄	28.86(2)	3.28	[(L)H ₄] ³⁺	38.1(1)	8.2		
			[(L)H ₅] ⁴⁺	43.8(2)	5.7		

Table 2. Complex formation constants of TETA,^[20] SBA-TETA, and SBA-15 with Cu²⁺ and Zn²⁺ at 25 °C, 0.1 M NaCl ionic strength, obtained from potentiometric data using the Hyperquad program. *Negative logarithm of the concentration of the free metal in solution, calculated for total [ligand] = 10⁻⁵ M and total [metal] = 10⁻⁶ M at pH 7.4. L refers to ligand: free TETA, TETA grafted on MMs material, -OH on SBA-15 material, respectively.

Specie	TETA				SBA-TETA				SBA-15			
	Cu		Zn		Cu		Zn		Cu		Zn	
	log β	log K	log β	log K	log β	log K	log β	log K	log β	log K	log β	log K
[MLH ₄] ⁵⁺					46.08(8)		44.0(3)					
[MLH ₃] ⁴⁺					42.0(1)	4.08	38.97(4)	5.03				
[MLH ₂] ³⁺					37.19(8)	4.84	32.48(5)	6.49				
[MLH] ²⁺	23.4(1)		18.06(6)		30.8(1)	6.39	25.54(5)	6.94			-1.7(1)	
[ML] ⁺	20.3(1)	3.1	12.24(3)	5.82	23.4(1)	7.4	17.77(5)	7.77	-5.80(7)			
[MLH ₁]			2.90(6)	9.34								
pM*		17.1		8.4		16.1		10.8		7.5		6.0

amplitude and 100 kHz modulation frequency. Bruker Xenon software (Bruker BioSpin, Rheinstetten, Germany) was used to collect data and for post processing.

2.6.3. UV-Vis Spectroscopy

UV-vis spectra were recorded on Agilent CARY 60 spectrophotometer equipped with a photomultiplier tube detector. Spectra were collected in the wavelength range 200–900 nm with a band width of 5.0 nm and at rate of 200 nm min⁻¹.

3. Results and Discussion

3.1. Physico-Chemical Characterizations

SBA-15 mesoporous silica was synthesized and then functionalized CPTMS and with TETA to obtain SBA-Cl and SBA-TETA (Scheme 1), respectively. The physico-chemical characterizations (SAXS, TEM, FTIR, N₂ adsorption isotherms, TGA) of the obtained samples^[21] are reported in Figure S1 and Table S1, Supporting Information.

Analysis of all SBA-TETA samples by TEM in bright field mode revealed the typical mesoporous structure that resulted mainly characterized by the presence of ordered pore channels (Figure 1). In side view (Figure 1A,B,E,F,I,L) they appeared as parallel channels in bright contrast, whereas the top views of the same samples (Figure 1C,D,G,H,M,N) highlighted the ordered hexagonal array of the pores. The above results point out that all examined samples (before and after Cu²⁺ and Zn²⁺ ions loading)

Table 3. The comparison of theoretical (HySS) and experimental (ICP-AES) results of copper and zinc competition studies.

Metal ion	Experiment 1		Experiment 2		
	Cu [ppm]	Zn [ppm]	Cu [ppm]	Zn [ppm]	
Initial	10.00	10.00	10.00	100.00	
Final ^{a)}	HySS	0.10	0.20	0.08	64.97
	ICP-OES	0.01	1.20	3.20	81.70

^{a)}After 24 h incubation at pH 4 and 25 °C.

share similar structure, being characterized by analogue hexagonal pore array and uniform pore size and no differences concerning their mesoporous structure were observed.

4. Protonation and Metal Complex Equilibria

The stability constants determined in potentiometric titrations can be used in calculating distributions and concentrations of metal species even in complex systems containing many ligands and metal ions, such as biological fluids (e.g., blood serum or gastric juice) and environmental solutions (e.g., sea water or natural water).^[29] Detailed discussions of chemical speciation in various biological fluids and tissues as well as examples of the application of various methods for determining the distribution of trace elements in biological systems are provided.^[30]

The aims of our potentiometric studies are as follows: i) obtaining full descriptions of equilibria, including the distribution of the species in the equilibrium system and determining their characteristics, such as solution structures (binding modes) of the species that are in equilibrium with each other; and ii) using equilibrium descriptions of these systems in modeling calculations to determine the species distributions of the constituents in conditions where experimental measurements cannot obtain data, for example, due to extremely low analytical/total concentrations.

SBA-TETA and SBA-15 were characterized through potentiometric titrations. As shown in Scheme 1, TETA molecule has four amino groups and hence four protonation constants (Table 1). The first two constants, log K₁ and log K₂, are related to the protons bound to the two-terminal primary-amine groups (-NH₂), while log K₃ and log K₄ constants are related to the protonation of the two secondary amine groups (NH). Potentiometric measurements of SBA-15 (Table 1) showed the presence of one protonation constant at pH 10.0 due to the dissociation of silanols (SiOH) into SiO⁻. A more acidic constant, not observed in our experiment, due to the protonation of SiOH into SiOH₂⁺, should occur at pH < 2.^[31]

SBA-TETA has five protonation constants, which can be attributed to the four nitrogen atoms of TETA and to free Si-OH, which may still occur also after SBA-15 functionalization. Indeed, the occurrence of free silanol groups in SBA-TETA

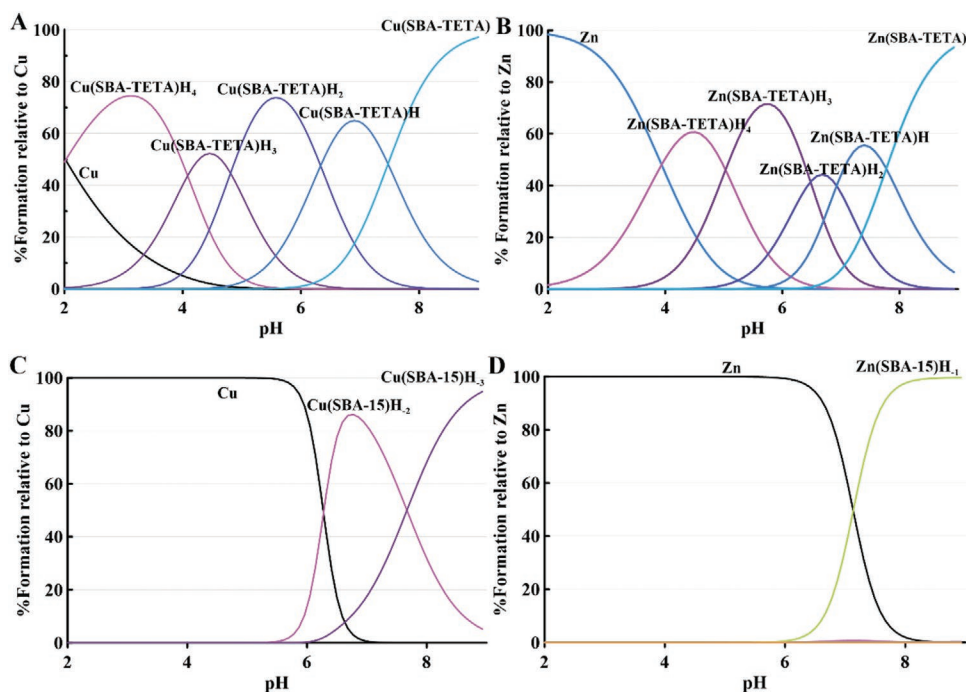


Figure 3. Speciation plots of A,B) SBA-TETA ($[TETA] = 1.00 \times 10^{-4}$ M, $[Cu^{2+}] = 1.00 \times 10^{-4}$ M, and $[Zn^{2+}] = 5 \times 10^{-5}$ M) and C,D) SBA-15 ($[-OH] = 1.00 \times 10^{-3}$ M, $[Cu^{2+}] = 1.00 \times 10^{-4}$ M, and $[Zn^{2+}] = 1 \times 10^{-4}$ M) metal complexes calculated on the basis of stability constants reported in Table 3. Charges are omitted for simplicity.

was confirmed by the FTIR band at 960 cm^{-1} (Figure S2B, Supporting Information). Hence, the highest protonation constants of SBA-TETA could be assigned to Si–OH dissociation ($\log K = 10.6$) and the terminal nitrogen atoms of grafted TETA ($\log K = 10.1; 9.2$), respectively (Table 1). Analogously to free TETA, the remaining two protonation constants ($\log K = 8.2; 5.7$) are assigned to the inner nitrogen atoms. By comparing log K values for free TETA and SBA-TETA a general shift toward higher pH is observed. This shift could be due to the presence of intramolecular hydrogen bonds, which makes proton dissociation more difficult for SBA-TETA compared to the free ligand.^[32]

In a recent pioneering study the pK_a s of ionizable ligands immobilized on nanoparticles (NPs) were determined through potentiometry, and compared with theoretical calculation studies.^[33] It was shown that apparent pK_a s of NP-immobilized ligands were significantly higher than those of the free ligands in solution. The apparent pK_a increased with increasing both NPs and cation size, while decreased with increasing salt concentration (particularly for salt concentration < 0.05 M). Even for very low concentrations of NPs, the local environment of the acid groups determines, through a balance of chemical free energy, electrostatic, van der Waals, steric, and packing interactions, its protonation state. The degree of dissociation was affected by the restriction/immobilization of the –COOH groups on the NPs surface and, possibly, by other factors such as NPs curvature.^[33]

Figure 2 shows the speciation plot of SBA-TETA and SBA-15. At neutral pH SBA-TETA is positively charged ($[(MMs)H_4]^{4+}$), while SBA-15 is not dissociated and remains uncharged.

The copper and zinc complexation by SBA-TETA and SBA-15 was then investigated through potentiometry (Figure 3). Copper complexation starts at very low pH, since at pH 2 about 50% of Cu^{2+} ions are already bound to SBA-TETA (Figure 3A). The log K values of the formed complexes are lower than protonation constants of the free SBA-TETA (Table 2). This suggests the involvement of all dissociated groups in the metal coordination. Above pH 3, the protons of $[Cu(SBA-TETA)H_4]^{5+}$ complex dissociates, and only at pH 9 all nitrogen atoms of TETA ligand are involved in metal chelation. Even at basic pH copper complexes with SBA-TETA remain stable.

The studies of metal complex formation with SBA-TETA were performed at 2:1, 1:1, and 1:2 metal:ligand molar ratios and the obtained results were analyzed with Hyperquad software. Only 1:1 metal:ligand stoichiometry was formed (Table 2) and further confirmed by EPR studies.

HySS program allowed to calculate pM parameter (on the base of $\log \beta$ in Table 2). The higher the pM , the lower the concentration of free M^{n+} in solution. Hence a high pM means a high stability of metal–ligand complexes. The pM value depends on the pH of the aqueous solution. Figure 4 shows that the pM of both Cu^{2+} and Zn^{2+} in the presence of SBA-TETA sharply increases already at pH 4 meaning that copper and zinc can be strongly adsorbed on that functionalized mesoporous silica.

Table 2 reports pM at pH 7.4 for SBA-TETA complexes with copper in comparison with the respective complexes with free TETA ligand. The pCu (=16.1) value for SBA-TETA complexes is slightly lower than the corresponding pCu value of Cu-TETA complexes ($pCu^{TETA} = 17.1$). The lowering of pCu can be caused by the rigidity of the TETA ligand bound to the mesoporous material, which may make difficult obtaining planar copper

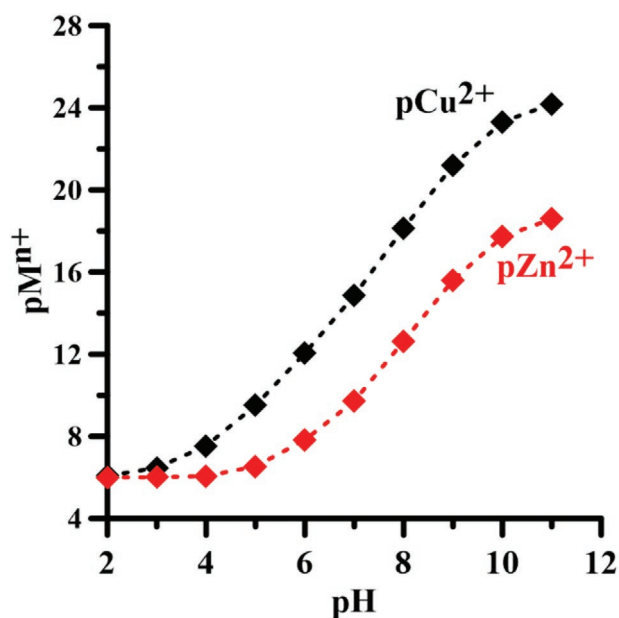


Figure 4. Relationship between pMn^{+} of SBA-TETA and growing pH values.

coordination, which is characteristic for free TETA chelate with copper ions.^[34]

The stoichiometry of zinc complexes is the same of that of copper complexes (metal:ligand = 1:1), although the stability is slightly lower (Table 2). The $[Zn(SBA-TETA)H_4]^{5+}$ complexes start to form above pH 2 and to carry out proton dissociation at pH 4, where only about 50% of zinc ions are bound. The log K values of zinc complexes are lower than respective protonation constants of free ligand and it is likely that all ligand binding sites are involved in the zinc coordination. At the reference pH 7.4, zinc complexes with SBA-TETA ($pZn = 10.8$) are more stable than those with free TETA ($pZn^{TETA} = 8.4$) and in equimolar ligand and metal solution 100% of zinc ions remain bound to SBA-TETA in the pH range 6–9 (Figure 3B). The coordination number and the geometry of zinc complexes depend only on ligand size and charge, while there are no ligand field stabilization effects and nor constraints on complex geometry as in the case of copper complexes.^[35] In most zinc complexes a slightly distorted tetrahedral coordination frequently occurs.^[35] This enhances Lewis acidity of the metal center as well as the acidity of a coordinated water molecule.

In contrast to SBA-TETA, SBA-15 does not form stable complexes neither with copper nor with zinc ions (Figure 2C,D). Only above pH 6, SBA-15 forms weak metal complexes with low stability constants (Table 2). This confirms the importance of TETA grafting on SBA-15 to obtain an effective adsorbent.

4.1. Comparison between the Potentiometric Data and the Data Obtained from the Adsorption Isotherm

In recent studies, the isotherms of copper and zinc ions were studied by means of ICP-OES. The adsorption pH = 4 was chosen after the analysis of speciation diagrams of copper and

zinc hydrolysis (Figure S2, Supporting Information), while at this pH there is no precipitation of copper and zinc hydroxides. 15 mg of SBA-TETA were treated for 24 h at 25 °C with 10 mL solution containing growing concentration of metal ion. The obtained results showed that SBA-TETA adsorbs copper at a higher extent than zinc. Indeed, the maximal adsorbed amounts, are 23.9 and 13.6 mg g⁻¹ for copper and zinc, respectively.^[21] The maximal loading of copper on SBA-TETA is comparable to 29.1 mg g⁻¹ the value obtained by mean of potentiometric titrations (see Figure 3A; pH 4). The slight discrepancy between the two values can be attributed to a higher experimental error of ICP-OES respect to potentiometric measurements. Indeed, the experimental method used before ICP measurements require an additional sample filtration step and do not permit a strict control of pH during metal adsorption process on SBA-TETA.

As far as zinc is concerned, potentiometric measurements (see Figure 3B; pH 4) show the maximum metal loading 18.5 mg g⁻¹. In this case the greatest discrepancy, in addition to the same probable reasons set out above for copper, may be due to the fact that the zinc complex is less stable and perhaps after a treatment period of 24 h, part of complexes hydrolyzes.

4.1.1. Competitive Adsorption of Cu²⁺ and Zn²⁺ on SBA-TETA

Theoretical speciation studies with HySS program^[25] allow to evaluate the competition between two (or more) metal ions for ligand binding sites in solution. This approach was recently used to evaluate the competition between copper and zinc ions toward free TETA.^[20] In this work, speciation studies, carried out by means of HySS software,^[25] were used to evaluate the free metal ion content in the solution after treatment with SBA-TETA (Table 3). The HySS software uses the protonation constants (Table 1) and complexes formation constants (Table 2) of SBA-TETA with both copper and zinc ions but does not consider the formation of mixed SBA-TETA-Cu-Zn complexes. Cu²⁺ ions bind more preferably to SBA-TETA than and Zn²⁺ ions. The results were compared with ICP-AES experimental data in the same ligand and metals concentration conditions.

According to the theoretical competition studies with HySS program (see Section 2.4.1), SBA-TETA in the equimolar metal ion solution, can coordinate both metal ions (Figure 5A) and there are still free metal binding sites (free ligand: (SBA-TETA)H₅, (SBA-TETA)H₄, and (SBA-TETA)H₃, Figure 5A). In the same theoretical calculations with a ten times excess of zinc ions (Figure 5B) all metal binding sites are saturated above pH 4, and the excess of zinc forms Zn(OH)₂ above pH 8. At pH 4 the calculated free copper and zinc concentrations are 0.08 and 64.97 ppm, respectively.

The theoretical calculations were compared with experimental data. In the solution containing 10 ppm metal concentration the remaining free copper content was 0.01 ppm (theoretical calculation 0.10 ppm), while zinc concentration was 1.20 (theoretical calculation 0.2 ppm). In the solution containing a Zn:Cu = 10:1 concentration ratio, 3.2 ppm of copper (theoretical calculation 0.08 ppm) and 81.7 ppm (theoretical concentration 64.97 ppm) of zinc ions remained unbound. The differences

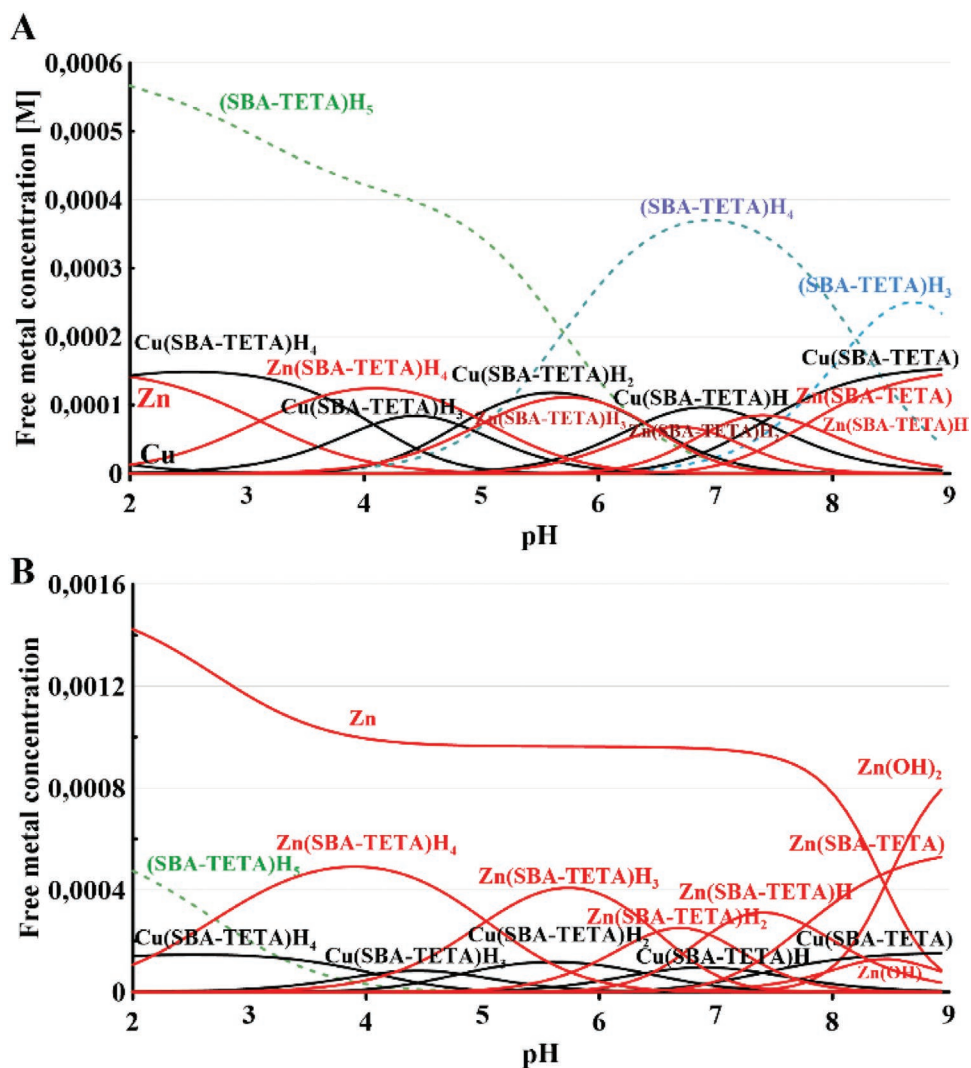


Figure 5. Theoretical competition studies between zinc and copper ions with SBA-TETA calculated with HySS program on the base of the protonation constants (Table 2) and complex formation constants ($\log \beta$) of SBA-TETA in Table 3: A) MMs functionalized with $[TETA] = 7.24 \times 10^{-4} \text{ M}$, $[Cu^{2+}] = 1.57 \times 10^{-4} \text{ M}$ (10 ppm), and $[Zn^{2+}] = 1.53 \times 10^{-4} \text{ M}$ (10 ppm); B) MMs functionalized with $[TETA] = 7.24 \times 10^{-4} \text{ M}$, $[Cu^{2+}] = 1.57 \times 10^{-4} \text{ M}$ (10 ppm), and $[Zn^{2+}] = 1.53 \times 10^{-3} \text{ M}$ (100 ppm).

between theoretical and experimental data are likely due to the experimental errors of ICP-AES measurements (filtration of the samples, high LOQ) without pH control during experiment or due to the formation of mixed SBA-TETA-Cu-Zn complexes with different stability constants. Potentiometry is a highly precise technique and as shown in our studies, can be used for ligand grafting quantification as well as for the determination of surface charge. Next to the metal-complex stability constant data, potentiometry provides the maximum metal loading data. The greatest advantage of potentiometry is the lack of buffer solutions, which influence metal coordination studies by competition with ligand for metal binding sites or/and formation of mixed metal-ligand-buffer complexes.^[36]

The complex formation stability constants provide important data of complex stability and can be used for theoretical competition studies in biological systems (e.g., in human serum competition with Human Serum Albumin), where experimental

data are difficult to obtain. The SC-Database provides access to published stability constants for metal complexes of ≈ 9800 ligands.^[37] and deliver data for competition studies.

4.2. Spectroscopic Metal Complex Characterization

In order to investigate metal coordination sites (previously indicated in the potentiometric studies) and geometry of the zinc and copper complexes, three distinct spectroscopic techniques were used.

4.2.1. Zinc Complex Characterization by ssNMR

NMR spectroscopy is a potent analytical tool for identification of the chemical composition of a given sample.^[38] In this

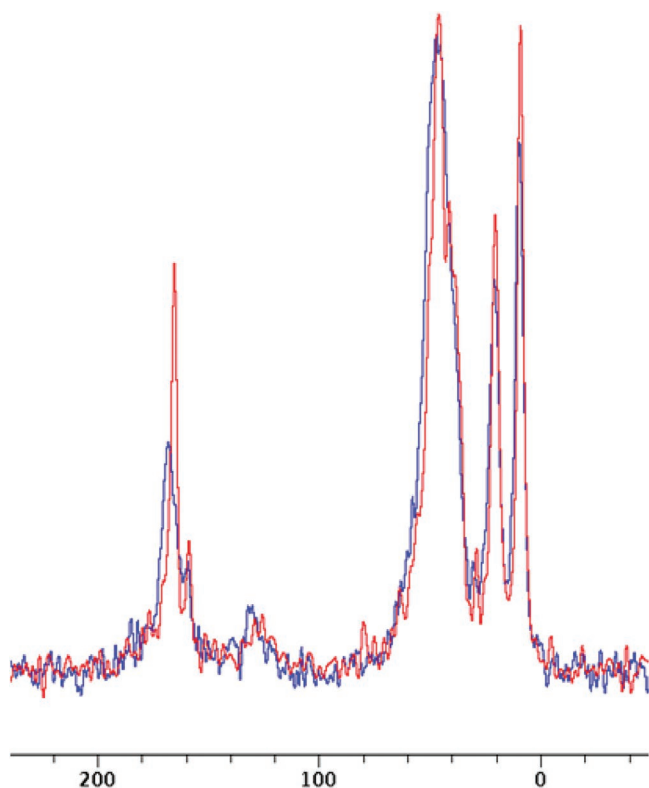


Figure 6. ^{13}C solid state NMR spectra of SBA-TETA (red) before and after Zn^{2+} ion adsorption (blue).

study, we investigate the interaction between Zn^{2+} ions and SBA-TETA, using solid state 400 MHz NMR spectrometers. **Figure 6** shows the NMR spectra of before and after Zn^{2+} ion adsorption. The figure shows clear shift mainly in the peak

observed around 175 ppm proposing that the ion interaction is mainly through the nitrogen sites atoms.

4.2.2. Copper Complex Characterization by EPR

EPR known also as electron spin resonance is a potent tool to probe species with unpaired electrons such as the organic free radicals^[15,39] and the paramagnetic transition metals.^[40–42] EPR is an analog of NMR as it provides chemical and structural information by probing the electron spin rather than the nuclear spin. The existence of unpaired electrons is common as electrons usually paired forming diamagnetic molecules, making EPR superior for selective sites studies. For example one can study the specific binding site of macromolecules such as the heme group in hemoglobin and myoglobin offering a powerful tool to monitor only the active sites in the macromolecules.^[42,43] Moreover, EPR can be used to screen reactions that involve paramagnetic reactive intermediates, elucidate the structure of paramagnetic inorganic molecules, and to determine the oxidation state of transition metal ions.^[41,44] For example, copper can have different oxidation states such as Cu^+ and Cu^{2+} where Cu^+ is d^{10} system with no unpaired electron hence no EPR signal can be observed while Cu^{2+} is d^9 with one unpaired electron that can be detected by EPR spectroscopy. Moreover, EPR spectrum contains information about all interactions of the unpaired electron spin and the magnetic moments of nuclei spin in the vicinity of the electron spin.^[41,45] Thus, EPR spectroscopy is widely used for structural elucidation of inorganic copper complexes and copper enzymes in addition to confirm copper binding with biomolecules. In this study we employed x-band EPR spectroscopy to investigate copper interaction with SBA-TETA. **Figure 7** shows the x-band EPR at 100 K of SBA-TETA after copper adsorption and the

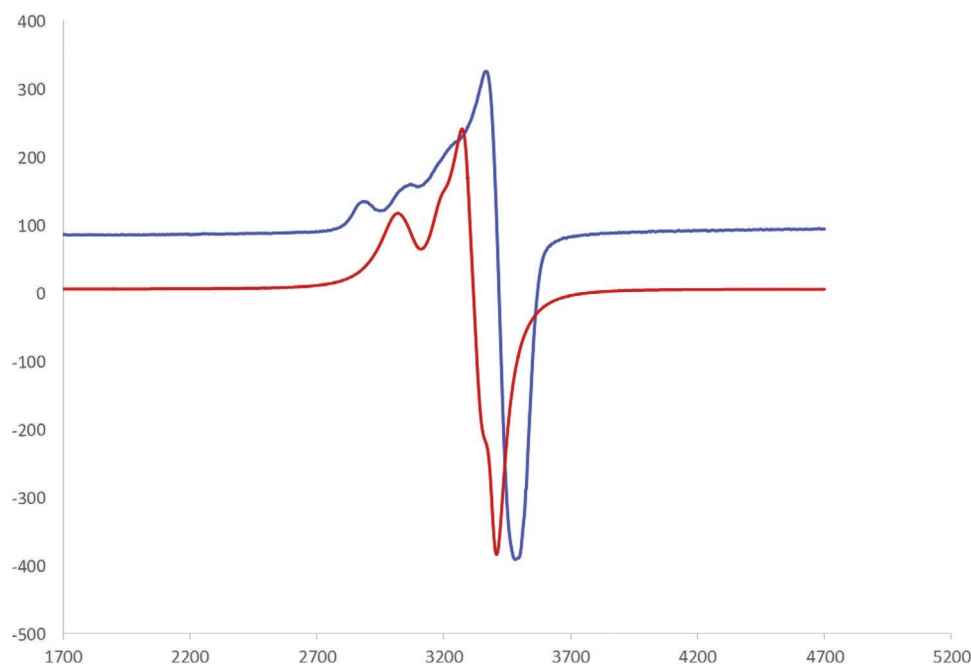


Figure 7. CW EPR spectra of copper-SBA-TETA (blue) and free copper salt (red) recorded at 100 K.

Table 4. EPR parameters of the free copper and copper complexes with SBA-TETA compared with the literature data.^[46]

Assumed composition of the complex	Obtained EPR results			Assumed composition of the complex	Literature EPR results ^{a)}		
	$A_{ } \pm 3, G$	$g_{ } \pm 0.0005$	$g_{\perp} \pm 0.0005$		$A_{ } \pm 3, G$	$g_{ } \pm 0.005$	$g_{\perp} \pm 0.005$
Cu(NO ₃) ₂	170	2.1778	2.1223	Cu(H ₂ O) ₆ ²⁺	117	2.420	2.091
Cu-SBA-TETA	182	2.2306	2.0661	Cu(TETA)Cl ₂	184	2.200	2.072
Cu-SBA-(TETA) ₂ Cl ₂	–	–	–	Cu(TETA) ₂ Cl ₂	164	2.201	2.070

^{a)}Solution of Cu(NO₃)₂ in an ethanol–water mixture (1:1), solution of TETA and CuCl₂ (2:1) in ethanol, solution of TETA and CuCl₂ (4:1) in ethanol, respectively.

copper spectrum of used copper salt ions. The figure shows a clear difference between the free copper salts ions compared with the spectrum of copper-SBA-TETA providing an evidence of copper interaction with SBA-TETA. The results show significant differences of both g -values and hyperfine coupling constant ($A_{||}$) of the copper salt and Cu-SBA-TETA complex (Table 4). The results confirmed that SBA-TETA completely coordinated copper with without any remaining free copper traces.

In order to determine the composition of copper complexes formed on the surface of SBA-TETA, we analyzed the EPR spectra of Cu and Cu/SBA-TETA system (Figure 7). This allowed us to obtain the spin Hamiltonian parameters $g_{||}$, g_{\perp} , and $A_{||}$ for the spectra of copper complexes and to compare them with reference spectra of free TETA with copper ions^[46] (Table 4) found in literature.

The parameters of red line correspond to Cu(NO₃)₂ complex of copper and are consistent with the literature data, while blue line data refer to Cu/SBA-TETA sample obtained with an excess of copper ions (See Section 2.6). The estimated values (Table 4) and a comparison with published data allowed us to suggest that the complex formed on the surface of SBA-TETA has the composition Cu(TETA)Cl₂, while polyamine complexes are not formed. The copper complex has distorted square planar conformation, due to the presence of silanol in the metal coordination core.

4.2.3. Copper Complex Characterization by UV–vis

The comparison of lyophilized samples with the same hydrated samples (and dried under vacuum, see Section 2.6) of SBA-15, SBA-NH₂, and SBA-TETA (Figure S3, Supporting Information) shows clearly the presence of water molecule in the copper coordination shell of all studied samples.

The Cu/SBA-TETA sample has a blue color, Cu/SBA-NH₂ is green, while Cu/SBA-15 does not coordinate copper ions and has pale blue color of Cu(H₂O)₆²⁺ complex (Figure S4, Supporting Information). The UV–vis spectra of Cu/TETA and Cu/SBA-TETA (Figure S4, Supporting Information) show clearly d-d transitions and confirm direct inclusion of copper ions in the amine complex. The λ_{\max} at 440 nm for Cu/TETA system can be attributed to a distorted square planar conformation. In the Cu/SBA-TETA system, the λ_{\max} is shifted to the longer wavelengths due to the presence of Cu–O bond and participation of silanol in metal coordination core.

5. Conclusions

SBA-TETA is a mesoporous material functionalized with TETA copper and zinc chelating agent. SBA-TETA joins versatility of mesoporous materials to load a large amount of cargo, environmental-friendly, and bioavailability, with TETA high efficiency in metal coordination. Such a combination gives an efficient tool for medical diagnostic, theragnostic, or metal clearance, but before being used, SBA-TETA complexes and their water solution equilibria need to be described. Potentiometry technique was used for the first time for ligand content quantification in the SBA-TETA material and for the determination of metal complex formation constants. Moreover, metal complexes were characterized by EPR and ssNMR spectroscopy. The obtained data were compared with classical adsorption studies giving rewarding results. Potentiometry is a fast and economic technique, which can be used for water solution equilibria studies with metal ions and deliver stability data of the formed complexes, which are necessary to establish possible competition reactions with human endogenous molecules and metal ions. In summary, potentiometric studies deliver more precise data of metal coordination studies respect to more popular techniques for the characterization of mesoporous materials and permit theoretical competition studies with other ligands in solution.

Supporting Information

Supporting Information is available from the Wiley Online Library or from the author.

Acknowledgements

A.S. acknowledges financial support from FIR 2019 and MIUR (FFABR 2017).

Conflict of Interest

The authors declare no conflict of interest.

Keywords

electron paramagnetic resonance, metal coordination, nuclear magnetic resonance, potentiometry, speciation diagrams

Received: March 26, 2020

Revised: April 21, 2020

Published online: June 3, 2020

- [1] a) M. Lovell, J. Robertson, W. Teesdale, J. Campbell, W. Markesbery, *J. Neurol. Sci.* **1998**, *158*, 47; b) A. I. Bush, *Trends Neurosci.* **2003**, *26*, 207.
- [2] P. A. Adlard, A. I. Bush, *J. Alzheimer's Dis.* **2006**, *10*, 145.
- [3] J. L. Vivero-Escoto, R. C. Huxford-Phillips, W. Lin, *Chem. Soc. Rev.* **2012**, *41*, 2673.
- [4] K. S. Siddiqi, A. Husen, S. S. Sohrab, M. O. Yassin, *Nano. Res. Lett.* **2018**, *13*, 231.
- [5] a) G. Liu, P. Men, P. L. Harris, R. K. Rolston, G. Perry, M. A. Smith, *Nano Lett.* **2006**, *406*, 189; b) G. Liu, P. Men, G. Perry, M. A. Smith, in *Progress in Brain Research*, Vol. 180, Elsevier, New York **2009**, p. 97.
- [6] D. McLachlan, T. P. Kruck, W. J. Lukiw, S. S. Krishnan, *Can. Med. Assoc. J.* **1991**, *145*, 793.
- [7] a) C. Loske, A. Gerdemann, W. Schepl, M. Wycislo, R. Schinzel, D. Palm, P. Riederer, G. Münch, *Eur. J. Biochem.* **2000**, *267*, 4171; b) C. W. Ritchie, A. I. Bush, A. Mackinnon, S. Macfarlane, M. Mastwyk, L. MacGregor, L. Kiers, R. Cherny, Q.-X. Li, A. Tammer, *Arch. Neurol.* **2003**, *60*, 1685.
- [8] G. Liu, P. Men, W. Kudo, G. Perry, M. A. Smith, *Nano Lett.* **2009**, *455*, 187.
- [9] I. W. Hamley, *Chem. Rev.* **2012**, *112*, 5147.
- [10] L. Miller, G. Winter, B. Baur, B. Witulla, C. Solbach, S. Reske, M. Lindén, *Nanoscale* **2014**, *6*, 4928.
- [11] J. E. Lee, N. Lee, T. Kim, J. Kim, T. Hyeon, *Acc. Chem. Res.* **2011**, *44*, 893.
- [12] L. Yi, T. Wu, W. Luo, W. Zhou, J. Wu, *Neural Regener. Res.* **2014**, *9*, 69.
- [13] a) Q. He, Z. Zhang, F. Gao, Y. Li, J. Shi, *Small* **2011**, *7*, 271; b) X. He, H. Nie, K. Wang, W. Tan, X. Wu, P. Zhang, *A Chemistry* **2008**, *80*, 9597.
- [14] S. Bhattacharyya, M. Dixit, *Dalton Trans.* **2011**, *40*, 6112.
- [15] S. Al-Harathi, J. I. Lachowicz, M. E. Nowakowski, M. Jaremko, Ł. Jaremko, *J. Inorg. Biochem.* **2019**, *198*, 110716.
- [16] D. C. Crans, *Coord. Chem. Rev.* **2017**, *352*, 398.
- [17] D. L. Suarez, S. Goldberg, C. Su, *Mineral-Water Interfacial Reactions*, Vol. 715, ACS Symposium Series, American Chemical Society, Washington, DC **1998**, pp. 136–178.
- [18] T. de F. Paulo, H. D. Abruña, I. C. N. Diógenes, *Langmuir* **2012**, *28*, 17825.
- [19] P. W. Schindler, in *Metal Ions in Biological Systems*, Vol. 18, Marcel Dekker Inc., New York/Basel **1984**, p. 105.
- [20] V. M. Nurchi, G. Crisponi, M. Crespo-Alonso, J. I. Lachowicz, Z. Szewczuk, G. J. Cooper, *Dalton Trans.* **2013**, *42*, 6161.
- [21] J. I. Lachowicz, G. R. Delpiano, D. Zanda, M. Piludu, E. Sanjust, M. Monduzzi, A. Salis, *J. Environ. Chem. Eng.* **2019**, *7*, 103205.
- [22] L. Medda, M. F. Casula, M. Monduzzi, A. Salis, *Langmuir* **2014**, *30*, 12996.
- [23] a) W. Wu, W. Guo, Z. Ji, Y. Liu, X. Hu, Z. Liu, *J. Dispersion Sci. Technol.* **2018**, *39*, 594; b) M. Barczak, *J. Solid State Chem.* **2018**, *258*, 232.
- [24] G. Gran, *Analyst* **1952**, *77*, 661.
- [25] L. Alderighi, P. Gans, A. Ienco, D. Peters, A. Sabatini, A. Vacca, *Coord. Chem. Rev.* **1999**, *184*, 311.
- [26] A. Albert, E. P. Serjeant, *Ionization Constants of Acids and Bases: A Laboratory Manual*, Methuen, London **1962**.
- [27] T. Kiss, É. A. Enyedy, T. Jakusch, *Coord. Chem. Rev.* **2017**, *352*, 401.
- [28] I. Nagypal, M. Beck, *Coord. Chem. Rev.* **1982**, *43*, 233.
- [29] A. E. Martell, R. J. Motekaitis, *Determination and Use of Stability Constants*, VCH publishers, Hoboken, NJ **1992**.
- [30] G. Berthon, *Handbook of Metal-Ligand Interactions in Biological Fluids*, Marcel Dekker, NY **1995**.
- [31] Z. Wu, D. Zhao, *Chem. Commun.* **2011**, *47*, 3332.
- [32] J. I. Lachowicz, V. M. Nurchi, G. Crisponi, M. de Guadalupe Jaraquemada-Pelaez, M. Ostrowska, J. Jezierska, E. Gumienna-Kontecka, M. Peana, M. A. Zoroddu, D. Choquesillo-Lazarte, *J. Inorg. Biochem.* **2015**, *151*, 94.
- [33] D. Wang, R. J. Nap, I. Lagzi, B. Kowalczyk, S. Han, B. A. Grzybowski, I. Szleifer, *J. Am. Chem. Soc.* **2011**, *133*, 2192.
- [34] P. Comba, S. P. Gavrish, Y. D. Lampeka, P. Lightfoot, A. Peters, *J. Chem. Soc., Dalton Trans.* **1999**, *1999*, 4099.
- [35] R. R. Crichton, *Biological Inorganic Chemistry: A New Introduction to Molecular Structure and Function*, Elsevier, NY **2012**.
- [36] M. T. Beck, I. Nagypál, *Chemistry of Complex Equilibria*, Vol. 30, Akadémiai Kiadó, Budapest **1990**, p. 141.
- [37] SCQuery, The IUPAC Stability Constants Database, Academic Software (Version 5.5), Royal Society of Chemistry, Cambridge **1993**, 2005.
- [38] a) P. Westermark, U. Engström, K. H. Johnson, G. T. Westermark, C. Betsholtz, *Proc. Natl. Acad. Sci. USA* **1990**, *87*, 5036; b) D. F. Moriarty, D. P. Raleigh, *Biochemistry* **1999**, *38*, 1811.
- [39] a) S. M. Mattar, A. H. Emwas, *Chem. Phys. Lett.* **2003**, *368*, 724; b) S. M. Mattar, A. H. Emwas, L. A. Calhoun, *J. Phys. Chem. A* **2004**, *108*, 11545; c) J. Al-Nu'airat, B. Z. Dlugogorski, I. Oluwoye, X. Gao, M. Altarawneh, *Proc. Combust. Inst.* **2019**, *37*, 3091; d) G. Fang, X. Chen, W. Wu, C. Liu, D. D. Dionysiou, T. Fan, Y. Wang, C. Zhu, D. Zhou, *Environ. Sci. Technol.* **2018**, *52*, 14352; e) S. M. Mattar, A. H. Emwas, A. D. Stephens, *Chem. Phys. Lett.* **2002**, *363*, 152.
- [40] a) S. M. Mattar, A. D. Stephens, A. H. Emwas, *Chem. Phys. Lett.* **2002**, *352*, 39; b) A. H. M. Emwas, Z. A. Al-Talla, X. Guo, S. Al-Ghamdi, H. T. Al-Masri, *Magn. Reson. Chem.* **2013**, *51*, 255; c) S. Ghosh, V. Garcia, K. Singewald, S. M. Damo, S. Saxena, *Appl. Magn. Reson.* **2018**, *49*, 1299; d) T. Matsuo, T. Kono, I. Shobu, M. Ishida, K. Gonda, S. Hirota, *Chem. - Eur. J.* **2018**, *24*, 2767.
- [41] H. Liang, C. Xia, A.-H. Emwas, D. H. Anjum, X. Miao, H. N. Alshareef, *Nano Energy* **2018**, *49*, 155.
- [42] X.-C. Su, J.-L. Chen, *Acc. Chem. Res.* **2019**, *52*, 1675.
- [43] a) F. Alahmari, B. Davaasuren, A.-H. Emwas, P. M. Costa, A. Rothenberger, *Inorg. Chim. Acta* **2019**, *488*, 145; b) L. M. Moreira, A. L. Poli, J. P. Lyon, F. Aimbire, J. C. Toledo Jr, A. J. Costa-Filho, H. Imasato, *J. Porphyrins Phthalocyanines* **2010**, *14*, 199.
- [44] D. A. Svistunenko, J. Dunne, M. Fryer, P. Nicholls, B. J. Reeder, M. T. Wilson, M. G. Bigotti, F. Cutruzzola, C. E. Cooper, *Biophys. J.* **2002**, *83*, 2845.
- [45] a) H. Ouellet, K. Rangelova, M. LaBarre, J. B. Wittenberg, B. A. Wittenberg, R. S. Magliozzo, M. Guertin, *J. Biol. Chem.* **2007**, *282*, 7491; b) A. Tyryshkin, S. Dikanov, E. Reijerse, C. Burgard, J. Hüttermann, *J. Am. Chem. Soc.* **1999**, *121*, 3396; c) E. G. Evans, M. J. Pushie, K. A. Markham, H.-W. Lee, G. L. Millhauser, *Structure* **2016**, *24*, 1057.
- [46] Y. Shenberger, A. Shimshi, S. Ruthstein, *J. Phys. Chem. B* **2015**, *119*, 4824.

**ADVANCED
MATERIALS**
INTERFACES

Supporting Information

for *Adv. Mater. Interfaces*, DOI: 10.1002/admi.202000544

Improving Metal Adsorption on Triethylenetetramine (TETA) Functionalized SBA-15 Mesoporous Silica Using Potentiometry, EPR and ssNMR

Joanna Izabela Lachowicz, Abdul-Hamid Emwas, Giulia Rossella Delpiano, Andrea Salis, Marco Piludu, Lukasz Jaremko, and Mariusz Jaremko**

SUPPORTING INFORMATION

Improving metal adsorption studies on functionalized nanomaterials using potentiometry, EPR and ssNMR. The SBA-TETA case study.

*Joanna Izabela Lachowicz*¹, Abdul-Hamid Emwas², Giulia Rossella Delpiano³, Andrea Salis³, Marco Piludu⁴, Lukasz Jaremko⁵ and Mariusz Jaremko*⁵.*

¹Department of Medical Sciences and Public Health, University of Cagliari, Cittadella Universitaria, 09042 Monserrato, Italy

²Core Labs, King Abdullah University of Science and Technology (KAUST), 23955-6900 Thuwal, Saudi Arabia.

³Department of Chemical and Geological Sciences, University of Cagliari, Cittadella Universitaria, 09042 Monserrato, Italy

⁴Department of Biomedical Sciences, University of Cagliari, Cittadella Universitaria, 09042 Monserrato, Italy

⁵Division of Biological and Environmental Sciences and Engineering (BESE), King Abdullah University of Science and Technology (KAUST), 23955-6900 Thuwal, Saudi Arabia.

Small angle X-ray scattering (SAXS) pattern, reporting the scattering intensity as a function of the scattering vector q (\AA^{-1}), of SBA-15, is typical of hexagonal phases with an intense peak relative to the reflections of the planes 100, and two less intense peaks due to 110 and 200 planes. The structural order is maintained after the functionalization, showing a value of the lattice parameter a , around 107-110 \AA . N_2 adsorption/desorption isotherms at 77 K, allowed to measure the surface area (S_{BET}) which was 813 m^2/g for SBA-15, and 373 m^2/g for SBA-TETA. The mean pore diameter was 61.4 \AA for SBA-15 and 51.4 \AA for SBA-TETA. The specific surface area (S_{BET}), pore volume (V_p) and the mean pore diameter (d_p) values are reported in Table S1. Thermogravimetric analysis (TGA) of SBA-15, SBA-Cl and SBA-TETA samples confirm the successful functionalization of SBA-15 with TETA chelating agent. TGA also allowed to estimate the amount of TETA ligand grafted on SBA-15 which was 134 mg/g (Table S1).

Fourier transform infrared spectroscopy (FTIR) confirmed the successful functionalization of SBA-15 with CPTMS and TETA ligand^[1]. In particular, the band at 1650 cm^{-1} is assigned to $-\text{NH}_2$ bending).

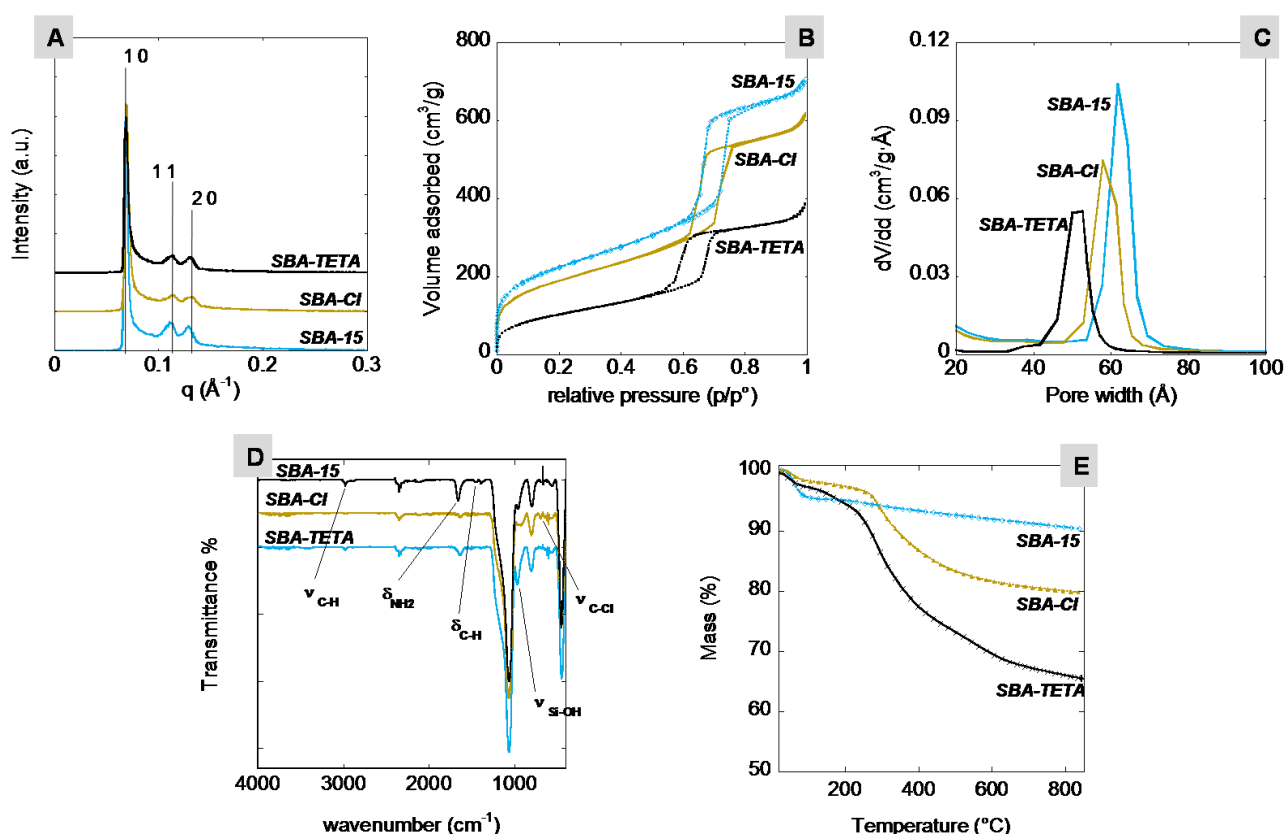


Figure S1. Characterization of SBA-15, SBA-Cl, and SBA-TETA mesoporous silica samples. A) SAXS patterns. B) N_2 -adsorption/desorption isotherms. C) Pore size distribution calculated (BJH method) from the desorption branch. D) FTIR spectra. E) Thermogravimetric analysis.

Table S1. Structural and textural data of the synthesized samples.

Sample	^a S _{BET} (m ² /g)	^b V _p (cm ³ /g)	^c d _p (Å)	^d a (Å)	^e Δm (%)		^g L(mg/g)
					< 200 °C	>200 °C	
SBA-15	813.40	1.007	61.4	108 ± 4	4.5	5.0	-
SBA-Cl	667.14	0.937	57.8	110 ± 5	2.8	18.5	135
SBA-TETA	373.15	0.597	51.4	107 ± 3	2.9	31.9	134 (124*)

^aSurface area calculated by the BET method. ^bPore volume from the desorption branch calculated at p/p°=0.99 by BJH method. ^cPore diameter from the desorption branch calculated by BJH method. ^dLattice parameter obtained by SAXS $a = d \cdot 2/(3)^{0.5} \cdot (h^2 + k^2 + hk)^{0.5}$; *data obtained by potentiometric titration.

Potentiometric titrations also allowed the determination of TETA loading, that is the amount (mg) of TETA grafted per g of SBA-15. Considering 0.002 mmol of TETA (MW=146.23 g/mol) grafted on 2.4 mg SBA-TETA a TETA loading of 124 mg/g was obtained. This value is consistent with that obtained by TGA (134 mg/g, see Table 1). Moreover, the obtained TETA loadings corresponds to 5.13 % (from TGA) and 4.76 % (g/g) (from potentiometric titration) of nitrogen, which can be compared with 4.9 % (g/g) obtained through elemental analysis data (see Table S1).

Table S2 Valori di pK_a degli ioni ammonio derivanti dal TETA (25 °C). Tra parentesi i valori di incertezza sull'ultima cifra.

Reazione	pK_a
$\text{TETA-H}_4^{4+} \rightleftharpoons \text{TETA-H}_3^{3+} + \text{H}^+$	3,28(2)
$\text{TETA-H}_3^{3+} \rightleftharpoons \text{TETA-H}_2^{2+} + \text{H}^+$	6,28(2)
$\text{TETA-H}_2^{2+} \rightleftharpoons \text{TETA-H}^+ + \text{H}^+$	9,11(4)
$\text{TETA-H}^+ \rightleftharpoons \text{TETA} + \text{H}^+$	9,79(5)

Table S3. Mass percentages of C, H and N in synthesized mesoporous siliceous samples.

Sample	% C (mass)	% C (mol)	% H (mass)	% H (mol)	% N (mass)	% N (mol)	C:Nratio ^a
SBA-15	0.38	0.0316	0.47	0.466	-	-	-
SBA-TETA	12.04	1.002	1.07	1.062	4.90	0.350	2.9:1 (2.25:1)

^a% molar ratio between C and N. In brackets the theoretical mol ratio.

Table S3 shows the percentages in mass (% g element / material) and in moles (% mol element / g material) of the elements C, H and N in the synthesized materials.

In the aminopropyl group of SBA-Cl, the theoretical ratio C: N is 3: 1 and the ratio actually measured is 3.2: 1 (0.366: 0.116, very close to the theoretical one). In the triethylenetetraminopropyl group present in the SBA-TETA (obtained from SBA-Cl), the ratio C: N is 9: 4 (i.e. 2.25: 1) and that actually measured is \approx 2.9 : 1 (1.002: 0.350, slightly close to the theoretical one). It can be concluded that the molar ratio between C and N has essentially been maintained. This is proof of the success of the grafting of these groups during the functionalization process. The quantity of SBA-TETA subjected to elemental analysis was 2.8 mg. The molar ratio between N and the TETA group is 4: 1, therefore considering the % in moles of N (0.350), in 2.8 mg of material the % in moles of TETA is equal to 0.0875. By a simple calculation:

$0.0875 \text{ mol}_{\text{TETA}} : 100 \text{ g} = x \text{ mol}_{\text{TETA}} : 0.0028 \text{ g}$, from which $x = 2.45 \cdot 10^{-6} \text{ mol}_{\text{TETA}}$ ($2.45 \cdot 10^{-3} \text{ mmol}_{\text{TETA}}$)

From this analysis the amount of TETA in the sample is equal to 0.875 mmol / g, or 128 mg / g, considering the molar mass of the TETA equal to 146.235 mg / mmol.

Hydrogen occurs both in the functionalizing groups and in the silanols that have not reacted and its percentage has not been considered in the previous calculations. In theory, the sample of SBA-15, whose structure is only siliceous (consisting only of Si, O and H), should not contain C; the small percentage of this element is substantially likely due to possible traces of the surfactant used as templating agent not perfectly removed from the material during the calcination.

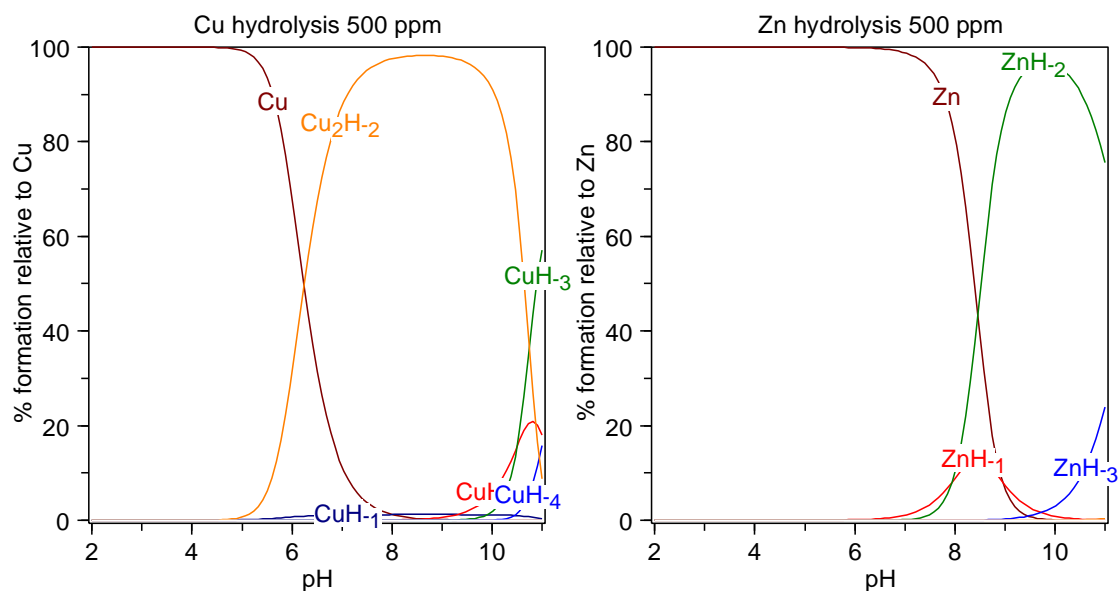


Figure S2. Speciation plots of copper and zinc ions hydrolysis in water. The constants for the Zn^{2+} and Cu^{2+} hydroxides at 25 °C and 0.1 M ionic strength, taken from Baes and Mesmer [Baes Jr, C.; Mesmer, R., *The Hydrolysis of Cations*. *RE Krieger, Malabar, Wiley, New York, 1976, 1986.*]. Charges are omitted for simplicity.

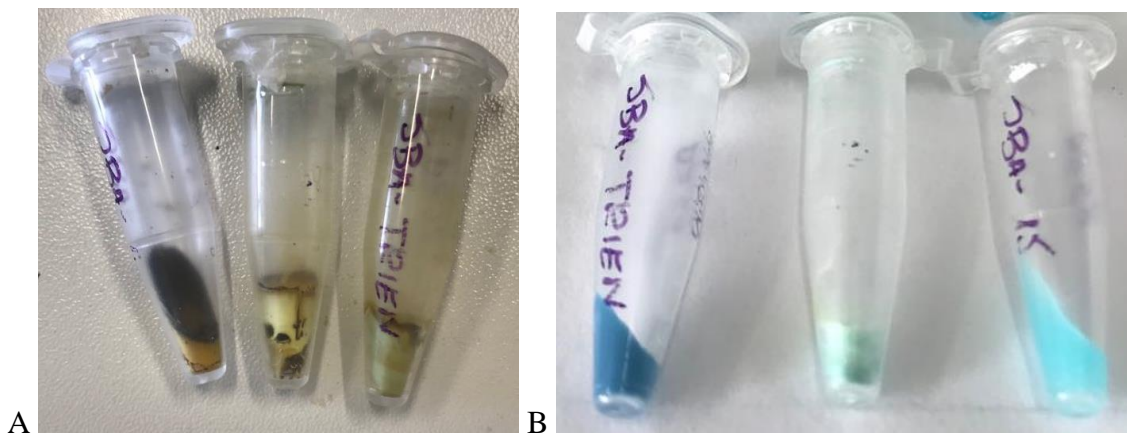


Figure S3. A) Lyophilized materials of (from left to right): SBA-15, SBA-NH₂ and SBA-TETA;
B) Re-hydrated materials of (from left to right): SBA-TETA, SBA-NH₂ and SBA-15.

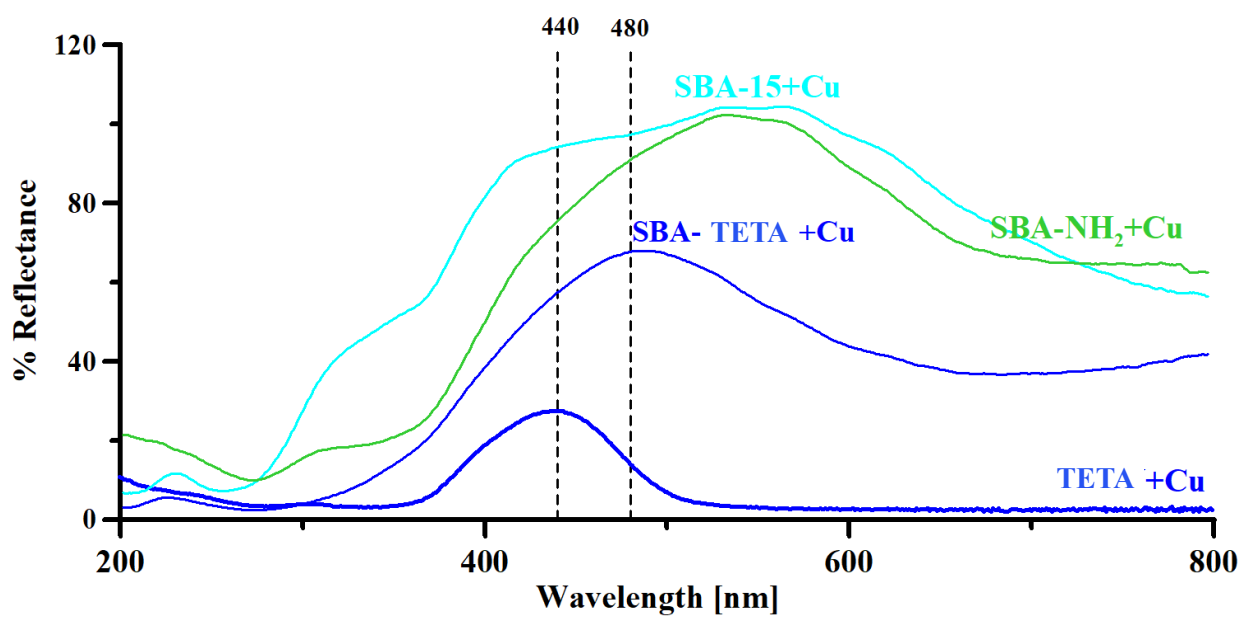


Figure S4. UV-Vis reflectance spectra of copper complexes with SBA-15, SBA-NH₂ and SBA-TETA, compared with complex of copper with free TETA ligand.

References

- [1] R. Hossain, R. K. Nekouei, I. Mansuri, V. Sahajwalla, ACS Sustainable Chemistry & Engineering 2018, 7, 1006.

Paper III *(submitted)*

***Grafting of 2,8-dithia-5-aza-2,6-pyridinophane macrocycle on
SBA-15 mesoporous silica for removal of Cu²⁺ and Cd²⁺ ions
from aqueous solutions: synthesis, adsorption, and complex
stability studies***

Giulia Rossella Delpiano¹, Alessandra Garau¹, Vito Lippolis¹, Joanna Izabela Lachowicz^{2,} and
Andrea Salis^{1,3,*}.*

¹*University of Cagliari, Department of Chemical and Geological Science, Cittadella Universitaria,
09042 Monserrato-Cagliari, Italy*

²*University of Cagliari, Department of Medical Sciences and Public Health, Cittadella Universitaria,
09042 Monserrato-Cagliari, Italy*

³*Consorzio Interuniversitario per lo Sviluppo dei Sistemi a Grande Interfase (CSGI), via della
Lastruccia 3, 50019, Sesto Fiorentino (FI), Italy. Unità Operativa University of Cagliari, Italy.
Cittadella Universitaria, SS 554 bivio Sestu, 09042 Monserrato (CA), Italy*

Abstract

Silica-based mesoporous materials have received growing attention in the metal recovery from industrial processes, although in general, the adsorption of metal ions by silanols is rather poor. Nevertheless, a great improvement of metal ions removal from aqueous solutions can be achieved by grafting metal-chelators on the particles' surface. Combining metal-chelating properties of organic ligands, with high surface area of mesoporous silica particles make these hybrid nanostructured materials a new horizon in metal recovery, sensing and controlled storage of metal ions in industrial and mining processes. Here, 2,8-dithia-5-aza-2,6-pyridinophane (L) macrocycle was grafted on SBA-15 mesoporous silica to obtain SBA-L mesoporous adsorbent for the removal of Cd^{2+} and Cu^{2+} ions from aqueous solution in a broad pH range (4-11). By grafting about 0.3 mmol/g of L on SBA-15 a maximum loading capacity of 20.9 mg/g and 31.8 mg/g was obtained for Cu^{2+} and Cd^{2+} , respectively. The adsorption kinetics can be described with the pseudo-second order model while the adsorption isotherm (298 K) follows the Langmuir model. The latter, together with potentiometric studies suggested that the adsorption mechanism is based on metal chelation by the grafted macrocycle. Finally, an almost complete metal recovery can be achieved at pH 1.

Keywords

Functionalized ordered mesoporous silica; azathiamacrocycles; metal complexes; potentiometry, speciation diagrams, adsorption isotherm

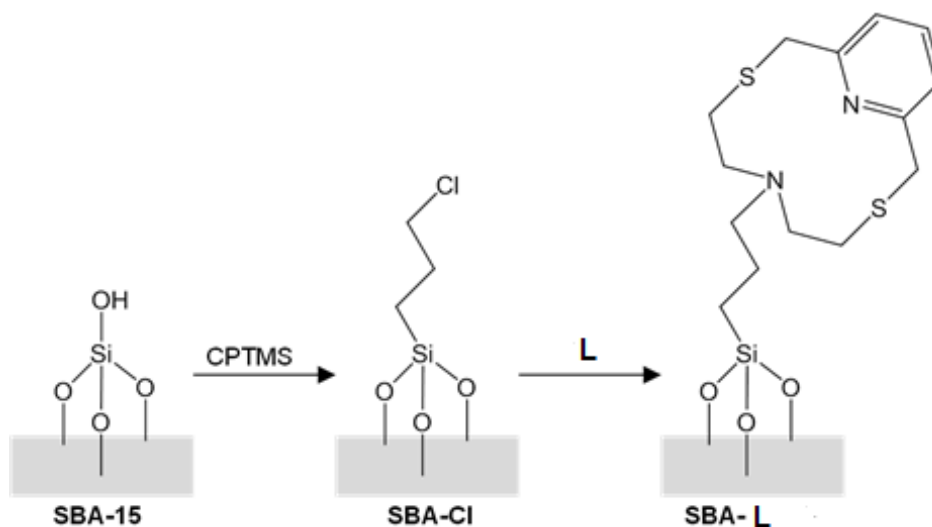
1. Introduction

Heavy metals and their ionic forms can be toxic for the environment and living organisms even at very low concentrations^[1]. For this reason, their uncontrolled release in the soil or surface waters should be avoided.

Industry and mining are the main sources of metal contamination, particularly of water-soluble metal ions. Once in water metal ions can be easily assumed by living organisms, thus interfering with their biological processes. Moreover, the accumulation in the human organism of heavy metal ions has been recognized as the source of several diseases^[2]. The expansion of new metal-based technologies, for instance electronics for Information Technology (IT), mining and processing of metal ions worldwide^[3], is increasing the risks deriving from heavy metal pollution. In addition, the rapid development of industrial processes gives rise to the obtainment of new types of contaminating wastes for which conventional purification treatments (such as coagulation, precipitation, filtration, and others) are not effective. In order to limit and possibly invert this negative trend, new fast, effective, and economic methods for metal ions removal from the environment are needed. Moreover, once recovered, metal ions can be reused according to the principles of the circular economy^[4]. Over the years, several materials have been considered for metal ions recovery^[5]. In particular, ordered mesoporous silicas (OMS) have high surface areas, tuneable pore sizes, low toxicity and can be easily functionalized. Among several applications in the field of heterogeneous catalysis^[6] and biocatalysis^[7], functionalized OMS have been used as adsorbents for the effective removal of numerous organic pollutants^[8] as well as metal ions^[9].

Grafting metal-chelating ligands on OMS surface is a promising way in obtaining effective metal ion adsorbents^[10, 11], with the possibility of metal recovery by changing the system conditions (e.g. pH, solvent, temperature, etc.). Moreover, functional OMS are a new frontier in selective metal sensing, and some examples of effective silica-modified electrodes for electrochemical detection of organic pollutants and metal ions have been recently reported^[12].

Among hundreds of known metal-chelating molecules, macrocycle ligands are particularly interesting due to their ability to bind alkaline earth, transition (particularly heavy) metals both in water and organic solvents on changing their molecular structure and nature of donor atoms^[13, 14]. The ligand-metal binding property is mainly provided by the presence of electron-donor atoms with appropriate soft-hard properties, while metal selectivity can be modulated by the macrocycle ring size and conformation properties^[13]. Aromatic rings, often introduced into a macrocycle to provide a structurally rigid moiety, are important factors for the coordination chemistry of azacrown compounds, especially with small-size polyamines^[15]. For instance, Blake et al.^[16] studied extensively the coordination properties towards the “borderline” and “soft” metal ions Cu^{2+} , Zn^{2+} , Cd^{2+} , Hg^{2+} , and Pb^{2+} , of the pyridine based, N_2S_2 -donating 12-membered macrocycle 2,8-dithia-5-aza-2,6-pyridinophane (hereafter referred also as **L**). Their results showed that 1:1 complexes with Cu^{2+} and Hg^{2+} are the most stable, while at the same time **L** displays a higher binding ability for Cd^{2+} and Pb^{2+} with respect to Zn^{2+} , due to the presence of the soft S-donors.



Scheme 1. Schematic representation of 2,8-dithia-5-aza-2,6-pyridinophane (**L**) ligand grafting on SBA-15 mesoporous material. CPTMS=(3-chloropropyl)trimethoxysilane,

Here the macrocycle **L** was grafted on SBA-15 to give SBA-L adsorbent according to Scheme 1. The aim of this work was to exploit the ligand-metal chelating property to create an innovative and

reusable adsorbent for the effective metal ions removal from aqueous solutions. The chelating ability of SBA-L toward Cu^{2+} and Cd^{2+} was determined by means of potentiometric studies, as well as by determining the adsorption kinetics and isotherms. In addition, we present the best conditions for the full recovery of these metal ions from the SBA-L mesoporous adsorbent.

2. Experimental Section

2.1. Chemicals

Pluronic copolymer P123 (EO₂₀PO₇₀EO₂₀) tetraethylorthosilicate, TEOS ($\geq 99\%$); (3-chloropropyl)trimethoxysilane, CPTMS ($\geq 97\%$); copper(II) chloride dihydrate, $\text{CuCl}_2 \cdot 2\text{H}_2\text{O}$ ($\geq 99.0\%$), cadmium(II) chloride CdCl_2 ($\geq 99.0\%$), toluene ($\geq 99.7\%$), dimethylformamide (DMF, $\geq 99.9\%$), Anhydrous Acetaldehyde ($>99\%$), Diethyl ether (99.8%), ethanol (99.8%), acetone ($\geq 99\%$), HCl (37%), NaCl, NaOH pellets, ammonium, oxalyldihydrazide ($>98\%$) were purchased from Sigma-Aldrich (Milano, Italy). Diethyl ether (99.8%), and ethanol (99.8%) were purchased from Honeywell. Acetonitrile (MeCN) was distilled over CaH_2 . Copper and Cadmium stock Normex solutions (1000 ppm in HNO_3 2% m/m) were Carlo Erba products.

A previously described method was used in the preparation of 0.1 M carbonate free KOH solution^[17]. L and SBA-L solutions were acidified with stoichiometric equivalents of HCl. Metal solutions were prepared by dissolving the required amount of metal salt in pure double distilled water, to which a stoichiometric amount of HCl was previously added to prevent hydrolysis. These solutions were standardized by the complexometric method with EDTA and proper indicators.

2.2. Synthesis of L, SBA-15 and SBA-L

2,8-dithia-5-aza-2,6-pyridinophane (L) was prepared according to the previously described procedure^[16]. The synthesis of SBA-15 mesoporous silica and its functionalization with (3-chloropropyl)trimethoxysilane (CPTMS) were performed according to our previous work^[18]. Then,

a mass of 100 mg of SBA-Cl was dispersed in 25 mL of anhydrous acetonitrile, with 93 mg of K_2CO_3 and 40 mg of L. The resulting suspension was kept under stirring at 90°C for 48h under nitrogen atmosphere. SBA-L was collected by filtration, washed with acetonitrile, dichloromethane and water, and dried under vacuum overnight. The liquid phase was treated to recover the unreacted L.

2.3. Physico-Chemical Characterizations

The structural characterization of SBA-15 was performed by small-angle X-rays scattering (SAXS) and Transmission Electron Microscopy (TEM) analysis. SAXS patterns were recorded with a S3-MICRO SWAX camera system (Hecus X-ray System, Graz, Austria). $CuK\alpha$ radiation of wavelength 1.542Å was provided by a Genix X-ray generator, operating at 30 kV and 0.4 mA. TEM analysis of was performed with a Jeol JEM 1400 Plus, operating at 120 kV. The textural parameters of the materials such as the surface area (Brunauer-Emmett-Teller, B.E.T.), pore size distribution (Barrett-Joyner-Halenda, B.J.H.) were determined by N_2 adsorption/desorption isotherms at 77 K carried out on an ASAP 2020 instrument. FTIR spectroscopy was carried out through a Bruker Tensor 27 spectrophotometer equipped with a diamond-ATR accessory and a DTGS detector. A number of 128 scans with a resolution of 2 cm^{-1} were averaged in the spectral range $4000\text{ cm}^{-1} - 400\text{cm}^{-1}$. Thermogravimetric Analysis (TGA) using a STA6000 - Perkin Elmer in the 25–850°C range, under oxygen flow (heating rate = $10^\circ\text{C}/\text{min}$; flow rate = 40 mL min^{-1}).

2.4. Quantitative analysis of Cd^{2+} and Cu^{2+} concentrations in water

Cd^{2+} concentrations in aqueous solutions were analysed by inductively coupled plasma optical emission spectroscopy (ICP-OES). The operational parameters were as follows: RF Power: 1.2 kW. Plasma gas: 12 L min^{-1} , Aux gas: 1.0 L min^{-1} , Nebulizer flow 0.7 L min^{-1} . Emission lines (nm): Cd (214.439, 226.502 and 228.802). Ar (419.832 and 737.212) was used as internal standard. No spectral

interference was observed. The standard solutions ranging from 0.01 to 300 mg/L in 1% nitric acid were prepared by the analytical dilution of Normex standard cadmium solutions. LOD was determined at 0.05 mg/L. Cu^{2+} concentrations in aqueous solutions were analysed through a colorimetric method^[19]. Briefly, the coloured adduct of Cu^{2+} with oxalyldihydrazide was formed at pH 9 upon mixing Cu^{2+} solution with citric acid, ammonium hydroxide, acetaldehyde and oxalyldihydrazide. The absorbance of the solutions was measured at 540 nm after 30 min incubation in the dark.

2.5. Determination of adsorption kinetics and isotherms

The adsorption kinetics of Cu^{2+} or Cd^{2+} on SBA-L were carried out by suspending 15 mg of mesoporous adsorbent in 10 mL of 5 mg L⁻¹ (for copper) and 3.5 mg L⁻¹ (for cadmium) of metal solution for time intervals ranging from 2 min to 24 h at pH 5 (for copper solutions) and pH 7 (for cadmium solutions). All samples were kept under rotation (22 rpm) at 298 K. The process was then stopped, and the solution was filtered through Ø 0.2 µm syringe cellulose filter (Minisart Syringe Filter). For the isotherm studies, mesoporous materials were treated with metal ion solutions of variable concentration, ranging from 0.5 to 300 mg L⁻¹; the reactions were stopped after 5h. The residual copper and cadmium concentrations in the water solution after adsorption on SBA-L were quantified by Vis-spectrometry (upon colorimetric method) and ICP-OES, respectively. Each experiment was carried out at least in triplicate.

The adsorption kinetics was quantified by measuring the decrease of metal ion (either copper or cadmium) concentration in the adsorbing solution, at given times. The adsorption isotherms were determined by plotting the adsorbed amount q_t of Cu^{2+} and Cd^{2+} (mg g⁻¹) versus the equilibrium concentration C_{eq} of Cu^{2+} and Cd^{2+} (mg L⁻¹) in the adsorbing solution. The kinetic and isotherm experimental data were fitted through three different isotherm and kinetic models described previously^[18].

2.6. Potentiometric and spectrophotometric measurements

Protonation and complex-formation equilibrium studies were carried out in 0.1 M NaCl at 298.1 ± 0.1 K using an automatic Metrohm titrator under the same conditions previously described^[10]. The OMS (SBA-15 and SBA-L) samples were stored at 50 °C and cooled in a desiccator to room temperature before being weighed (analytical weight scale, precision ± 0.01 mg). The working OMS content was 3.0–3.1 mg in 20 mL of water. The total mmol of the ligand in SBA-L was determined by the NaOH titration. The operating ligand concentration was 3.7×10^{-4} (free L) and 4.5×10^{-5} (for L grafted on SBA-15; SBA-L). The studies of complex formation were carried using constant ligand concentration, and 1:1, 1:2, and 1:5 metal/ligand molar ratios. Each measurement, both for ligand protonation and metal-complex experiments, was repeated at least three times to verify the repeatability. Protonation and complex formation data were analysed using the Hyperquad and Hyss software^[20].

The UV-Vis measurements were carried with Varian Cary 60 spectrophotometer. The pH combined glass electrode was daily calibrated with buffer solutions (pH 4.00, pH 7.00, pH 9.00 Mettler Toledo).

3. Results and Discussion

3.1. Physico–Chemical Characterizations

The structural characterization of SBA-15 was carried out by using a transmission electron microscopy (TEM) and a small angle X-rays scattering (SAXS) analyses. TEM images in Figure 1 clearly show the presence of parallel channels forming a hexagonal array of pores. The SAXS plot in Figure 2A has the typical pattern of hexagonal phases. It consists of an intense peak relative to the reflections of the planes 10, and two less intense peaks due to planes 11 and 20, with a resulting lattice parameter of 116.8 Å (Table 1).

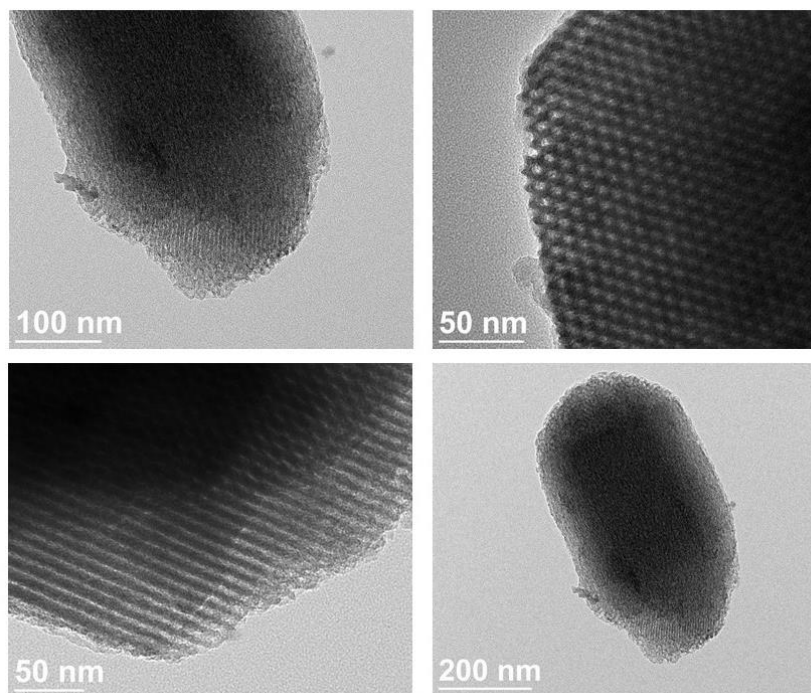


Figure 1. TEM analysis micrographs of SBA-15. Bar = 50 nm, 100 nm and 200 nm.

The textural characterization of the samples was carried out through N₂ adsorption/desorption isotherms at 77 K (Figure 2B) resulting in a surface area of 692 m²/g (Table 1). A hysteresis cycle due to the capillary condensation confirms the mesoporosity of the SBA-15 sample. The pore size distribution obtained by applying the BJH method^[21] to the desorption branch of the isotherm has a maximum at 66 Å (Table 1).

Table 1. Characterization of SBA-15 mesoporous silica.

Sample	^a S _{BET} (m ² /g)	^b d _p (Å)	^c a (Å)
SBA-15	692	66	116.8

^aSurface area calculated by the BET method; ^bPore diameter calculated by applying the BJH method to the isotherm desorption branch; ^cLattice parameter obtained by SAXS $a = d \cdot 2 / (3)^{0.5} \cdot (h^2 + k^2 + hk)^{0.5}$

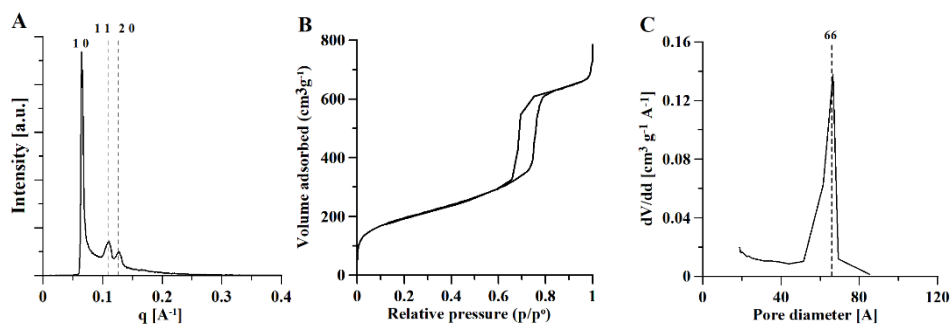


Figure 2. Characterization of SBA-15 mesoporous silica. A) SAXS patterns. B) N₂-adsorption/desorption isotherms. C) Pore size distribution calculated through the BJH method from the desorption branch.

Thermogravimetric analysis (TGA) was used to characterize the functionalized SBA-15 (Figure 3). The mass loss (%) in function of the temperature (°C) of SBA-15, SBA-Cl (19 %) and SBA-L (26 %) samples confirm the successful functionalization of SBA-15 with both CPTMS and L macrocycle (Figure 3). TGA also allowed to estimate the amount of L ligand grafted on SBA-15 which was 70 mg/g (Table 2).

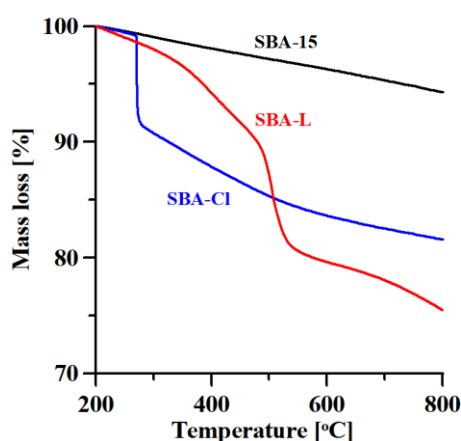


Figure 3. Thermal analysis of SBA-15, SBA-Cl and SBA-L.

Table 2. Characterization of original and functionalized SBA-15 samples.

Sample	Mass loss %	Loading (mg/g)	Loading (mol/g)
SBA-15	6	-	
SBA-Cl	19	130	$1.68 \cdot 10^{-3}$

SBA-L	26	70	$0.291 \cdot 10^{-3}$
-------	----	----	-----------------------

3.2 Adsorption kinetics and isotherms

The adsorption kinetics of Cu^{2+} and Cd^{2+} ions on SBA-L from aqueous solution was then studied. The pH of adsorption kinetics and isotherms was chosen on the basis of metal hydrolysis speciation plots^[22] and metal-complex formation stability constants on the SBA-L surface (discussed in section 3.2.2.). It was essential to work at pH where the metal-complex formation is at 100%, and at the same time there is neither metal hydrolysis nor precipitation. For these reasons, Cu^{2+} adsorption was carried out at pH = 5 where the species $[\text{Cu}(\text{SBA}(\text{SiO})(\text{L}))]^+$ is prevalent (see section 3.3.2.), while pH = 7 was chosen for Cd^{2+} where the $[\text{Cd}(\text{SBA}(\text{SiO})(\text{L}))]^+$ species is predominant (see section 3.3.2.). Figure 4A shows the adsorption kinetics of Cu^{2+} and Cd^{2+} on SBA-L. The adsorbed amount (q_t) increases when the contact time (t) increases, until a constant value (q_e) corresponding to the adsorption equilibrium is reached. It can be observed that for both cations, the adsorption equilibrium is reached after about 30 min. Under these conditions, the q_e of Cu^{2+} on SBA-L was 24 mg/g ($2 \cdot 10^{-4}$ mol/g), while that of Cd^{2+} was $q_e = 3.5$ mg/g ($5.5 \cdot 10^{-5}$ mol/g). Three different kinetic models (namely, pseudo-first order, pseudo-second order, and intraparticle diffusion model) were tested as shown in Figure 4B-D. The fitting of the experimental data using the pseudo-first order gave low correlation coefficients (Table 3), thus, suggesting the inadequacy of this model to describe both Cu^{2+} and Cd^{2+} adsorption on SBA-L. On the contrary, the pseudo-second order model resulted in a very good fitting, as demonstrated by the high correlation coefficients ($R^2 > 0.99$). The values of q_e calculated from pseudo-second order model are 3.57 mg/g for Cu^{2+} and 23.8 mg/g for Cd^{2+} . The good fitting of the pseudo-second order model to the adsorption data suggests that the adsorption of the metal ions on the adsorbent sites is the rate determining step^[23]. The fit of the intraparticle diffusion model (Figure 4D) is of lower quality than that of the pseudo-second order model, thus supporting the goodness of the latter which gives the best description of the kinetic data.

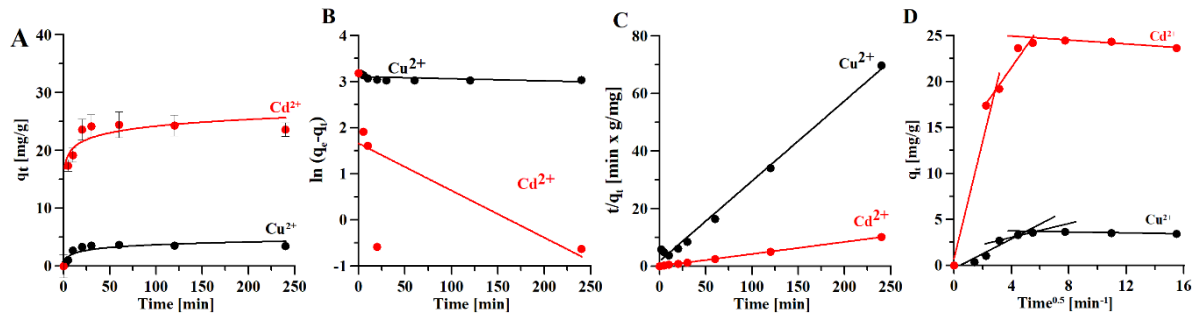


Figure 4. Adsorption kinetics of Cu^{2+} (black) and Cd^{2+} (red) on SBA-L. A) Adsorbed amount q_t versus time. B) Pseudo-first order model; C) Pseudo-second order model; D) Intraparticle diffusion model. For Cu^{2+} kinetics studies: Initial metal ion concentration = 5 ppm; pH = 4; stirring speed = 22 rpm; T = 298 K. For Cd^{2+} kinetics studies: Initial metal ion concentration = 3.5 ppm; pH = 7; stirring speed = 22 rpm; T = 298 K.

Table 3. Comparison among kinetic models for Cu^{2+} and Cd^{2+} adsorption on SBA-L.

Ion	^a Pseudo First Order			^b Pseudo Second Order			^c Intraparticle Diffusion		
	k' (1/min)	q_e cal (mg/g)	R^2	k'' (g/mg·min)	q_e cal (mg/g)	R^2	k_i (g·mg ⁻¹ min ^{-0.5})	x_i (mg/g)	R^2
Cu^{2+}	$5 \cdot 10^{-4}$	22.28	0.2874	0.06	3.57	0.9927	0.81	-0.362	0.8297
							0.38	1.52	0.9688
							-0.03	3.82	0.9441
Cd^{2+}	$1 \cdot 10^{-2}$	3.61	0.3464	0.16	23.81	0.9996	6.39	0.71	0.9591
							2.22	12.62	0.8888
							-0.11	25.36	0.9322

^aPseudo-First Order linearized equation^[24]: $\ln(q_e - q_t) = \ln q_e - k't$; where k' is the pseudo-first order constant;

^bPseudo-Second Order linearized equation^[24] $\frac{t}{q_t} = \frac{1}{k'' \cdot q_e^2} + \frac{t}{q_e}$; where k'' is the pseudo-second order constant;

^cIntraparticle diffusion model linearized equation^[24] $q_t = k_i \cdot t^{0.5} + x_i$; where k_i is the intraparticle diffusion constant.

The adsorption isotherms (Figure 5) show that the maximum adsorbed amount of metal ions, corresponding to the plateaus, are 20.9 mg/g (0.329 mmol/g) for Cu^{2+} and 31.8 mg/g (0.284 mmol/g) for Cd^{2+} (Table 4). The shape of the isotherms is consistent with Langmuir model which considers the formation of a monolayer of adsorbate on the adsorbent's surface. This is consistent with the

formation of a metal/L complex at 1:1 molar ratio (L concentration in SBA-L is equal to 0.291 mmol/g and corresponds to 70 mg/g found by TGA analysis).

The Gibbs Energy (ΔG^0) for the adsorption process (Table 4) was calculated according to the equation: $\Delta G^0 = -RT \ln K_e^0$, where R is the universal gas constant ($8.314 \text{ J}\cdot\text{K}^{-1}\cdot\text{mol}^{-1}$), T is the absolute temperature (298 K) and K_e^0 is the thermodynamic equilibrium constant, calculated by means of the equation^[25]:

$$K_e^0 = \frac{K_L \cdot 1000 \cdot MM_{\text{Adsorbate}} \cdot [\text{Adsorbate}]^0}{\gamma}$$

where K_L is the Langmuir constant (L/mg), $MM_{\text{Adsorbate}}$ is the molar mass of the adsorbate (g/mol), $[\text{Adsorbate}]^0$ is the standard concentration of the adsorbate (1 mol/L) and γ is the activity coefficient (dimensionless)^[25]. As reported in Table 4, the ΔG^0 was negative for both adsorption processes, more precisely -25.5 kJ/mol and -33.7 kJ/mol for Cu^{2+} and Cd^{2+} , respectively. These data confirm the spontaneous nature of the adsorption process.

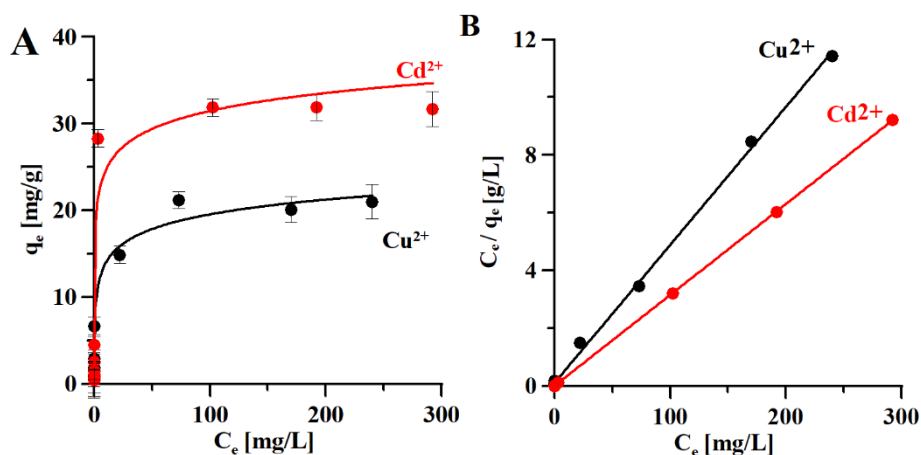


Figure 5. Adsorption isotherm of Cu^{2+} and Cd^{2+} on SBA-L A). Adsorption data were fitted using linearized Langmuir isotherms B). Adsorption experiments were carried out for 24 h at pH=4 (for copper) and pH=7 (for cadmium) and T=298 K.

Table 4. Langmuir adsorption isotherm parameters for Cu^{2+} and Cd^{2+} on SBA-L.

Ion	pH	Langmuir					
		^a K _L (L/mg)	^b q _M (mg/g)	q _M (mmol/g)	R ²	K _e ^o	ΔG ^o (kJ/mol)
Cu ²⁺	5.0	0.468	20.9	0.329	0.999	2.97×10 ⁴	-25.5
Cd ²⁺	7.0	7.16	31.8	0.284	1	8.05×10 ⁵	-33.7

^aLangmuir constant and ^bmaximum monolayer coverage capacity obtained by the linearized form of the Langmuir

isotherm model equation $\frac{C_e}{q_e} = \frac{1}{K_L \cdot q_M} + \frac{1}{q_M} C_e$. [26]

3.3 Protonation and metal-complex equilibria

The stability in aqueous solutions, the equilibrium formation constant, solubility and other properties of macrocycle-metal ion complexes depend on different factors, namely the nature of the metal ion, the structure of the ligand and the composition of the complex. The most important metal ion-related factors are the oxidation state, the ion size, the electron shell structure and coordination requirements. Factors related to the ligand are the flexibility, the charge, the nature and number of donor sites, and the molecular structure^[13]. The combination of all these factors make difficult the exact prediction of the ligand/metal complex-stability; however, numerous literature experimental data show some local trends^[27]. Generally, aliphatic azamacrocycles form stable and inert complexes (i.e., complexes that decompose slowly under the action of external factors or competing ligands) with metal ions even in very acidic solutions. Nevertheless, the practical application of the complexes is limited by low complexation kinetics^[13].

The stability of metal/aliphatic ligands complexes is strongly influenced by the entropy. Free, aliphatic macrocyclic ligands are present in the solutions as a mixture of several conformers in dynamic equilibrium, because of metal-complex formation they lose some of their degrees of freedom and the entropy decreases. Importantly, the total entropy (system and environment) increases due to the release of water molecules from the metal ion-hydration shell. Conversely, structurally rigid macrocyclic ligands retain a conformation in the metal complex similar to that they possess as free

ligand, therefore the entropy of the system increases upon complexation less than in the case of aliphatic systems, which is thermodynamically more favourable^[27]. In addition, the rigid macrocycles' structure can impose a particular coordination geometry to the metal centre, while open-chain chelators are more easily adjusted to the coordination characteristics of the metal centre^[28]. For this reason, an increase in the ligand rigidity could increase the binding selectivity toward specific cations^[29].

In previous studies, Blake et al.^[16] presented L ligand coordination mode and complex stability with Cu^{2+} , Zn^{2+} , Cd^{2+} , Hg^{2+} , and Pb^{2+} ions investigated by the means of potentiometry (water solution, $I = 0.1\text{M NMe}_4\text{NO}_3$, $[\text{L}] = 1.0 \times 10^{-3}\text{ M}$) and single crystal structure. Metal complexation of L in aqueous solution generally occurs at acidic pH values to give $[\text{ML}]^{2+}$ species and it is followed by the formation of hydroxo- complexes $[\text{ML}(\text{OH})]^+$ at alkaline pHs. In case of Zn^{2+} , Cd^{2+} , Hg^{2+} and Pb^{2+} hydroxo-complexes the precipitation occurs at slightly alkaline pHs and unable the potentiometric studies. The stability of the formed complexes increases in the order $\text{Zn}^{2+} < \text{Pb}^{2+} < \text{Cd}^{2+} < \text{Cu}^{2+} < \text{Hg}^{2+}$. Noteworthy, Cu^{2+} and Hg^{2+} complexes have higher stability compared to complexes with other known polyamine ligands. The lowest stability of the Zn^{2+} complexes (which normally is similar to the Cd^{2+} and Pb^{2+} complexes with polyamine) could be explained by the presence of the soft S-donors, within the macrocyclic framework. In agreement with a general $\text{N} > \text{S}$ donor affinity trend for the studied metal ions, and with a better binding ability of a pyridine nitrogen toward transition and post-transition divalent cations, the L ligand forms less stable complexes than its structural analogue containing only N-donors in the aliphatic portion of the ring^[30], and more stable complexes than [12]aneNS₂O (1-aza-4,10-dithia-7-oxacyclododecane)^[31].

The aim of our studies was the determination of metal/ligand complex stoichiometry, metal binding sites and complex formation constants for the ligand grafted on the surface of SBA-L mesoporous material. To compare the metal/free ligand complex formation with the metal complexes formed on the surface of L-grafted mesoporous material, we performed potentiometric titrations of free and

grafted L ligand with metal ions under the same experimental conditions. As compared to previously published data by Blake et al.^[16], we used lower ligand and metal concentrations in order to avoid precipitation of hydroxo-complexes. Moreover, we used UV-Vis spectroscopy to determine metal binding sites in water solution on changing pH conditions. Finally, FTIR spectroscopy was used to determine the metal-binding sites of the complexes in solid state.

3.3.1. Free ligand protonation and metal-complex equilibria

The potentiometric titrations allowed to calculate one protonation constant of free L in the basic environment (Table 5) that can be assigned to the aliphatic nitrogen atom, rather than pyridine nitrogen, which dissociate normally at acidic pH^[32].

Table 5. Protonation constants (log K) of L, L grafted on SBA-15 and cumulative formation constants (log β) of Cu²⁺ and Cd²⁺ complexes with free L and L grafted on SBA-15 at 25 °C, 0.1 M NaCl ionic strength, calculated using the Hyperquad program for potentiometric measurements. The constants for the Cu²⁺ and Cd²⁺ hydroxides at 25 °C and 0.1 M ionic strength, are taken from the literature^[22]. (*) Cumulative constant ([ML]²⁺ + 2OH⁻ = [ML(OH)₂]).

Formed Species	Literature data (log K) ^[16]	Experimental data (log K)	
	Free L	Free L	Formed Species for functionalized OMS
[LH] ⁺	8.32(1)	8.73(2)	[SBA(SiOH)(L)] 9.48(5)
[LH ₂] ²⁺	1.5 (1)	-	[SBA(SiOH)(LH)] ⁺ 8.8(2)
	Literature data (log K) ^[16]	Experimental data (log β)	
[CuL] ²⁺	10.05(7)	9.54(6)	[Cu(SBA(SiO)(L))] ⁺ 21.4(7) [Cu(SBA(SiO)(L))(OH)] 14.6(5)
[CuL(OH)] ⁺	6.09(4)	0.71(6)	
[CuL(OH) ₂]	2.3(1)	-	
[CdL] ²⁺	9.12(2)	6.25(4)	
[CdL(OH) ₂]	-	-11.0(5)*	

		$[\text{Cd}(\text{SBA}(\text{SiO})(\text{L}))]^+$	19.0(1)
		$[\text{Cd}(\text{SBA}(\text{SiO})(\text{L}))(\text{OH})_4]^{-3}$	-13.5(5)

The $[\text{CuL}]^{2+}$ complexes start forming already at very low pH values (Figure 6B). The formation of $[\text{CuL}(\text{OH})]^+$ complex occurs above pH 8 (Figure 6B) probably due to deprotonation of water molecule in the metal coordination sphere. The formation of the $[\text{CdL}]^{2+}$ 1:1 complex takes place from pH 5, in our experimental conditions.

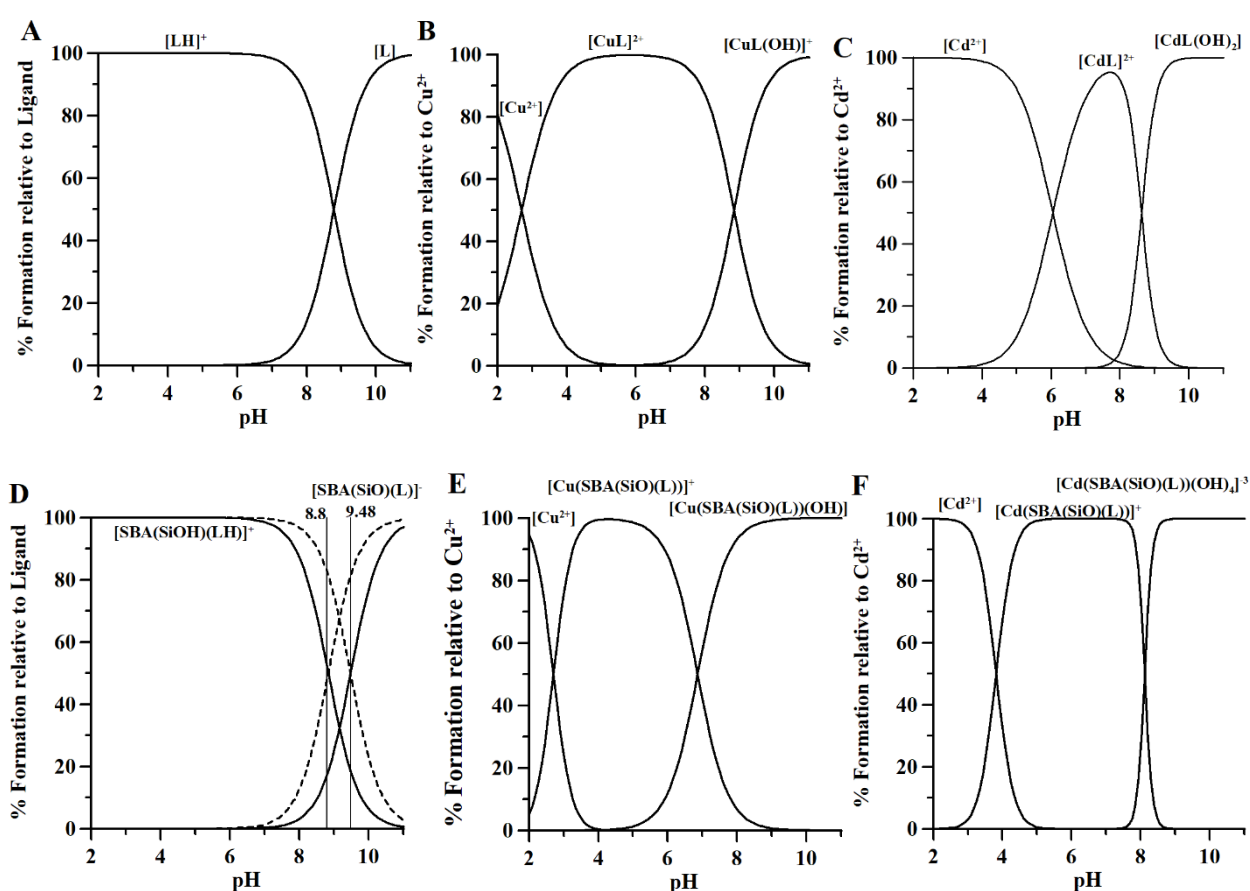
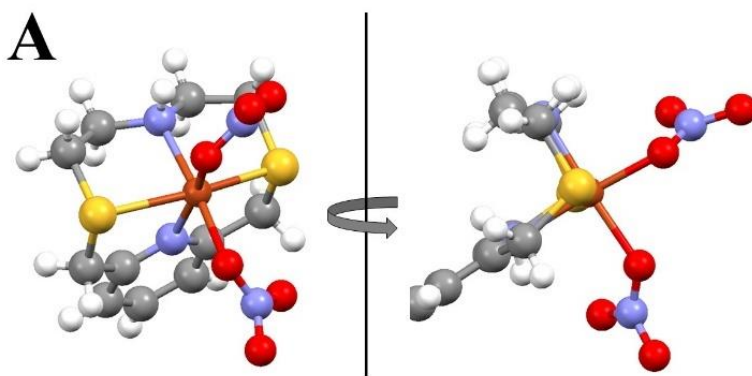


Figure 6. Speciation plot of free L (A) and grafted on SBA-15 (D)*. Distribution curves of (B) and (E) Cu^{2+} ; (C) and (F) Cd^{2+} complexes with free L and grafted on SBA-15, respectively. Plots calculated on the base of stability constants (Table 5) with Hyss program^[20]. (*) Dashed lines represents species deriving from a partial deprotonation of $[\text{SBA}(\text{SiOH})(\text{LH})]^+$ either of the silanol groups or the grafted $[\text{LH}]^+$ groups according to proper $\log K$ (Table 5) values.

In the previous studies^[16], the coordination mode in $[\text{CuL}](\text{NO}_3)_2$ complex was determined by X-ray crystallography using single crystals obtained in EtOH:MeCN (50:50) solution. The central metal ion

was coordinated by six donor atoms in the octahedral geometry, namely two N- and two S-donor atoms of the ligand, and two O- atoms from nitrate anions. (Figure 7A). Here we analysed the complex structure in aqueous solution by the means of UV-Vis and FTIR spectroscopies. It can be observed in Figures 7B and 7C that at acidic pHs the $[\text{CuL}]^{2+}$ complex is formed (green colour solution) and the characteristic d-d band with maximum at 730 nm can be assigned to the presence of nitrogen atom(s) in the Cu^{2+} coordination core, while the band below 400 nm can be assign to $\text{S}(\sigma) \rightarrow \text{Cu}^{2+}$ charge transfer (LMCT)^[33] The bands at high energy correspond to intramolecular $\pi \rightarrow \pi^*$ and $n \rightarrow \pi^*$ transitions^[34]. On increasing the pH, the hypso- and hypochromic shift of the bands at 380 and 730 nm can be observed. Such changes could be due to a changing of the donor atom set in the metal coordination core. Of note, potentiometric studies showed a proton dissociation above pH 8 (Figure 6B), which could be assigned to the dissociation of water molecule. The Figure 5D presents the FTIR spectra of free L and the Cu^{2+}/L complex in the solid state. Upon the metal-complex formation, the slight shift of the bands in the $400\text{-}2000\text{ cm}^{-1}$ region, and the slight enlargement of the bands in the $1600\text{-}1700\text{ cm}^{-1}$ region can be observed. Significant changes can be observed in the region $2000\text{-}4000\text{ cm}^{-1}$, where the new bands in the region $3200\text{-}3600\text{ cm}^{-1}$ appears and could be associated to the presence of water molecules in the complex and relative intramolecular hydrogen bonds.



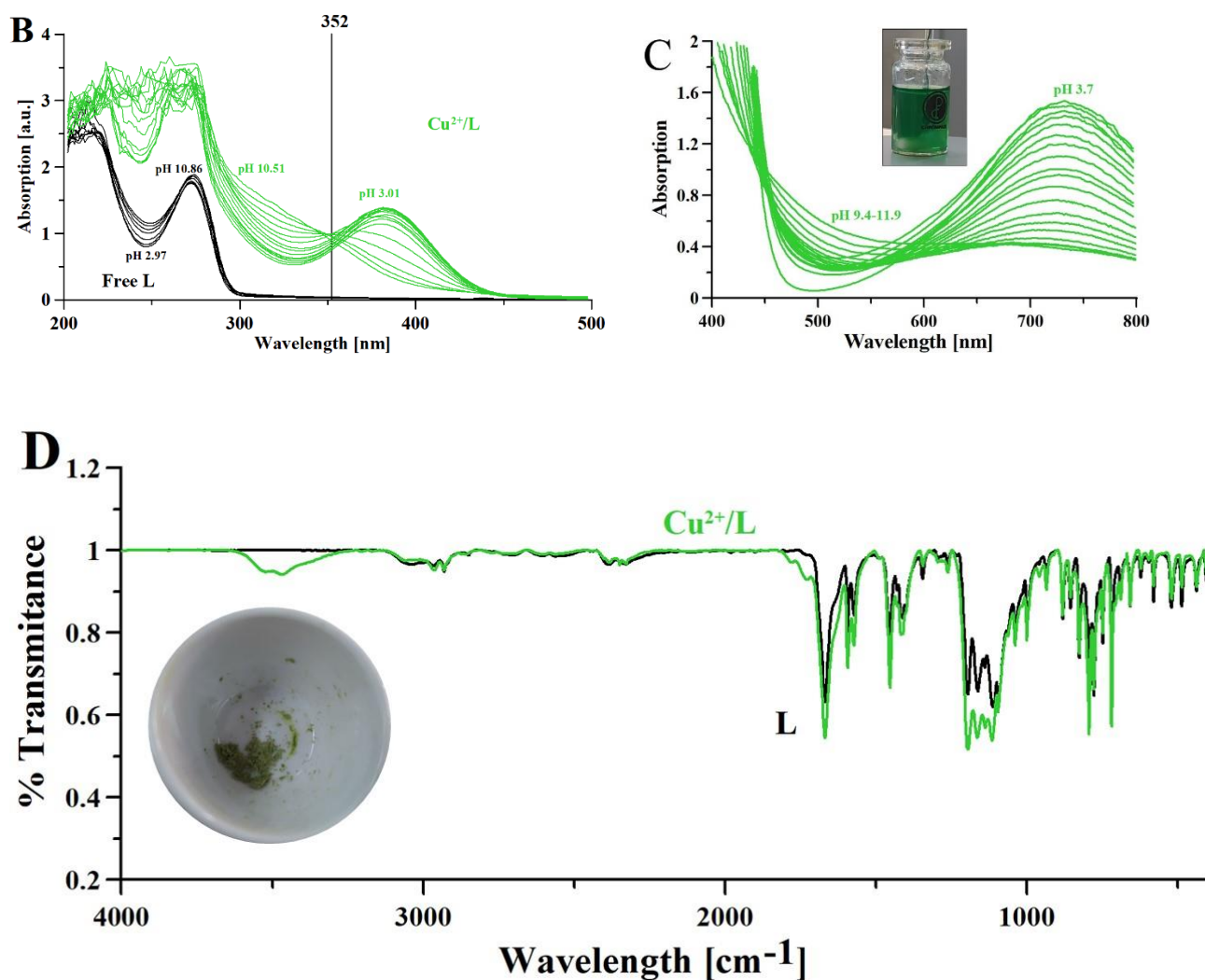


Figure 7. Characterization of the Cu^{2+}/L complex in solution and in the solid state. A) Crystal structure of $[\text{CuL}](\text{NO}_3)_2$ complex (CCDC n. 238263). Data available on <https://www.ccdc.cam.ac.uk/structures/>. UV-Vis spectrum of the Cu^{2+}/L (1: 1 molar ratio) complex in $\text{MeCN}:\text{H}_2\text{O}$ (50:50 v/v) solution B) 200-500 nm spectral range: $C_{\text{L}} = C_{\text{Cu}^{2+}} = 1 \text{ mM}$, $l = 1 \text{ cm}$, C) 500-800 nm spectral range: $C_{\text{L}} = C_{\text{Cu}^{2+}} = 10 \text{ mM}$, $l = 1 \text{ cm}$. D) Solid state FTIR spectra of free L (black) and Cu^{2+}/L complex (green).

As previously shown by Blake et al.^[16] L forms complexes with Cd^{2+} ion. In our experimental conditions, the $[\text{CdL}]^{2+}$ complex forms above pH 4 (Figure 6C) and remains stable even at basic pH, where the hydroxo complexes $[\text{CdL}(\text{OH})]^+$, and $[\text{CdL}(\text{OH})_2]$ are formed (only the cumulative formation constant for the latter was determined in the experimental conditions used), most likely due to dissociation of a water molecule in the metal coordination core. The FTIR spectrum of the Cd^{2+}/L complex resembles that of the Cu^{2+} complex, suggesting the same coordination model of the ligand,

with only slight changes in 3200 cm^{-1} region and higher intensity of the bands in the 3400-3600 cm^{-1} region.

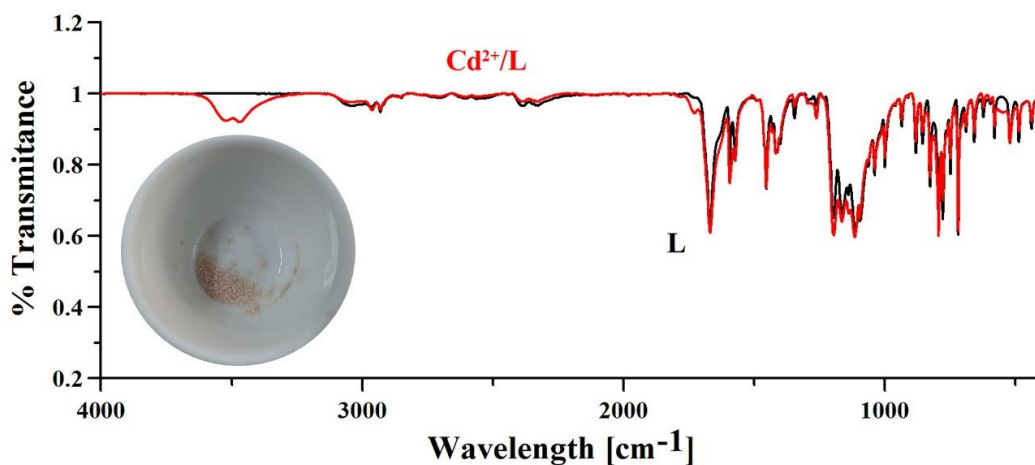


Figure 8. Solid state FTIR spectra of free L (black) and Cd^{2+}/L complex (red).

3.3.2. SBA-L protonation and metal-complex equilibrium

In the next step, we investigated the metal coordination pattern on the L functionalized mesoporous material by the means of potentiometry and FTIR measurements. The potentiometric studies showed their great utility in the studies of functionalized OMS and their metal-complexes^[10] and were used to establish the stoichiometry and stability of the formed complex on the SBA-L surface, and to some extent, can indicate the donor atoms in the metal coordination core. The FTIR spectra showed the changes in the spectroscopic bands, which can be assigned to the complex formation and indicates the donor atoms in the metal complex.

The potentiometric titration of functionalized OMS let us establish the protonation constants and the precise ligand and dissociating silanol groups concentration on the OMS surface. Of note, the L concentration (grafted on SBA-15) calculated with potentiometric titration was established 0.3 mmol/g and corresponds perfectly to 70 mg/g ligand loading calculated with TGA analysis. In addition, potentiometric data allowed us calculating the cumulative stability constants (Table 5) of the formed Cu^{2+} and Cd^{2+} complexes with L grafted on mesoporous material.

In order to assign precisely the protonation constants of L grafted on SBA-15 and dissociating silanol groups (SiOH), we introduce [SBA(SiOH)(LH)]⁺ nomenclature for the purpose of this section to indicate the fully protonated functionalised OMS material. In the previous studies (in the same experimental conditions) the silanol groups of SBA-15 had one protonation constant ($\log K=10.0$)^[10], due to the dissociation of silanols (SiOH) into SiO⁻. Grafting L on SBA-15 leads to two distinct protonation constants (Table 5), $\log K_1 = 8.8(2)$ for the aliphatic nitrogen of L and $\log K_2 = 9.48(5)$ for silanol groups (SiOH). Importantly, in our experimental conditions the molar ratio between silanols and nitrogens is equal to 3.2. Moreover, the slight differences in the pK values of free ligand, SBA-15 and the final [SBA(SiOH)(LH)]⁺ material suggest the intramolecular hydrogen bonds between nitrogen and oxygen atoms of silanols at different pHs.

As shown in our previous studies^[10], silanols of SBA-15 do not form stable complex with metal ions, but can participate to the coordination shell of the metal ion in the presence of other ligands grafted on the OMS surface. In some cases, such co-participation can enhance the overall stability of the formed metal complex. Indeed, the cumulative formation constants of the Cu²⁺ and Cd²⁺ complexes with L grafted on SBA-15 are higher with respect to the complexes formed with the free L (Table 5). Furthermore, the Cu²⁺ and Cd²⁺ complexes with L grafted on SBA-15 start to form at lower pHs (Figure 6E and F) respect to the metal complexes with free L. This enhancement in the complex formation constants could be also due to the higher local concentration of metal binding sites on the SBA surface, which is a characteristic feature of ligands grafted on mesoporous materials with high surface areas.

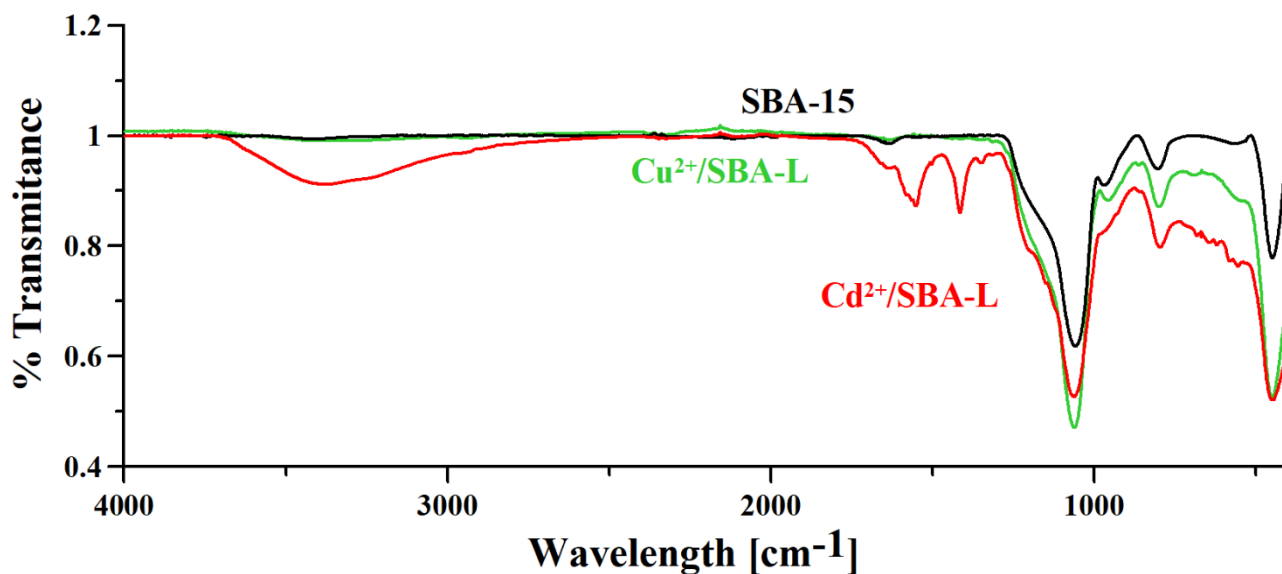


Figure 9. FTIR spectra of SBA-15 (black) and Cu^{2+} (green) and Cd^{2+} (red) complexes on the surface of SBA-L. The $\text{Cu}^{2+}/\text{SBA-L}$ and $\text{Cd}^{2+}/\text{SBA-L}$ were filtered and dried after the isotherm studies, where the metal loading was maximum (pH = 4 for Cu^{2+} and pH = 7 for Cd^{2+}).

Figure 9 shows the FTIR spectra of the free SBA-15 and the Cu^{2+} and Cd^{2+} complexes with SBA-L. The new bands in the regions 1200-2000 and 3000-4000 cm^{-1} relative to the complex formation, are clearly visible in the spectrum of the $\text{Cd}^{2+}/\text{SBA-L}$ complex to suggest that the nitrogen atoms are present in the coordination sphere of the metal. The bands between 3000-4000 cm^{-1} can be associated to the presence of water molecules in the metal complex, which form intramolecular bonds. This data is in accordance with potentiometric studies (Figure 6F), which showed that water molecules in the complex dissociate above pH 8.

3.4. Desorption and material renewal studies

The analysis of adsorption isotherms data in comparison with those obtained in potentiometric titrations, suggest that the metal/ligand chelation is a unique adsorption mechanism on the grafted mesoporous material SBA-L. Indeed, the incubation of metal-loaded mesoporous material in hydrochloric acid solution (0.1 M; pH 1) for 15 min leads to the full recovery of metal-free SBA-L. The process of metal recovery and then successive re-use of SBA-L for ligand chelation can be

repeated successfully. In our experimental conditions, material was used and recycled minimum 3 times

4. Conclusions

The fast development of metal-based industries demands new metal-recovery materials, which enables lower metal release into environment and permits metal re-use. Grafting metal chelators on the surface of mesoporous materials is an effective technology that satisfies both requirements. In the present work 2,8-dithia-5-aza-2,6-pyridinophane (L) ligand was grafted on the SBA-15 mesoporous material surface (SBA-L). The kinetic studies showed fast Cu^{2+} and Cd^{2+} adsorption (~ 30 min), while adsorption isotherms and potentiometric studies revealed the metal chelation as a unique adsorption mechanism. The adsorption isotherms show an almost complete saturation of adsorbing sites of SBA-L according to a 1:1 stoichiometry between the ligand and the cations in our experimental conditions. This suggests that the adsorbing performance of SBA-L could be modulated by changing the loading of L macrocycle grafted on SBA-15 surface. Moreover, potentiometric studies showed that the formation constants of the metal/ligand complexes (metal = Cu^{2+} and Cd^{2+}) on the mesoporous material surface are higher than those for the complexes formed by free ligand in solution, probably due to the participation of silanols in the metal coordination core. The metal desorption from the mesoporous material is fast and occurs at low pHs (e.g. 1 or below), where the metal/ligand complexes are not formed. The overall results obtained here are promising for the potential use of this new type of nanostructured functional material for the adsorption/recovery and/or storage of Cu^{2+} and Cd^{2+} ions from aqueous solutions.

Acknowledgements

FIR 2020, Fondazione di Sardegna (FdS) (Progetti Biennali di Ateneo annualità 2018-2019) are acknowledged for financial support. GRD thanks MIUR PON-RI (DOT1304455) for financing her PhD scholarship.

Conflict of Interest

The authors declare no conflict of interest.

References

- [1] J. Aaseth, G. Crisponi, O. Anderson, *Chelation therapy in the treatment of metal intoxication*, Academic Press, 2016.
- [2] A. Luch, *Molecular, Clinical and Environmental Toxicology: Volume 3: Environmental Toxicology*, Vol. 101, Springer Science & Business Media, 2012.
- [3] S. Luckeneder, S. Giljum, A. Schaffartzik, V. Maus, M. Tost, *Global Environmental Change* 2021, 69, 102303.
- [4] G. Sharma, B. Thakur, A. Kumar, S. Sharma, M. Naushad, F. J. Stadler, *Carbohydrate Polymers* 2020, 241, 116258; M. Yan, D. Wang, J. Qu, J. Ni, C. W. Chow, *Water research* 2008, 42, 2278; H. A. Hasan, M. H. Muhammad, *Journal of Water Process Engineering* 2020, 33, 101035.
- [5] I. L. Calugaru, C. M. Neculita, T. Genty, G. J. Zagury, *Journal of environmental management* 2018, 212, 142; A. Chatterjee, J. Abraham, *Biotechnology Letters* 2019, 41, 319; A. Thirunavukkarasu, R. Nithya, R. Sivashankar, *Reviews in Environmental Science and Bio/Technology* 2020, 1.
- [6] E. M. Usai, M. F. Sini, D. Meloni, V. Solinas, A. Salis, *Microporous and mesoporous materials* 2013, 179, 54.
- [7] M. Piras, A. Salis, M. Piludu, D. Steri, M. Monduzzi, *Chemical Communications* 2011, 47, 7338.
- [8] C. Vittoni, G. Gatti, I. Braschi, E. Buscaroli, G. Golemme, L. Marchese, C. Bisio, *Materials* 2020, 13, 2690.
- [9] G. Kickelbick, *Angewandte Chemie International Edition* 2004, 43, 3102; W. Li, D. Zhao, *Chemical Communications* 2013, 49, 943; B. Szczeńniak, J. Choma, M. Jaroniec, *Chemical Communications* 2020, 56, 7836.
- [10] J. I. Lachowicz, A. H. Emwas, G. R. Delpiano, A. Salis, M. Piludu, L. Jaremko, M. Jaremko, *Advanced Materials Interfaces* 2020, 7, 2000544.
- [11] P. Duenas-Ramirez, C. Bertagnolli, R. Müller, K. Sartori, A. Boos, M. Elhabiri, S. Bégin-Colin, D. Mertz, *Journal of Colloid and Interface Science* 2020, 579, 140; M. Laprise-Pelletier, M. Bouchoucha, J. Lagueux, P. Chevallier, R. Lecomte, Y. Gossuin, F. Kleitz, M.-A. Fortin, *Journal of Materials Chemistry B* 2015, 3, 748.
- [12] A. M. Sacara, V. Nairi, A. Salis, G. L. Turdean, L. M. Muresan, *Electroanalysis* 2017, 29, 2602; A.-M. Sacara, F. Pitzalis, A. Salis, G. L. Turdean, L. M. Muresan, *ACS Omega* 2019, 4, 1410; N. Cotoian, L. M. Mureşan, A. Salis, L. Barbu-Tudoran, G. L. Turdean, *Water, Air, & Soil Pollution* 2020, 231, 1.
- [13] A. D. Zubenko, O. A. Fedorova, *Russian Chemical Reviews* 2020, 89, 750.
- [14] B.-L. Su, X.-C. Ma, F. Xu, L.-H. Chen, Z.-Y. Fu, N. Moniotte, S. B. Maamar, R. Lamartine, F. Vocanson, *Journal of Colloid and Interface Science* 2011, 360, 86; M. Sperling, X.-p. Yan, B. Welz, *Spectrochimica Acta Part B: Atomic Spectroscopy* 1996, 51, 1875.
- [15] A. G. Algarra, M. G. Basallote, R. Belda, S. Blasco, C. E. Castillo, J. M. Llinares, E. García-España, L. Gil, M. Á. Máñez, C. Soriano, *Wiley Online Library*, 2009.
- [16] A. J. Blake, A. Bencini, C. Caltagirone, G. De Filippo, L. S. Dolci, A. Garau, F. Isaia, V. Lippolis, P. Mariani, L. Prodi, *Dalton Transactions* 2004, 2771.
- [17] A. Albert, E. P. Serjant, *Chapman and Hall*, London, 1984 (Chapter 2).

- [18] J. I. Lachowicz, G. R. Delpiano, D. Zanda, M. Piludu, E. Sanjust, M. Monduzzi, A. Salis, *Journal of Environmental Chemical Engineering* 2019, 7, 103205.
- [19] I.-C. Apat, *Manuali e linee guida* 2003, 29, 2003.
- [20] L. Alderighi, P. Gans, A. Ienco, D. Peters, A. Sabatini, A. Vacca, *Coordination Chemistry Reviews* 1999, 184, 311.
- [21] E. P. Barrett, L. G. Joyner, P. P. Halenda, *Journal of the American Chemical Society* 1951, 73, 373.
- [22] C. Baes Jr, R. Mesmer, *Jon Wiley & Sons: New York* 1976.
- [23] L. N. Nemeş, L. Bulgariu, *Open Chemistry* 2016, 14, 175.
- [24] E. Da'na, N. De Silva, A. Sayari, *Chemical Engineering Journal* 2011, 166, 454.
- [25] E. C. Lima, A. Hosseini-Bandegharaei, J. C. Moreno-Piraján, I. Anastopoulos, *Journal of Molecular Liquids* 2019, 273, 425.
- [26] I. D. Mall, V. C. Srivastava, N. K. Agarwal, I. M. Mishra, *Chemosphere* 2005, 61, 492.
- [27] N. Dyatlova, V. Y. Temkina, K. Popov, 1988 Moscow: *Khimiya*. Ed. Ovsyannikova, 544.
- [28] R. E. Mewis, S. J. Archibald, *Coordination Chemistry Reviews* 2010, 254, 1686.
- [29] P. Antunes, P. M. Campello, R. Delgado, M. G. Drew, V. Félix, I. Santos, *Dalton Transactions* 2003, 1852.
- [30] J. Costa, R. Delgado, *Inorganic Chemistry* 1993, 32, 5257.
- [31] C. Caltagirone, A. Bencini, F. Demartin, F. A. Devillanova, A. Garau, F. Isaia, V. Lippolis, P. Mariani, U. Papke, L. Tei, *Dalton Transactions* 2003, 901.
- [32] A. Casale, A. De Robertis, F. Licastro, *Thermochimica acta* 1989, 143, 289.
- [33] M. Kodera, T. Kita, I. Miura, N. Nakayama, T. Kawata, K. Kano, S. Hirota, *Journal of the American Chemical Society* 2001, 123, 7715.
- [34] B. Chen, H. Yao, W. Huang, P. Chattopadhyay, J. Lo, T. Lu, *Solid state sciences* 1999, 1, 119.

Paper IV



Article

Adsorption of Malachite Green and Alizarin Red S Dyes Using Fe-BTC Metal Organic Framework as Adsorbent

Giulia Rossella Delpiano ¹, Davide Tocco ¹, Luca Medda ², Edmond Magner ^{3,*} and Andrea Salis ^{1,4,*}

¹ Dipartimento di Scienze Chimiche e Geologiche, Università di Cagliari, Cittadella Universitaria, S.S. 554 bivio Sestu, 09042 Monserrato (CA), Italy; delpiano@unica.it (G.R.D.); davide.tocco@unica.it (D.T.)

² Laboratorio NEST Scuola Normale Superiore di Pisa, 56127 Pisa, Italy; medda.luc@gmail.com

³ Department of Chemical Sciences, Bernal Institute, University of Limerick, Limerick V94 T9PX, Ireland

⁴ Consorzio Interuniversitario per lo Sviluppo dei Sistemi a Grande Interfase (CSGI), Unità Operativa University of Cagliari, 09042 Monserrato (CA), Italy

* Correspondence: edmond.magner@ul.ie (E.M.); asalis@unica.it (A.S.)

Abstract: Synthetic organic dyes are widely used in various industrial sectors but are also among the most harmful water pollutants. In the last decade, significant efforts have been made to develop improved materials for the removal of dyes from water, in particular, on nanostructured adsorbent materials. Metal organic frameworks (MOFs) are an attractive class of hybrid nanostructured materials with an extremely wide range of applications including adsorption. In the present work, an iron-based Fe-BTC MOF, prepared according to a rapid, aqueous-based procedure, was used as an adsorbent for the removal of alizarin red S (ARS) and malachite green (MG) dyes from water. The synthesized material was characterized in detail, while the adsorption of the dyes was monitored by UV-Vis spectroscopy. An optimal adsorption pH of 4, likely due to the establishment of favorable interactions between dyes and Fe-BTC, was found. At this pH and at a temperature of 298 K, adsorption equilibrium was reached in less than 30 min following a pseudo-second order kinetics, with k'' of 4.29×10^{-3} and $3.98 \times 10^{-2} \text{ g}\cdot\text{mg}^{-1} \text{ min}^{-1}$ for ARS and MG, respectively. The adsorption isotherm followed the Langmuir model with maximal adsorption capacities of $80 \text{ mg}\cdot\text{g}^{-1}$ (ARS) and $177 \text{ mg}\cdot\text{g}^{-1}$ (MG), and K_L of $9.30\cdot 10^3 \text{ L}\cdot\text{mg}^{-1}$ (ARS) and $51.56\cdot 10^3 \text{ L}\cdot\text{mg}^{-1}$ (MG).

Keywords: metal organic frameworks; wastewater remediation; adsorption; malachite green; alizarin red S



Citation: Delpiano, G.R.; Tocco, D.; Medda, L.; Magner, E.; Salis, A. Adsorption of Malachite Green and Alizarin Red S Dyes Using Fe-BTC Metal Organic Framework as Adsorbent. *Int. J. Mol. Sci.* **2021**, *22*, 788. <https://doi.org/10.3390/ijms22020788>

Received: 16 December 2020

Accepted: 10 January 2021

Published: 14 January 2021

Publisher's Note: MDPI stays neutral with regard to jurisdictional claims in published maps and institutional affiliations.



Copyright: © 2021 by the authors. Licensee MDPI, Basel, Switzerland. This article is an open access article distributed under the terms and conditions of the Creative Commons Attribution (CC BY) license (<https://creativecommons.org/licenses/by/4.0/>).

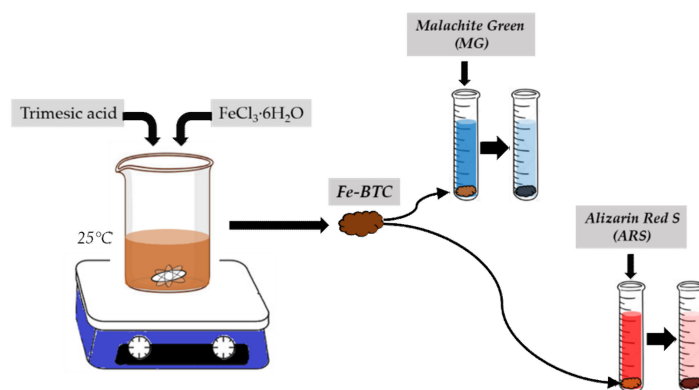
1. Introduction

Synthetic organic dyes are among the most harmful polluting agents. It is estimated that 80,000 tons of dyes are produced and consumed each year [1]. They are cheap, offer a wide range of colors, and are used for numerous applications in the paper, tanning, pharmaceutical, photographic, and cosmetic industries [2]. However, synthetic dyes are mainly earmarked for the textile industry, as they possess reactive groups which have a strong binding ability for fiber [3]. The colors of dye molecules are due to chromogenic groups which absorb visible light. Indeed, dye molecules generally have a complex aromatic structure which is often characterized by a high chemical stability. Unfortunately, dyes are highly toxic and can have carcinogenic and mutagenic effects on living organisms, even at low concentrations [4]. In addition, due to their ability to absorb light, the release of dyes into surface waters also causes unwanted effects in the aquatic ecosystem. These effects arise from a reduced level of penetration of the sun's rays in water, which alters photosynthetic cycles and reduces the oxygen supply in the water body [5]. Due to their high chemical stability, the removal of dyes from water is a challenging issue [6]. Numerous methods have been proposed to remove dyes from wastewaters, such as electrochemical degradation [7,8], membrane-based separation [9], ultrafiltration [10], extraction [11], and biological treatment [12]. While these methods have a number of advantages, they cannot be applied on a large scale due to high costs, secondary pollution, production of waste, etc [3].

Adsorption is a simple method of dye removal that has significant advantages. Indeed, it can be applied to almost any type of dye or mixtures of dyes, it does not require any special equipment or pretreatment, and it can be repeated a number of times until the adsorbent has reached its maximal adsorbing capacity. Adsorption processes are also economic as they can be carried out in mild conditions, reducing the actual costs to that of the adsorbent, which can be selected accordingly [13,14]. The main features of a good adsorbent are high surface area, high adsorption capacity, short adsorption times, and economic and environmentally-friendly production process.

Metal organic frameworks (MOFs) are organic-inorganic hybrid porous materials characterized by a cage-like structure consisting of an array of metal cations held together by organic linkers [15]. Thanks to their large surface area, tunable structural properties and thermal stability, MOFs have been studied for a range of applications, including catalysis [16], gas storage [17,18], enzyme carriers [19,20], sensing [21], and adsorption [22–24]. The adsorption capacities of MOFs toward dyes are remarkable [25]. Tian et al. prepared a water-stable cationic Fe-based metal organic framework (CPM-97-Fe) for the adsorption of both anionic and cationic dyes, with adsorption capacities ranging from 157 to 831 mg/g [26]. There are many types of MOFs and, depending on the material, they can range from low to high cost. The lowest cost materials are those whose synthesis is rapid and requires mild conditions as well as environmentally-friendly solvents and reagents. Recently, Sanchez-Sanchez et al. proposed a facile and rapid method to synthesize a Basolite F300-like Fe-BTC MOF under environmentally and economically sustainable conditions (few minutes at room temperature using water as solvent) [27]. This material, was used as a support for enzyme immobilization [28]. To the best of our knowledge, there are only a few studies about dyes' adsorption using Fe-BTC [29–33]. While adsorption properties of Fe-BTC are significant (e.g., up to 1105 mg/g of methylene blue) [34], the synthetic procedures used require high temperatures or the use of organic solvents.

The purpose of this work was to examine the adsorption properties of a Fe-BTC MOF, synthesized according to the method described by Sanchez-Sanchez et al. [27], to remove the anionic dye alizarin red S (ARS) and the cationic dye malachite green (MG) from water (Scheme 1). ARS is a synthetic anthraquinonic acid–base indicator [35,36], used in histology to stain and locate calcium deposits in tissues [37], in geology to identify carbonate minerals, and widely used in textile dyeing. MG is a toxic and carcinogenic triphenylmethane dye, and is widely used in the textile and food industries, as well as in aquaculture as an antifungal, antimicrobial, and antiparasitic agent [38–41]. The synthesized MOF was characterized by means of XRD (X-ray diffraction), N_2 -adsorption isotherms, SEM (Scanning Electro Microscopy), FTIR (Fourier-Transform Infrared Spectroscopy), TGA (Thermogravimetric Analysis), and ELS (Electrophoretic Light Scattering) techniques. The adsorption kinetics and isotherms of MG and ARS on Fe-BTC MOF were determined in water at room temperature (298 K) by means of UV-Vis spectroscopy to examine the application of Fe-BTC MOF for the removal of toxic dyes from waters.



Scheme 1. Use of Fe-BTC metal organic framework (MOF) for adsorption of alizarin red (S) and malachite green.

2. Results

2.1. Physico-Chemical Characterizations

Figure 1a shows the XRD pattern of the synthesized Fe-BTC MOF. The pattern is well resolved with peaks at $2\theta = 11^\circ, 19^\circ, 24^\circ, 28^\circ$ and 34° , in agreement with the literature reports for Fe-BTC MOF [42,43]. The surface area and pore size distribution were obtained by N_2 adsorption/desorption isotherms (Figure 1b), using the Brunauer–Emmett–Teller (BET) and Barrett–Joyner–Halenda (BJH) methods. The specific surface area was $443 \text{ m}^2/\text{g}$ and a multi-modal pore size distribution ranged from 4 to 40 nm (Figure S2). Thermogravimetric analysis (Figure 1c) showed a typical two-step decomposition pattern. The initial mass loss at $T < 100^\circ\text{C}$ is due to the removal of water from the powder. The mass loss in the range $100\text{--}325^\circ\text{C}$ can be attributed to the loss of coordination water [44]. Finally, the mass loss from 325 to 520°C is ascribed to the decomposition of the organic moiety (trimesic acid) of the MOF [45,46]. The FTIR spectrum of Fe-BTC MOF is shown in Figure 1d. The broad band from 3400 to 3600 cm^{-1} is due to the O-H stretching of adsorbed water. The bands at 1627 and 1572 cm^{-1} and at 1450 and 1372 cm^{-1} are assigned to the asymmetric and the symmetric stretching of the carboxylate groups of Fe-BTC [29,46,47], respectively. The peaks between 770 and 450 cm^{-1} are due to the bending of aromatic C-H bonds.

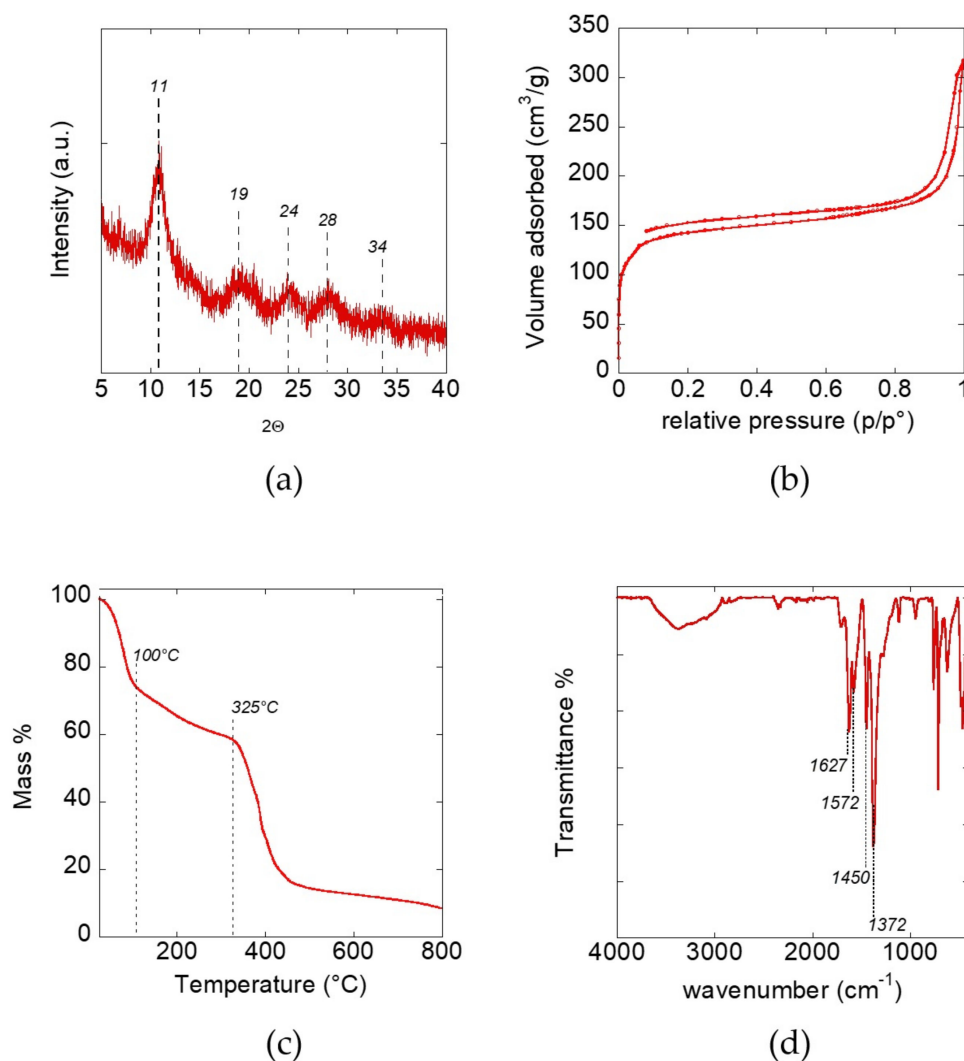
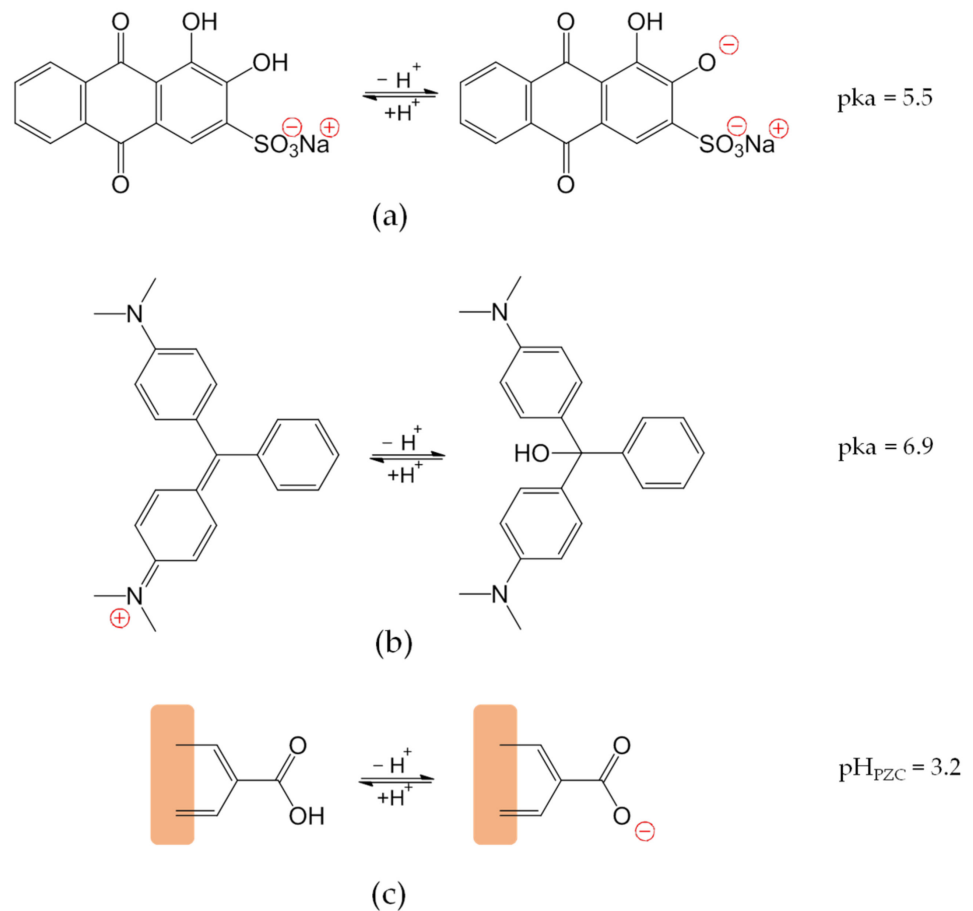


Figure 1. Characterization of Fe-BTC MOF. (a) XRD pattern; (b) N_2 physisorption isotherm; (c) Thermogravimetric analysis; (d) FT-IR spectrum.

2.2. Effect of pH on Dyes Adsorption on Fe-BTC MOF

The synthesized Fe-BTC MOF was used to adsorb alizarin red S (ARS) and malachite green (MG) from water. Some studies have shown that dye adsorption on MOFs was governed by electrostatic interactions [48]. Thus, it is expected that the pH of the adsorbing solution affects the amount of adsorbed dye as a consequence of the presence/absence of electric charges on both the dye molecules and the adsorbent surface. The pK_a of ARS and MG are 5.5 [49] and 6.9 [39], respectively. The former is due to the dissociation of one of the phenolic groups (Scheme 2) [50], and the latter to the conversion of the cation into a carbinol base through addition of OH^- (Scheme 2) [51,52].



Scheme 2. Acid–base equilibria of (a) Alizarin red S (ARS) (b) Malachite green (MG) and (c) Fe-BTC MOF.

The zeta potential of Fe-BTC suspension in water was measured over the pH range 3–7 (Figure 2a and Table S1). Fe-BTC is slightly positive at pH 3 ($\zeta = +8.3 \pm 3$ mV) and is negatively charged at pH > 4 ($\zeta = -10.3 \pm 3$ mV) with a pH_{PZC} (point of zero charge) value of about 3.2 [53], in agreement with the literature [32]. Figure 2b shows the effect of pH on the adsorbed amount at equilibrium (q_e , mg/g) of ARS and MG on Fe-BTC. The q_e values of MG are generally higher than those of ARS. Moreover, while the q_e of MG is unaffected by pH, that of ARS linearly decreases in the pH range 3–7.

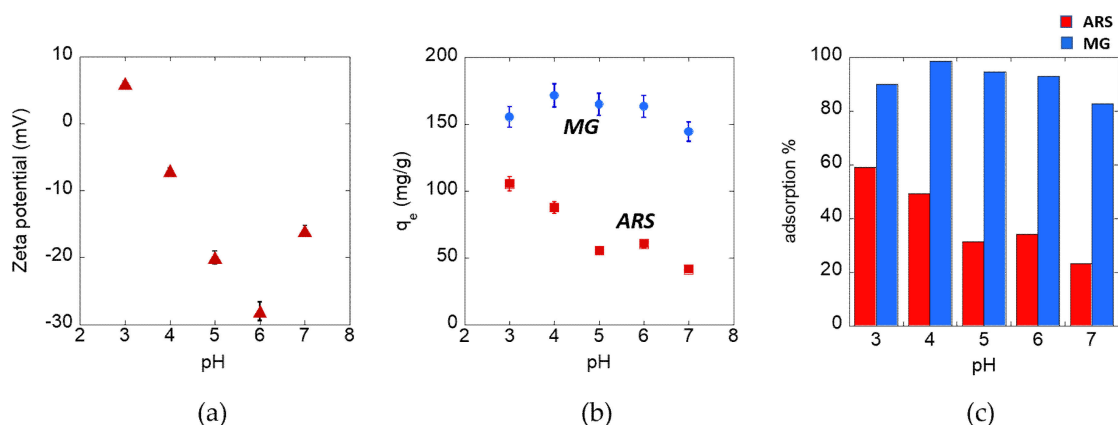


Figure 2. (a) Zeta potential of Fe-BTC as a function of pH; (b) Adsorption capacity (q_e) of Fe-BTC toward ARS and MG as a function of pH; (c) Percentage adsorption of dyes as a function of pH.

Since the pH_{PZC} (point of zero charge) of Fe-BTC is ca. 3.2 [53], anionic dyes are adsorbed to a lower extent than cationic dyes [54]. Hence, as compared with ARS, higher amounts of MG would be expected to be adsorbed. The two dyes also show different adsorption efficiency (adsorbed amount %) trends (Figure 2c and Table S1) with Fe-BTC possessing a maximum MG adsorption value of 98.5% at pH 4, while the highest value for ARS was 59.1% at pH 3 (Figure 2c). At pH 7, the adsorption capacity was still high for MG (82.9%), but quite low for ARS (23.3%). These trends can be explained by the fact that, at pH 7, MG is neutral, and thus adsorption would predominantly occur via van der Waals forces and would not be affected by electrostatic interactions. Adsorption of ARS on Fe-BTC is not favored at pH 7 as both the dye and the adsorbent are negatively charged.

2.3. Adsorption Kinetics

The adsorption kinetics of MG and ARS on Fe-BTC MOF were examined in aqueous solution (pH = 4, 298 K). The adsorption process was rapid for both dyes, reaching equilibrium values (corresponding to the plateau in Figure 3a) in 30 min for ARS and 15 min for MG. Under these conditions ($T = 298$ K, pH = 4, initial concentrations of MG and ARS of 1.5 mM), the q_e of MG on Fe-BTC MOF was 177.3 mg/g, while that of ARS reached $q_e = 80.4$ mg/g. The experimental data were fitted to three different kinetic models, namely, the pseudo-first order (Figure 3b), the pseudo-second order (Figure 3c), and the intraparticle diffusion models (Figure 3d). The kinetic parameters obtained by each model are listed in Table 1. The fitting of the experimental data using the pseudo-first order gave low correlation coefficients (Table 1), thus, demonstrating the inadequacy of this model to describe both ARS and MG adsorption on Fe-BTC. On the contrary, the pseudo-second order model resulted in a very good fitting, as demonstrated by the high correlation coefficients ($R > 0.99$) and a good residuals plot (Figure S3b). Moreover, the values of q_e calculated from pseudo-second order models (177.31 mg/g for MG and 81.09 mg/g for ARS) are very similar to the experimentally observed values (177.28 mg/g for MG and 80.39 mg/g for ARS, Figure 3a). The values of the kinetic constant (k'') confirmed that the adsorption process for MG ($k'' = 3.98 \times 10^{-2}$ g·mg⁻¹ min⁻¹) was faster than that for ARS ($k'' = 4.29 \times 10^{-3}$ g·mg⁻¹ min⁻¹). The fit of the model to the adsorption data demonstrate that the adsorption of the dyes on the adsorbent sites is the rate determining step [29,55]. Figure 3d shows the variation of q_t versus $t^{0.5}$ according with the intraparticle diffusion model. The slopes of the three straight lines in Figure 3d represent the kinetic constants of the different steps (1, external diffusion; 2, internal diffusion; and 3, adsorption) involved in the adsorption of ARS and MG dyes on Fe-BTC MOF. However, the fit of this model is of lower quality than that of the pseudo-second order model (Figure S3c), which gives the best description of the obtained kinetic data.

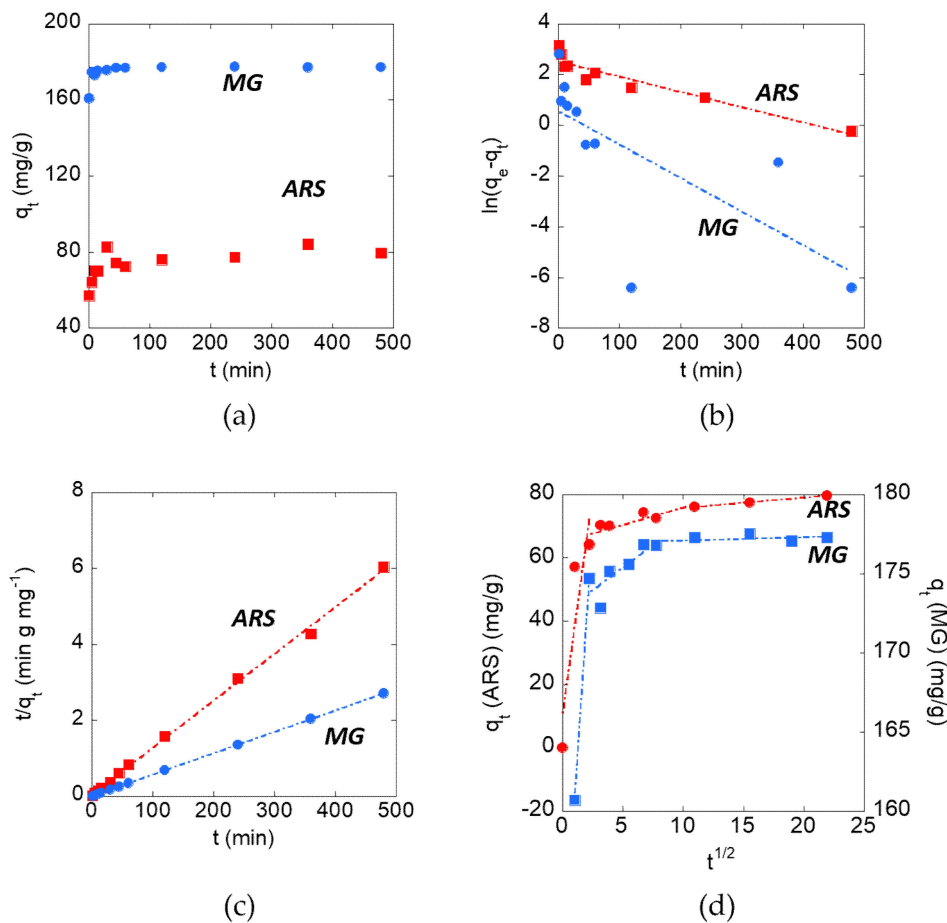


Figure 3. (a) Amount of alizarin red S and malachite green adsorbed, q_t , as a function of contact time. The data were fit using linearized kinetics models; (b) Pseudo-first order; (c) Pseudo-second order; (d) Intraparticle diffusion. The experiments were carried out in water at pH = 4 and $T = 298$ K.

Table 1. Comparison among different adsorption kinetic models for MG and ARS on Fe-BTC MOF.

	$q_{e\ exp}$ (mg g^{-1})	Pseudo-First Order			Pseudo-Second Order			Intraparticle Diffusion		
		k' (min^{-1})	$q_{e\ cal}$ (mg g^{-1})	R	k'' ($\text{g mg}^{-1} \text{min}^{-1}$)	$q_{e\ cal}$ (mg g^{-1})	R	k_i ($\text{g mg}^{-1} \text{min}^{-1/2}$)	x_i (mg g^{-1})	R
ARS	80.39	5.98×10^{-3}	12.78	0.946	4.29×10^{-3}	81.09	0.992	27.77 1.10 0.33	10.44 64.81 72.38	0.885 0.873 0.999
MG	177.28	1.3210^{-2}	1.75	0.707	3.98×10^{-2}	177.31	1	11.33 0.58 0.02	149.38 172.51 176.88	1 0.828 0.434

2.4. Adsorption Isotherms

The adsorption isotherms of ARS and MG on Fe-BTC MOF ($T = 298$ K, pH 4) are shown in Figure 4a. The MOF adsorbed MG to a greater extent than ARS, reaching the maximal adsorbed amounts ($q_{e,max}$), corresponding to the isotherm plateaus, $q_{e,max} = 177.3$ mg/g and $q_{e,max} = 80.4$ mg/g for MG and ARS, respectively. Then, experimental data were tested by applying a fitting procedure based on different linearized isotherm models, namely, Temkin (Figure 4b), Freundlich (Figure 4c), and Langmuir (Figure 4d). The constants associated with each model are reported in Table 2.

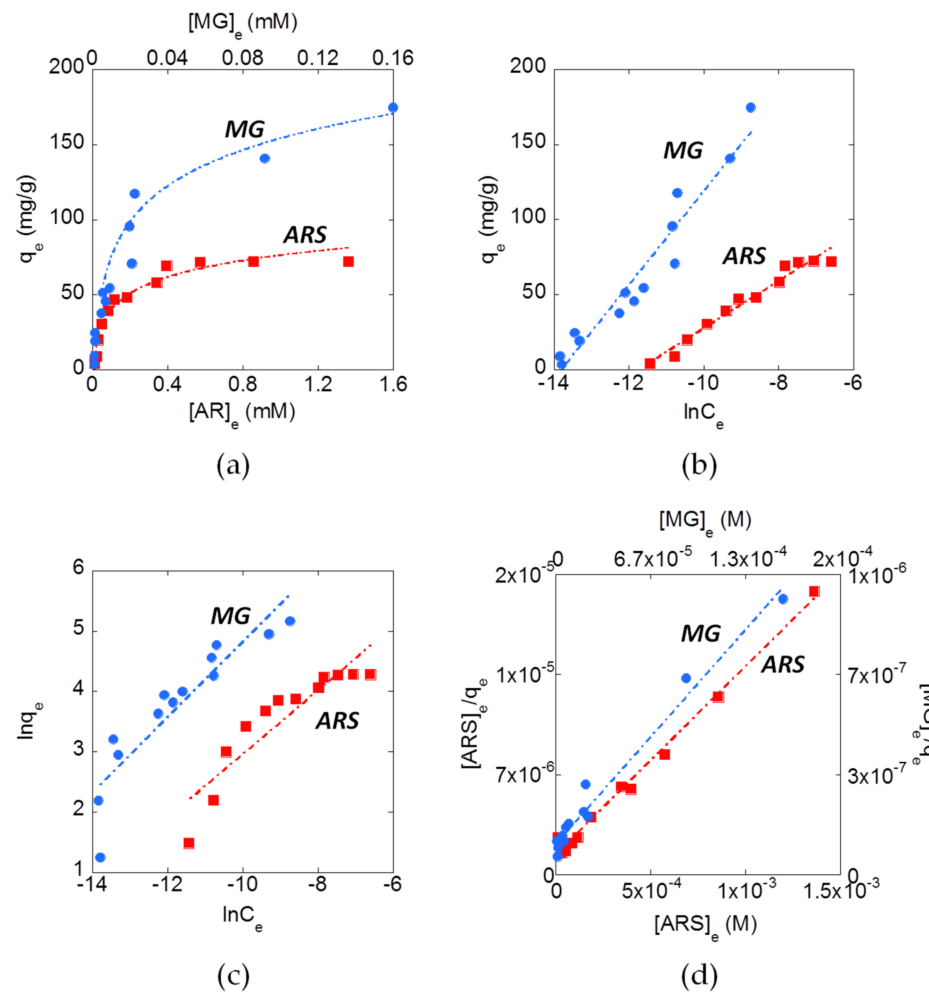


Figure 4. (a) Adsorption isotherms of MG and ARS with MOF where q_e is a function of the equilibrium concentration. Adsorption data were fitted using linearized isotherms; (b) Temkin; (c) Freundlich; (d) Langmuir. The experiments were carried out in distilled water for 24 h, at $T = 298$ K.

Table 2. Comparison among different isotherm models for ARS and MG adsorption on Fe-BTC MOF ($\text{pH} = 4$, $T = 298$ K).

	b_T	Temkin		Freundlich			Langmuir			ΔG° (KJ mol ⁻¹)
		A_T (L mg ⁻¹)	R	K_F (L mg ⁻¹)	$1/n$	R	K_L (L mg ⁻¹)	$q_{e,max}$ (mg g ⁻¹)	R	
ARS	157.59	$1.28 \cdot 10^5$	0.982	$3.85 \cdot 10^3$	0.529	0.910	$9.30 \cdot 10^3$	79.88	0.995	-54.21
MG	79.34	$9.87 \cdot 10^5$	0.967	$63.77 \cdot 10^3$	0.624	0.909	$51.56 \cdot 10^3$	187.24	0.967	-58.61

By comparing the correlation coefficients (R) obtained by applying the different linearized isotherms to the experimental data, with the resulting residual plots (Figure S4), the Langmuir model fits the experimental data better than the other two models. This indicates that a monolayer of adsorbate (dye molecules) was formed on the adsorbent surface (Fe-BTC MOF). Generally, the larger the Langmuir constant K_L , the more favorable the adsorption process [56]. This confirms that adsorption of MG ($K_L = 51.56 \cdot 10^3$ L/mg) was favored over that of ARS ($K_L = 9.30 \cdot 10^3$ L/mg) [57]. Then, the Langmuir constant, K_L , was used to calculate the thermodynamic equilibrium constant K_e^0 by means of the equation [58] as:

$$K_e^0 = \frac{K_L M M_{\text{Adsorbate}} [\text{Adsorbate}]^0}{\gamma} \quad (1)$$

where $MM_{\text{Adsorbate}}$ is the molecular mass of the adsorbate ($MM_{\text{MG}} = 364.91 \text{ g mol}^{-1}$ and $MM_{\text{ARS}} = 342.26 \text{ g mol}^{-1}$), $[\text{Adsorbate}]^\circ$ is the standard concentration of the adsorbate (1 mol L^{-1}), and γ is the activity coefficient (dimensionless) that can be considered to have a value of 1 in dilute solution. The K_e^0 values thus calculated were used to determine the standard Gibbs free energy (ΔG^0) for the adsorption process, according to the relationship:

$$\Delta G^0 = -RT \ln K_e^0 \quad (2)$$

where R is the universal gas constant ($8.314 \text{ J K}^{-1} \text{ mol}^{-1}$) and T is the absolute temperature (298.13 K). As shown in Table 2, ΔG^0 values were $-54.21 \text{ kJ mol}^{-1}$ and $-58.61 \text{ kJ mol}^{-1}$ for the adsorption of ARS and MG, respectively. This indicates that, in standard conditions, the desorption \rightleftharpoons adsorption equilibrium lies far to the right for both dyes, in agreement with experimental observations.

3. Discussion

The adsorption of malachite green on a range of MOFs has been reported [59–62]. Table 3 summarizes the data from studies relevant to the present work. Among the various types of MOFs tested, the lowest performing in terms of dye adsorption capacity were Cu-BTC [57] and Mil-53-Al-NH₂ [59]. Both the ZIF-67 prepared by Jin et al. [61] and the UiO-66 prepared by Embaby et al. [55] acted as strong adsorbents with q_e values of 2545 and 400 mg/g, respectively, with adsorption times between 30 and 60 min. The Fe-BTC synthesized by Huo et al. [32] and the mixed-ligand Cu-BDC-BTC compound prepared by Shi et al. [60] had adsorption capacities comparable to those obtained here, 205 and 185 mg/g, respectively, but the time required for the adsorption process (120 min) was four times higher than that obtained by us (30 min).

Table 3. Comparison with other systems like that studied in this article.

Adsorbent	T (°C)	Synthesis		Dye	$q_e^{(exp)}$ (mg/g)	t (min)	Kinetic k'' (g·mg ⁻¹ ·min)	Isotherm		Ref.
		t (h)	Solvent					Model	K (L·mg ⁻¹)	
Fe-BTC	25	<1	H ₂ O	Alizarin red S	80	30	4.29×10^{-3}	Langmuir	$9.30 \cdot 10^3$	This work
				Malachite green	177	30	3.98×10^{-2}	Langmuir	$51.56 \cdot 10^3$	
Fe-BTC	150	12	H ₂ O	Malachite green	205	120	$6.67 \cdot 10^{-3}$	Freundlich	6.49	[32]
UiO-66	120	1	DMF	Alizarin red S	400	36	$2.3 \cdot 10^{-4}$	Langmuir	0.06	[55]
Cu-BTC	100	10	EtOH/DMF	Methylene blue	4.68	10	42.39	Langmuir	1.89	[57]
Mil-53(Al)-NH ₂	150	24	DMF/H ₂ O	Malachite green	37.8	200	-	Langmuir	0.29	[59]
				Methylene blue	45.2	200	-	Langmuir	0.67	
Cu-BTC/BDC	120	12	EtOH	Malachite green	185	-	-	Freundlich	-	[60]
ZIF-67/PAN	25	<1	H ₂ O	Malachite green	2545	60	$2.7 \cdot 10^{-3}$	Langmuir	0.05	[61]
NH-ZIF-67	25	<1	MeOH	Malachite green	114.1	240	-	-	-	[62]

Li et al. found that the absorption capacity of MIL-53(Al) increased after functionalization with amino groups [59], an increase that can be attributed to hydrogen bond interactions [62] between the amino groups of the dye molecules and the amino groups of MIL-53(Al)-NH₂; the adsorption capacity achieved by this system is, however, rather low (45.2 mg/g in the case of methylene blue and 37.8 mg/g in the case of malachite green). Jin et al. prepared a ZIF-67 MOF integrated on a polyacrylonitrile membrane to recover the MOF from water solution at the end of the adsorption process [61]. This system had an adsorption capacity of 2545 mg/g of MG, and the time required to complete the process was 60 min. The only study reported to date on the adsorption of alizarin red S by MOFs (Table 3) was carried out by Embaby et al., who reported an adsorption capacity of 400 mg/g for ARS on zirconium-based MOF UiO-66 [55].

Most studies have confirmed that the Langmuir isotherm is the optimal model to describe the adsorption of dyes on the MOF materials described in this study, with the

pseudo-second order model representing the best kinetic model. However, in addition to fast kinetics and a high adsorbing capacity, the successful use of an adsorbent for environmental remediation should not be assessed only based on its performance, but also in terms of factors such as cost and ease of preparation. The majority of reports on the use of MOFs utilize synthetic methods that use organic solvents and/or high temperatures. For example, among the adsorbents with higher q_e , the synthesis of UiO-66 was carried out in 1 h in dimethylformamide at 120 °C [55], while Cu-BDC-BTC was prepared in ethanol by heating to 120 °C, for 12 h [60]. The Fe-BTC synthesized by Huo et al., despite being prepared in water, required long synthetic times (12 h) and high temperatures (150 °C in an autoclave) [32]. The most interesting material, both from the point of view of the high adsorbing capacity and of synthesis conditions (25 °C in H₂O), was the ZIF-67/PAN fibrous membrane proposed by Jin et al. [61]. However, one of the starting reagents of this MOF is the 2-methylimidazole, which is a carcinogenic compound [63,64]. The Fe-BTC used here is significantly easier (and lower cost) to prepare, in an environmentally-friendly manner, with synthesis in less than 1 h at room temperature, using distilled water as the solvent and the reagents, FeCl₃ and trimesic acid.

4. Material and Methods

4.1. Chemicals

Tris(hydroxymethyl)-aminomethane (TRIS, ≥99.8%) was purchased from Bio-Rad Laboratories. Iron(III) chloride (97%), sodium hydroxide, trimesic acid, and 4-[[4-(dimethylamino)phenyl](phenyl)methylidene]-*N,N*-dimethylcyclohexa-2,5-dien-1-iminium chloride (malachite green) were purchased from Sigma-Aldrich. 3,4-Dihydroxy-9,10-dioxo-2-anthracenesulfonic acid (alizarin red S) was purchased as the sodium salt from Fluka Chemie.

4.2. Synthesis and Characterization of Fe-BTC MOF

The Fe-BTC type MOF was prepared following the procedure reported by Sanchez-Sanchez et al. [27,65]. Briefly, 0.3048 g of FeCl₃ was dissolved in 10.203 mL of distilled water. Then, a solution containing 0.263 g of trimesic acid, 3.685 mL of NaOH 1.06 M, and 6.388 mL of H₂O was added dropwise under stirring. The solid was collected by filtration under vacuum, washed with distilled water, and dried in air.

X-ray diffraction (XRD) analysis was carried out using an X'PERT Pro PANalytical diffractometer using a Cu K_α radiation source. The data were collected from 5 to 40° with a 2θ step size of 0.013, for 99.19 s. The N₂ adsorption/desorption isotherms at 77 K were carried out on a ASAP 2020 (Micromeritics) instrument to obtain the surface area (Brunauer–Emmett–Teller, BET) [66] and pore size distribution (Barrett–Joyner–Halenda, BJH) [67]. The FTIR analysis was performed using a Bruker Tensor 27 spectrophotometer equipped with a diamond-ATR accessory and a DTGS detector. A number of 128 scans at a resolution of 2 cm⁻¹ were averaged in the spectral range 4000–400 cm⁻¹. Thermal analysis data were collected with a STA6000 (Perkin Elmer) thermal analyzer in the 25–850 °C range, under oxygen flow (heating rate = 10 °C/min, flow rate = 40 mL min⁻¹). The Zeta potential of Fe-BTC was measured using a Zetasizer Nano ZSP (Malvern Instruments) in backscatter configuration (θ = 173°), at a laser wavelength of λ = 633 nm, using Zetasizer software (version 7.03) to analyze the data. Zeta potential values were calculated by means of the Henry equation using water as the dispersant medium (ε_r = 78.5 and η = 0.89 cP at 25 °C) and $f(\kappa a) = 1.5$ (Smoluchowski approximation). The sample was prepared by suspending Fe-BTC (2 mg/mL) in distilled water adding HCl and NaOH to vary the pH from 3 to 7. Before the measurements the samples were sonicated for 30 min and left stirring overnight. The scattering cell temperature was fixed at 25 °C.

4.3. Adsorption Studies

A mass of 100 mg of the synthesized MOF was dispersed in 1 mL of distilled water using a vortex mixer (Figure S1a). To evaluate the optimal pH for the adsorption process, a series of Eppendorf tubes were filled with 1 mL of dye solution and 35 μL of solid dispersion

(Figure S1a) at different pH in the range 3–7. The pH was measured using a Metrohm pH-meter and adjusted adding small volumes of HCl and NaOH solutions. All the mixtures were put in a rotating mixer overnight, and then collected by centrifugation (1000 rpm for 1 min). The concentration of dye in the solutions before and after adsorption experiments was determined using a Cary 60 UV-Vis spectrophotometer (Agilent) ($\lambda = 516$ nm for ARS and 620 nm for MG). The solutions were diluted in Tris-HCl buffer (pH 7, 10 mM) to ensure a constant pH during the measurements, since the absorbance peaks of the dyes, especially in the case of ARS, are influenced by pH [68,69].

Adsorption kinetic studies were carried out analyzing samples withdrawn at different times (from 1 min to 8 h) at a fixed pH of 4 and at a constant concentration of the dyes (1.5 mM). Adsorption isotherms at $T = 298$ K were obtained at constant adsorption time (24 h) and pH (4) at varying initial dye concentrations (from 0.01 to 2 mM).

4.3.1. Adsorption Kinetic Models

The adsorption kinetics were studied by measuring the decrease in concentration of the dyes in solution at given times (q_t) through the following equation,

$$q_t = \frac{(C_i - C_t)V}{m} \quad (3)$$

where C_i and C_t are the dye concentrations at time = 0 and time = t , while V and m are the volumes of the solution and the mass of the solid, respectively.

The experimental data were fitted using the linearized equations of three different kinetic models. A pseudo-first order model as follows:

$$\ln(q_e - q_t) = \ln q_e - k' \cdot t \quad (4)$$

A pseudo-second order model [70,71] as follows:

$$\frac{t}{q_t} = \frac{1}{q_e^2 \cdot k''} + \frac{t}{q_e} \quad (5)$$

and an intraparticle diffusion model [72] as follows:

$$q_e = k_i \cdot t^{1/2} + x_i \quad (6)$$

where q_e is the amount of adsorbed dye at the equilibrium, k' , k'' and k_i are the pseudo-first order constant, pseudo-second order constant, and intraparticle diffusion constant, respectively.

4.3.2. Adsorption Isotherm Models

The adsorption isotherms were obtained by plotting the experimentally adsorbed amounts of dyes, q_e , versus the equilibrium concentration, C_e . The experimental data were fitted through three different isotherm models', i.e., Temkin (Equation (7)), Freundlich (Equation (8)), and Langmuir (Equation (9)), in their linearized forms [73]:

$$q_e = \frac{RT}{b_T} \ln A_T + \frac{RT}{b_T} \ln C_e \quad (7)$$

where q_e is the amount of adsorbed dye at the equilibrium, $q_{e,max}$ is the maximum monolayer coverage capacity, b_T is the Temkin constant, and A_T is the Temkin equilibrium binding constant.

$$\ln q_e = \ln K_F + \frac{1}{n} \ln C_e \quad (8)$$

where $1/n$ (dimensionless) and K_F are the Freundlich constants, the heterogeneity factor, and support capacity (characteristic of each adsorbate-adsorbent pair), respectively.

$$\frac{C_e}{q_e} = \frac{1}{q_m \cdot K_L} + \frac{1}{q_m} C_e \quad (9)$$

where K_L is the Langmuir constant [5,74].

5. Conclusions

An Fe-BTC MOF was synthesized following the procedure proposed by Sanchez-Sanchez et al. The structure of the material was characterized by XRD, while its pore diameter distribution (4–40 nm) and surface area (443 m²/g) were determined from N₂ adsorption/desorption isotherms. The zeta potential of aqueous dispersions of Fe-BTC was determined by ELS and a point of zero charge (pH_{pzc}) of 3.2 was obtained. Further qualitative characterizations were carried out using FTIR and TGA techniques. The data obtained were comparable with those reported in the literature. Then, the Fe-BTC was used as an adsorbent for the removal of two toxic dyes from water, alizarin red S (ARS) and malachite green (MG). The adsorption capacity was measured as a function of time and of the concentration of dye required to obtain the kinetic profiles and the adsorption isotherms of the process, respectively. The adsorption of both dyes was rapid (<30 min) as compared with other reports, which reached equilibrium generally in 60–200 min. The Langmuir model provided the best fit to the adsorption process, with maximum adsorption capacities of 80 and 177 mg/g for ARS and MG on Fe-BTC MOF, respectively. The data obtained for adsorption on to Fe-BTC MOF compare favorably with literature reports. However, what distinguishes this work is the green method used to synthesize the adsorbing material. Indeed, the synthesis of the Fe-BTC MOF was performed in an aqueous solution at room temperature in less than 1 h, unlike the generally used syntheses which require organic solvents or high temperatures and longer times. Furthermore, the adsorption rate of the dyes was higher than most of the other reported MOFs. Future work could be devoted to test the adsorption performance of other toxic dyes or even other classes of toxic substances and to verify the feasibility of continuous processes or on a larger scale. Further work is needed to find the optimal conditions for dye desorption and MOF reuse for multiple adsorption cycles.

Supplementary Materials: Supplementary materials can be found at <https://www.mdpi.com/1422-0067/22/2/788/s1>.

Author Contributions: Conceptualization, A.S. and G.R.D.; investigation, G.R.D. and D.T.; data curation, writing—original draft preparation, G.R.D., D.T., L.M., E.M., and A.S.; writing—review and editing, G.R.D., D.T., L.M., E.M., and A.S.; supervision, A.S. and E.M. All authors have read and agreed to the published version of the manuscript.

Funding: This research was funded by MIUR PON-RI (DOT1304455).

Institutional Review Board Statement: Not applicable.

Informed Consent Statement: Not applicable.

Data Availability Statement: The data presented in this study are available in this paper and supplementary file.

Acknowledgments: W. Redington and F. Otero Diez (University of Limerick) for the XRD characterization.

Conflicts of Interest: The authors declare no conflict of interest. The funders had no role in the design of the study; in the collection, analyses, or interpretation of data; in the writing of the manuscript, or in the decision to publish the results.

Abbreviations

MOF	Metal organic frameworks
MG	Malachite green
ARS	Alizarin red S
XRD	X-ray diffraction
FTIR	Fourier transform infrared spectroscopy
TGA	Thermogravimetric analysis

References

1. Hessel, C.; Allegre, C.; Maisseu, M.; Charbit, F.; Moulin, P. Guidelines and legislation for dye house effluents. *J. Environ. Manag.* **2007**, *83*, 171–180. [[CrossRef](#)] [[PubMed](#)]
2. Martínez-Huitle, C.A.; Brillas, E. Decontamination of wastewaters containing synthetic organic dyes by electrochemical methods: A general review. *Appl. Catal. B Environ.* **2009**, *87*, 105–145. [[CrossRef](#)]
3. Bilal, M.; Asgher, M. Sandal reactive dyes decolorization and cytotoxicity reduction using manganese peroxidase immobilized onto polyvinyl alcohol-alginate beads. *Chem. Cent. J.* **2015**, *9*, 47. [[CrossRef](#)] [[PubMed](#)]
4. Zhang, F.; Ma, B.; Jiang, X.; Ji, Y. Dual function magnetic hydroxyapatite nanopowder for removal of malachite green and Congo red from aqueous solution. *Powder Technol.* **2016**, *302*, 207–214. [[CrossRef](#)]
5. Mashkoo, F.; Nasar, A.; Inamuddin; Asiri, A.M. Exploring the reusability of synthetically contaminated wastewater containing crystal violet dye using tectona grandis sawdust as a very low-cost adsorbent. *Sci. Rep.* **2018**, *8*, 1–16. [[CrossRef](#)]
6. Collivignarelli, M.C.; Abbà, A.; Carnevale Miino, M.; Damiani, S. Treatments for color removal from wastewater: State of the art. *J. Environ. Manag.* **2019**, *236*, 727–745. [[CrossRef](#)]
7. Amaterz, E.; Tara, A.; Bouddouch, A.; Taoufyq, A.; Bakiz, B.; Lazar, F.; Gilliot, M.; Benhachemi, A.; Bazzi, L.; Jbara, O. Hierarchical flower-like SrHPO₄ electrodes for the photoelectrochemical degradation of Rhodamine B. *J. Appl. Electrochem.* **2020**. [[CrossRef](#)]
8. Zhang, X.; Shao, D.; Lyu, W.; Xu, H.; Yang, L.; Zhang, Y.; Wang, Z.; Liu, P.; Yan, W.; Tan, G. Design of magnetically assembled electrode (MAE) with Ti/PbO₂ and heterogeneous auxiliary electrodes (AEs): The functionality of AEs for efficient electrochemical oxidation. *Chem. Eng. J.* **2020**, *395*. [[CrossRef](#)]
9. Ge, Q.; Wang, P.; Wan, C.; Chung, T.S. Polyelectrolyte-promoted Forward Osmosis-Membrane Distillation (FO-MD) hybrid process for dye wastewater treatment. *Environ. Sci. Technol.* **2012**, *46*, 6236–6243. [[CrossRef](#)]
10. Yang, C.; Xu, W.; Nan, Y.; Wang, Y.; Hu, Y.; Gao, C.; Chen, X. Fabrication and characterization of a high performance polyimide ultrafiltration membrane for dye removal. *J. Colloid Interface Sci.* **2020**, *562*, 589–597. [[CrossRef](#)]
11. Bukman, L.; De Souza, V.R.; Fernandes, N.R.C.; Caetano, W.; Batistela, V.R.; Hioka, N. Reverse micellar extraction of dyes based on fatty acids and recoverable organic solvents. *Sep. Purif. Technol.* **2020**, *242*. [[CrossRef](#)]
12. Madhushika, H.G.; Ariyadasa, T.U.; Gunawardena, S.H.P. Biological decolourization of textile industry wastewater by a developed bacterial consortium. *Water Sci. Technol.* **2020**, *80*, 1910–1918. [[CrossRef](#)]
13. Katheresan, V.; Kannedo, J.; Lau, S.Y. Efficiency of various recent wastewater dye removal methods: A review. *J. Environ. Chem. Eng.* **2018**, *6*, 4676–4697. [[CrossRef](#)]
14. Rodríguez-Couto, S.; Osma, J.F.; Toca-Herrera, J.L. Removal of synthetic dyes by an eco-friendly strategy. *Eng. Life Sci.* **2009**, *9*, 116–123. [[CrossRef](#)]
15. Furukawa, H.; Cordova, K.E.; O’Keeffe, M.; Yaghi, O.M. The chemistry and applications of metal-organic frameworks. *Science* **2013**, *341*. [[CrossRef](#)] [[PubMed](#)]
16. Jiao, L.; Wang, Y.; Jiang, H.L.; Xu, Q. Metal–Organic Frameworks as Platforms for Catalytic Applications. *Adv. Mater.* **2018**, *30*, e1703663. [[CrossRef](#)]
17. Alqadami, A.A.; Naushad, M.; Alothman, Z.A.; Ahamad, T. Adsorptive performance of MOF nanocomposite for methylene blue and malachite green dyes: Kinetics, isotherm and mechanism. *J. Environ. Manag.* **2018**, *223*, 29–36. [[CrossRef](#)]
18. Ghanbari, T.; Abnisa, F.; Wan Daud, W.M.A. A review on production of metal organic frameworks (MOF) for CO₂ adsorption. *Sci. Total Environ.* **2020**, *707*, 135090. [[CrossRef](#)]
19. Pitzalis, F.; Carucci, C.; Naseri, M.; Fotouhi, L.; Magner, E.; Salis, A. Lipase Encapsulation onto ZIF-8: A Comparison between Biocatalysts Obtained at Low and High Zinc/2-Methylimidazole Molar Ratio in Aqueous Medium. *ChemCatChem* **2018**, *10*, 1578–1585. [[CrossRef](#)]
20. Naseri, M.; Pitzalis, F.; Carucci, C.; Medda, L.; Fotouhi, L.; Magner, E.; Salis, A. Lipase and Laccase Encapsulated on Zeolite Imidazolate Framework: Enzyme Activity and Stability from Voltammetric Measurements. *ChemCatChem* **2018**, *10*, 5425–5433. [[CrossRef](#)]
21. Lustig, W.P.; Mukherjee, S.; Rudd, N.D.; Desai, A.V.; Li, J.; Ghosh, S.K. Metal-organic frameworks: Functional luminescent and photonic materials for sensing applications. *Chem. Soc. Rev.* **2017**, *46*, 3242–3285. [[CrossRef](#)] [[PubMed](#)]
22. Li, J.; Wang, X.; Zhao, G.; Chen, C.; Chai, Z.; Alsaedi, A.; Hayat, T.; Wang, X. Metal-organic framework-based materials: Superior adsorbents for the capture of toxic and radioactive metal ions. *Chem. Soc. Rev.* **2018**, *47*, 2322–2356. [[CrossRef](#)] [[PubMed](#)]
23. Samokhvalov, A. Adsorption on Mesoporous Metal-Organic Frameworks in Solution: Aromatic and Heterocyclic Compounds. *Chem. Eur. J.* **2015**, *21*, 16726–16742. [[CrossRef](#)] [[PubMed](#)]

24. Jiang, D.; Chen, M.; Wang, H.; Zeng, G.; Huang, D.; Cheng, M.; Liu, Y.; Xue, W.; Wang, Z.W. The application of different typological and structural MOFs-based materials for the dyes adsorption. *Coord. Chem. Rev.* **2019**, *380*, 471–483. [[CrossRef](#)]
25. Lv, S.W.; Liu, J.M.; Wang, Z.H.; Ma, H.; Li, C.Y.; Zhao, N.; Wang, S. Recent advances on porous organic frameworks for the adsorptive removal of hazardous materials. *J. Environ. Sci. (China)* **2019**, *80*, 169–185. [[CrossRef](#)] [[PubMed](#)]
26. Tian, S.; Xu, S.; Liu, J.; He, C.; Xiong, Y.; Feng, P. Highly efficient removal of both cationic and anionic dyes from wastewater with a water-stable and eco-friendly Fe-MOF via host-guest encapsulation. *J. Clean. Prod.* **2019**, *239*, 117767. [[CrossRef](#)]
27. Sanchez-Sanchez, M.; De Asua, I.; Ruano, D.; Diaz, K. Direct Synthesis, Structural Features, and Enhanced Catalytic Activity of the Basolite F300-like Semiamorphous Fe-BTC Framework. *Cryst. Growth Des.* **2015**, *15*, 4498–4506. [[CrossRef](#)]
28. Gascón, V.; Carucci, C.; Jiménez, M.B.; Blanco, R.M.; Sánchez-Sánchez, M.; Magner, E. Rapid in Situ Immobilization of Enzymes in Metal–Organic Framework Supports under Mild Conditions. *ChemCatChem* **2017**, *9*, 1182–1186. [[CrossRef](#)]
29. García, E.R.; Medina, R.L.; Lozano, M.M.; Pérez, I.H.; Valero, M.J.; Maubert Franco, A.M. Adsorption of azo-dye Orange II from aqueous solutions using a metal-organic framework material: Iron- benzenetricarboxylate. *Materials (Basel)* **2014**, *7*, 8037–8057. [[CrossRef](#)]
30. Han, Q.; Wang, Z.; Chen, X.; Jiao, C.; Li, H.; Yu, R. Facile Synthesis of Fe-based MOFs (Fe-BTC) as Efficient Adsorbent for Water Purifications. *Chem. Res. Chin. Univ.* **2019**, *35*, 564–569. [[CrossRef](#)]
31. Guesh, K.; Caiuby, C.A.D.; Mayoral, Á.; Díaz-García, M.; Díaz, I.; Sanchez-Sanchez, M. Sustainable Preparation of MIL-100 (Fe) and Its Photocatalytic Behavior in the Degradation of Methyl Orange in Water. *Cryst. Growth Des.* **2017**, *17*, 1806–1813. [[CrossRef](#)]
32. Huo, S.H.; Yan, X.P. Metal-organic framework MIL-100 (Fe) for the adsorption of malachite green from aqueous solution. *J. Mater. Chem.* **2012**, *22*, 7449–7455. [[CrossRef](#)]
33. Jia, Y.; Jin, Q.; Li, Y.; Sun, Y.; Huo, J.; Zhao, X. Investigation of the adsorption behaviour of different types of dyes on MIL-100 (Fe) and their removal from natural water. *Anal. Methods* **2015**, *7*, 1463–1470. [[CrossRef](#)]
34. Tan, F.; Liu, M.; Li, K.; Wang, Y.; Wang, J.; Guo, X.; Zhang, G.; Song, C. Facile synthesis of size-controlled MIL-100 (Fe) with excellent adsorption capacity for methylene blue. *Chem. Eng. J.* **2015**, *281*, 360–367. [[CrossRef](#)]
35. Zhu, C.; Jiang, C.; Chen, S.; Mei, R.; Wang, X.; Cao, J.; Ma, L.; Zhou, B.; Wei, Q.; Ouyang, G.; et al. Ultrasound enhanced electrochemical oxidation of Alizarin Red S on boron doped diamond(BDD) anode: Effect of degradation process parameters. *Chemosphere* **2018**, *209*, 685–695. [[CrossRef](#)]
36. Hanif, S.; Shahzad, A. Removal of chromium(VI) and dye Alizarin Red S (ARS) using polymer-coated iron oxide (Fe₃O₄) magnetic nanoparticles by co-precipitation method. *J. Nanoparticle Res.* **2014**, *16*. [[CrossRef](#)]
37. Legan, L.; Retko, K.; Ropret, P. Vibrational spectroscopic study on degradation of alizarin carmine. *Microchem. J.* **2016**, *127*, 36–45. [[CrossRef](#)]
38. Srivastava, S.; Sinha, R.; Roy, D. Toxicological effects of malachite green. *Aquat. Toxicol.* **2004**, *66*, 319–329. [[CrossRef](#)]
39. Culp, S.J.; Beland, F.A. Malachite Green: A Toxicological Review. *J. Am. Coll. Toxicol.* **1996**, 219–238. [[CrossRef](#)]
40. Hashimoto, J.C.; Paschoal, J.A.R.; De Queiroz, J.F.; Reyes, F.G.R. Considerations on the use of malachite green in aquaculture and analytical aspects of determining the residues in fish: A review. *J. Aquat. Food Prod. Technol.* **2011**, *20*, 273–294. [[CrossRef](#)]
41. Sacara, A.M.; Nairi, V.; Salis, A.; Turdean, G.L.; Muresan, L.M. Silica-modified Electrodes for Electrochemical Detection of Malachite Green. *Electroanalysis* **2017**, *29*, 2602–2609. [[CrossRef](#)]
42. Pangkumhang, B.; Jutaporn, P.; Sorachoti, K.; Khamdahsag, P.; Tanboonchuy, V. Applicability of iron (III) Trimesic (Fe-BTC) to enhance lignin separation from pulp and paper wastewater. *Sains Malays.* **2019**, *48*, 199–208. [[CrossRef](#)]
43. Du, M.; Li, L.; Li, M.; Si, R. Adsorption mechanism on metal organic frameworks of Cu-BTC, Fe-BTC and ZIF-8 for CO₂ capture investigated by X-ray absorption fine structure. *RSC Adv.* **2016**, *6*, 62705–62716. [[CrossRef](#)]
44. Salazar-Aguilar, A.D.; Vega, G.; Casas, J.A.; Vega-Díaz, S.M.; Tristan, F.; Meneses-Rodríguez, D.; Belmonte, M.; Quintanilla, A. Direct hydroxylation of phenol to dihydroxybenzenes by H₂O₂ and fe-based metal-organic framework catalyst at room temperature. *Catalysts* **2020**, *10*, 172. [[CrossRef](#)]
45. Majano, G.; Ingold, O.; Yulikov, M.; Jeschke, G.; Pérez-Ramírez, J. Room-temperature synthesis of Fe-BTC from layered iron hydroxides: The influence of precursor organisation. *CrystEngComm* **2013**, *15*, 9885–9892. [[CrossRef](#)]
46. Yang, Y.; Bai, Y.; Zhao, F.; Yao, E.; Yi, J.; Xuan, C.; Chen, S. Effects of metal organic framework Fe-BTC on the thermal decomposition of ammonium perchlorate. *RSC Adv.* **2016**, *6*, 67308–67314. [[CrossRef](#)]
47. Dhakshinamoorthy, A.; Alvaro, M.; Chevreau, H.; Horcajada, P.; Devic, T.; Serre, C.; Garcia, H. Iron(iii) metal-organic frameworks as solid Lewis acids for the isomerization of α -pinene oxide. *Catal. Sci. Technol.* **2012**, *2*, 324–330. [[CrossRef](#)]
48. Hasanzadeh, M.; Simchi, A.; Shahriyari Far, H. Nanoporous composites of activated carbon-metal organic frameworks for organic dye adsorption: Synthesis, adsorption mechanism and kinetics studies. *J. Ind. Eng. Chem.* **2020**, *81*, 405–414. [[CrossRef](#)]
49. Niazi, A.; Ghalie, M.; Yazdanipour, A.; Ghasemi, J. Spectrophotometric determination of acidity constants of Alizarine Red S in water, water-Brij-35 and water-SDS micellar media solutions. *Spectrochim. Acta Part A Mol. Biomol. Spectrosc.* **2006**, *64*, 660–664. [[CrossRef](#)]
50. Chin, Y.P.; Abdul Raof, S.F.; Sinniah, S.; Lee, V.S.; Mohamad, S.; Abdul Manan, N.S. Inclusion complex of Alizarin Red S with β -cyclodextrin: Synthesis, spectral, electrochemical and computational studies. *J. Mol. Struct.* **2015**, *1083*, 236–244. [[CrossRef](#)]
51. Cheriaa, J.; Khaireddine, M.; Rouabhia, M.; Bakhrouf, A. Removal of triphenylmethane dyes by bacterial consortium. *Sci. World J.* **2012**, *2012*. [[CrossRef](#)] [[PubMed](#)]

52. Ghodbane, I.; Kherrrat, R.; Zougar, S.; Lamari, R.; Haddadji, R.; Medjram, M.S. Kinetic study and characterization of a platinum electrode/sensitive membrane for malachite green detection. *Sens. Rev.* **2018**, *38*, 335–344. [[CrossRef](#)]
53. Zhang, B.L.; Qiu, W.; Wang, P.P.; Liu, Y.L.; Zou, J.; Wang, L.; Ma, J. Mechanism study about the adsorption of Pb(II) and Cd(II) with iron-trimesic metal-organic frameworks. *Chem. Eng. J.* **2020**, *385*, 123507. [[CrossRef](#)]
54. Mon, M.; Bruno, R.; Ferrando-Soria, J.; Armentano, D.; Pardo, E. Metal-organic framework technologies for water remediation: Towards a sustainable ecosystem. *J. Mater. Chem. A* **2018**, *6*, 4912–4947. [[CrossRef](#)]
55. Embaby, M.S.; Elwany, S.D.; Setyaningsih, W.; Saber, M.R. The adsorptive properties of UiO-66 towards organic dyes: A record adsorption capacity for the anionic dye Alizarin Red S. *Chin. J. Chem. Eng.* **2018**, *26*, 731–739. [[CrossRef](#)]
56. Hasan, Z.; Choi, E.J.; Jhung, S.H. Adsorption of naproxen and clofibric acid over a metal-organic framework MIL-101 functionalized with acidic and basic groups. *Chem. Eng. J.* **2013**, *219*, 537–544. [[CrossRef](#)]
57. Lin, S.; Song, Z.; Che, G.; Ren, A.; Li, P.; Liu, C.; Zhang, J. Adsorption behavior of metal-organic frameworks for methylene blue from aqueous solution. *Microporous Mesoporous Mater.* **2014**, *193*, 27–34. [[CrossRef](#)]
58. Lima, E.C.; Hosseini-Bandegharai, A.; Moreno-Piraján, J.C.; Anastopoulos, I. A critical review of the estimation of the thermodynamic parameters on adsorption equilibria. Wrong use of equilibrium constant in the Van't Hoof equation for calculation of thermodynamic parameters of adsorption. *J. Mol. Liq.* **2019**, *273*, 425–434. [[CrossRef](#)]
59. Li, C.; Xiong, Z.; Zhang, J.; Wu, C. The Strengthening Role of the Amino Group in Metal-Organic Framework MIL-53 (Al) for Methylene Blue and Malachite Green Dye Adsorption. *J. Chem. Eng. Data* **2015**, *60*, 3414–3422. [[CrossRef](#)]
60. Shi, Z.; Li, L.; Xiao, Y.; Wang, Y.; Sun, K.; Wang, H.; Liu, L. Synthesis of mixed-ligand Cu-MOFs and their adsorption of malachite green. *RSC Adv.* **2017**, *7*, 30904–30910. [[CrossRef](#)]
61. Jin, L.; Ye, J.; Wang, Y.; Qian, X.; Dong, M. Electrospinning Synthesis of ZIF-67/PAN Fibrous Membrane with High-capacity Adsorption for Malachite Green. *Fibers Polym.* **2019**, *20*, 2070–2077. [[CrossRef](#)]
62. Li, F.; Zheng, K.; Zhang, H.; Duan, C.; Xi, H. Nanoscale Hierarchically Porous Metal-Organic Frameworks: Facile Synthesis, Mechanism Research, and Application. *ACS Sustain. Chem. Eng.* **2019**, *7*, 11080–11087. [[CrossRef](#)]
63. Wu, X.; Huang, M.; Kong, F.; Yu, S. Short communication: Study on the formation of 2-methylimidazole and 4-methylimidazole in the Maillard reaction. *J. Dairy Sci.* **2015**, *98*, 8565–8571. [[CrossRef](#)] [[PubMed](#)]
64. Schlee, C.; Markova, M.; Schrank, J.; Laplagne, F.; Schneider, R.; Lachenmeier, D.W. Determination of 2-methylimidazole, 4-methylimidazole and 2-acetyl-4-(1,2,3,4-tetrahydroxybutyl)imidazole in caramel colours and cola using LC/MS/MS. *J. Chromatogr. B Anal. Technol. Biomed. Life Sci.* **2013**, *927*, 223–226. [[CrossRef](#)] [[PubMed](#)]
65. Gascón, V.; Jiménez, M.B.; Blanco, R.M.; Sanchez-Sanchez, M. Semi-crystalline Fe-BTC MOF material as an efficient support for enzyme immobilization. *Catal. Today* **2018**, *304*, 119–126. [[CrossRef](#)]
66. Brunauer, S.; Emmett, P.H.; Teller, E. Adsorption of Gases in Multimolecular Layers. *J. Am. Chem. Soc.* **1938**, *60*, 309–319. [[CrossRef](#)]
67. Barrett, E.P.; Joyner, L.G.; Halenda, P.P. The determination of pore volume and area distributions in porous substances. Computations from nitrogen isotherm. *J. Am. Chem. Soc.* **1951**, *73*, 373–380. [[CrossRef](#)]
68. Jamal, M.M.E.; Mousaoui, A.M.; Naoufal, D.M. Effect of Operating Parameters on Electrochemical Degradation of Alizarin Red S on Pt and BDD Electrodes. *Port. Electrochim. Acta* **2014**, *32*, 233–242. [[CrossRef](#)]
69. Yu, S.; Yuan, X.; Yang, J.; Yuan, J.; Shi, J.; Wang, Y.; Chen, Y. Spectrochimica Acta Part A: Molecular and Biomolecular Spectroscopy A chemometric-assisted method for the simultaneous determination of malachite green and crystal violet in water based on absorbance–pH data generated by a homemade pH gradient apparatus. *Spectrochim. Acta Part A Mol. Biomol. Spectrosc.* **2015**, *150*, 403–408. [[CrossRef](#)]
70. Ho, Y.S.; McKay, G. Pseudo-second order model for sorption processes. *Process Biochem.* **1999**, *34*, 451–465. [[CrossRef](#)]
71. Azizian, S. Kinetic models of sorption: A theoretical analysis. *J. Colloid Interface Sci.* **2004**, *276*, 47–52. [[CrossRef](#)] [[PubMed](#)]
72. Qiu, H.; Lv, L.; Pan, B.C.; Zhang, Q.J.; Zhang, W.M.; Zhang, Q.X. Critical review in adsorption kinetic models. *J. Zhejiang Univ. Sci. A* **2009**, *10*, 716–724. [[CrossRef](#)]
73. Lachowicz, J.I.; Delpiano, G.R.; Zanda, D.; Piludu, M.; Sanjust, E.; Monduzzi, M.; Salis, A. Adsorption of Cu²⁺ and Zn²⁺ on SBA-15 mesoporous silica functionalized with triethylenetetramine chelating agent. *J. Environ. Chem. Eng.* **2019**, *7*. [[CrossRef](#)]
74. Mall, I.D.; Srivastava, V.C.; Agarwal, N.K.; Mishra, I.M. Removal of congo red from aqueous solution by bagasse fly ash and activated carbon: Kinetic study and equilibrium isotherm analyses. *Chemosphere* **2005**, *61*, 492–501. [[CrossRef](#)]

Supporting information

Adsorption of Malachite Green and Alizarin Red S dyes using Fe-BTC metal organic framework as adsorbent

Giulia Rossella Delpiano¹, Davide Tocco¹, Luca Medda², Edmond Magner^{3*}, Andrea Salis^{1,4*}

¹ Dipartimento di Scienze Chimiche e Geologiche, Università di Cagliari, Cittadella Universitaria, S.S. 554 bivio Sestu, 09042 Monserrato (CA), Italy; delpiano@unica.it (G.R.D.); davide.tocco@unica.it (D.T.)

² Laboratorio NEST Scuola Normale Superiore di Pisa, 56127 Pisa, Italy; medda.luc@gmail.com

³ Department of Chemical Sciences, Bernal Institute, University of Limerick, Limerick V94 T9PX, Ireland

⁴ Consorzio Interuniversitario per lo Sviluppo dei Sistemi a Grande Interfase (CSGI), Unità Operativa University of Cagliari, Monserrato (CA) 09042, Italy

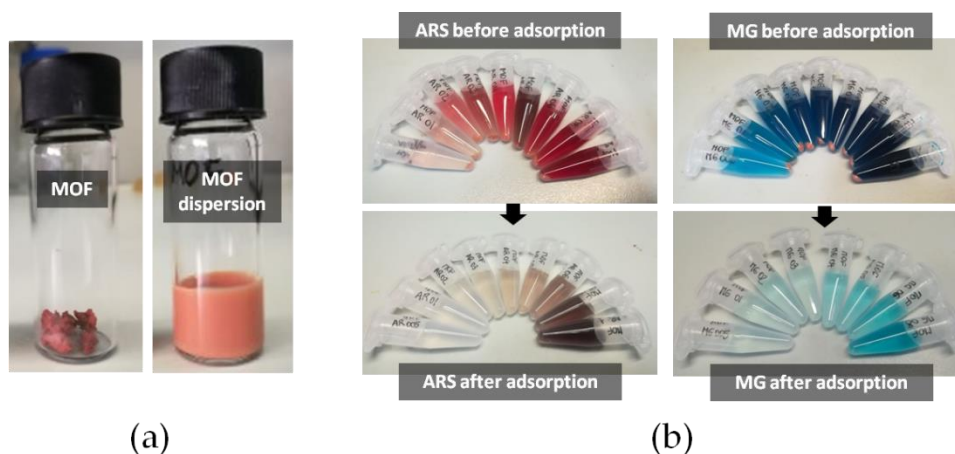


Figure S1 - Images of a) the synthesized MOF before and after dispersion in distilled water; b) Solutions of ARS and MG prior to and after (20 h) adsorption .

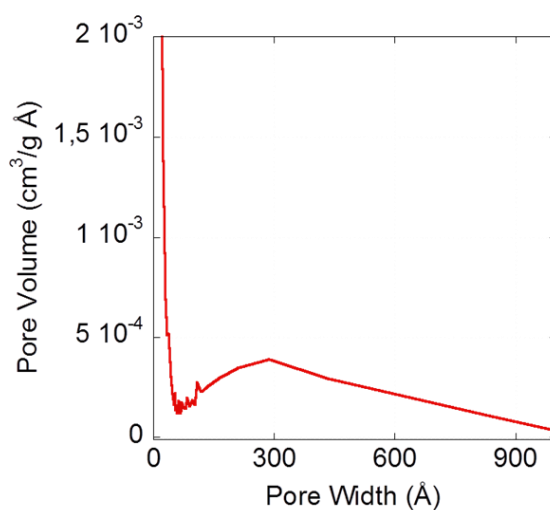


Figure S2 – Pore size distribution (BJH method).

Table S1. Zeta potential of Fe-BTC dispersed in H₂O and the percentage of dyes adsorbed at different pH values (initial concentration of dyes of 1.5 mM).

pH	Fe-BTC Zeta potential (mV)	ARS adsorption%	MG adsorption%
3	+ 6	59.1	89.3
4	- 7	49.2	98.5
5	- 20	31.3	94.7
6	- 28	34.1	93.1
7	-16	23.3	82.9

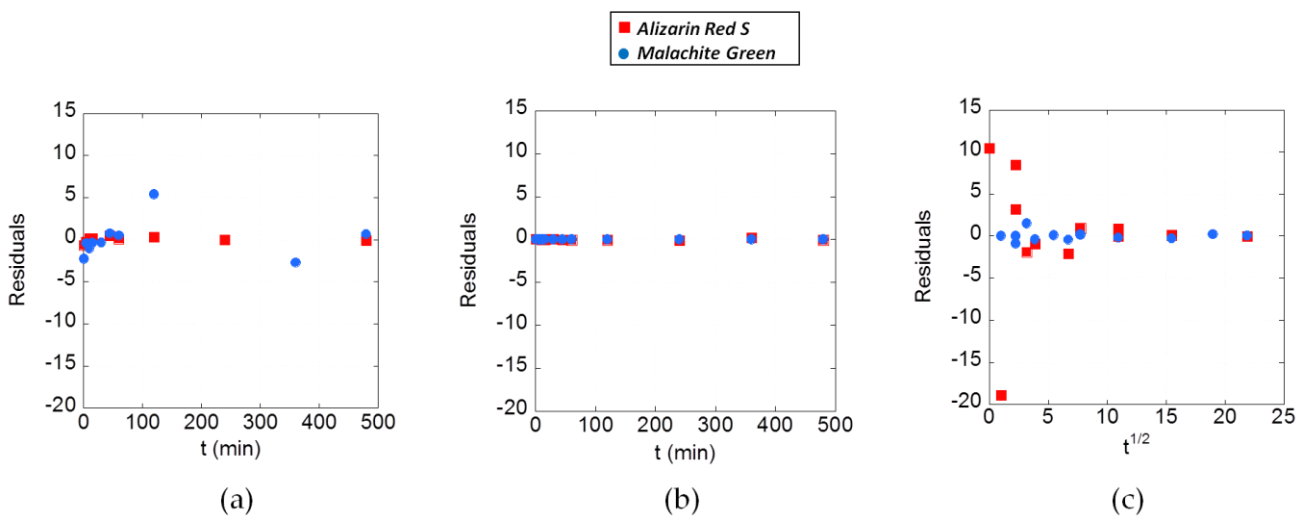


Figure S3 – Residuals graph relative to a) Pseudo-First order, b) Pseudo-Second order and c) Intraparticle diffusion kinetic models.

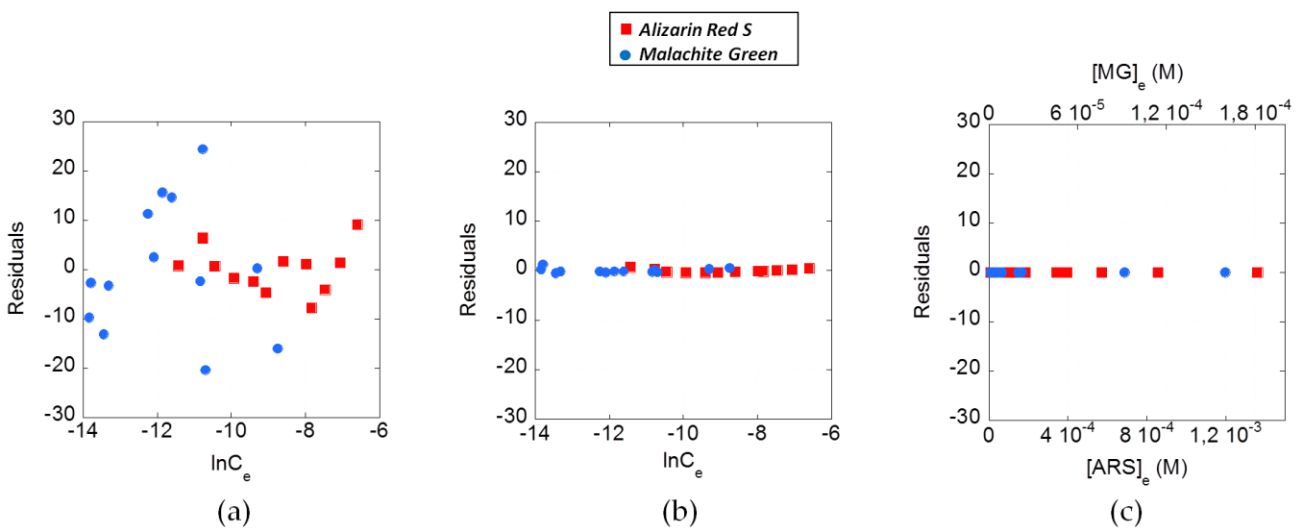


Figure S4 – Residuals graph relative to a) Temkin, b) Freundlich and c) Langmuir isotherms models.

Aknowledgements

I am infinitely grateful to my parents who gave me the opportunity to study at university, for always supporting me and encouraging me to pursue my goals despite the difficulties.

I thank the professors who have been able to instill curiosity in me.

I thank the colleagues who have become friends during this long journey.

I thank my supervisor, Prof. Andrea Salis, for everything he has taught me over the years.

I thank my co-supervisors, Prof. Edmond Magner and Dr. Katia Testa for their infinite openness.

I thank my colleague, Dr. Joanna Lachowicz for her precious collaboration and for making working together so pleasant.

I thank the team of the University of Cluj Napoca, Prof. Graziella Turdean, Prof. Liana Muresan and Dr. Nicoleta Cotolan for welcoming me in their laboratory for a period that, albeit short, I remember with joy.

I thank the students I followed during my PhD, Dr. Debora Todde, Dr. Alessandra Cogoni, Dr. Davide Zanda, Dr. Ionela Petcu, Dr. Giovanni Russo, because they have been a source of great satisfaction for me.

I thank the ex PhD coordinator, Prof. Stefano Enzo, and the current coordinator, Prof. Carla Cannas, for their patience and openness towards me and my colleagues.

I also thank those who will read this thesis, which represents the conclusion of a path that is so important to me.

La borsa di dottorato è stata cofinanziata con risorse del
Programma Operativo Nazionale Ricerca e Innovazione 2014-2020 (CCI 2014IT16M2OP005),
Fondo Sociale Europeo, Azione I.1 "Dottorati Innovativi con caratterizzazione Industriale"

